

Numerical Experiments of Atmospheric Boundary Layer flows: interplay between distributed drag elements and buoyancy effects

THÈSE N° 8409 (2018)

PRÉSENTÉE LE 16 FÉVRIER 2018

À LA FACULTÉ DE L'ENVIRONNEMENT NATUREL, ARCHITECTURAL ET CONSTRUIT
LABORATOIRE DES SCIENCES CRYOSPHERIQUES
PROGRAMME DOCTORAL EN MÉCANIQUE

ÉCOLE POLYTECHNIQUE FÉDÉRALE DE LAUSANNE

POUR L'OBTENTION DU GRADE DE DOCTEUR ÈS SCIENCES

PAR

Varun SHARMA

acceptée sur proposition du jury:

Prof. F. Gallaire, président du jury
Prof. M. Lehning, Prof. M. Parlange, directeurs de thèse
Prof. S. Mobbs, rapporteur
Prof. M. Calaf, rapporteur
Prof. A. Berne, rapporteur



ÉCOLE POLYTECHNIQUE
FÉDÉRALE DE LAUSANNE

Suisse
2018

On any given Sunday
you're gonna win
or
you're gonna lose.
— Tony D'Amato

To Sindhu and Sushi Aaji
and, in the memory of
Kusum Aaji, Dada and Dadaji...

Acknowledgements

This thesis was possible due to the support of a vast array of friends and colleagues who made the journey enjoyable and worthwhile. They could very well be considered as co-authors of the work presented in the following pages. While I shall attempt to put to words, the gratitude I feel towards them, it is quite likely that I shall fall well short in this endeavour and a more talented and equipped writer would perhaps be necessary.

First and foremost I must thank my *team* of thesis advisors, Marc Parlange, Marc Calaf and Michael Lehning. I can never thank Marc Parlange enough for allowing me to join his laboratory, EFLUM, in the first months of my stay at EPFL. I was exposed to a vast array of exciting research projects and scientific questions and sparked my interest in atmospheric turbulence, large-eddy simulations and modelling. I am most thankful that he introduced me to Marc Calaf without whom, my thesis would have never been possible. The long discussions we have had about science and life were a constant source of motivation and nourishment during the long journey that is a doctoral thesis. It has been a great pleasure of mine to work and collaborate with him and his budding team at the University of Utah, particularly Gerard Cortina who incredible energy and passion for science continue to amaze me. I hope we are able to continue working together in the coming years.

As evidenced by the topics in the thesis, I transitioned from studying wind farms to snow-atmosphere interactions particularly drifting and blowing snow. This reflected my growing involvement in the research activities of my new research home "CRYOS", headed by Michael "Michi" Lehning. I thank Michi for welcoming me into CRYOS and exposing me to the cryospheric sciences, a hitherto unknown field for me. His explanations and patience as I grappled with new topics as allowed me to smoothly transition into this exciting new domain and I am certain that we have many years of fruitful work to come.

I am grateful to my thesis jury, led by the jury President, Francois Gallaire, whose fluid mechanics courses I thoroughly enjoyed, Alexis Berne, who agreed to be on my committee and particularly to Steven Mobbs, who in spite of his incredibly busy schedule, travelled to Lau-

Acknowledgements

sanne for the viva-voce and provided an insightful critique of the thesis.

My stay at EPFL and Lausanne started a couple of years before my doctoral thesis as I came here for my masters studies. I was fortunate to have a close-knit group of friends who, in the words of John Keats, *brought Lausanne into existence*. My life here would have certainly been dreary if not for Diego, Allen and Edgar, who were my flatmates at Preverenges, Vijay and Vasia for the laughs, the (*too long* !) discussions and the travels, Ana Karina and Fernando, with whom I had the most incredible vacation in Mexico and Fede, Manu and Catherine for jokes, dinners and random fun!

I must acknowledge my colleagues at the erstwhile EFLUM; Francesco Ciocca, who was my very first research *advisor*, Theophile Mande, Natalie Ceperley, Raphael Mutzner, Marc Diebold, Steven Weijs. A special thank you to Marie-jo who was of immense help during my first few years at EPFL. My time in EFLUM overlapped most significantly with Holly Oldroyd and Marco Giometto with whom I had long conversations about science and research and I am particularly happy to have been able to discuss, share time and learn from them.

Working as a part of CRYOS has been both incredibly fun as well as an enriching experience and I consider myself lucky to be a part of this team. I shared the office with two amazing individuals, Annelen and Tristan and I am forever indebted to them. Many many thanks go out to Don Comola, Johan, Jerome, Adrien, Mahdi and last but certainly not the least, Hendrik, for all the lunches and coffees and the beers at *Satellite*.

It is impossible for me to thank enough my parents for the journey thus far, and to my brother, who fortunately chose to come to Lausanne for his studies and giving me the joy of living together after many years apart. I am thankful to Sindhu and Sushi Aaji for all that they have done for me. This thesis is dedicated to them and to the memory of my grandparents.

Finally, I thank Celine for the love and support during the course of my thesis without which I found have found it impossible to finish. I can assure her that I am working very hard to improve my movie suggestions!

And so, it begins ...

Lausanne, The fifth day of February, 2018

V.

Abstract

Anthropogenic emissions of greenhouse gases due to human activity is causing global warming and inducing climate change. A major implication of global warming is the decreasing ice mass in the polar regions resulting in sea-level rise. It is now known that sublimation of drifting and blowing snow is one of the dominant terms of the mass balance of Antarctica. There are various efforts underway to curtail greenhouse gas emissions and mitigate the impact of global warming. One of the most promising solutions involves using non-polluting renewable sources of electricity. Global wind energy estimates have been shown to be far in excess of current and projected energy requirements. From a fluid dynamics perspective, turbulence in the lowest region of the atmosphere, known as the Atmospheric boundary layer (ABL) exerts significant control on both wind energy extraction systems as well as drifting and blowing snow particles, both of which can be considered as distributed drag elements that act as a sink of momentum.

The first part of the thesis is concerned with large-eddy simulations (LES) of the turbulent, time-varying ABL with an immersed wind farm. First, a new time-adaptive wind turbine model for LES is introduced that enables the wind turbines to yaw and realign with the incoming wind vector, similar to real wind turbines. The performance of the new model is tested with in a neutrally-stratified ABL forced with a time varying geostrophic wind as well as a synthetic time-changing thermal ABL. Next, the effect of extensive terrestrial wind farms on the spatio-temporal structure of the diurnally-evolving ABL is explored. It is shown that extensive wind farms substantially perturb the vertical structure of the stable boundary layer and the dynamics of the 'morning' transition. The effect of these perturbations on the potential power output of an extensive wind farm output is also analysed. Finally, flow characteristics through finite-sized wind farms and the influence of the wind-farm configuration on modulating this evolution is explored using LES. The principal aim for this part of the thesis is to identify regions of flow-adjustment and flow equilibrium within the wind farm. Three diagnostic variables, namely, the wind-farm induced effective surface roughness, the wake viscosity and the wake-expansion coefficient are also computed using the LES-generated database and are used to characterize the flow.

Abstract

In the second part of the thesis, LES of drifting and blowing snow are performed with the aim of calculating sublimation of saltating snow grains. The Thorpe and Mason [1966] model for calculating the mass lost from a sublimating snow grain is the basis of all existing estimates of drifting snow sublimation. This model is revisited to test its validity for saltating snow grains. It is shown that residence times for saltating snow grains are such that using the steady-state model of sublimation losses by the Thorpe and Mason (TM) approach is questionable. Furthermore, the residence times were found to be independent of the imposed pressure gradient and buoyancy. The relaxation time needed for the unsteady mass loss rate to reconcile with the TM solution is found to be comparable to typical residence times for saltating grains and the resulting errors due to use of the TM approach are quantified.

Keywords: Atmospheric Boundary Layer; Large-eddy Simulation; Wind Energy; Drifting and Blowing Snow; Sublimation

Résumé

Les émissions de gaz à effet de serre dues à l'activité humaine sont responsables de profonds changements climatiques, notamment du réchauffement de la planète. Une des conséquences majeures de ce réchauffement est la fonte des glaces polaires et l'augmentation du niveau de la mer que cela cause. Il est aujourd'hui établi qu'une partie importante de l'érosion de la couche neigeuse de l'Antarctique provient de la sublimation des particules de neige en saltation ou en suspension turbulente. De nombreuses initiatives existent cherchant à réduire les émissions de gaz à effet de serre et à limiter le réchauffement climatique, notamment en augmentant la part d'électricité produite par des énergies renouvelables et non-polluantes. Dans cette optique, les ressources potentielles d'énergie éolienne dépassent de loin les besoins énergétiques actuels et futurs. Les deux processus discutés ici, l'extraction d'énergie éolienne et la sublimation de la neige en suspension ou saltation, sont fortement influencés par les échanges turbulents de la région la plus basse de l'atmosphère, la couche limite atmosphérique (CLA). Du point de vue mécanique aussi bien les champs d'éoliennes que les particules de neige peuvent être considérés comme des sources discrètes de traînée, donc des puits de quantité de mouvement.

La première partie de cette thèse s'intéresse aux simulations numériques Large-Eddy Simulations (LES) des échanges turbulents de la CLA ainsi que de ses variations temporelles au-dessus d'un champ d'éoliennes. J'introduis dans un premier temps un nouveau modèle adaptatif de turbine éolienne pour les LES qui permet un réalignement dynamique des turbines avec la direction incidente du vent, et l'ajustement de l'angle de lacet, comme dans les turbines réelles. Ce modèle est testé dans un flux atmosphérique stratifié de façon neutre, avec un vecteur de vent géostrophique ainsi qu'une couche limite atmosphérique artificielle qui varient dans le temps. J'étudie ensuite les effets de champs d'éoliennes terrestres extensifs sur la structure spatio-temporelle des cycles diurnes de la CLA. Je montre en particulier que de très grands champs d'éoliennes perturbent la structure verticale d'une CLA stable ainsi que la dynamique des transitions matinales. Les effets de ces perturbations sur la puissance potentielle générée par ces champs étendus d'éoliennes sont ensuite analysés. Pour finir, j'explore les caractéristiques du flux à travers de champs d'éolienne finis, et l'influence de la configuration de ces champs sur son évolution avec des LES. L'objectif principal de cette

Résumé

partie du travail est d'identifier les régions d'ajustement et d'équilibrage du flux dans les champs d'éolienne. Trois variables sont utilisées pour cela : la rugosité de surface effective, la viscosité de sillage, et le coefficient d'expansion de sillage, tous trois calculés à partir des données générées par les LES.

La seconde partie de la thèse traite de la sublimation de particules de neige en saltation et en suspension à partir de LES. Actuellement, le modèle le plus répandu pour calculer la masse de neige en suspension perdue par sublimation est celui de Thorpe et Mason [1966]. Il est utilisé pour des prédictions à petite et grande échelle de la perte de masse neigeuse dans les régions polaires et alpines. Je revisite ce modèle et teste sa validité pour les particules de neige en saltation. Je montre que les temps de résidence des particules de neige dans un flux turbulent sont tels, que cela remet en cause l'hypothèse de pertes stationnaires lors de la sublimation, comme supposé dans le modèle de Thorpe et Mason (TM). Les temps de relaxation qui seraient nécessaires pour permettre au taux de perte de masse de retomber aux valeurs trouvées par la solution TM sont du même ordre que les temps de résidence typiques pour des particules en saltation. L'erreur due à l'approche TM est quantifiée à la fin de cette partie.

Mots Clés : Couche limite atmosphérique ; Simulation des Grandes Échelles ; Énergie éolienne ; Transport éolien de la neige ; Sublimation

Contents

Acknowledgements	v
Abstract (English/Français)	vii
Introduction	1
I	19
1 An LES model for a time-adaptive wind turbine	21
1.1 Introduction	21
1.2 The Large Eddy Simulation approach	23
1.3 The time-adaptive wind turbine algorithm	26
1.4 Study Cases	31
1.5 Study case (A): Imposed time varying geostrophic wind under a neutral atmospheric stratification	32
1.6 Study Case (B): A diurnal cycle	34
1.7 Conclusions	38
2 Perturbations to the spatial and temporal characteristics of the diurnally-varying atmospheric boundary layer due to an extensive wind farm	45
2.1 Introduction	45
2.2 Methodology and Validation	49
2.2.1 Description of Large-eddy Simulations	49
2.2.2 Simulations and Validation using CASES-99 dataset	50
2.3 Evolution of the diurnally-varying ABL	52
2.4 Analysis	60
2.4.1 Mean Kinetic Energy Budget	60
2.4.2 Formation and Growth of the CBL	61
2.4.3 Phenomenology of the Low-level Jet	64

Contents

2.4.4	Effective Roughness Lengths of a wind farm during a diurnally varying ABL	67
2.5	Summary and Conclusions	70
3	Evolution of flow characteristics through finite-sized wind farms and influence of turbine arrangement	81
3.1	Introduction	81
3.2	Theoretical framework	83
3.2.1	Wake models and the wake-expansion coefficient	83
3.2.2	Wind-farm induced effective surface roughness and wake-viscosity	85
3.2.3	Extension to finite-sized wind farms	86
3.3	Large eddy simulation and study cases	88
3.3.1	Simulation Details	88
3.3.2	Post-processing of LES output	90
3.4	Results	90
3.4.1	Evolution of Mean and Turbulent Flow Quantities	90
3.4.2	The wind-farm induced effective surface roughness	96
3.4.3	The wake-expansion coefficient	98
3.5	Discussion and Conclusions	99
II		105
4	Large-eddy simulation of drifting and blowing snow	107
4.1	Introduction	107
4.2	Flow equations	107
4.2.1	SGS model	108
4.2.2	Lower-boundary condition for Eulerian quantities	109
4.3	Surface-flow coupling	109
4.3.1	Aerodynamic entrainment	110
4.3.2	Rebound and splash entrainment	111
4.4	Dynamics of particles in flow	112
4.5	Numerics	114
4.6	Conclusions	115
5	On the suitability of the Thorpe-Mason model for calculating sublimation of saltating snow	119
5.1	Introduction	119
5.2	Comparison between NUM and TM solutions: EXPERIMENT I and II	122
5.3	Large-eddy simulations of saltating snow	124
5.3.1	Experiment III and IV: simulation details	124
5.3.2	Results	126
5.4	Discussion and conclusion	129
	Summary and Conclusions	136

A Perturbation to a stratocumulus-topped boundary layer due to a very large wind farm	143
A.1 Introduction	143
A.2 Simulation details	144
A.3 Results	145
A.3.1 Perturbations to the cloud field	145
A.3.2 Some profiles of mean and turbulent statistics	146
A.4 Conclusions	148
B Mean kinetic energy of finite sized wind farms	149
B.1 Introduction	149
B.2 Theoretical framework	149
B.3 Results	152
B.3.1 Portrait of mean and turbulent quantities for a representative case	152
B.3.2 Identification of relevant flow regions using MKE budgets	154
B.3.3 MKE budget within the windfarm	159
B.4 Conclusions	165
Curriculum Vitae	169

Introduction

Climate Change - from implications to mitigation

There is currently an extraordinary churning in the scientific, economical and political spheres of our lives as we take cognizance of the changing climate of our planet, its causes, wide ranging implications in agriculture, energy and ecology, and the possible solutions for adaptation and mitigation of the emerging challenges. There is over all, broad agreement in the scientific community that climate change is attributable to human activity, and is occurring at such a rapid pace that possible solutions to mitigate its impact can potentially upend the established systems of economic activity and progress that commenced with the Industrial Revolution two centuries ago. The Intergovernmental Panel on Climate Change (IPCC), in its Fifth Assessment Synthesis Report [Pachauri et al., 2014], unequivocally states: “Human influence on the climate system is clear and recent anthropogenic emissions of greenhouse gases are the highest in history. Recent climate changes have had widespread impacts on human and natural systems.”

In the sphere of energy production, curtailing emissions of greenhouse gases due to generation of electricity is seen as highly promising with non-polluting, renewable sources of electricity becoming increasingly widespread in the past three decades. Wind energy in particular has been identified as a bountiful resource that is sufficient in meeting a large fraction of the global electricity requirements [Jacobson and Archer, 2012]. Wind energy extraction systems are advancing rapidly due to innovation in multiple domains, ranging from better turbine blade design [Sørensen, 2011, Schubel and Crossley, 2012] and improved rotor systems [Chalmers and Spooner, 1999] to new materials allowing for ever larger turbines [Brøndsted et al., 2005] and offshore construction technology to extend wind farms farther away from the coasts [Roddier et al., 2010]. Experience from the first generation of wind farms built in the North Sea in the 1970s highlighted the meteorological and fluid-dynamical controls on wind farm efficiency and present-day efforts benefit greatly from improved wind farm design based on high-fidelity simulation tools available both for fluid-structure interaction [Churchfield et al., 2012] and weather forecasting [Roulston et al., 2003].

With regards to the implications of climate change, the IPCC report [Pachauri et al., 2014]

Introduction

further states: “Warming of the climate system is unequivocal, and since the 1950s, many of the observed changes are unprecedented over decades to millennia. The atmosphere and ocean have warmed, the amounts of snow and ice have diminished, and sea level has risen.” The sea level rise in particular is attributed to loss of snow and ice content particularly from Antarctica, which contains the largest stockpile of freshwater in the world. It has been shown comprehensively that the mass loss from Antarctica is intimately linked to sea-level rise in the past century [Rignot et al., 2011]. Upon further analysis, drifting and blowing snow has, in the past decade been identified as one of the dominant terms of the mass balance of Antarctica, particularly in the coastal plains and the adjoining slopes that connect to the high plateau [Van den Broeke et al., 2004, van den Broeke et al., 2006]. This is true at hourly, daily, monthly and yearly time-scales.

Understanding and predicting atmospheric motions is at the core of tackling global warming and climate change. This is particularly true of the lowest region of the atmosphere, which is also of most consequence to our lives. It is here that we carry out most of our economic activity, grow crops that sustain our population, inhabit and use vast human-built infrastructures. This region is also where all of the anthropogenic emissions and pollutants originate and are transported, wind farms operate to generate electricity and drifting and blowing snow occur. The defining feature of this layer is the ubiquitous presence of turbulence at scales ranging from a few millimetres to a few kilometres at the tropics. This is reflected by its name as the Atmospheric Boundary Layer (ABL). Turbulence in the ABL is essentially an interplay between shear in the flow and buoyancy forces. Shear in the flow principally comes from friction at earth’s surface and creates instabilities that propagate throughout the ABL. Buoyancy forces are driven by the heating and cooling of the earth’s surface, which acts as a lower boundary of the ABL. The highly turbulent nature of the ABL implies fast mixing and rapid transport of heat, moisture and other scalars. This fact also makes it imperative for researchers studying transport processes in the ABL to have a firm grasp over the origin and nature of turbulence.

Wind turbines with dimensions $\mathcal{O}(100\text{ m})$ and snow particles being transported by the air with dimensions $\mathcal{O}(100\ \mu\text{m})$ can both be considered as distributed drag elements that act as a sink of momentum and increase the friction in the ABL. Snow particles additionally exchange heat and mass with the surrounding air. The perturbations induced by the presence of wind turbines and particles in the flow interact non-linearly with background shear and buoyancy and these perturbations can either be damped or amplified to result in large-scale effects with important consequences.

Numerical weather prediction and climate modelling has often been considered as the *holy grail* of scientific computing since the advent of computers and their utilization for scientific research. Work on numerical methods, global atmospheric measurement systems and global warming and climate change have had a deep symbiotic relationship with challenges and improvements in one area often spurring development in the others. It is remarkable for example to note that simulating the weather was one of the earliest tasks given to the first general-purpose ‘computer’ [see Charney et al., 1950, who used the ENIAC at the United States Army’s Ballistic Research Laboratory]. Relatively soon after the pioneering work of Phillips

[1956] who performed the first General Circulation Model (GCM) simulation, Manabe and Wetherald [1975] and Hansen et al. [1981] showed that doubling carbon dioxide levels results in 1.5-4 degree centigrade rise in mean global temperatures. Discovery of global warming and improved understand of its implications are a result of continual development and use of GCM models in the past five decades.

The development of the GCM models inspired the earliest large-eddy simulation (LES) models which had its advent for the purpose of meteorological applications [Deardorff, 1970c] and has since revolutionized fluid dynamics research in many different domains. While both the LES and the GCMs solve the Navier-Stokes equations, they utilize different formulations relevant to the scales being simulated. Furthermore, the GCM is typically used to solve a boundary-value problem while the LES is used to solve initial-value problems. The largest scales simulated by a typical LES, $\mathcal{O}(1000\text{ m})$, are usually an order of magnitude smaller than the smallest scales resolved by a typical GCM $\mathcal{O}(10\text{ km})$. The LES is able to make use of the scale-invariance property of turbulence in the inertial sub-range to parametrize small-scale (subgrid-scale) motions and is thus used for micro-meteorological problems in the ABL. On the other hand, GCMs employ semi-empirical formulations for subgrid-scale mixing and are used for simulating much longer time scales covering the entire globe. Thus, due to the scale separation, GCMs and LESs have been quite independent in their development and utilization.

This thesis uses state-of-the art LES models for understanding the interaction between the turbulent ABL and wind farms on one hand and simulating the sublimation of drifting and blowing snow on the other. The former is crucial for mitigation of the implications due to global warming and climate change, while the latter is a critical process in the mass balance of Antarctica and the associated sea-level rise. In the following section, the state of the research of three topics, namely, large-eddy simulations of atmospheric flows, wind energy extraction in the atmospheric boundary layer and sublimation of drifting and blowing snow, is described.

State of Research

Large-eddy simulations of Atmospheric Flows

The main principle of the large-eddy simulation (LES) technique is that one explicitly solves for the large scales of the flow while the small scales are modelled using what are known as subgrid-scale (SGS) or subfilter-scale models. The theoretical foundations of the LES are based on two hypotheses of Kolmogorov [1941b,a], which state the universality of small-scale motions and the existence of a cascade of energy from large scales to the small scales through an inertial subrange. The larger scales of motion are responsible for production of energy as well as for transport of momentum, temperature and moisture across the ABL. Furthermore, it is the larger scales that show variation depending upon the boundary conditions, such as geometry of the boundaries, fluxes of heat and moisture and surface drag. The smallest scales, that is scales beyond the inertial subrange are considered to be isotropic in nature. They are universal in all turbulent flows and are not affected by the boundary conditions.

Introduction

LES is accomplished by *low-pass filtering* of the Navier-Stokes equations and using resolved-scale flow quantities to parametrize the effect of the filtered smaller scales. The distinguishing features of an LES model for the ABL are the assumptions of hydrostatic balance, incompressibility of the flow and use of similarity solutions as boundary conditions for the lower boundary. The first ever LES model is attributed to the work of Deardorff [1970a,b,c] in simulating the ABL. An important improvement was that by Moeng [1984], Albertson and Parlange [1999a] and Albertson and Parlange [1999b] who introduced the pseudospectral collocation approach of Orszag [1969] to LES. Following these pioneering efforts, the LES-based methodology has been successfully applied to study a wide range of ABL phenomena from flow over internal boundary layers [Albertson and Parlange, 1999b], stratified boundary layer problems [Kumar et al., 2009], flows around vegetation canopies [Yue et al., 2007], pollen transport [Chamecki et al., 2009], flow in urban and sub-urban environments [Giometto et al., 2016] and many others. The LES methodology has thus become a mainstay of research of the ABL in the past two decades.

The SGS model, which lies at the heart of any LES technique has seen tremendous improvement from the first closure scheme by Smagorinsky [1963], which used the concept of constant turbulent eddy viscosity, to the development of scale-aware dynamic eddy-viscosity models that make use of the Germano Identity [Germano, 1992]. In this thesis, the Lagrangian scale-dependent dynamic Smagorinsky (LASD) model of Bou-Zeid et al. [2005] is used. This model essentially applies the Germano Identity to Lagrangian parcels of fluid. There exist a wide variety of SGS models apart from those based on the eddy-viscosity concept such as the similarity models [Bardina et al., 1980, Stolz and Adams, 1999], the classic approach of Deardorff [1973] in solving a SGS TKE equation and vorticity based methods [Misra and Pullin, 1997]. A completely different approach that uses only numerical dissipation to represent molecular viscous dissipation is known as the implicit LES [Grinstein et al., 2007].

Wind Energy Extraction in the Atmospheric Boundary Layer

The most widespread technology for extracting and producing large-scale energy from atmospheric flows is the use of arrays of horizontal axis wind turbines. Understanding the interaction between wind farms and the background turbulent flow has advanced through a variety of different approaches - wind tunnel experiments with scaled models, mast-measurements in existing wind farms, development of analytical models as well as numerical simulations. These studies have been motivated and targeted towards different goals and end-users, primarily wind energy companies aiming to maximize electricity generation from wind farm installations and meteorologists attempting to understand the effect of wind farms on the climate at micro- and meso- scales.

Beginning with the classic work of Betz [see Snel, 2003, Vermeer et al., 2003, for review] on general single rotor aerodynamics, and the seminal contributions of Jensen [1983] towards applying those principles to wind turbines, initial studies focused on modelling the mean-flow of the wake downstream of a single wind turbine. These so called 'wake-models' were extended and applied to the complicated scenario of multi-turbine wind farms where nonlinear wake-

turbine and wake-wake interactions dominate the flow. These models, though being semi-empirical, with a multitude of tuning parameters, remain extremely popular within the wind-energy industry, due to their simplicity and low computation development and cost. A notable improvement in the tools employed by the wind-energy industry in the past decade is the use of Reynolds-averaged Navier-Stokes (RANS) solvers. A majority of these solvers utilize eddy-viscosity closure models suitably tuned to account for the presence of the wind turbines, following the pioneering study of Ainslie [1988]. Further development of these models remains an important area of research, an example of which, is the development of the dynamic wake meandering model of Larsen et al. [2008]. These developments have helped wind farm owners in identifying profitable sites for wind farm installation, optimizing the spacing of wind turbines and predict maintenance costs on account of turbulence.

Another branch of research is aimed at computing the global wind-power potential and the possible effects of large-scale wind-farm deployment on climate dynamics. Studies such as Keith et al. [2004], Barrie and Kirk-Davidoff [2010] and Wang and Prinn [2010] used general circulation models (GCMs) and used the concept of enhanced surface roughness to model the effect of large wind farms [Frandsen, 1992, Calaf et al., 2010, Meneveau, 2012]. Numerical studies at similar scales have also focussed on understanding the perturbations induced by wind farms on weather and climate. The goal of these studies was to understand potential impact of wind farms on the surface energy budgets and the local hydro-meteorology. Studies by Roy et al. [2004], Kirk-Davidoff and Keith [2008] and Roy and Traiteur [2010] found that large wind farms modify the surface sensible and latent heat fluxes resulting in lower air temperatures during daytime and warmer air temperatures at nighttime.

Differences in the aim and scope of each of such studies has required different research methodologies. For example, the earliest wake models were tested and calibrated using limited point-measurements from offshore wind farms and wind tunnel experiments. On the other hand, in the numerical studies mentioned above, mesoscale and global circulation models have been used wherein wind farms have been parametrized either as elevated sinks of mean kinetic energy and sources of turbulence or as enhanced surface roughness. A common feature of all these different approaches has been the low fidelity of the the turbulent flow-field information, either due to the lack of sufficient experimental data, limitations of measurement techniques, or simplified turbulence representation in numerical models.

Within this context, the introduction of the LES as a tool to study wind farm-ABL interaction is a comparatively new and major development and is rapidly being applied to the whole spectrum of problems discussed above, i.e, from single blade aerodynamics to influence of wind turbines at atmospheric mesoscales. Improvements in SGS modelling discussed in the previous section have played a major role in allowing for accurate simulations of wind farms immersed in the ABL. Validation of the LES results with detailed wind tunnel experiments has proven to be extremely successful [Cal et al., 2010, Wu and Porté-Agel, 2011] and given credence to its suitability as an wind farm design tool [Goit and Meyers, 2015]. However, LES is a computationally expensive technique with current use limited to academia and research groups. Initially, LES-based work was performed in the idealized setting of an 'infinite' wind

farm [Calaf et al., 2010]. More recently, LES of finite-sized wind farms have also been performed [Stevens et al., 2015, Abkar et al., 2016, Allaerts and Meyers, 2017].

Sublimation of Drifting and Blowing Snow

The earliest studies on understanding the causes and implications of drifting and blowing snow were motivated by its influence on the hydrology in latitudes which receive significant precipitation in the form of snow. It was discovered that sublimation losses were responsible for taking away vast quantities of precipitating snow [Tabler, 1975]. Schmidt [1972] put forth perhaps the first model for sublimation of drifting and blowing snow based on an earlier study of sublimation of solitary ice grains by Thorpe and Mason [1966]. Over time, studies uncovered various aspects of sublimation rates from drifting and blowing snow and its dependence on the effect of air speed, temperature and relative humidity and grain size distribution. Lee [1975] introduced the concept of *ventilation* to account for turbulent exchange of heat and mass. Since the time of the earliest polar explorers, scientists have noticed the ubiquitous, unidirectional wind with large drifting and blowing snow. Beginning with the pioneering study by Budd [1966] who measured the particle size distributions of drifting and blowing snow in Antarctica, the continent has served as a vast laboratory for understanding mechanisms of aeolian transport of snow, with study by Mann et al. [2000] being perhaps the most comprehensive field experiment till date on computing sublimation from snow in transport. Due to increasing concerns of climate change, there is an increased interest in computing sublimation in Antarctica. Large-scale modelling studies have shown the importance of sublimation of blowing snow on the mass balance [Gallée et al., 2001, van den Broeke et al., 2006, Lenaerts et al., 2012, Barral et al., 2014].

Understanding the mechanics of the aeolian transport of snow have benefited greatly from research in allied subjects such as sand transport in deserts and sediment transport in river beds. Turbulent transport of granular material originating at the surface can be classified into two modes, namely, saltation and suspension. Saltation consists of the *heavier* particles being transported along the surface via short, ballistic trajectories with heights less than 10 cm and involves mechanisms of rebound and splashing of grains [Doorschot and Lehning, 2002, Comola and Lehning, 2017]. Suspension on the other hand refers to transport of *lighter* grains at higher elevations and over large distances without contact with the surface. As a first-order approximation, particles in suspension follow the turbulent air flow and this fact makes modelling of suspension far easier than saltation.

Both saltation as well as suspension of grains commence with aerodynamic entrainment of these particles when the shear stress at the surface exceeds a threshold value. Bagnold [1941] provided an early model for aerodynamic entrainment by linking the threshold shear stress with the particle diameter and density and the fluid density. The empirical coefficients in this model have since been adjusted for snow by Clifton et al. [2006]. Anderson and Haff [1991] developed a model for rebound entrainment using extensive computer simulations. For a long time, the parametrizations for splash entrainment were purely empirical [Anderson and Haff, 1991, Shao and Li, 1999, Sugiura and Maeno, 2000] that were deduced from a large number

of wind tunnel and computational experiments. Finally, Kok and Renno [2009] developed a physically based model based on conservation of mass and momentum and using principles of statistical mechanics. Snow surface erosion is distinct from that of sand due to greater heterogeneity of the particle diameters and strong cohesion forces between the snow particles. Schmidt [1980] modified the formulation by Bagnold [1941] for snow to account for cohesion and elasticity of snow grains. A major improvement in splash entrainment for heterogeneous granular surfaces with cohesive grains and particularly snow was put forth recently by Comola and Lehning [2017].

The earliest simulations of sublimation of drifting and blowing snow extended the models of Thorpe and Mason [1966] and Schmidt [1972] and combined these with boundary layer flow solvers based on RANS and surface-flow coupling as described in the previous paragraph. Notable examples are the Prairie Blowing Snow Model (PBSM) by Pomeroy et al. [1993] and the PIEKTUK by Déry and Yau [1999]. An updated version of the PIEKTUK that formulates a double-moment Eulerian transport scheme of snow [Déry and Yau, 2001] is the foundation of blowing snow models in popular large-scale models such as RACMO [Lenaerts et al., 2012] and Meso-NH [Vionnet et al., 2014]. These models have been used extensively to compute the mass balance of Antarctica at regional and continental scales.

The first fully-coupled simulations of saltation in an turbulent flow were performed using Reynolds-averaged flow solvers (RANS) [Shao and Li, 1999, Nemoto and Nishimura, 2004, Almeida et al., 2007] that simulated only the mean velocity and used statistical models to characterize turbulence. Groot Zwaaftink et al. [2011] coupled a thermodynamic snowpack model with a RANS-type flow solver to calculate snowdrift sublimation in complex terrain and found a 10% reduction in snow deposition on leeward slopes due to sublimation. Following the work of Vinkovic et al. [2006], Dupont et al. [2013] in formulating LES models for sand saltation, Groot Zwaaftink et al. [2014] implemented the first LES-saltation model for snow using an Eulerian-Lagrangian, two-way coupled flow-snow particle transport solver which included advanced stochastic models of aerodynamic, rebound and splash entrainment. Recent studies by Dai and Huang [2014], Huang et al. [2016], Huang and Wang [2016] have extended Groot Zwaaftink et al. [2014]’s model in an attempt to compute sublimation losses in the snow saltation layer.

Objectives and Organization of the thesis

The objectives of the thesis are to perform very high resolution large-eddy simulations of the atmospheric boundary layer for two distinct scenarios, both involving distributed drag elements in the presence of buoyancy forces. In the first scenario, simulations of very-large (or *infinite*) wind farms immersed in a transient ABL are performed and analysed. Quasi-steady flow scenarios for different stable [Lu and Porté-Agel, 2011, Aitken et al., 2014, Abkar and Porté-Agel, 2015, Bhaganagar and Debnath, 2015] and unstable conditions [Lu and Porté-Agel, 2015] for wind farms have been explored recently using LES. Atmospheric flow is however by nature, transient and thus one of the main focus of the thesis is to study the impact of wind farms on

Introduction

the diurnal cycle, which is a continual process of formation, growth, quasi-stationarity and ultimately decay of the convective boundary layer (CBL) followed by a similar cycle for the stable boundary layer (SBL). During the course of a diurnal cycle, winds change both their magnitude and direction substantially. Thus, before performing simulations of a diurnally-varying ABL, a new wind turbine model for LES was developed that allowed for the yawing of the plane of rotation to accurately capture the interaction between such a time-varying ABL flow and the immersed wind turbines. Additional work was done to simulate a neutral ABL flow over a finite-sized wind farm to study the formation and growth of the internal boundary layer due to the drag imposed by the turbines and to ultimately compare the results with those from flows over *infinite* wind farms.

In the second scenario, simulations of sublimation drifting and blowing snow are performed with a focus on saltating ice grains. Most modelling studies of sublimation of snow in motion have been done using mesoscale models that are too coarse to resolve the length and time scales required to simulate saltating snow grains. In fact, in these studies, only sublimation of grains in suspension is computed and it is assumed that the saltation layer is saturated and thus there is no sublimation from grains in saltation. Recently, this view has been challenged using LES [Dai and Huang, 2014, Huang and Wang, 2016] who showed that sublimation losses in the saltation layer are not negligible, particularly for wind speeds close to the threshold velocities for aeolian transport, wherein a majority of aeolian snow transport occurs via saltation rather than suspension. However, these LES studies use the classic equilibrium model of Thorpe and Mason [1966] to compute mass loss from a snow grain, similar to the mesoscale models mentioned earlier. The objective in this thesis is to question the use of the Thorpe and Mason formulation for sublimation from saltating ice grain.

The thesis is organized into two parts, with the Part I consisting of three chapters pertaining to LES of wind farms while Part II consists of two chapters regarding the LES of drifting and blowing snow undergoing sublimation. The chapters are organized as below:

- **Chapter 1:** In this chapter, a new large eddy simulation model for time-adaptive wind turbines is introduced. The new algorithm enables the wind turbines to dynamically realign with the incoming wind vector and self-adjust the yaw orientation with the incoming wind vector similar to real wind turbines. The performance of the new model is tested, firstly with a neutrally stratified atmospheric flow forced with a time varying geostrophic wind vector and secondly with a synthetic time-changing thermal atmospheric boundary layer.
- **Chapter 2:** The effect of extensive terrestrial wind farms on the spatio-temporal structure and dynamics of the diurnally-evolving atmospheric boundary layer is explored in this chapter. High-resolution large-eddy simulations of a realistic diurnal cycle with an embedded wind farm are performed using the time-adaptive wind turbine model developed in Chapter 1. Simulations are forced by a constant geostrophic velocity with time-varying surface boundary conditions derived from a selected period of the CASES-99 field campaign.

- **Chapter 3:** Evolution of flow characteristics through finite-sized wind farms and the influence of the wind-farm configuration on modulating this evolution is explored through numerical simulations. The principal aim for the study is to identify regions of flow-adjustment and flow equilibrium within the wind farm. Towards this aim, a suite of five large-eddy simulations (LES) of the neutral atmospheric boundary layer with extremely long streamwise domains are performed with embedded finite-sized wind farms of different streamwise and spanwise spacing. Three diagnostic variables, namely, the wind-farm induced effective surface roughness, the wake viscosity and the wake-expansion coefficient are computed using the LES-generated database and are used to characterize the flow.
- **Chapter 4:** A detailed description of the LES model for simulating sublimation of drifting and blowing snow is provided in this chapter. The Navier-Stokes equations are solved in the Eulerian frame of reference along with Lagrangian particles that enter the flow due to aerodynamic, rebound and splash entrainment. The entrainment mechanisms are modelled using stochastic parametrizations derived from theory. Two models for sublimation of ice grains are implemented with one being the classic model of Thorpe and Mason [1966] while the other is the heat and mass balance equations of individual ice grains.
- **Chapter 5:** The Thorpe and Mason (TM) model for calculating the mass lost from a sublimating snow grain is the basis of all existing small and large-scale estimates of drifting snow sublimation and the associated snow mass balance of polar and alpine regions. This model is revisited in this chapter to test its validity for calculating sublimation from saltating snow grains.

In addition to the above chapters, there are two additional appendices at the end of the thesis. Appendix A described preliminary results of an LES study to uncover perturbations induced in a stratocumulus-topped boundary layer due to wind farms and is inspired by the results in Chapter 2. Appendix B describes a mean kinetic energy budget (MKE) of the ABL flows simulated in Chapter 3 and is an extension of the analysis presented in that chapter.

Bibliography

- Mahdi Abkar and Fernando Porté-Agel. Influence of atmospheric stability on wind-turbine wakes : A large-eddy simulation study. *Phys. Fluids*, 27(035104):1–19, 2015. doi: 10.1063/1.4913695.
- Mahdi Abkar, Ahmad Sharifi, and Fernando Porté-Agel. Wake flow in a wind farm during a diurnal cycle. *J. Turbul.*, 2016.
- J.F. Ainslie. Calculating the flowfield in the wake of wind turbines. *J. Wind Eng. Ind. Aerodyn.*, 27(1):213 – 224, 1988.
- Matthew L Aitken, Branko Kosović, Jeffrey D Mirocha, and Julie K Lundquist. Large eddy simulation of wind turbine wake dynamics in the stable boundary layer using the weather research and forecasting model. *J. Renewable Sustainable Energy*, 6(3):033137, 2014.
- J.D. Albertson and M.B. Parlange. Natural integration of scalar fluxes from complex terrain. *Water Resour. Res.*, 23:239–252, 1999a.
- J.D. Albertson and M.B. Parlange. Surface length-scales and shear stress: Implications for land-atmosphere interaction over complex terrain. *Water Resour. Res.*, 35:2121–2131, 1999b.
- Dries Allaerts and Johan Meyers. Boundary-layer development and gravity waves in conventionally neutral wind farms. *Journal of Fluid Mechanics*, 814:95–130, 2017.
- MP Almeida, JS Andrade, and Hans Jürgen Herrmann. Aeolian transport of sand. *The European Physical Journal E*, 22(3):195, 2007.
- RS Anderson and PK Haff. Wind modification and bed response during saltation of sand in air. In *Aeolian Grain Transport 1*, pages 21–51. Springer, 1991.
- Ralph Alger Bagnold. *The physics of blown sand and desert dunes*. New York: Methuen, 1941.
- Jorge Bardina, Joel H Ferziger, and William Craig Reynolds. Improved subgrid-scale models for large-eddy simulation. In *American Institute of Aeronautics and Astronautics, Fluid and Plasma Dynamics Conference, 13th, Snowmass, Colo., July 14-16, 1980, 10 p.*, 1980.

Bibliography

- H. Barral, C. Genthon, A. Trouvilliez, C. Brun, and C. Amory. Blowing snow in coastal adÃ©lie land, antarctica: three atmospheric-moisture issues. *The Cryosphere*, 8(5):1905–1919, 2014. doi: 10.5194/tc-8-1905-2014. URL <https://www.the-cryosphere.net/8/1905/2014/>.
- DB Barrie and DB Kirk-Davidoff. Weather response to a large wind turbine array. *Atmos. Chem. Phys.*, 10(2):769–775, 2010.
- Kiran Bhaganagar and Mithu Debnath. The effects of mean atmospheric forcings of the stable atmospheric boundary layer on wind turbine wake. *J. Renewable Sustainable Energy*, 7(1): 013124, 2015.
- Elie Bou-Zeid, Charles Meneveau, and Marc Parlange. A scale-dependent lagrangian dynamic model for large eddy simulation of complex turbulent flows. *Physics of Fluids*, 17(2):025105, 2005. doi: 10.1063/1.1839152. URL <http://dx.doi.org/10.1063/1.1839152>.
- Povl Brøndsted, Hans Lilholt, and Aage Lystrup. Composite materials for wind power turbine blades. *Annu. Rev. Mater. Res.*, 35:505–538, 2005.
- WF Budd. The drifting of nonuniform snow particles1. *Studies in Antarctic Meteorology*, pages 59–70, 1966.
- Raúl Bayoán Cal, José Lebrón, Luciano Castillo, Hyung Suk Kang, and Charles Meneveau. Experimental study of the horizontally averaged flow structure in a model wind-turbine array boundary layer. *Journal of Renewable and Sustainable Energy*, 2(1), 2010.
- M. Calaf, C.Meneveau, and J. Meyers. Large eddy simulation study of fully developed wind-turbine array boundary layers. *Phys. Fluids*, 22(015110):1–16, 2010.
- BJ Chalmers and E Spooner. An axial-flux permanent-magnet generator for a gearless wind energy system. *IEEE Transactions on Energy Conversion*, 14(2):251–257, 1999.
- Marcelo Chamecki, Charles Meneveau, and Marc B Parlange. Large eddy simulation of pollen transport in the atmospheric boundary layer. *Journal of Aerosol Science*, 40(3):241–255, 2009.
- Jules G Charney, Ragnar Fjørtoft, and J von Neumann. Numerical integration of the barotropic vorticity equation. *Tellus*, 2(4):237–254, 1950.
- Matthew J Churchfield, Sang Lee, John Michalakes, and Patrick J Moriarty. A numerical study of the effects of atmospheric and wake turbulence on wind turbine dynamics. *Journal of turbulence*, (13):N14, 2012.
- Andrew Clifton, Jean-Daniel Rüedi, and Michael Lehning. Snow saltation threshold measurements in a drifting-snow wind tunnel. *Journal of Glaciology*, 52(179):585–596, 2006.
- Francesco Comola and Michael Lehning. Energy- and momentum-conserving model of splash entrainment in sand and snow saltation. *Geophysical Research Letters*, 44(3):1601–1609, 2017. ISSN 1944-8007. doi: 10.1002/2016GL071822. URL <http://dx.doi.org/10.1002/2016GL071822>. 2016GL071822.

- Xiaoqing Dai and Ning Huang. Numerical simulation of drifting snow sublimation in the saltation layer. *Scientific reports*, 4:6611, 2014. ISSN 2045-2322. doi: 10.1038/srep06611. URL <http://www.pubmedcentral.nih.gov/articlerender.fcgi?artid=4196100&tool=pmcentrez&rendertype=abstract>.
- James W Deardorff. Preliminary results from numerical integrations of the unstable planetary boundary layer. *Journal of the Atmospheric Sciences*, 27(8):1209–1211, 1970a.
- James W Deardorff. A numerical study of three-dimensional turbulent channel flow at large reynolds numbers. *Journal of Fluid Mechanics*, 41(2):453–480, 1970b.
- James Warner Deardorff. A three-dimensional numerical investigation of the idealized planetary boundary layer. *Geophysical and Astrophysical Fluid Dynamics*, 1(3-4):377–410, 1970c.
- JW Deardorff. The use of subgrid transport equations in a three-dimensional model of atmospheric turbulence. *J. Fluids Eng*, 95(429-438):181, 1973.
- Stephen J Déry and MK Yau. A bulk blowing snow model. *Boundary-Layer Meteorology*, 93(2): 237–251, 1999.
- Stephen J Déry and MK Yau. Simulation of blowing snow in the canadian arctic using a double-moment model. *Boundary-Layer Meteorology*, 99(2):297–316, 2001.
- Judith J. J. Doorschot and Michael Lehning. Equilibrium saltation: Mass fluxes, aerodynamic entrainment, and dependence on grain properties. *Boundary-Layer Meteorology*, 104(1): 111–130, Jul 2002. ISSN 1573-1472. doi: 10.1023/A:1015516420286. URL <https://doi.org/10.1023/A:1015516420286>.
- Sylvain Dupont, Gilles Bergametti, Béatrice Marticorena, and Serge Simoëns. Modeling saltation intermittency. *Journal of Geophysical Research: Atmospheres*, 118(13):7109–7128, 2013.
- S. Frandsen. On the wind speed reduction in the center of large clusters of wind turbines. *J. Wind Eng. Ind. Aerodyn.*, 39:251–265, 1992.
- Hubert Gallée, Gilbert Guyomarc’h, and Eric Brun. Impact of snow drift on the antarctic ice sheet surface mass balance: Possible sensitivity to snow-surface properties. *Boundary-Layer Meteorology*, 99(1):1–19, Apr 2001. ISSN 1573-1472. doi: 10.1023/A:1018776422809. URL <https://doi.org/10.1023/A:1018776422809>.
- M Germano. Turbulence: the filtering approach. *Journal of Fluid Mechanics*, 238:325–336, 1992.
- M. G. Giometto, A. Christen, C. Meneveau, J. Fang, M. Krafczyk, and M. B. Parlange. Spatial characteristics of roughness sublayer mean flow and turbulence over a realistic urban surface. *Boundary-Layer Meteorol.*, pages 1–28, 2016.

Bibliography

- Jay P. Goit and Johan Meyers. Optimal control of energy extraction in wind-farm boundary layers. *Journal of Fluid Mechanics*, 768:5–50, 2015. doi: 10.1017/jfm.2015.70.
- Fernando F Grinstein, Len G Margolin, and William J Rider. *Implicit large eddy simulation: computing turbulent fluid dynamics*. Cambridge university press, 2007.
- C. D. Groot Zwaaftink, H. Löwe, R. Mott, M. Bavay, and M. Lehning. Drifting snow sublimation: A high-resolution 3-d model with temperature and moisture feedbacks. *Journal of Geophysical Research: Atmospheres*, 116(D16):n/a–n/a, 2011. ISSN 2156-2202. doi: 10.1029/2011JD015754. URL <http://dx.doi.org/10.1029/2011JD015754>. D16107.
- C. D. Groot Zwaaftink, M. Diebold, S. Horender, J. Overney, G. Lieberherr, M. B. Parlange, and M. Lehning. Modelling small-scale drifting snow with a lagrangian stochastic model based on large-eddy simulations. *Boundary-Layer Meteorology*, 153(1):117–139, Oct 2014. ISSN 1573-1472. doi: 10.1007/s10546-014-9934-2. URL <https://doi.org/10.1007/s10546-014-9934-2>.
- James Hansen, Donald Johnson, Andrew Lacis, Sergej Lebedeff, Pius Lee, David Rind, and Gary Russell. Climate impact of increasing atmospheric carbon dioxide. *Science*, 213(4511): 957–966, 1981.
- Ning Huang and Zheng-Shi Wang. The formation of snow streamers in the turbulent atmosphere boundary layer. *Aeolian Research*, 23:1–10, 2016.
- Ning Huang, Xiaoqing Dai, and Jie Zhang. The impacts of moisture transport on drifting snow sublimation in the saltation layer. *Atmospheric Chemistry and Physics*, 16(12):7523–7529, 2016.
- Mark Z. Jacobson and Cristina L. Archer. Saturation wind power potential and its implications for wind energy. *Proceedings of the National Academy of Sciences*, 109(39):15679–15684, 2012. doi: 10.1073/pnas.1208993109. URL <http://www.pnas.org/content/109/39/15679.abstract>.
- N.O. Jensen. *A note on wind generator interaction*, pages 1—16. Risø-M; No.2411, 1983. ISBN 87-550-0971-9.
- D.W. Keith, J.F. DeCarolis, D.C. Denkenberger, D.H. Lenschow, S.L. Malyshev, S. Pacala, and P.J. Rasch. The influence of large-scale wind power on global climate. *Proc. Natl. Acad. Sci. USA*, 101(46):16115–16120, 2004.
- D. B. Kirk-Davidoff and D. W. Keith. On the climate impact of surface roughness anomalies. *J. Atmos. Sci.*, 65:2215–2234, 2008.
- Jasper F. Kok and Nilton O. Renno. A comprehensive numerical model of steady state saltation (comsalt). *Journal of Geophysical Research: Atmospheres*, 114(D17):n/a–n/a, 2009. ISSN 2156-2202. doi: 10.1029/2009JD011702. URL <http://dx.doi.org/10.1029/2009JD011702>. D17204.

- Andrey Nikolaevich Kolmogorov. Dissipation of energy in locally isotropic turbulence. In *Dokl. Akad. Nauk SSSR*, volume 32, pages 16–18, 1941a.
- Andrey Nikolaevich Kolmogorov. The local structure of turbulence in incompressible viscous fluid for very large reynolds numbers. In *Dokl. Akad. Nauk SSSR*, volume 30, pages 299–303, 1941b.
- Vijayant Kumar, Gunilla Svensson, a. a M Holtslag, Charles Meneveau, and Marc B. Parlange. Impact of surface flux formulations and geostrophic forcing on large-eddy simulations of diurnal atmospheric boundary layer flow. *J. Appl. Meteorol. Clim.*, 49:1496–1516, 2009.
- Gunner C. Larsen, Helge Aa. Madsen, Kenneth Thomsen, and Torben J. Larsen. Wake meandering: a pragmatic approach. *Wind Energy*, 11(4):377–395, 2008.
- Lang Wah Lee. *Sublimation of snow in turbulent atmosphere*. PhD thesis, University of Wyoming, 1975.
- J. T. M. Lenaerts, M. R. van den Broeke, S. J. Déry, E. van Meijgaard, W. J. van de Berg, Stephen P. Palm, and J. Sanz Rodrigo. Modeling drifting snow in Antarctica with a regional climate model: 1. Methods and model evaluation. *Journal of Geophysical Research: Atmospheres*, 117(D5):n/a–n/a, 2012. ISSN 01480227. doi: 10.1029/2011JD016145. URL <http://doi.wiley.com/10.1029/2011JD016145>.
- H. Lu and F. Porté-Agel. Large-eddy simulation of a very large wind farm in a stable atmospheric boundary layer. *Physics of Fluids*, 23(065101):1–19, 2011.
- Hao Lu and Fernando Porté-Agel. On the impact of wind farms on a convective atmospheric boundary layer. *Boundary-Layer Meteorology*, 157(1):81–96, 2015.
- Syukuro Manabe and Richard T Wetherald. The effects of doubling the co2 concentration on the climate of a general circulation model. *Journal of the Atmospheric Sciences*, 32(1):3–15, 1975.
- GW Mann, PS Anderson, and SD Mobbs. Profile measurements of blowing snow at halley, antarctica. *Journal of Geophysical Research: Atmospheres*, 105(D19):24491–24508, 2000.
- Charles Meneveau. The top-down model of wind farm boundary layers and its applications. *J. Turbul.*, 13:N7, 2012.
- Ashish Misra and Dale I Pullin. A vortex-based subgrid stress model for large-eddy simulation. *Physics of Fluids*, 9(8):2443–2454, 1997.
- Chin-hoh Moeng. A Large-Eddy-Simulation Model for the Study of Planetary Boundary-Layer Turbulence. *J. Atmos. Sci.*, 41(13):2052–2062, 1984.
- M Nemoto and K Nishimura. Numerical simulation of snow saltation and suspension in a turbulent boundary layer. *Journal of Geophysical Research: Atmospheres*, 109(D18), 2004.

Bibliography

- Steven A Orszag. Numerical methods for the simulation of turbulence. *The Physics of Fluids*, 12(12):II–250, 1969.
- R. K. Pachauri, M. R. Allen, V. R. Barros, J. Broome, W. Cramer, R. Christ, J. A. Church, L. Clarke, Q. Dahe, P. Dasgupta, N. K. Dubash, O. Edenhofer, I. Elgizouli, C. B. Field, P. Forster, P. Friedlingstein, J. Fuglestedt, L. Gomez-Echeverri, S. Hallegatte, G. Hegerl, M. Howden, K. Jiang, B. Jimenez Cisneroz, V. Kattsov, H. Lee, K. J. Mach, J. Marotzke, M. D. Mastrandrea, L. Meyer, J. Minx, Y. Mulugetta, K. O'Brien, M. Oppenheimer, J. J. Pereira, R. Pichs-Madruga, G.-K. Plattner, Hans-Otto Pörtner, S. B. Power, B. Preston, N. H. Ravindranath, A. Reisinger, K. Riahi, M. Rusticucci, R. Scholes, K. Seyboth, Y. Sokona, R. Stavins, T. F. Stocker, P. Tschakert, D. van Vuuren, and J.-P. van Ypserle. *Climate Change 2014: Synthesis Report. Contribution of Working Groups I, II and III to the Fifth Assessment Report of the Intergovernmental Panel on Climate Change*. IPCC, Geneva, Switzerland, 2014.
- Norman A Phillips. The general circulation of the atmosphere: A numerical experiment. *Quarterly Journal of the Royal Meteorological Society*, 82(352):123–164, 1956.
- JW Pomeroy, DM Gray, and PG Landine. The prairie blowing snow model: characteristics, validation, operation. *Journal of Hydrology*, 144(1-4):165–192, 1993.
- E. Rignot, I. Velicogna, M. R. van den Broeke, A. Monaghan, and J. T. M. Lenaerts. Acceleration of the contribution of the greenland and antarctic ice sheets to sea level rise. *Geophysical Research Letters*, 38(5):n/a–n/a, 2011. ISSN 1944-8007. doi: 10.1029/2011GL046583. URL <http://dx.doi.org/10.1029/2011GL046583>. L05503.
- Dominique Roddier, Christian Cermelli, Alexia Aubault, and Alla Weinstein. Windfloat: A floating foundation for offshore wind turbines. *Journal of renewable and sustainable energy*, 2(3):033104, 2010.
- Mark S Roulston, Daniel T Kaplan, J Hardenberg, and Leonard A Smith. Using medium-range weather forecasts to improve the value of wind energy production. *Renewable Energy*, 28(4): 585–602, 2003.
- S. Baidya Roy and J. J. Traiteur. Impacts of wind farms on surface air temperatures. *Proc. Nat. Acad. Sci. USA.*, 107(42):17899–17904, 2010.
- S.B. Roy, S.W. Pacala, and R.L. Walko. Can large wind farms affect local meteorology? *J. Geophys. Res.*, 109(D19101):1–6, 2004.
- R. A. Schmidt. Threshold wind-speeds and elastic impact in snow transport. *Journal of Glaciology*, 26(94):453–467, 1980. doi: 10.3189/S0022143000010972.
- R.A. Schmidt. Sublimation of wind-transported snow—a model. *USDA Forest Service research paper RM-United States, Rocky Mountain Forest and Range Experiment Station*, 1972.
- Peter J Schubel and Richard J Crossley. Wind turbine blade design. *Energies*, 5(9):3425–3449, 2012.

- Yaping Shao and An Li. Numerical modelling of saltation in the atmospheric surface layer. *Boundary-Layer Meteorology*, 91(2):199–225, May 1999. ISSN 1573-1472. doi: 10.1023/A:1001816013475. URL <https://doi.org/10.1023/A:1001816013475>.
- Joseph Smagorinsky. General circulation experiments with the primitive equations: I. the basic experiment. *Monthly weather review*, 91(3):99–164, 1963.
- Herman Snel. Review of aerodynamics for wind turbines. *Wind Energy*, 6(3):203–211, 2003.
- Jens Nørkær Sørensen. Aerodynamic aspects of wind energy conversion. *Annual Review of Fluid Mechanics*, 43:427–448, 2011.
- Richard J. A. M. Stevens, Dennice F. Gayme, and Charles Meneveau. Coupled wake boundary layer model of wind-farms. *J. Renewable Sustainable Energy*, 7(2), 2015.
- S Stolz and Nikolaus A Adams. An approximate deconvolution procedure for large-eddy simulation. *Physics of Fluids*, 11(7):1699–1701, 1999.
- K Sugiura and N Maeno. Wind-tunnel measurements of restitution coefficients and ejection number of snow particles in drifting snow: determination of splash functions. *Boundary-Layer Meteorology*, 95(1):123–143, 2000.
- Ronald D Tabler. Estimating the transport and evaporation of blowing snow. *Great Plains Agric Counc Publ*, 1975.
- A. D. Thorpe and B. J. Mason. The evaporation of ice spheres and ice crystals. *British Journal of Applied Physics*, 17(4):541, 1966. ISSN 0508-3443. doi: 10.1088/0508-3443/17/4/316. URL <http://iopscience.iop.org/0508-3443/17/4/316>.
- Michiel van den Broeke, Willem Jan van de Berg, Erik van Meijgaard, and Carleen Reijmer. Identification of Antarctic ablation areas using a regional atmospheric climate model. *Journal of Geophysical Research*, 111(D18):D18110, 2006. ISSN 0148-0227. doi: 10.1029/2006JD007127. URL <http://doi.wiley.com/10.1029/2006JD007127>.
- Michiel R Van den Broeke, Carleen H Reijmer, and Roderik S W V A N D E Wal. A study of the surface mass balance in Dronning Maud Land , Antarctica , using automatic weather station S. *Journal of Glaciology*, 50(171):565–582, 2004.
- L.J. Vermeer, J.N. Sørensen, and A. Crespo. Wind turbine wake aerodynamics. *Progress in Aerospace Sciences*, 39(6):467 – 510, 2003. ISSN 0376-0421. URL <http://www.sciencedirect.com/science/article/pii/S0376042103000782>.
- Ivana Vinkovic, Cesar Aguirre, Michel Ayrault, and Serge Simoëns. Large-eddy simulation of the dispersion of solid particles in a turbulent boundary layer. *Boundary-layer meteorology*, 121(2):283, 2006.

Bibliography

- V. Vionnet, E. Martin, V. Masson, G. Guyomarc'H, F. Naaim-Bouvet, A. Prokop, Y. Durand, and C. Lac. Simulation of wind-induced snow transport and sublimation in alpine terrain using a fully coupled snowpack/atmosphere model. *Cryosphere*, 8(2):395–415, 2014. ISSN 19940424. doi: 10.5194/tc-8-395-2014.
- Chien Wang and Ronald G Prinn. Potential climatic impacts and reliability of very large-scale wind farms. *Atmos. Chem. and Phys.*, 10(4):2053–2061, 2010.
- Y-T. Wu and F. Porté-Agel. Large-eddy simulation of wind-turbine wakes: Evaluation of turbine parametrizations. *Boundary-Layer Meteorol.*, 138:345–366, 2011.
- Wusi Yue, Charles Meneveau, Marc B. Parlange, Weihong Zhu, René van Hout, and Joseph Katz. A comparative quadrant analysis of turbulence in a plant canopy. *Water Resour. Res.*, 43(5), 2007. W05422.

Part I

1 An LES model for a time-adaptive wind turbine

An edited version of this chapter was published in the journal *Wind Energy* by John Wiley & Sons, Ltd. Copyright ©2015 John Wiley & Sons, Ltd. All rights reserved.

Sharma, V., Calaf, M., Lehning, M., and Parlange, M. B. (2016) Time-adaptive wind turbine model for an LES framework. *Wind Energ.*, 19: 939–952. doi: 10.1002/we.1877.

To view the published open abstract, go to <http://dx.doi.org> and enter the DOI

V.S developed the numerical model, implemented it in the LES code, took part in the research design, performed simulations, analyzed the data and contributed to the writing of the paper

1.1 Introduction

Studies in wind energy have developed rapidly over the past few years, with works investigating a wide range of problems, such as wind turbine aerodynamics [Snel, 1998, Burton et al., 2001], wake interactions [Voutsinas et al., 1990, Frandsen, 1992, González-Longatt et al., 2011] or large-scale wind farm and atmosphere interaction [Roy et al., 2004, Keith et al., 2004, Kirk-Davidoff and Keith, 2008, Barrie and Kirk-Davidoff, 2010]. The Large Eddy Simulation (LES) technique has increasingly been implemented to gain insight into the wind energy question. Its inherent high spatio-temporal resolution, together with its capacity for resolving the large scale flow phenomena, has allowed for a wide variety of LES-Wind Energy studies. In most works, the flow is forced with a pressure gradient to better control the mean wind direction of the turbulent flow. While this procedure is simple and has provided great insight into the study of wake structures, harvesting of wind power in large wind farms, or farm layout effects,

it is a limiting factor for more realistic scenarios.

A new generation of atmospheric LES codes have been proven to accurately reproduce time changing atmospheric flows when forced with close to realistic conditions, including Coriolis effects [Kumar et al., 2006]. Yet, it hasn't been possible to study wind turbine characteristics under such changing conditions because of the limited flexibility of the wind turbine models used within the LES simulations. Current turbine models don't allow for automatic rotation and alignment of the turbine's nacelle with the changing wind conditions, hence the current need to properly prescribe the incoming flow such that it is perpendicular to the turbines' rotor disk. Porté-Agel et al. [2013] investigated the effect of wind direction change and the wind farm layout on wake interaction. This work required a large set of numerical simulations, each one forced with a fixed pressure gradient corresponding to a new wind vector orientation. Recent studies such as Sescu and Meneveau [2014] utilize a 'proportional-integral' control algorithm that artificially constrains the mean flow to be in the streamwise direction while maintaining statistical stationarity.

Coupled mesoscale-microscale simulation methods are being explored for wind resource estimation and for guiding wind farm siting and operational decisions [Gopalan et al., 2014]. The increasingly popular WRF-LES technique, especially useful for studying flows in complex terrain and non-idealized settings, is being adopted for wind energy research as well. Notable works include Mirocha et al. [2013, 2014], where nested LES simulations with wind turbines modelled using the generalized actuator disk model have been used to study the ABL-WT interaction in realistic forcing conditions and compared with field and turbine data.

At the other end of the research spectrum is the development of high-fidelity aero-elastic models such as FAST [Jonkman and Buhl Jr, 2005] at NREL with additional capabilities for wind turbine control mechanisms such as yaw-correction, pitch control [Fleming et al., 2013]. These models provide a very detailed description of real-world wind turbines, but require high spatial and temporal resolution of the flow to compute the WT forces, power output and loads. Thus, to the best of our knowledge, such models have not been used to parametrize wind turbines in simulations of large wind farms embedded in a full ABL simulation.

Previous works also show an increasing interest in better understanding the changes induced by the interaction of turbine wakes with the underlying land-surface - e.g changes in evapotranspiration, land surface temperature and crop growth [Calaf et al., 2011, Lu and Porté-Agel, 2011, Roy, 2011, Yang et al., 2012, Zhang et al., 2013]. Assessing these changes experimentally would require large and expensive field experiments [Rajewski et al., 2013]. In addition, experimental conditions are sometimes so complex that fully decomposing the effects of the multiple elements in play becomes an almost impossible task. Numerical simulations are a valuable tool to independently assess the effects of turbines, and for these numerical simulations to reproduce more realistic conditions, the simulations need to partly capture the time evolution of the atmospheric flow. Thus, for studying the behaviour of wind turbines, their corresponding wakes, and the interaction with the surrounding flow and land-surface, a time-adaptive wind turbine algorithm is needed. At present, wind turbines timely-synchronize their aerodynamic profile and yaw-alignment with the changing mean wind conditions according

to pre-established power curves and configured operational schemes. The time varying flow conditions are extracted using wind vanes and cup anemometers installed at the nacelle and the wind turbine adjusts to pre-established configuration setups.

It is well known that wind conditions under convective conditions are radically different than those encountered under stably stratified regimes. Wind direction changes happen regularly under convective regimes with elevated turbulent intensity periods, while under stably stratified periods the flow tends to be less turbulent.

In this work a numerical algorithm that permits for the wind turbine to automatically readjust its yaw alignment with the local incoming wind conditions is presented. The wind turbine algorithm is equipped with a flexible time averaging function that allows to compute the averaged incoming wind vector, and dynamically adjust the turbine's yaw. At present, the incoming wind vector is measured at hub height as with traditional wind vanes and cup anemometers installed behind the rotor blades. The new algorithm uses the actuator disk model with additional rotation similar to that used in Wu and Porté-Agel [2011], and a LES code based on pseudo-spectral numerics and dynamic subgrid-scale model, similar to the one presented in past works [Porté-Agel et al., 2013, Bou-Zeid et al., 2005, Kumar et al., 2006, Calaf et al., 2011] is implemented.

In Sect. 1.2, the LES code is presented in detail together with the sub-grid model and the boundary conditions. Section 1.3 introduces the new time adaptive wind turbine algorithm and Sect. 1.4 introduces the study cases considered. Sections 1.5 and 1.6 describe two specific examples in which the new algorithm has been applied. Results are presented with respect to power availability at different daytime periods with the corresponding properties associated to this available power.

1.2 The Large Eddy Simulation approach

The numerical code solves for the non-dimensional, filtered Navier-Stokes equations for an incompressible flow in hydrostatic equilibrium, together with the continuity equation. The rotational form of the filtered Navier-Stokes equations is used in order to ensure conservation of mass and energy of the inertial terms [Orzag and Pao, 1974]. The effect of temperature is introduced into the momentum equations using a thermal buoyancy term as a result of using the Boussinesq approximation. The full set of equations being solved is therefore,

$$\frac{\partial \tilde{u}_i}{\partial x_i} = 0, \tag{1.1}$$

$$\frac{\partial \tilde{u}_i}{\partial t} + \tilde{u}_j \left(\frac{\partial \tilde{u}_i}{\partial x_j} - \frac{\partial \tilde{u}_j}{\partial x_i} \right) = -\frac{1}{\rho} \frac{\partial \tilde{p}}{\partial x_i} - \frac{\partial \tilde{\tau}_{ij}}{\partial x_j} + g \left(\frac{\tilde{\theta} - \hat{\theta}}{\hat{\theta}} \right) + f(\tilde{u}_2 - v_G) \delta_{i1} - f(\tilde{u}_1 - u_G) \delta_{i2} + f_i, \tag{1.2}$$

$$\frac{\partial \tilde{\theta}}{\partial t} + \tilde{u}_j \frac{\partial \tilde{\theta}}{\partial x_j} = -\frac{\partial \pi_j}{\partial x_j}, \quad (1.3)$$

where $\tilde{\theta}$ is the filtered potential temperature, \tilde{u}_i represents the LES filtered velocity component in the i direction ($i = 1, 2, 3$), and \tilde{p} is the resolved dynamic pressure term formulated so as to satisfy the divergence-free condition. The deviatoric part of the momentum sub-grid stress term, $\tilde{\tau}_{ij}$ is modelled with the Lagrangian scale dependent model from Bou-Zeid et al. [2005], and the corresponding sub-grid scalar flux of potential temperature is modelled using the adaptation of the Lagrangian scale dependent model for scalars introduced in Calaf et al. [2011]. The f term represents the Coriolis factor and u_G and v_G represent the streamwise and cross-streamwise components of the geostrophic wind. Here the tilde ($\tilde{\cdot}$) represents the LES filtering at the grid size (Δ), and ($\hat{\cdot}$) represents a secondary filtering operation at a spacing two times the grid size (2Δ). In equation 1.2, δ_{ij} is the Kronecker delta ($\delta_{ij} = 1$ for $i = j$, 0 otherwise).

The effect of atmospheric stratification is introduced by the potential temperature acting as an active scalar to modify the buoyancy of the air enhancing vertical displacements of air parcels, and thus the momentum equation. This is introduced in equation 1.2 using the Boussinesq approximation for the potential temperature. The effect of the wind turbines is introduced by a combination of a drag force and a tangential force, both acting into the momentum equation through the f_i term (see Sect. 1.3 for extended details). Because the simulations are done for large Reynolds numbers and the bottom surface as well as the wind turbines are parametrised, the viscous effects and the molecular diffusive effects are neglected.

The numerical discretisation of the equations follows the one introduced by Moeng [1984] and Albertson and Parlange [1999a,b]. This means that a pseudo-spectral discretisation is used, with second order finite-differences in the vertical direction and Fourier transforms in the horizontal directions. Because of the Fourier based methods in both horizontal directions, the domain is fully periodic and no lateral boundary conditions are needed: hence, the domain size tends to infinity in practical effects. A second order Adams-Bashforth scheme is used for the time integration. In addition, the non-linear convective terms are de-aliased with the 3/2 rule [Canuto et al., 1988].

The code is fully parallelised using Message Passing Interface (MPI), and the FFTW library [Frigo and Johnson, 2005] is employed for the Fourier transforms. The pressure solver for parallel runs is based on the pipeline Thomas algorithm [Povitsky and Morris, 2000]. A zero vertical velocity and a zero shear stress are imposed as top boundary conditions for the momentum equations. For the surface boundary conditions, a non-slip condition is imposed for the vertical velocity and for the horizontal components of the momentum equation an equivalent shear stress is imposed using the log-law with atmospheric stability correction

[Parlange and Brutsaert, 1993, Bou-Zeid et al., 2005, Hultmark et al., 2013],

$$\tau_{i,3}(x, y, z_1) = - \left[\frac{k \sqrt{(\hat{u}_1^2 + \hat{u}_2^2)}}{\ln(z_1/z_0) + \psi_m(z_1/L)} \right]^2 n_i. \quad (1.4)$$

Here, i is the specific direction in the plane parallel to the surface ($i = 1, 2$), and n_i is a unitary directional vector defined as: $n_i = \hat{u}_i / \sqrt{\hat{u}_1^2 + \hat{u}_2^2}$. The shear stress is imposed at $z_1 = \Delta z/2$ because of the staggered grid, thus the velocities used are evaluated at that same height (first numerical grid point with values of u_i , $i = 1, 2$ available). The \hat{u}_i represents a double filtering operation (at 2Δ grid spacing) on horizontal components of the flow, which is equivalent to a local average (see Bou-Zeid et al. [2005], Hultmark et al. [2013] for further details in this filtering).

The surface roughness is constant over the entire numerical domain and has a value of $z_0 = 0.1$ m which corresponds to a ground surface with low crops [Stull, 1988]. For the numerical integration of the momentum equation, the vertical derivatives of the horizontal velocity components are also needed. These are parametrised at the first grid point also using Monin-Obukhov similarity theory [Brutsaert and Parlance, 1992],

$$\partial_3 \tilde{u}_i(x, y, z_1) = \left(\frac{\sqrt{\tau}}{\kappa z} \right) n_i, \quad (1.5)$$

with $\tau = \sqrt{\tau_{1,3}^2 + \tau_{2,3}^2}$. In a similar fashion as for the momentum, the kinematic sensible heat flux is computed at the first staggered grid point using Monin-Obukhov similarity theory,

$$H_s(x, y, z_1) = \frac{\kappa^2 [\theta_s - \tilde{\theta}(x, y, z_1)] \left(\sqrt{\hat{u}_1^2 + \hat{u}_2^2} \right)}{\left[\ln\left(\frac{z_1}{z_0}\right) + \psi_m(z/L) \right] \left[\ln\left(\frac{z_1}{z_{0,h}}\right) + \psi_h(z/L) \right]}. \quad (1.6)$$

where the surface temperature (θ_s) is imposed as bottom boundary condition for (see Sect. 1.4 for the specific values used). The stability correction functions (ψ) implemented are those from Brutsaert [2005]. Different formulations exist depending upon stability and the appropriate choice of functions is made based upon the Obukhov length (L) defined as,

$$L = \frac{-u_*^3 \bar{\theta}_s}{\kappa g \overline{w'\theta'_s}}, \quad (1.7)$$

where u_* is the friction velocity, $\bar{\theta}$ is the mean potential temperature, κ the Von Karman constant ($\kappa = 0.4$), and $\overline{w'\theta'}$ the surface sensible heat flux. For the unstable scenario the

stability correction functions are given by,

$$\psi_m(z/L) = \begin{cases} \ln(a - z/L) - 3b(z/L)^{1/3} + \frac{ba^{1/3}}{2} \ln \left[\frac{(1+x)^2}{(1-x+x^2)} \right] + \\ \sqrt{3}ba^{1/3} \tan^{-1}[(2x-1)/\sqrt{3}] + \psi_0 & \text{for } z/L \leq b^{-3} \\ \psi_m(b^{-3}) & \text{for } z/L > b^{-3} \end{cases} \quad (1.8)$$

and,

$$\psi_h = [(1-d)/n] \ln[(c + y^n)/c] \quad (1.9)$$

In the above equation, $a = 0.33$, $b = 0.41$, $c = 0.33$, $d = 0.057$, $n = 0.78$ and $x = (-z/La)^{1/3}$. $\psi_0 = (-\ln a + \sqrt{3}ba^{1/3}\pi/6)$. For the stable scenario, the stability correction functions are

$$\begin{aligned} \psi_m(z/L) &= -a \ln[z/L + (1 + (z/L)^b)^{1/b}] \\ \psi_h(z/L) &= -c \ln[z/L + (1 + (z/L)^d)^{1/d}] \end{aligned} \quad (1.10)$$

where $a = 6.1$, $b = 2.5$, $c = 5.3$ and $d = 1.1$. The scalar surface roughness has been taken to be one tenth of the momentum surface roughness ($z_{0,h} = z_0/10$) [Brutsaert et al., 1989]. The stability correction functions were initially developed from experimental studies on statistically homogeneous surfaces. It is understood that the wind turbines might have an effect on the precise parametrisation of the stability correction functions, but lack of new experimental data on this precise matter doesn't allow for a better numerical approach at the present time.

1.3 The time-adaptive wind turbine algorithm

Wind turbines are introduced as an additional body force in the Navier-Stokes equations similar to previous studies [Jimenez et al., 2007, 2008, Calaf et al., 2010, Wu and Porté-Agel, 2011, Yang et al., 2012]. The force exerted by the turbine onto the fluid is computed using the classical actuator disk (AD) concept [Burton et al., 2001], which states that a wind turbine induces an equivalent drag force proportional to the square of the unperturbed incoming wind velocity (u_∞^2), the frontal area swept by the rotor blades A and the thrust coefficient (C_T),

$$F_t = -\frac{1}{2} \rho C_T u_\infty^2 A. \quad (1.11)$$

The total area swept by the blades is treated as a circular disk as illustrated in 1.1(a). In a large wind farm with many turbines where the corresponding wakes interact with each other, it is not possible to define an unperturbed incoming velocity (u_∞). Instead, a local velocity in front

1.3. The time-adaptive wind turbine algorithm

of the turbine's rotor disk (u_d) is used. This is related to the upstream unperturbed velocity through the induction factor (a) as $u_\infty = u_d / (1 - a)$.

The AD model is as a first-order approach to parameterizing wind turbines in LES, which does not capture blade-scale fluid motions such as tip vortices. However, a detailed numerical study from Wu and Porté-Agel [2011] showed that the AD model is sufficient to reproduce the far wake characteristics. By introducing additional tangential forces, the near wake characteristics can also be well reproduced without the need of numerically resolving the wind turbine blades. The model used in the present study is adopted from Meyers and Meneveau [2010], which is similar to the AD with rotation model proposed by Wu and Porté-Agel [2011], but with further simplifications regarding geometry and operation of the wind turbine blades. The forces introduced by the model as described as follows

$$\begin{aligned} f_t &= -\frac{1}{2}\rho C'_T \langle \bar{u} \rangle_d^2 \\ f_\theta &= \frac{1}{2}\rho C'_P \langle \bar{u} \rangle_d^2 \frac{\langle u \rangle_d}{\Omega r} \end{aligned} \tag{1.12}$$

where f_t is the standard drag force per unit area and f_θ is the tangential force per unit area at distance r from the centre. The actual force can be found by multiplying Equation 1.12 with an area element $r dr d\theta$. These parameterizations use 'modified' thrust and power coefficients, C'_T and C'_P respectively. To avoid the local heterogeneities in the velocity field and because the turbine disk is composed of many LES grid points, a disk averaged velocity is used to compute the thrust on the flow due to the spinning blades. Additionally, the disk-averaged velocity is averaged in time using an exponential weighted moving average to secure the numerical stability of the LES code by avoiding shocks and discontinuities. In Equation 1.12, $\langle \rangle_d$ represents disk averaging and the overline ($\bar{}$) represents time averaging. For the complete derivation of the above expressions, the reader may refer to Meyers and Meneveau [2010]. Only a brief summary of the assumptions used to derive Equation 1.12 are provided here for the sake of brevity.

The derivation begins using the blade element-momentum (BEM) theory, which combines the concept of conservation of linear and angular momentum with the blade element forces. This is based on the premise that these forces are solely responsible for the change in momentum of air passing through an annular disc [Burton et al., 2001]. It is assumed that the blades are 'optimally adapted' to the time-averaged incoming velocity (\bar{V}) such that the tip-speed ratio ($\lambda = \omega R / \bar{V}$) remains constant. It is also assumed that the ratio of lift and drag coefficients of the blades are kept constant using active pitch control. These optimality conditions imply that a detailed description of the blade geometry is no longer necessary. Balancing the lift and drag forces with the change in momentum and recasting the resulting equations in standard expressions for thrust and drag forces results in new coefficients C'_P and C'_T . These are related to standard coefficients as $C'_P = C_P / (1 - a)^3$ and $C'_T = C_T / (1 - a)^2$ respectively. In this work, values for C'_P, C'_T and a are chosen as 0.8, 1.334 and 0.25 respectively. Angular velocity (Ω) is

fixed at 1.5 rad/sec or 3.33×10^3 dimensionless units. These values are similar to the values in Meyers and Meneveau [2010].

Numerical implementation of the wind turbine model requires that the local forces described in Equation 1.12 are distributed onto the LES grid points. In this context, two mutually exclusive and exhaustive scenarios arise based on the orientation of the disk with respect to the LES mesh - the ‘perfectly-aligned’ case where the WT disk is coplanar with one of the two vertical Cartesian coordinate surfaces and the more general ‘mis-aligned’ case. Before these cases are analysed, consider (x,y,z) to be the streamwise, cross-stream and vertical directions respectively of the LES mesh. Figure 1.1(b) presents an example of the ‘perfectly-aligned’ case where the WT is aligned with the y - z plane. The points represent the LES grid points and the associated ‘cell’ for each point is created by a mesh with spacing of Δy and Δz in the horizontal and vertical directions respectively. Local forces computed using Equation 1.12 on a fine, disk-attached, Cartesian 1000×1000 mesh with a resolution of 0.1m. These forces are then ‘up-scaled’ to LES grid points by a filtering operation. The upscaled normal and tangential forces (F_t and F_θ respectively) at any LES grid point $(y, z) \equiv (i, j)$ in Fig. 1.1(b) can be computed as,

$$F_t^{(i,j)} = \frac{1}{\rho(\Delta x \Delta y \Delta z)} \iint f_t \text{ker}(y', z') dy' dz', \quad (1.13)$$

$$F_\theta^{(i,j)} = \frac{1}{\rho(\Delta x \Delta y \Delta z)} \iint f_\theta \text{ker}(y', z') dy' dz',$$

where $\text{ker}(y, z)$ is the kernel of the filter used for upscaling. In this work, the filter has a kernel, $\text{ker}_{i,j}(y', z') = \text{BOX}(y') \times \text{BOX}(z') \times H(R - \|(y', z')\|)$, where

$$\text{BOX}(y') = \begin{cases} 1 & j - \frac{\Delta y}{2} \leq y' \leq j + \frac{\Delta y}{2} \\ 0 & \text{elsewhere} \end{cases} \quad (1.14)$$

with analogous formulation for $\text{BOX}(z')$. The heavyside function (H) is used to restrict the upscaling operation to within the WT disk. This kernel implies that all local forces within a cell are upscaled to it's associated LES grid point. A common kernel used in other studies is the Gaussian kernel [Wu and Porté-Agel, 2011, 2013]. The Gaussian filter however requires a width parameter as input. Additionally it is not conservative when applied numerically. Note that the upscaled forces are normalized by density (ρ) and volume ($\Delta x \Delta y \Delta z$) such that they can be directly added to the filtered LES equations which are solved per unit mass. The integration is computed numerically on the fine mesh. Since the local drag force term (f_t) is equal throughout the disc, the expression for the upscaled drag force (F_t) can be reduced to

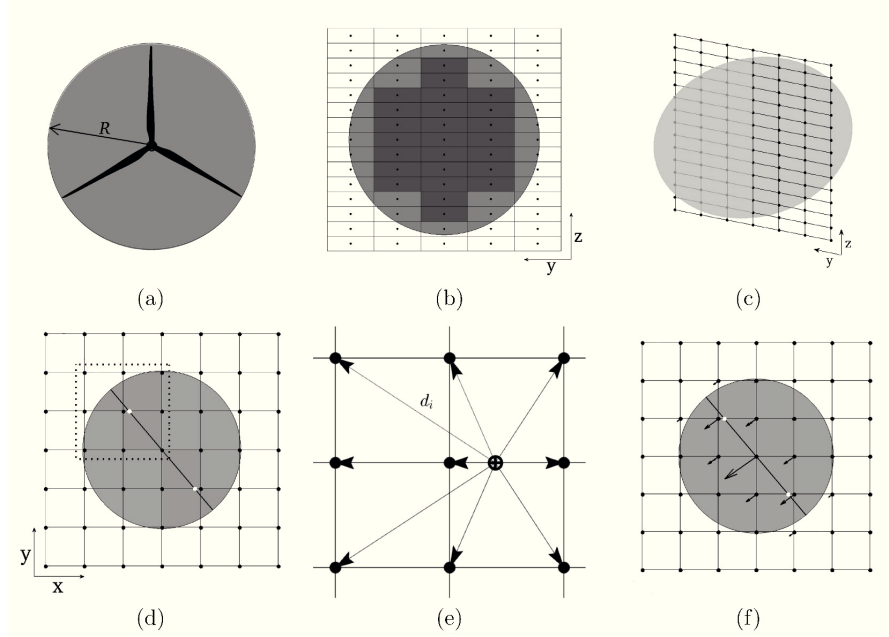


Figure 1.1 – Computational details of the new wind turbine algorithm. Subplot (a) shows a scheme of the classic actuator disk, and subplot (b) shows the numerical decomposition of the actuator disk on a regular LES grid. The cells near the boundary of the disk (for e.g, light grey coloured cells) have area overlap coefficient ($\gamma_{i,j} < 1.0$). Inner cells (for e.g, cells coloured dark gray) have $\gamma_{i,j} = 1.0$. Subplot (c) illustrates the misalignment of a wind turbine with respect to the LES grid, due to the changing incoming wind conditions. Subplot (d) is a top view of the wind turbine rotor disk (solid black line), the surrounding LES grid points (coloured black) and ‘pseudo-LES’ grid points (coloured white). Subplot (e) illustrates the ‘pseudo-LES’ grid point (\oplus) and the closest LES grid points (\bullet). Subplot (f) illustrates the final distribution of forces due to a misaligned wind turbine.

$$F_t^{(i,j)} = -\frac{1}{2} C_T' \langle \bar{u} \rangle_d^2 \frac{\gamma_{i,j}}{\Delta x}, \quad (1.15)$$

where overlap coefficient $\gamma_{i,j}$ is the fraction of area of the cell associated to point (i, j) that lies within the disk. In Fig. 1.1(b), for example, the interior cells with dark shading have $\gamma_{i,j} = 1$. For the boundary cells $\gamma_{i,j} < 1$, the precise value can be computed by using the relationship $\iint \text{ker}_{i,j}(y', z') dy' dz' = \gamma_{i,j} \Delta y \Delta z$.

It is clear that the ‘perfectly-aligned’ case is an idealized scenario. Indeed, the majority of previous works used a mean pressure gradient in the streamwise direction to enforce the mean flow direction in order to model the WTs as being perfectly aligned. In this study, a new WT model is developed that allows treatment of non-idealized cases of misaligned WTs with respect to the Cartesian LES grid. This is needed to study the interaction of WTs with time changing ABL conditions. A novel methodology to suitably model the generic ‘mis-

aligned' scenario is described as follows. Figure 1.1(c) shows a WT disk 'out-of-plane' of the y-z coordinate surface unlike Fig. 1.1(b). The essential problem with the 'mis-aligned' scenario is that in most cases, the LES grid points lying along the vertical diameter are the only LES points on the disk. This is better illustrated by looking at a horizontal plane cutting through the WT disk at hub-height, as shown in Fig. 1.1(d). In this figure, the shaded circular region marks the horizontal extent of the WT disk in all possible orientations. The inclined black line corresponds to the projection of the disk in the orientation shown in Fig. 1.1(c). Here, the Cartesian grid represents the LES grid lines.

It can be seen that, besides the center point, there are no other LES grid points within the disk. To solve this problem, a two-step process is followed. First, local forces are computed using the disk-attached fine mesh and upscaled to 'pseudo-LES' grid points as it was done in the 'perfectly-aligned' case. The 'pseudo-LES' grid points are identified as follows. Consider the normal to the WT disk to be oriented along the direction of the incoming horizontal velocity. Let the angle made by the normal with the x-axis be denoted by ξ . If $\xi < 45^\circ$, LES grid lines parallel to x-axis are chosen, else those parallel to y-axis are chosen. The corresponding intersection of the chosen grid lines with the WT disk are identified as 'pseudo-LES' grid points. As an illustration, in Fig. 1.1(d), ξ is slightly less than 45° . Thus, grid lines parallel to x-axis are chosen and their intersection with the disk are considered as the 'pseudo-LES' grid points (shown in Fig. 1.1(d) and (f) as white grid points).

The next step involves distributing the upscaled forces from the 'pseudo-LES' points to the nearest LES grid points in the same horizontal plane using the inverse distance weighting (IDW) technique [Shepard, 1968]. In Fig. 1.1(d), a region surrounding one of the pseudo-LES grid points is demarcated by a dotted square. This region is zoomed into in Fig. 1.1(e), which shows a nine point stencil of LES grid points (\bullet) containing a single 'pseudo-LES' grid point (\oplus). Let the upscaled force at this point be F_\oplus . Then the resulting force at the i^{th} LES grid point, F_i is computed as follows

$$F_i = F_\oplus \frac{d_i^{-1}}{\sum_i d_i^{-1}}, \quad (1.16)$$

where d_i is the distance between the 'pseudo-LES' grid point and the i_{th} LES grid point. An example of the resulting force field in a 'mis-aligned' scenario is presented in Fig. 1.1(f). The arrows are scaled according to magnitude of force. Tangential forces have been neglected for sake of clarity and hence all force lines are normal to plane of the WT. The error induced in the above approximation is that the forces are no longer originating at the same plane but are distributed in a 3D 'cloud' of LES grid points surrounding the 'mis-aligned' WT disk.

To summarize the parametrizations in the two scenarios, in the 'perfectly-aligned' case, local forces from Equation 1.12 are upscaled directly to the LES grid points using Equation 1.13 whereas in the 'mis-aligned' scenario, the local forces are first upscaled to the 'pseudo-LES' grid points, which are further distributed onto the LES grid points using IDW. (Note that in

the very exceptional case of $\xi = 45^\circ$, the ‘pseudo-LES’ grid points coincide with the LES grid points.)

1.4 Study Cases

A standard simulation under neutral atmospheric conditions is developed to test the performance of the new wind turbine model (A), and a *synthetic* diurnal cycle (B) is used to explore the changes occurring within a large wind farm due to thermal variations in the flow. Simulations are performed in a computational domain of size $(\pi \times \pi \times 2)z_i$, where z_i is the height of the initial boundary layer, set at 1000m. The numerical domain is decomposed in $N_x = N_y = 128$ and $N_z = 256$ grid points in the corresponding Cartesian directions. The time-step for the simulations is fixed to 0.2 s physical time, or equivalently 1.2×10^{-3} of non-dimensional time units (time is normalised with u_G and z_i).

Initially, a *warm-up* simulation was run to obtain fully developed velocity and scalar fields, which were *a posteriori* used to initialise the two performance tests. The *warm-up* simulation was developed by considering a neutrally stratified atmospheric boundary layer (ABL) with an imposed constant surface temperature of 290 K. The ABL was forced using a constant geostrophic wind $(u_G, v_G) \equiv (6, 0) \text{ m/s}$. The potential temperature was initialised with a constant value of 290 K up to z_i (ensuring the neutral stratification also close to the surface), along with a capping inversion of 0.012 K/m from z_i to the top of the domain. For the top boundary, Neumann condition was used for potential temperature, with $\frac{\partial \theta}{\partial z} = 0.005 \text{ K/m}$. This value was chosen to provide ventilation for the upper atmosphere. However, upon performing simulations with different flux values, it was found to be inconsequential to much of the boundary layer apart from the top of the computational domain.

The implemented wind turbines had a hub height (z_h) of 100 m, with a diameter (D) fixed at 100 m. A total of 24 wind turbines were placed in a rectilinear grid pattern, with 4 rows and 6 columns, such that the spacing in the x and y directions is $8D$ and $5D$, respectively. Note that the LES code uses periodic boundary conditions, thus the wind farm is essentially infinite. The *warm-up* simulation was run for 17 h of physical time (367.2 units of non-dimensional time) such that the flow is fully developed and a Wind Turbine Array Boundary Layer (WTABL) is established. The velocity and scalar fields at the end of this simulation were stored and re-used as initial conditions for the following two study cases (A and B).

With the aim of testing the performance of the new wind turbine algorithm, the *warm-up* simulation was continued for an extra 18 h. During the initial 6 h of physical time, the geostrophic wind was progressively rotated up to 30° around the vertical axis. Next, the simulation was continued for an additional twelve hours after the rotation was completed, until a new equilibrium was established. The absolute magnitude of the geostrophic wind vector was kept constant during the course of the simulation. The wind turbines progressively corrected their yaw orientation every ten minutes based on the time averaged orientation of the velocity at the turbine rotor disk. For this specific study case, the time averaging was done over a time period of 10 minutes; however this is an adjustable variable. Results will show how

the wind turbines' yaw orientation progressively follows the mean incoming wind.

The second study case consists of a *synthetic* ABL diurnal cycle also with wind turbines. To simulate the diurnal cycle, a sinusoidal function with a 24 h time period and an amplitude of 8.7 K (which is 3% of the fixed surface temperature of 290 K) was imposed as a time-varying surface boundary condition. Figure 3(a) shows the change in surface temperature, $\Delta\theta$ ($\Delta\theta = \theta_s(t) - \theta_s(t_0)$ with $\theta_s(t_0) = 290$ K). The simulation was run for 50 h of physical time, executing two complete diurnal cycles within that time period. The computational time for such simulations was 3,600 and 10,000 CPU hours for study case A and B respectively. The simulations exhibit some of the main characteristics of the flow in a large wind farm under a highly temporally and spatially variable atmospheric flow. This analysis has only been possible thanks to the flexibility of the new numerical algorithm that permits the wind turbines to dynamically adapt to the changing surrounding conditions.

1.5 Study case (A): Imposed time varying geostrophic wind under a neutral atmospheric stratification

The aim of the first study case is to check whether the new wind turbine model is able to adapt to the time changing incoming wind vector. Towards this aim, the mean flow of the ABL was progressively rotated in time, by linearly rotating the geostrophic wind. For the sake of simplicity and to be able to only focus on the performance of the wind turbines in readjusting to an ABL with rotating mean flow, an atmospheric neutral stratification was considered.

The simulation was initialised with the velocity and scalar fields from the *warm-up* simulation (see Sect. 1.4 for further details). Initially, the wind turbines had a mean orientation of 25 degrees. The geostrophic wind was made to rotate by an additional 30° in the following 6 h, and later it was kept fixed for the final 12 h. The wind turbines' configuration is set-up such that wind turbines' correct their orientation every 10 minutes, based on the time averaged orientation of the rotor disk averaged velocity ($\tan^{-1}(\langle v \rangle_d / \langle u \rangle_d)$).

Figure 1.2 shows the change in orientation of the mean flow at hub height, with respect to the streamwise direction (x) (represented by the dashed line), together with the time adapting orientation of the wind turbines (solid line). The turbines' orientation has been averaged over the 24 WTs, and the shaded region presents the corresponding standard deviation between the different wind turbines in the farm. The *staircase* shape of the turbine's curve is due to the 10 min averaging step. Results show how the WTs are capable of tracking the changing mean flow direction and correcting their own orientation accordingly. Note that the mean flow at the hub region experiences inertia to rotation. Thus the rotation is slower than the rotation of the forcing geostrophic wind. The simulation should be rotationally invariant, which means that in the limiting case of a fully developed flow with the rotated geostrophic wind, results should be statistically similar to the *warm-up* simulation. However, the limiting case is approached through oscillations in velocity magnitude and orientation. In Fig. 1.2 the orientation of the mean flow initially overshoots the theoretically enforced flow orientation, reaching a maximum orientation of 65°, opposed to the 55° expected. However by the end

1.5. Study case (A): Imposed time varying geostrophic wind under a neutral atmospheric stratification

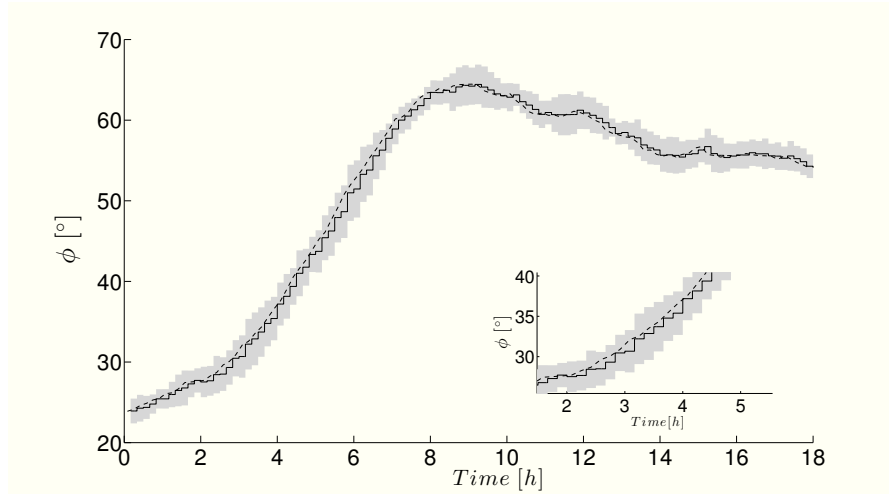


Figure 1.2 – Time changing mean horizontal wind orientation at hub-height (dashed line) and time readjustment of the wind turbine’s averaged yaw (solid line). The gray shaded region represents the standard deviation of the yaw orientation between the different wind turbines. The run-time for this test is 18 h, where the geostrophic wind is constantly rotated over the first 6 h, and kept fixed for the following 12 h.

of the simulation, the flow recovers from its own inertia and becomes consistent with the enforced orientation with the flow as well as wind turbines having orientation of 55° .

The flow inertia, in terms of magnitude, can be observed in Fig. 1.3(a), where the magnitude of the horizontal velocity at hub-height decelerates in the first 6 h, coinciding with the period of rotation of the geostrophic wind. Once the enforced rotation stops, the simulation proceeds towards the new equilibrium stage, which under rotational invariance should bear statistical similarity to the conditions at the start of simulation (A). It can be seen that horizontal velocity at the hub indeed accelerates to finally reach a similar value by the end of the simulation (at 18 h) to the one from the beginning.

The power extracted from the ABL by the WTs can be computed by considering all the points in the domain that are imparted volume forces arising due to the wind turbines and the velocities at those corresponding points. Thus for any wind turbine i , the power available is computed as follows,

$$P_i = \sum_j \vec{F}_{i,j} \cdot \vec{u}_{i,j}, \quad (1.17)$$

where the summation index runs over all the LES points imparted with force due to the i -th WT. Initially, the corresponding WTs power is time averaged every 10 min ($\overline{P_i}$), and a posteriori, averaging is also done over all the WTs ($\langle \overline{P} \rangle_{WT}$). Note that the power computed using Equation 1.17 is not the power extracted by the rotor, and to be converted to electricity, but reflects the mean kinetic energy lost from the ABL due to presence of wind turbines. In Fig. 3(a), the normalized mean velocity at hub-height and its standard deviation is presented. The resultant wind farm averaged power, together with the corresponding standard deviation, is

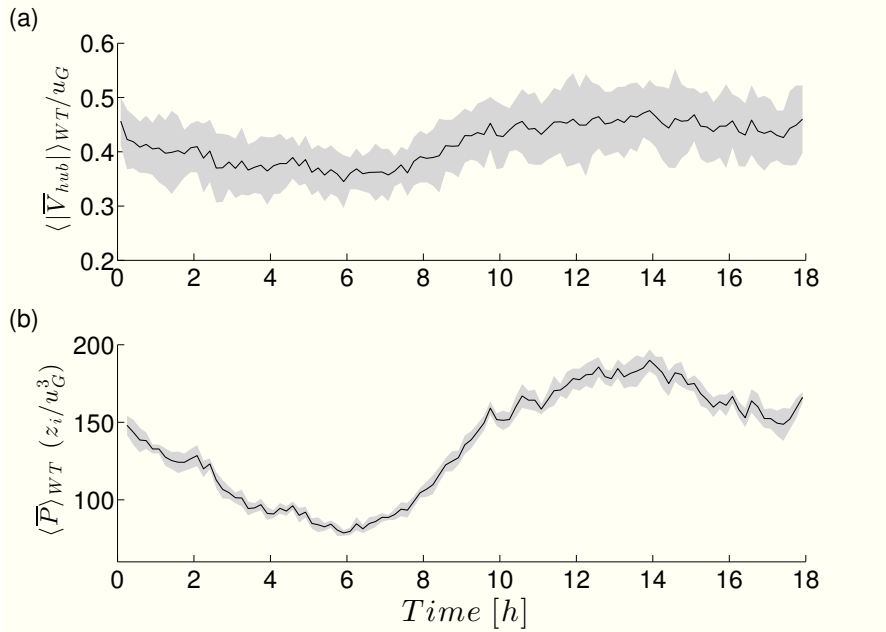


Figure 1.3 – Time evolution of magnitude of mean velocity at hub-height (a) and the extracted power (b). The shaded gray area represents the corresponding standard deviation of the mean wind velocity and extracted power between the 24 wind turbines.

shown in Fig. 1.3(b).

Note that the mean averaged velocity is non-dimensionalized with the geostrophic wind and the wind farm averaged power with the boundary layer height and the geostrophic wind as well. Following the same trend as the mean velocity, the power decreases up to the 6 h threshold, on account of decreasing hub velocity, and then increases between 6 h and 14 h, after which it decreases again at the end of the simulation, at 18h.

1.6 Study Case (B): A diurnal cycle

In the previous section, it has been shown that the new numerical algorithm performs well for modelling time-adaptive wind turbines, with the wind turbines adjusting to the time varying wind vector. Therefore, the new wind turbine algorithm allows for the modelling of wind turbines within a realistic time varying diurnal cycle flow, where the wind conditions dramatically change with the change in atmospheric stratification. Taking advantage of this new flexibility, a synthetic diurnal cycle is used to begin exploring in a first order approximation, the interaction between a large wind farm and a characteristic thermal ABL. To simulate a synthetic diurnal cycle, a time varying boundary condition for the surface temperature was enforced. For ease of analysis, a sinusoidal function with a time period of 24 h of physical time and an amplitude of 8.7 K (which is 3% of the fixed surface temperature of 290K) was imposed as shown in Fig. 1.4(a). The additional simulation parameters were kept equal to the *warm-up* simulation, from which the present study case was initialised.

Figure 1.4(a) shows the variation of the imposed surface temperature ($\Delta\theta_s = \theta_{s,t} - \theta_{s,t=0}$), and

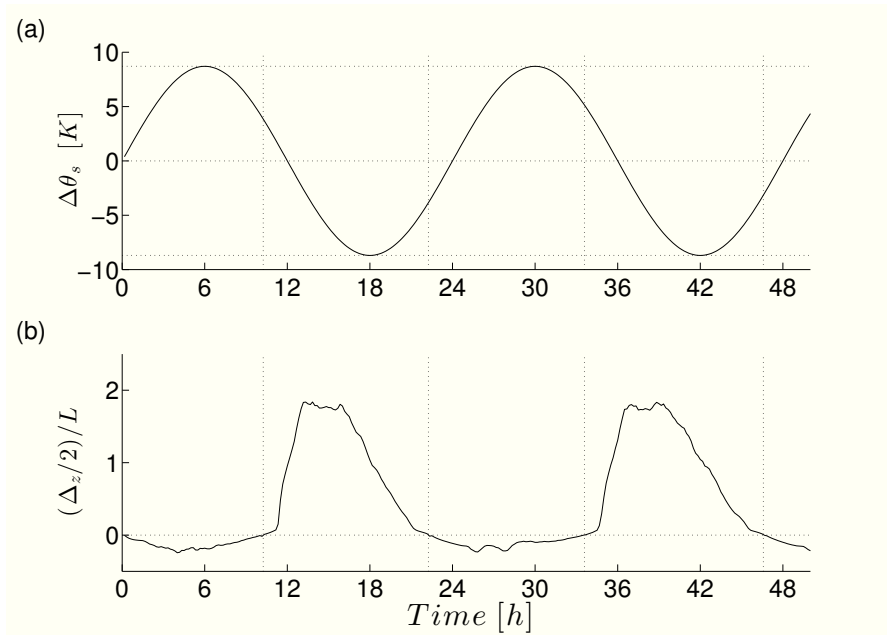


Figure 1.4 – Represents the thermal forcing conditions for two *synthetic* diurnal cycles (50h of physical time). Plot (a) shows the variation of the imposed surface temperature ($\Delta\theta_s = \theta_{s,t} - \theta_{s,t=0}$) as a sinusoidal function of time with an amplitude of 8.7K. Plot (b) illustrates the time evolution of the atmospheric stability with z/L , being $z = \Delta z/2$. The vertical dashed lines identify the time stamps where the atmospheric stability changes (10.25, 22.25, 33.83, 46.83 h). The horizontal dashed line identifies the change in sign.

Fig. 1.4(b) illustrates the corresponding change in atmospheric stratification, represented as z/L , with $z = \Delta z/2$ (physical height of the first numerical grid point). In both figures the x -axis represents the 50 h of real time numerically simulated.

Based on the change of sign in the stability parameter (z/L) from Fig. 1.4(b), the simulation can be divided into 5 regions of alternating stability conditions, with the first region being unstably stratified. The 5 regions are marked with 4 vertical dotted lines at 10.25, 22.25, 33.83 and 46.83 h, respectively. While the manner in which the diurnal cycle is artificially enforced is not very realistic, the stratification regimes illustrate the typical diurnal scenarios. As it would be expected, large differences are encountered on the wind vector both in magnitude and in direction.

Figure 1.5(a) shows the temporal variation of the wind turbine yaw alignment (solid line). The shaded region represents the standard deviation between the different wind turbines. It is very important to notice the difference in the standard deviation between the stably stratified regimes and the unstable ones. Also note how the orientation linearly increases during the stable regimes. The rate of change in the turbine's yaw alignment is better visualised in Fig. 1.5(b), which shows the magnitude of correction of the WTs every 10 minutes, averaged over the 24 WTs, together with the corresponding standard deviation. Overall, the correction in yaw during the unstable periods is an order of magnitude greater than that of the stably stratified periods. The standard deviation is also much higher during the unstable regimes as

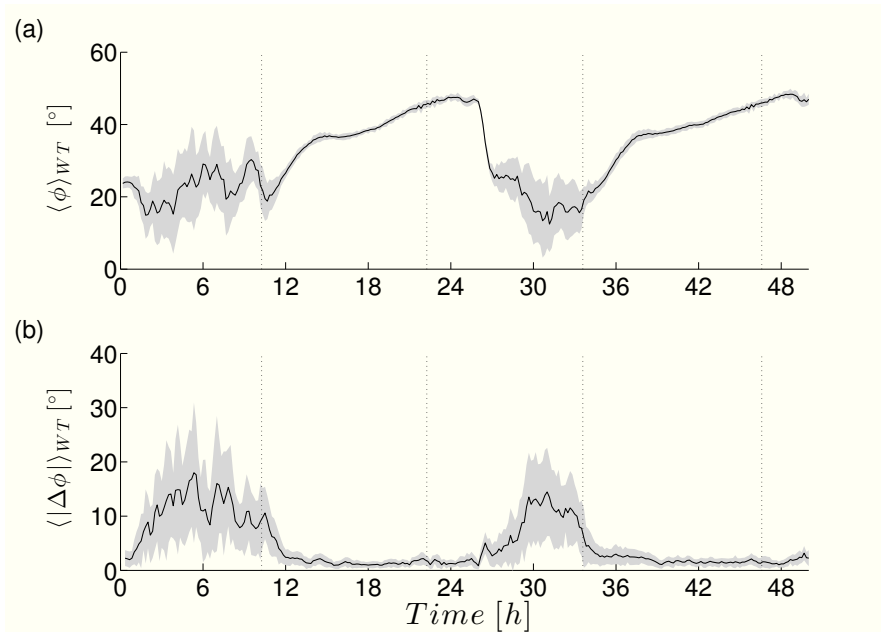


Figure 1.5 – Temporal variation of the wind turbines’ averaged yaw alignment (a), as the atmospheric stability changes (vertical dashed lines). The magnitude of correction of the WTs yaw alignment every 10 minutes is presented in Plot (b). It better illustrates the rate of change in the turbine’s yaw alignment. The shaded regions represent the corresponding standard deviations.

compared to the stable periods.

Similar to study case (A) (see Sect. 1.5), the corresponding hub height measured wind is now explored through the different stratification regimes. Figure 1.5(a) shows the corresponding velocity averaged over the 24 wind turbines (solid line) and the corresponding standard deviation associated with the variability between different turbines. The mean and standard deviation are greater during the unstable regimes compared to the stable periods. Correspondingly, the power extracted by the WTs from the ABL is shown with its mean and standard deviation in Fig. 1.5(b). It is very important to realise that, contrary to the standard belief, there is much more power available during day time. However, this comes with an associated high cost given by the high spatial and temporal variance. Therefore, in order to be able to harvest the wind resources available, it is necessary that wind turbines can cope with the high temporal variability. Note that the power extracted during the diurnal cycle is normalized using the overall time-averaged power extracted from study case A (in kinematic units), shown in Fig. 1.3(b). Because both study cases are driven by the same geostrophic forcing, this normalization provides an easy way to observe the differences in power extraction due to changes in stratification.

Further, it is interesting to look at the change in wind shear throughout the turbine’s rotor disk according to the different stability regimes. During the convective periods, the flow is largely dominated by large convective plumes and enhanced turbulence intensity, thus inducing a more mixed ABL. In contrast, nights are characterised by shallower boundary layers with

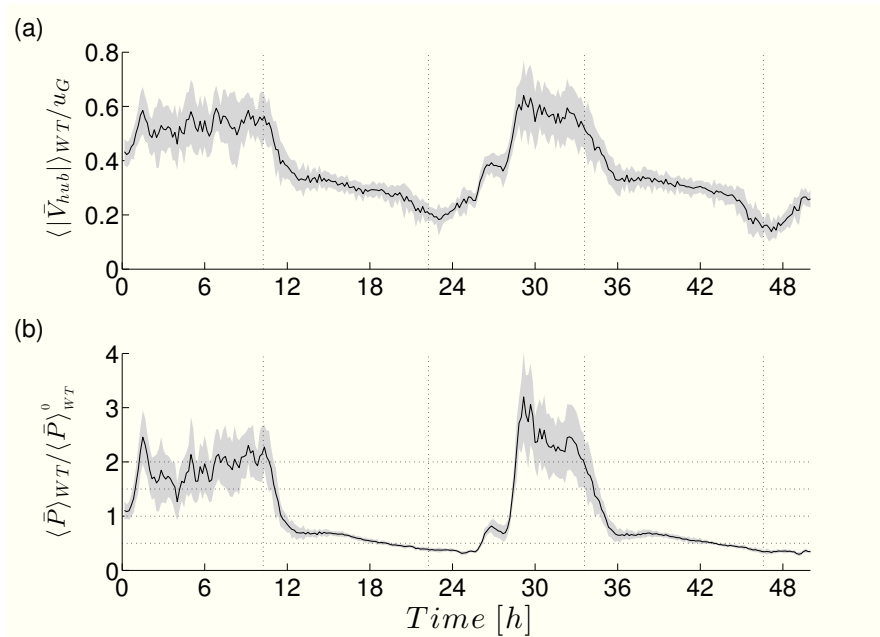


Figure 1.6 – Time evolution of the mean velocity (a) and the extracted power (b) for the diurnal cycle study case. The shaded gray area represents the corresponding standard deviation of the mean wind velocity and extracted power between the 24 wind turbines.

much less turbulence, and hence a completely different velocity profile. In this case, the effect of surface roughness and enhanced drag due to the turbines is felt in a much different manner compared to the unstable stratification. At night, velocity gradients are greater indirectly inducing a larger change of wind orientation with height. Not only is the shear enhanced during night time due to the vertical gradient of the velocity profile, but also a lateral shear is enhanced due to an increased change in wind direction throughout the rotor disk. This phenomena is well represented in Fig. 1.7(a).

Each shaded region represents a different vertical sector of the turbine’s rotor disk area. It can be observed that while during the convective regimes the vertical variability of the direction of the incoming wind vector (with respect to the Cartesian x -direction) is negligible, for the stable regimes there exists a change of even 20° throughout the turbine rotor dimensions. This enhanced vertical variability in the direction of the incoming wind vector induces a lateral shear on the turbine’s rotor disk. Figure 1.7(b) shows the associated standard deviation in the orientation of mean horizontal velocity for the same vertical sectors as in the above figure. It can be observed that there is larger variance during the unstable regimes, however, it can also be observed that larger vertical differences exist during the stable periods. For the sake of clarity, figure 1.7(c) represents the mean wind orientation at top ($z = z_h + D/2$), bottom ($z = z_h - D/2$) and center ($z = z_h$) of the rotor disk along with the average wind turbine orientation.

It is interesting to note that the wind turbine orientation follows the horizontal velocity orientation at hub height even in the stable regime inspite of the fact that the magnitude of horizontal velocity increases along the disk region while it’s inclination decreases. This shows

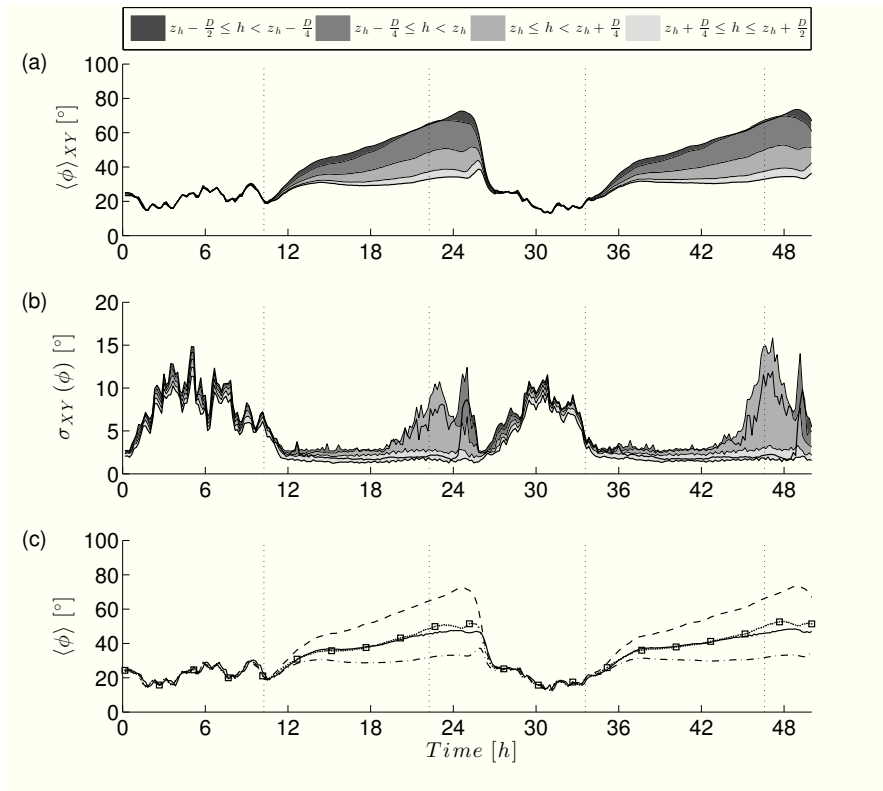


Figure 1.7 – It shows the mean angle of the incoming wind with respect to the stream-wise direction as a function of height (Plots (a) and (c)). Plot (c) shows the mean angle for $z = z_h + D/2$ (dot-dashed), $z = z_h - D/2$ (dashed) and $z = z_h$ (dotted with square markers) along with orientation of the wind turbines (solid) averaged over the 24 wind turbines. Plot (a) shows with a gray scale the progressive change in the angle of the mean horizontal velocity (time and planar average) as a function of height. Plot (b) illustrates the associated standard deviation.

the strength of the present algorithm for wind turbines where the WTs’ orientation is based on the disk-averaged velocity. Vertical variability of the angle of attack of the incoming wind vector is much more apparent from plots in Fig. 1.7 and strongly suggests that reorienting the WTs according to a single measure taken at hub height might be far from ideal, and more advanced methods using wind Lidar technology [Mikkelsen et al., 2013] should be rapidly developed.

1.7 Conclusions

Until now, most LES studies related to wind energy were done either using a fixed pressure gradient to ensure the mean wind direction to be perpendicular to the wind turbine rotor disk, or by forcing the flow with a geostrophic wind and timely readjusting the turbines orientation. In the cases studied here, it was possible to study wind farm conditions under close to realistic conditions with time varying wind directions. In this work a new LES model for a time-adaptive wind turbine has been introduced. The new algorithm enables the wind turbines to dynamically realign with the incoming wind vector. Therefore the modelled wind

turbines time-adjust the yaw orientation similar to a real wind turbine.

The performance of the new model was first tested under a simulation with controlled conditions. An ABL flow under neutral stratification was forced with a time changing geostrophic wind. The dynamical yaw-realignment of the wind turbines has been shown to accurately follow the orientation of the incoming wind vector. A posteriori, the new model was used to further explore the interaction between an idealized thermal ABL and an embedded wind farm. A close-to-realistic diurnal cycle was enforced with a changing surface temperature and a constant geostrophic forcing. Under these idealized ABL conditions, results show that contrary to popular understanding, there is a larger potential power to be harvested during the unstable time periods, but at the cost of designing wind turbines capable of adapting to the enhanced variance of these periods. On the contrary, stable periods provide less power, but are more constant over time.

Results also show that stable regimes are also characterised by an enhanced lateral shear induced by an increased change in wind direction with height. Therefore, the validity of traditional methods measuring incoming wind conditions through devices installed at the turbine's nacelle is called into question. The new LES model for time-adaptive wind turbines opens the potential for studies of a large array of real problems related to wind energy and their interaction with the surrounding atmospheric flow that previously couldn't be explored.

In the next chapter, a similar scenario with more realistic ABL forcing conditions coming from field experiments is considered, with corresponding time-changing surface boundary conditions, to further explore the power distribution and variability through a real ABL diurnal flow. Note that the aim of the work presented in this chapter was to introduce a new, more flexible, wind turbine model for being able to study more realistic ABL conditions. The two cases presented illustrate the performance of the model and show the potential use to further explore the interaction between WTs and realistic ABL flows.

Acknowledgements

This work was made possible by support received through the Swiss National Science Foundation (project No 200021 134892/1 and 200020 125092), CCES OSPER, the Swiss National Supercomputing Center (CSCS), the Scientific IT and Application Support (SCITAS) group at EPFL, the University of Utah and University of British Columbia.

Bibliography

- J.D. Albertson and M.B. Parlange. Natural integration of scalar fluxes from complex terrain. *Water Resour. Res.*, 23:239–252, 1999a.
- J.D. Albertson and M.B. Parlange. Surface length-scales and shear stress: Implications for land-atmosphere interaction over complex terrain. *Water Resour. Res.*, 35:2121–2131, 1999b.
- D. Barrie and D.B. Kirk-Davidoff. Weather response to a large wind turbine array. *Atmos. Chem. Phys.*, 10:769–775, 2010.
- E. Bou-Zeid, C. Meneveau, and M.B. Parlange. A scale-dependent lagrangian dynamic model for large-eddy simulation of complex turbulent flows. *Physics of Fluids*, 17:1–18, 2005.
- W. Brutsaert. *Hydrology: An Introduction*. Cambridge University Press, 2005.
- W Brutsaert, JHC Gash, MB Parlange, et al. Neutral humidity profiles in the boundary layer and regional evaporation from sparse pine forest. In *Annales Geophysicae*, volume 7, pages 623–630, 1989.
- Wilfried Brutsaert and Marc B Parlange. The unstable surface layer above forest: Regional evaporation and heat flux. *Water resources research*, 28(12):3129–3134, 1992.
- T. Burton, D. Sharpe, N. Jenkins, and E. Bossanyi. *Wind Energy Handbook*. Wiley, New York, 2001.
- M. Calaf, J. Meyers, and C. Meneveau. Large eddy simulation study of fully developed wind-turbine array boundary layers. *Physics of Fluids*, 22(015110):1–16, 2010.
- M. Calaf, M. B. Parlange, and C. Meneveau. Large eddy simulation of scalar transport in fully developed wind-turbine array boundary layers. *Physics of Fluids*, 23(126603):1–16, 2011.
- C. Canuto, M.Y. Hussaini, A. Quarteroni, and T.A. Zang. *Spectral Methods in Fluid Dynamics*. Springer-Verlag, Berlin, 1988.

Bibliography

- Paul Fleming, Pieter Gebraad, Jan-Willem van Wingerden, Sang Lee, Matt Churchfield, Andrew Scholbrock, John Michalakes, Kathryn Johnson, and Pat Moriarty. The sowfa super-controller: a high-fidelity tool for evaluating wind plant control approaches. *Proceedings of the European Wind Energy Association (Vienna, 2013)*, 2013.
- S. Frandsen. On the wind speed reduction in the center of large clusters of wind turbines. *J. Wind Eng. Ind. Aerodyn.*, 39:251–265, 1992.
- M. Frigo and S.G. Johnson. The design and implementation of fftw3. *Proceedings of the IEEE*, 93(2):216–231, 2005.
- F. González-Longatt, P. Wall, and V. Terzija. Wake effect in wind farm performance: Steady-state and dynamic behavior. *Renewable Energy*, 39(1):1–10, 2011. doi: 10.1016/j.renene.2011.08.053.
- Harish Gopalan, Christopher Gundling, Kevin Brown, Beatrice Roget, Jayanarayanan Sitaraman, Jefferey D Mirocha, and Wayne O Miller. A coupled mesoscale–microscale framework for wind resource estimation and farm aerodynamics. *Journal of Wind Engineering and Industrial Aerodynamics*, 132:13–26, 2014.
- M. Hultmark, M. Calaf, and M. B. Parlange. A new wall shear stress model for atmospheric boundary layer. *J. Atmos. Sci.*, 70:3460–3470, 2013.
- A. Jimenez, A. Crespo, E. Migoya, and J. Garcia. Advances in large-eddy simulation of a wind turbine wake. *J. Phys.:Conf. Ser.*, 75(012041):1–13, 2007. doi: doi:10.1088/1742-6596/75/1/012041.
- A. Jimenez, A. Crespo, E. Migoya, and J. Garcia. Large-eddy simulation of spectral coherence in a wind turbine wake. *Environ. Res.*, 3(015004):1–9, 2008. doi: doi:10.1088/1748-9326/3/1/015004.
- Jason M Jonkman and Marshall L Buhl Jr. Fast user’s guide. *Golden, CO: National Renewable Energy Laboratory*, 2005.
- D.W. Keith, J.F. DeCarolis, D.C. Denkenberger, D.H. Lenschow, S.L. Malyshev, S. Pacala, and P.J. Rasch. The influence of large-scale wind power on global climate. *Proceedings of the National Academy of Science*, 101(46):16115–16120, 2004.
- D. B. Kirk-Davidoff and D. W. Keith. On the climate impact of surface roughness anomalies. *J. Atmos. Sci.*, 65:2215–2234, 2008.
- V. Kumar, J. Kleissl, C. Meneveau, and M. B. Parlange. Large-eddy simulation of a diurnal cycle of the atmospheric boundary layer: Atmospheric stability and scaling issues. *Water Resources Research*, 42:1–18, 2006. doi: 10.1029/2005WR004651.
- H. Lu and F. Porté-Agel. Large-eddy simulation of a very large wind farm in a stable atmospheric boundary layer. *Physics of Fluids*, 23(065101):1–19, 2011.

- J. Meyers and C. Meneveau. Large eddy simulations of large wind-turbine arrays in the atmospheric boundary layer. *48th AIAA Aerospace Sciences Meeting Including the New Horizons Forum and Aerospace Exposition*, 4-7 January 2010.
- T. Mikkelsen, N. Angelou, K. Hansen, M. Sjöholm, M. Harris, C. Slinger, P. Hadley, R. Scullion, G. Ellis, and G. Vives. A spinner-integrated wind lidar for enhanced wind turbine control. *Wind Energy*, 16:625–643, 2013.
- JD Mirocha, B Kosovic, ML Aitken, and JK Lundquist. Implementation of a generalized actuator disk wind turbine model into the weather research and forecasting model for large-eddy simulation applications. *Journal of Renewable and Sustainable Energy*, 6(1):013104, 2014.
- Jeff Mirocha, Gokhan Kirkil, Elie Bou-Zeid, Fotini Katopodes Chow, and Branko Kosović. Transition and equilibration of neutral atmospheric boundary layer flow in one-way nested large-eddy simulations using the weather research and forecasting model. *Monthly Weather Review*, 141(3):918–940, 2013.
- C. H. Moeng. A large-eddy simulation model for the study of planetary boundary-layer turbulence. *J. Atmos. Sci.*, 41(2052), 1984.
- S. A. Orzag and Y. H. Pao. Numerical computation of turbulent shear flows. *Adv. Geophys.*, 18(224), 1974.
- Marc B Parlange and Wilfried Brutsaert. Regional shear stress of broken forest from radiosonde wind profiles in the unstable surface layer. *Boundary-Layer Meteorology*, 64(4):355–368, 1993.
- F. Porté-Agel, Y-T. Wu, and C-H. Chen. A Numerical Study of the Effects of Wind Direction on Turbine Wakes and Power Losses in a Large Wind Farm. *Energies*, 6(10):5297–5313, 2013. ISSN 1996-1073. doi: 10.3390/en6105297.
- A. Povitsky and P. J. Morris. A higher-order compact method in space and time based on parallel implementation of the thomas algorithm. *J. Comput. Phys.*, 161(1):182–203, 2000.
- D. A. Rajewski, E. S. Takle, J. K. Lundquist, S. Oncley, J. H. Prueger, T. W. Horst, M. E. Rhodes, R. Pfeiffer, J. L. Hatfield, K. K. Spoth, and R. K. Doorenbos. Crop wind energy experiment (cwex): Observations of surface-layer, boundary layer, and mesoscale interactions with wind farm. *BAMS*, May:655–672, 2013. doi: 10.1175/BAMS-D-11-00240.1.
- S. Baidya Roy. Simulating impacts of wind farms on local hydrometeorology. *J. Wind Eng. Ind. Aerodyn.*, 99:491–498, 2011.
- S.B. Roy, S.W. Pacala, and R.L. Walko. Can large wind farms affect local meteorology? *Journal of Geophysical Research*, 109(D19101):1–6, 2004.
- Adrian Sescu and Charles Meneveau. A control algorithm for statistically stationary large-eddy simulations of thermally stratified boundary layers. *Quarterly Journal of the Royal Meteorological Society*, 2014.

Bibliography

- Donald Shepard. A two-dimensional interpolation function for irregularly-spaced data. In *Proceedings of the 1968 23rd ACM national conference*, pages 517–524. ACM, 1968.
- H. Snel. Review of the present status of rotor aerodynamics. *Wind Energy*, 1(S1):46–69, 1998. doi: 10.1002/(SICI)1099-1824(199804)1:1+<46::AID-WE3>3.0.CO;2-9.
- R. B. Stull. *An Introduction to Boundary Layer Meteorology*. Springer Netherlands, 1988.
- S. G. Voutsinas, K. G. Rados, and A. Zervos. On the analysis of wake effects in wind parks. *J. Wind Eng. Ind. Aerodyn.*, 14:204–219, 1990.
- Y-T. Wu and F. Porté-Agel. Large-eddy simulation of wind-turbine wakes: Evaluation of turbine parametrizations. *Boundary-Layer Meteorology*, 138:345–366, 2011. doi: 10.1007/s10546-010-9569-x.
- Yu-Ting Wu and Fernando Porté-Agel. Simulation of Turbulent Flow Inside and Above Wind Farms: Model Validation and Layout Effects. *Boundary-Layer Meteorology*, 146(2):181–205, 2013. ISSN 1573-1472. doi: 10.1007/s10546-012-9757-y.
- X. Yang, S. Kang, and F. Sotiropoulos. Computational study and modeling of turbine spacing effects in infinite aligned wind farms. *Physics of Fluids*, 24(11):1–28, 2012.
- W. Zhang, C. D. Markfort, and F. Porté-Agel. Experimental study of the impact of large-scale wind farms on land-atmosphere exchanges. *Environmental research Letters*, 8(015002):1–8, 2013. doi: 10.1088/1748-9326/8/1/015002.

2 Perturbations to the spatial and temporal characteristics of the diurnally-varying atmospheric boundary layer due to an extensive wind farm

An edited version of this chapter was published in the journal *Boundary-Layer Meteorology* by Springer Nature. Copyright ©Springer Science+Business Media Dordrecht 2016. All rights reserved.

Sharma, V., Parlange, M.B. & Calaf, M. (2017) Perturbations to the Spatial and Temporal Characteristics of the Diurnally-Varying Atmospheric Boundary Layer Due to an Extensive Wind Farm. *Boundary-Layer Meteorol*, 162: 255. <https://doi.org/10.1007/s10546-016-0195-0>

To view the published open abstract, go to <http://dx.doi.org> and enter the DOI

V.S developed the numerical model, implemented it in the LES code, took part in the research design, performed simulations, analyzed the data and contributed to the writing of the paper

2.1 Introduction

The interaction of the turbulent atmospheric boundary layer (ABL) with an extremely large wind farm is studied by considering three distinct vertical regions of the flow. The bottom layer consists of the region between the surface and the bottom of the rotor-disk region and includes the surface layer of the standard ABL. The second layer is the rotor-disk region characterized by the presence of the wind-turbine wakes and thus this region is often referred to as the wake region. The third region consists of the flow above the top of the rotor-disk region extending up to the top of the ABL. Treating a wind farm as an enhanced surface roughness is perhaps the most common concept used to represent the atmospheric flow over turbines. Modelling of large-scale (in comparison to surface roughness) momentum-absorbing elements near the

Chapter 2. Perturbations to the spatial and temporal characteristics of the diurnally-varying atmospheric boundary layer due to an extensive wind farm

surface as enhanced surface roughness has counterparts in studies of flows over vegetated canopies and urban environments [Tseng et al., 2006, Giometto et al., 2016]. Note that, in the above framework, the ABL is partitioned vertically, and is dependent on neglecting entrance effects and the formation of an internal boundary layer that would be prominent features in a flow over a realistic finite-sized wind farm.

The rotor-disk region consists of an extremely complex flow with turbulent wakes of wind turbines interacting with each other as well as the background atmospheric turbulence simultaneously. The defining features of the wakes depend upon the blade-geometry and operation of the individual wind turbines, the spatial arrangement of these wind turbines in a wind farm and the turbulence characteristics of the atmospheric flow, which depend ultimately on the surface roughness and thermal stratification. This region has received much attention due to the wind-energy industry's focus on maximizing power production as well as lowering operational and maintenance costs. It is now well understood that when several wind turbines are clustered together forming a wind farm, the net harvested power is less than what theoretically would be extracted by an equal number of isolated turbines [Barthelmie et al., 2010]. Several works have analysed the effects of wind-turbine arrangement and wake superposition on the resultant harvested power [Barthelmie et al., 2007, 2009, Barthelemie and Jensen, 2010, Porté-Agel et al., 2013, Stevens et al., 2014] as well as wake interactions and the wake-recovery processes [Frandsen, 1992, Emeis and Frandsen, 1993, Frandsen et al., 2006, Cal et al., 2010, Markfort et al., 2012]. Analytical wake models for wind farms developed decades ago [S. Lissaman, 1979, Jensen, 1983, Katic et al., 1986] continue to serve as the bedrock of various engineering software packages used for wind-farm design such as the Wind Atlas Analysis and Application Program (WAsP).

With the availability of datasets from offshore wind farms such as the Horns Rev and Nysted wind farms located in the North Sea, most research has involved the standard case of wind turbines within a neutrally stratified atmospheric flow, which is also the most frequent stratification encountered in the marine ABL. The growing interest in terrestrial wind farms has resulted in research extending to scenarios where wind turbines are immersed in either a stably stratified or convective boundary layer (CBL). Results illustrate the relevance of accounting for the atmospheric stratification, showing major differences in power output, wake recovery, and turbulence intensity within the wind farm. For example, Baker and Walker [1984] found that the wake deficit behind a 2.5-MW wind turbine decreased by 10% in a flow with higher turbulence levels, indicating that in the CBL, the wake recovers more rapidly. These results are consistent with Iungo and Porté-Agel [2014] who used wind-lidar measurements. Keck et al. [2014], who analyzed the effect of atmospheric stability on wake meandering and the power production of wind turbines, showed that wind-turbine wakes are up to 10% weaker under unstable conditions, and found wake-induced power losses of up to 12% higher in very stable scenarios when compared to the neutral stratification. Using a thermally-stratified wind tunnel, Zhang et al. [2013] observed a 15% weaker wake deficit at the wake centre in the CBL, and concluded that in the CBL there is an enhanced radial momentum transfer within the turbines' wakes that leads to a more rapid momentum recovery. As a result of this

more rapid wake recovery, Churchfield et al. [2012] showed that for the case of a wind turbine placed behind another turbine, the power was between 15 – 20% higher under convective stratification.

In contrast, in the case of a wind farm immersed in a stably stratified flow, results were found to have an opposite trend. For example, Abkar and Porté-Agel [2013] found that momentum entrainment is limited by the thermal inversion leading to a slower wake recovery and a lower power production. They measured a 35% power reduction when the potential temperature lapse rate of the free atmosphere was increased from 1 to 10 Kkm⁻¹. Similarly, Barthelemie and Jensen [2010] estimated wind-farm efficiency reductions of up to 9% in stable conditions compared to the unstable scenario, for wind speeds of about 9 ms⁻¹. Results from Magnusson and Smedman [1994] also supported the fact that wind-turbine wake deficits are larger in the case of a stably stratified atmospheric flow. In addition Hancock and Pascheke [2010] showed that in a moderately stable boundary layer (SBL), the wind-turbine wake height is reduced and the far-wake width is increased when compared to the neutral case.

Abkar and Porté-Agel [2015] modelled a single wind turbine within three characteristic atmospheric stratifications showing how the turbulent kinetic energy (TKE) within the corresponding wakes is distributed, and with different intensities for different stabilities. Using a TKE budget analysis, they also showed how atmospheric stratification modifies the spatial distribution of the turbulence production, dissipation and transport terms within the wake. Their results confirmed a faster wake recovery in the convective regime due to an enhanced flow entrainment, with stronger wake meandering and a stronger axis asymmetry in the wake.

In comparison to the wake region, flow above and below the rotor-disk region has only recently been subjected to increasing scrutiny. One area of research is focused towards understanding the influence of terrestrial wind farms on microscale and mesoscale hydrometeorology. For example, Roy [2011] and Fitch et al. [2013a] using a large-scale numerical weather prediction model (such as the popular Weather Research and Forecasting (WRF) model) found that large wind farms modify the near-surface air temperature and humidity as well as the surface sensible and latent heat fluxes, resulting in lower air temperatures during daytime and warmer air at night. Similar trends were found in the field for existing large wind farms [Zhou et al., 2012, Xia et al., 2015]. While the reported values of these changes were small, these observations generated considerable interest since most terrestrial wind farms are installed over existing farmland and such perturbations have the potential to affect crop dynamics [Calaf et al., 2014] and irrigation demand [Higgins et al., 2015]. These simulations represented wind turbines as elevated momentum sinks and sources of TKE and contributions by Roy and Traiteur [2010], Fitch et al. [2012] and Abkar and Porté-Agel [2015] have successively increased the fidelity of such wind-farm representation.

Another branch of research is aimed at computing the global wind-power potential and the possible effects of large-scale wind-farm deployment on climate dynamics. Studies such as Keith et al. [2004], Kirk-Davidoff and Keith [2008], Barrie and Kirk-Davidoff [2010] and Wang and Prinn [2010] used general circulation models (GCMs) and used the concept of enhanced surface roughness to model the effect of large wind farms [Frandsen, 1992, Calaf et al., 2010,

Chapter 2. Perturbations to the spatial and temporal characteristics of the diurnally-varying atmospheric boundary layer due to an extensive wind farm

Meneveau, 2012].

The principal feature of atmospheric flow in the presence of a wind farm is the perturbed vertical momentum flux profile. This distinctive profile shows maximum shear stress at the top of the rotor disk, giving support to the enhanced surface roughness concept mentioned above. Beginning from the top of the rotor disk and moving towards the surface, the flow experiences a dramatic decrease in the stress, so much so that at the bottom of the rotor disk, the stress is in fact lower than the corresponding value in an unperturbed ABL at a similar height. This fact, coupled with the concept that dynamic stability of the ABL is governed largely by the thermal energy balance of the surface and turbulent mixing near the surface, implies that the presence of a wind farm can significantly alter the structure of the diurnally-varying ABL.

Quasi-steady flow scenarios for different stable [Lu and Porté-Agel, 2011, Aitken et al., 2014, Abkar and Porté-Agel, 2015, Bhaganagar and Debnath, 2015] and unstable conditions [Lu and Porté-Agel, 2015] for wind farms have been explored recently using large-eddy simulations (LES). However a diurnal cycle is by its nature, a continual process of formation, growth, quasi-stationarity and ultimately decay of the (unstable) CBL followed by a similar cycle for the SBL. Thus, not only the steady-state structure but the dynamical nature of the transient ABL can be potentially altered by wind farms. This is precisely what we set out to explore through our computational experiments of diurnal flow simulations in the presence of a wind farm. Two similar experiments have been performed by Fitch et al. [2013b], who used the WRF model to study the mesoscale influence of a finite-sized wind farm during the same diurnal cycle as used herein and by Abkar et al. [2016] who performed a high-resolution LES of a finite-sized wind farm to study the effects of an evolving ABL on the wakes of wind turbines. While these two studies have used different simulation methodologies and have different motivations as compared to the present study, they serve as important benchmarks to validate our results.

In Sect. 2.2, a concise description of the LES model used is provided along with a detailed description of the simulation set-up and the post-processing of the LES data (Sect. 2.2.1). Validation of the diurnal cycle simulation without wind farms is performed using field data and previous simulations of the well-known CASES-99 dataset (Sect. 2.2.2). Section 2.3 discusses the perturbations to the spatio-temporal structure of the evolving ABL induced by the wind farm by comparing bulk statistics of simulations with and without wind farms. In Sect. 2.4 we perform a mean kinetic energy (MKE) budget of the rotor-disk region of the wind farm (Sect. 2.4.1) and further focus on the effect of wind farms on the formation and growth of the CBL (Sect. 2.4.2), and the low-level jet formed during the late stable period (Sect. 2.4.3). The final part of the analysis focuses on the concept of considering wind farms as surfaces with enhanced roughness and the potential pitfalls in such an approach for terrestrial wind farms (Sect. 2.4.4). The results are placed in the context of providing specific implications for wind-farm operators and for climatologists studying the effect of large-scale wind-energy deployment on climate dynamics (Sect. 2.5).

2.2 Methodology and Validation

2.2.1 Description of Large-eddy Simulations

The atmospheric LES model used solves the non-dimensional, filtered, incompressible Navier-Stokes equations together with the continuity equation. To ensure conservation of mass and energy of the inertial terms, the rotational form of the filtered Navier-Stokes equations is used [Moeng, 1984]. Additionally, the advection-diffusion equation for the filtered potential temperature ($\tilde{\theta}$) is solved. The Boussinesq approximation is used to compute the buoyant forces in the Navier-Stokes equations by replacing relative density fluctuation (ρ'/ρ) with relative temperature fluctuations (θ'/θ). The subgrid-scale (SGS) fluxes for momentum and heat are modelled using the Lagrangian scale-dependent dynamic Smagorinsky model and its scalar counterpart [Bou-Zeid et al., 2005, Calaf et al., 2011]. The flow is driven by an imposed geostrophic flow with active Coriolis effects. Since the simulations are done to reproduce an extremely high Reynolds-number atmospheric flow, the viscous and molecular diffusive effects are neglected.

The code follows the numerical discretization of Moeng [1984] and Albertson and Parlange [1999a,b], where a pseudo-spectral discretization is used. Fourier transforms are used for the horizontal directions and second-order finite differences are used in the vertical direction. Use of Fourier methods implies that the domain is periodic in the horizontal directions and no lateral boundary conditions are needed and hence the domain size tends to infinity in practice. The equations are numerically integrated in time using a second-order Adams-Bashforth scheme, and the non-linear convective term is de-aliased with the 3/2 rule [Canuto et al., 1988]. The code is fully parallelized with Message Passing Interface (MPI), using the "Fastest Fourier Transform in the West" (FFTW) [Frigo and Johnson, 2005] for the Fourier transforms. The pressure solver is adapted for the parallel runs based on the pipeline Thomas algorithm [Povitsky and Morris, 2000].

At the upper boundary, a zero vertical velocity is imposed at the top of the numerical domain, together with a zero momentum flux for the momentum equations and a zero vertical gradient for the potential temperature. As bottom boundary conditions, a zero vertical velocity is imposed for the vertical component of the momentum equations, while an equivalent surface shear stress is imposed for the horizontal components. The shear stress is parametrized using Monin-Obukhov similarity theory [Monin and Obukhov, 1954], suitably adapted for LES using a methodology developed by Bou-Zeid et al. [2005] and Hultmark et al. [2013]. The atmospheric stability correction functions developed by Brutsaert [1992] are used with the scalar surface roughness length taken to be one tenth of the aerodynamic roughness length [Brutsaert et al., 1989]. Since the stability correction functions were initially developed for flat homogeneous surfaces and the wind turbines alter the momentum and heat fluxes near the surface, results should be considered as a first-order approximation. A lack of new experimental data does not allow for a better approach at the current time.

The wind-turbine model is based on the actuator disk concept using a parametrization developed by Meyers and Meneveau [2010] that provides formulations for both the axial as well

Chapter 2. Perturbations to the spatial and temporal characteristics of the diurnally-varying atmospheric boundary layer due to an extensive wind farm

as tangential forces. The inclusion of tangential forces allows for improved modelling of the near-wake region as shown by Wu and Porté-Agel [2011]. An additional improvement is the ability of the actuator disk to rotate around the vertical axis to reflect the yawing action of wind turbines. This is achieved by interpolating wind-turbine forces onto the LES grid points using inverse distance weighing. For complete details and mathematical formulations of the LES model and the wind-turbine model used, see Sharma et al. [2015].

2.2.2 Simulations and Validation using CASES-99 dataset

Two principal simulations were performed; (a) no wind turbines as the baseline study (designated as noWT) and (b) a full wind farm with 24 wind turbines arranged in four rows and six columns with spacing of $7D$ and $5D$ in the streamwise and cross-stream directions respectively (designated as WT24). An additional simulation, WT1, with a single wind turbine was also performed to illustrate the effect of loading on the SBL. All turbines have a hub-height (z_h) of 100 m with a rotor diameter (D) of 100 m, and all simulations have horizontal domain lengths of π km with vertical extent of 3 km. The computational grid consists of $128 \times 128 \times 384$ points resulting in a numerical discretization of $\Delta_x, \Delta_y = 24.54$ m in the horizontal and $\Delta_z = 7.81$ m in the vertical direction. An integration timestep of 0.2 s is used.

The Cooperative Atmosphere-Surface Exchange Study, CASES-99 [Poulos et al., 2002] dataset is used in this study. For simulation-based studies, a 58-h period beginning at 1400 h on 22 October 1999, for which the synoptic influences were found negligible, has proven to be especially useful. This period has been simulated using LES [Kumar et al., 2010], single column models [Svensson et al., 2011] and regional scale models [Shin and Hong, 2011]. A mesoscale study of flow in a hypothetical wind farm during the same period was also recently performed by Fitch et al. [2013b]. Here, a similar study using a comparatively higher resolution LES with an advanced SGS model is performed.

The simulations are forced using geostrophic wind components of $u_G = 9.5 \text{ m s}^{-1}$ and $v_G = 0$ throughout the entire height of the domain as shown in Fig. 2.1a; this also serves as the initial velocity condition. The initial condition for temperature is shown in Fig. 2.1b. Atmospheric LES need to be initialized with a turbulent flow field to reflect atmospheric turbulence, and is usually achieved by adding suitable fluctuations to the initial mean velocity and temperature profiles. In the present study, this noise is computed using the TKE profile shown in Fig. 2.1c. The diurnal cycle is simulated using the time-evolving surface temperature shown in Fig. 2.1d. Complete details, including the functional forms of these profiles can be found in Kumar et al. [2010].

The simulation fields are processed by first computing (block) time averages of the flow quantities $\alpha, \beta \in \{u, v, w, \theta\}$ (represented by the overbar) for each point of the grid, followed by spatial averaging along the two horizontal directions (represented by $\langle \rangle$). The correlation terms arising from these averaging operations are the traditional Reynolds flux terms as well as the dispersive stress terms; these quantities are also horizontally-averaged resulting in $\langle \overline{\alpha' \beta'} \rangle$ and $\langle \overline{\alpha'' \beta''} \rangle$ respectively. In addition to $\langle \overline{u} \rangle, \langle \overline{v} \rangle, \langle \overline{w} \rangle$ and $\langle \overline{\theta} \rangle$, we list below the principle terms

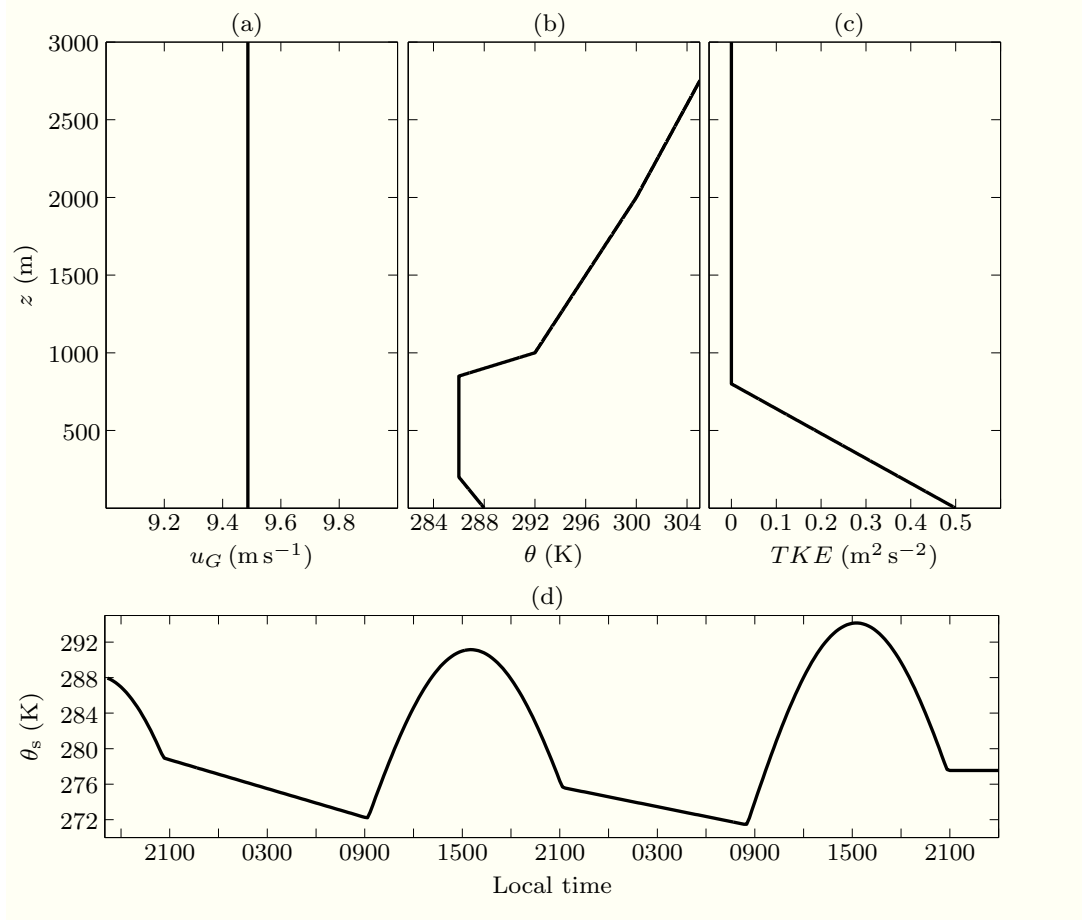


Figure 2.1 – Initial conditions for the diurnal cycle: (a) is the mean velocity, (b) the mean temperature profile, (c) TKE profile used for the random noise added on the mean velocity and temperature profiles, (d) temporal evolution of the imposed surface temperature.

of interest in our analysis,

$$|\vec{u}| = \langle \sqrt{\bar{u}^2 + \bar{v}^2 + \bar{w}^2} \rangle, \quad (2.1a)$$

$$MKE = 0.5 [\langle \bar{u} \rangle^2 + \langle \bar{v} \rangle^2 + \langle \bar{w} \rangle^2], \quad (2.1b)$$

$$TKE = 0.5 [\langle \bar{u}'u' \rangle + \langle \bar{v}'v' \rangle + \langle \bar{w}'w' \rangle], \quad (2.1c)$$

$$\tau_x = \langle \bar{u}'w' \rangle + \langle \bar{u}''w'' \rangle + \tau_{1,3}^{sgs}, \quad (2.1d)$$

$$\tau_y = \langle \bar{v}'w' \rangle + \langle \bar{v}''w'' \rangle + \tau_{2,3}^{sgs}, \quad (2.1e)$$

$$\tau = \sqrt{\tau_x^2 + \tau_y^2}, \quad (2.1f)$$

$$H_s = \langle \bar{w}'\theta' \rangle + \langle \bar{w}''\theta'' \rangle + \tau^{sgs, scalar}. \quad (2.1g)$$

It is thus evident that our analysis is focused on bulk flow statistics that vary only with height (z) and time (t). The time averaging is performed for a period of 10 min; the averaging time needs to be judiciously chosen such that small-scale turbulent fluctuations have been averaged

Chapter 2. Perturbations to the spatial and temporal characteristics of the diurnally-varying atmospheric boundary layer due to an extensive wind farm

while the larger diurnal trends are maintained. The inclusion of dispersive stresses and the use of bulk quantities justifies the use of a short averaging time of 10 min. On the other hand, this averaging time allows for the analysis of the transition events.

The simulation results are first validated using results from Kumar et al. [2010] and experimental data from the CASES-99 dataset. Results of the noWT simulation are principally used for validation, while the WT24 and WT1 simulation results are shown for reference and comparison. The first subplot in Fig. 2.2 shows the velocity magnitude at 10 m above the surface (u_{10}). The noWT simulation u_{10} time-series agrees well with the CASES-99 data as well as the results of Kumar et al. [2010]. In fact, in the convective regime, the noWT simulation results are closer to the experimental dataset than those of Kumar et al. [2010]. This could be a result of the improved scalar SGS model employed herein. Note that the observed values are point measurements having a more oscillatory signal compared to the simulated results, which are spatially averaged. The second subplot shows the inter-comparison of the surface sensible heat flux ($H_{s,surface} = H_s(z = \Delta_z/2, t)$) and the third subplot shows the intercomparison for the surface friction velocity ($u_* = \sqrt{\tau(z = \Delta_z/2, t)}$). In general, the noWT simulation results are broadly in agreement with the field-campaign dataset and the results of Kumar et al. [2010] having the same general trends with similar values. The four vertical dotted lines indicate the stability transition points $t_{s1} = 1010$ h on Day 2 (S→U), $t_{s2} = 1810$ h on Day 2 (U→S), $t_{s3} = 0940$ h on Day 3 (S→U) and $t_{s4} = 1800$ h on Day 3 (U→S), where (S→U) indicates a transition from stable to unstable (or convective) stratification and (U→S) the other way around. These transitions are also referred to as morning and evening transitions respectively. During the course of the simulation, the maximum absolute Obukhov length (L) was found to be approximately 40 m (apart from the transition periods, where L is undefined).

2.3 Evolution of the diurnally-varying ABL

In the previous section we described our methodology for the simulations and the analysis framework for post-processing the simulation data. We proceeded by validating our baseline simulation without the wind farm (noWT) with results from the existing literature. Here, we present the bulk statistics computed by these simulations. We begin with an illustration of mean velocity at hub-height for the WT24 and the WT1 simulations for a characteristic daytime (unstable) and a characteristic nighttime (stable) stratification shown in Fig. 2.3. Figure 2.3a,c illustrates the daytime (at 1100 h on Day 2) convective flow for the wind farm and the single wind-turbine cases, and Fig. 2.3b,d illustrates the nighttime (at 0300 h on Day 2) stable flow. A qualitative assessment of the WT24 simulation shows that during the convective period, wind turbines have a larger variance in orientation with shorter and broader wakes (see Fig. 2.3a). On the other hand, in the stable period, the velocity at hub-height is smaller and unidirectional with wakes being longer and narrower, resulting in a greater interaction with the downstream turbines (Fig. 2.3b). For the single wind-turbine case a similar differential behaviour between the convective and stable periods is observed except for the fact that in this case, velocities at hub-height are greater at nighttime (Fig. 2.3c). The fact that the wind-turbine model can dynamically correct its yaw finds greater utility in unstable conditions with a rapid

2.3. Evolution of the diurnally-varying ABL

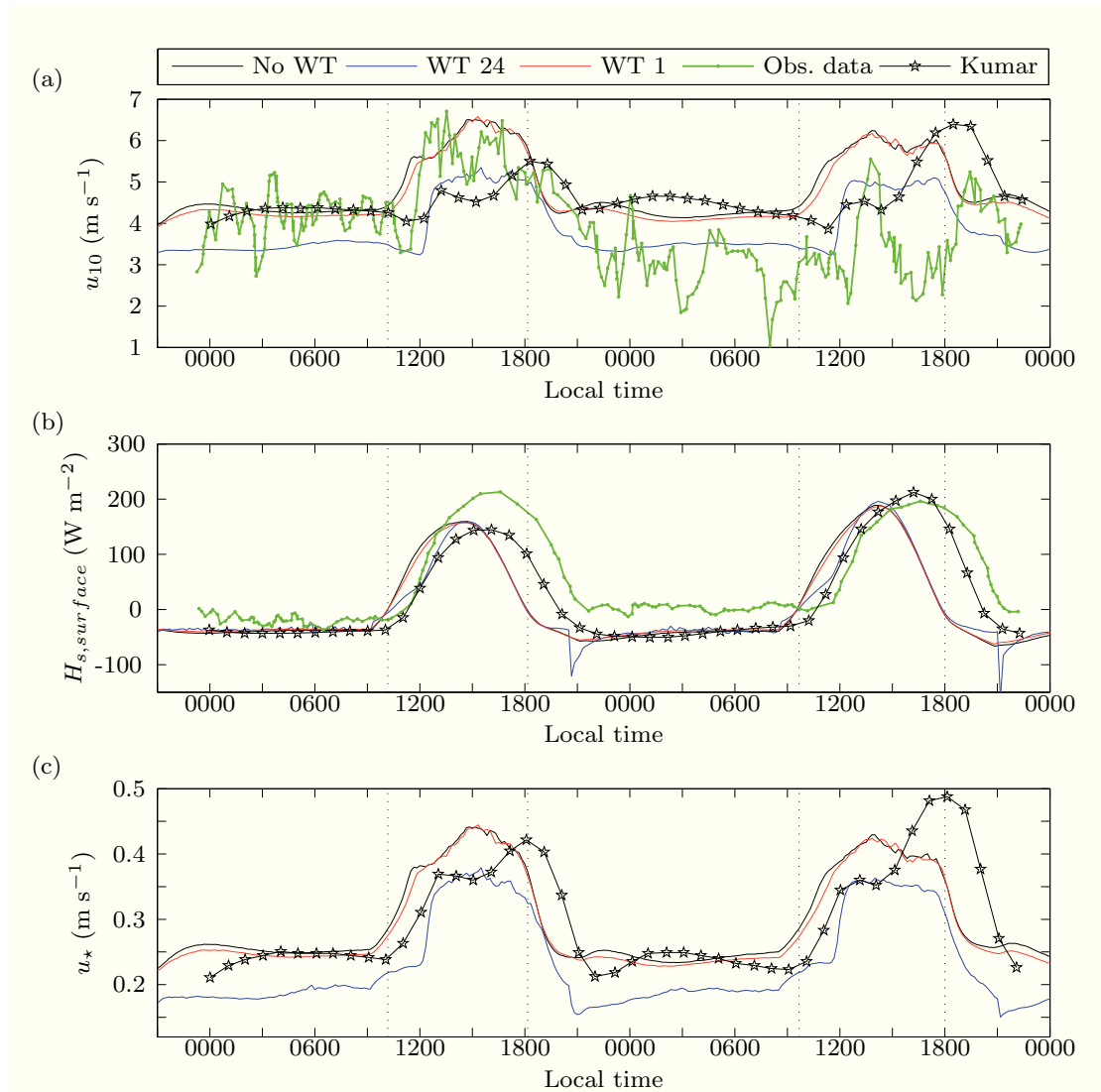


Figure 2.2 – Validation of the numerical simulations with the CASES-99 experimental data (green line) and the numerical results of Kumar et al. [2010] (stars). The black line represents the case without wind turbines, which is used for validation. The blue and red lines that represent the WT24 and WT1 simulations respectively are illustrated for reference. (a) 10-m mean wind speed [m s^{-1}], (b) surface sensible heat flux [W m^{-2}], (c) friction velocity [m s^{-1}]

Chapter 2. Perturbations to the spatial and temporal characteristics of the diurnally-varying atmospheric boundary layer due to an extensive wind farm

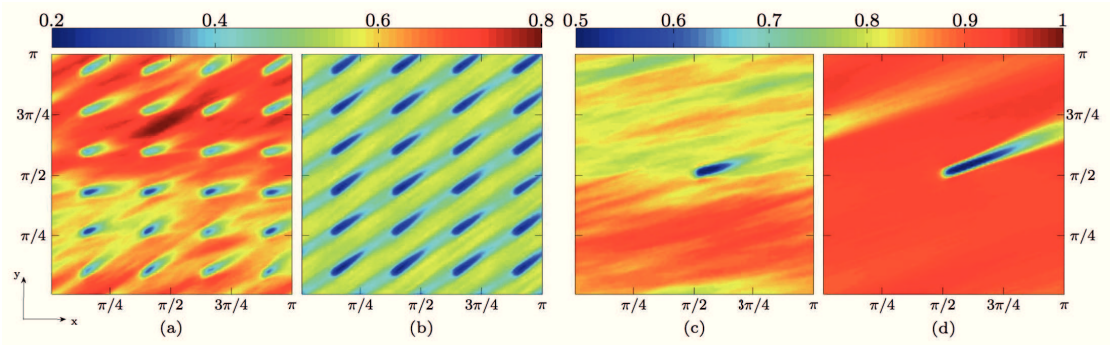


Figure 2.3 – Horizontal slices of the 10-min averaged, normalized velocity magnitude fields at hub-height for two characteristic periods of the WT24 and WT1 simulations. (a) WT24 daytime, (b) WT24 nighttime, (c) WT1 daytime, (d) WT1 nighttime.

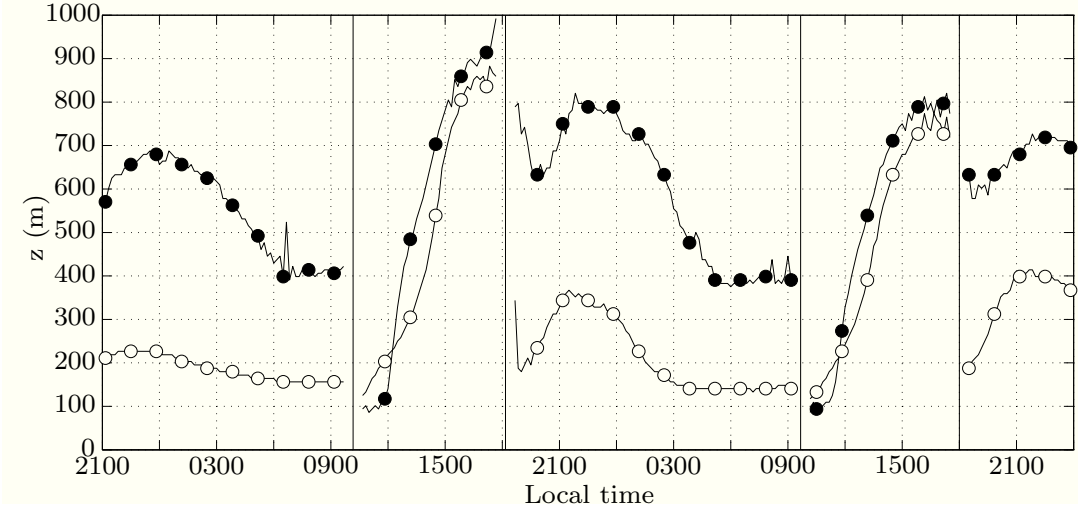


Figure 2.4 – Temporal evolution of the height of the ABL. The open markers represent the noWT simulation and the closed markers represent the WT24 simulation. Note that the ABL height is computed every 10 min based on bulk statistics. The four vertical lines mark the transition points at 1010 h and 1810 h on Day 2 and 0940 h and 1800 h on Day 3.

2.3. Evolution of the diurnally-varying ABL

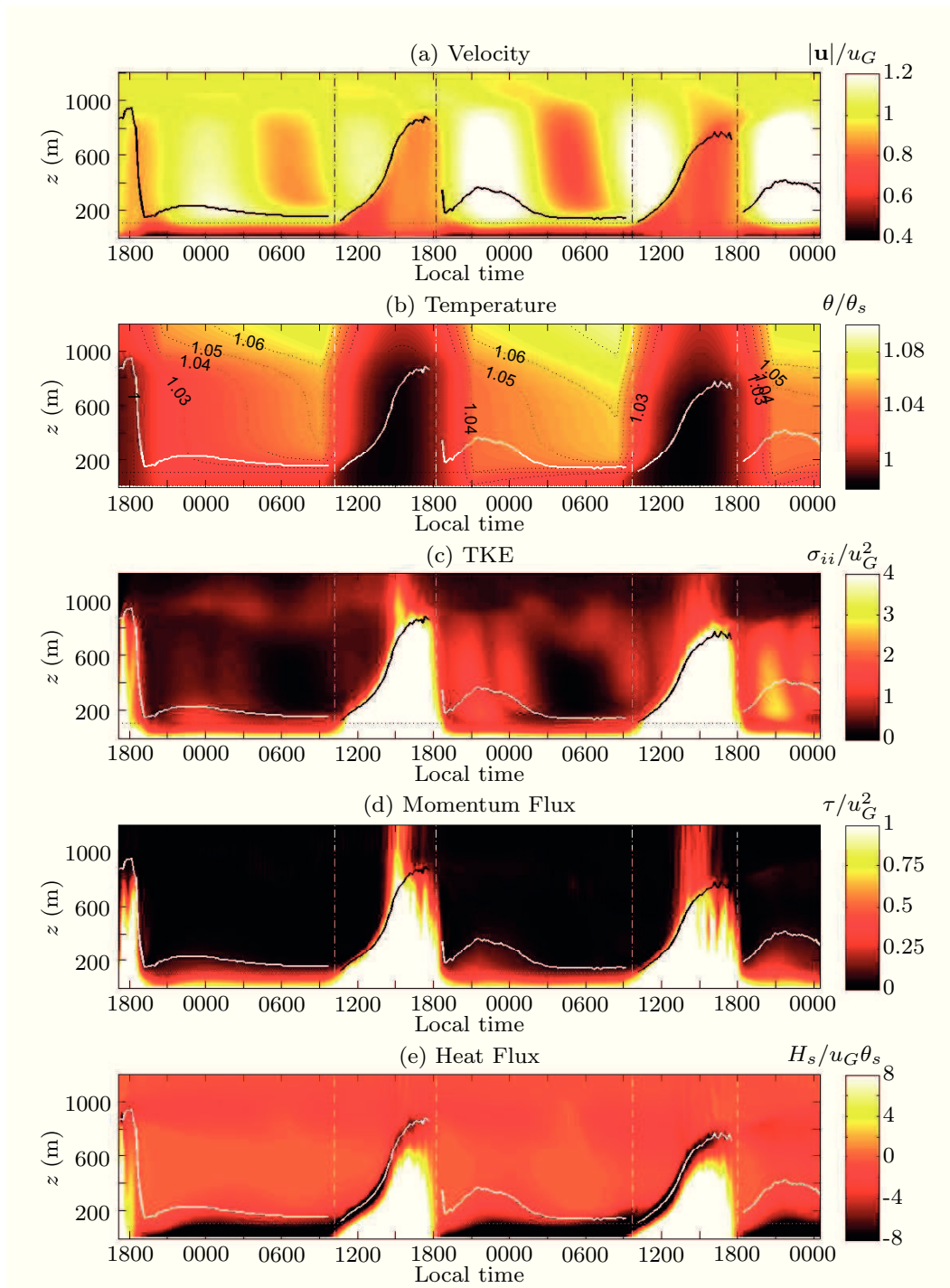


Figure 2.5 – noWT simulation: temporal evolution of the 10-min averaged vertical profiles of (a) velocity magnitude, (b) temperature, (c) TKE ($\times 10^3$), (d) net vertical momentum flux ($\times 10^3$) and (e) sensible heat flux ($\times 10^5$). Geostrophic velocity and surface temperature are used as normalization scales. The four vertical lines mark the transition points at 1010 h and 1810 h on Day 2 and 0940 h and 1800 h on Day 3. The horizontal line at 100-m height represents the wind turbine hub-height. The height of the ABL shown in Fig. 2.4 is super-imposed for reference.

Chapter 2. Perturbations to the spatial and temporal characteristics of the diurnally-varying atmospheric boundary layer due to an extensive wind farm

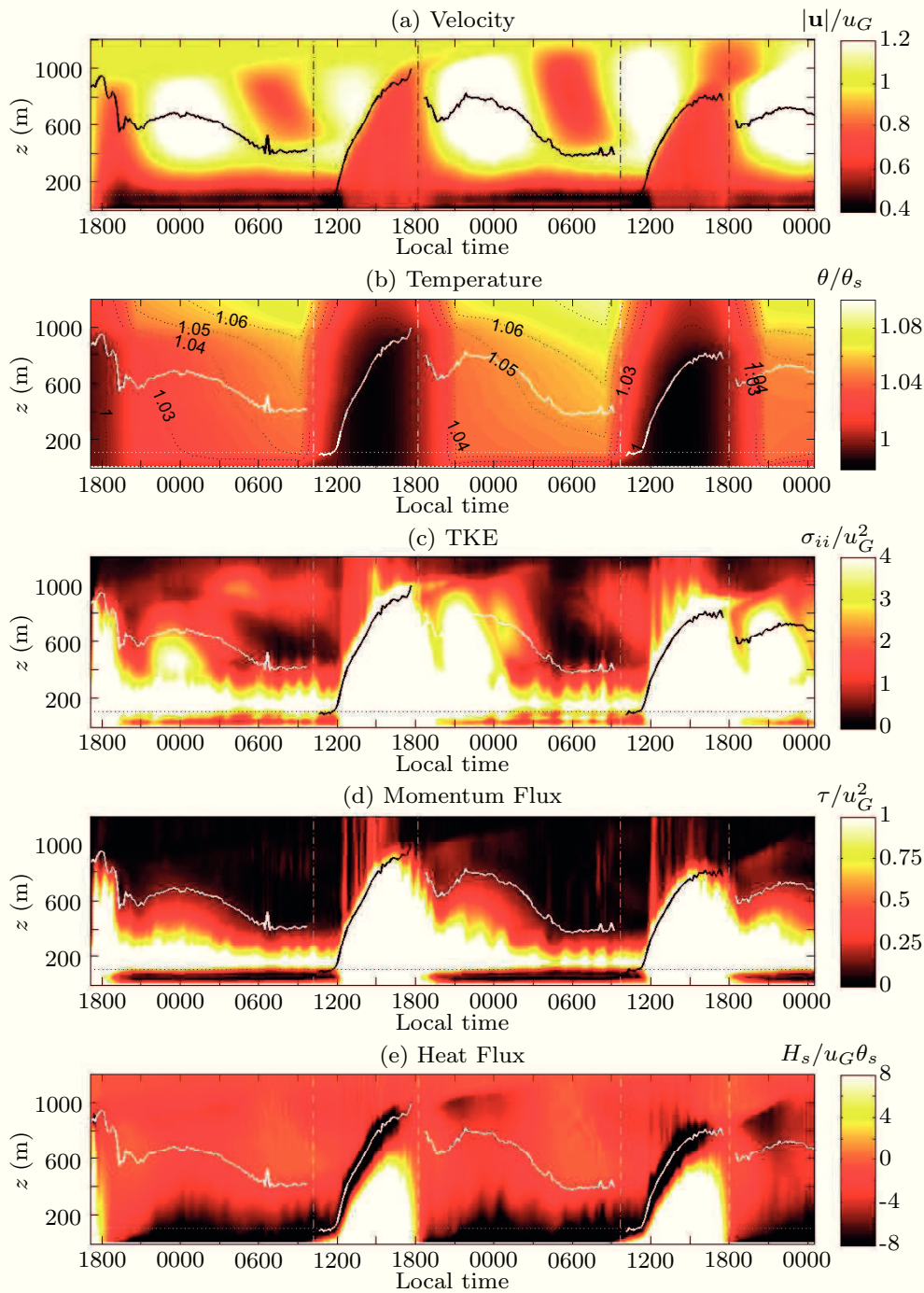


Figure 2.6 – WT24 simulation: temporal evolution of the 10-min averaged vertical profiles of (a) velocity magnitude, (b) temperature, (c) TKE ($\times 10^3$), (d) net vertical momentum flux ($\times 10^3$) and (e) sensible heat flux ($\times 10^5$). Geostrophic velocity and surface temperature are used as normalization scales. The four vertical lines mark the transition points at 1010 h and 1810 h on Day 2 and 0940 h and 1800 h on Day 3. The horizontal line at 100-m height represents the wind turbine hub-height. The height of the ABL shown in Fig. 2.4 is super-imposed for reference.

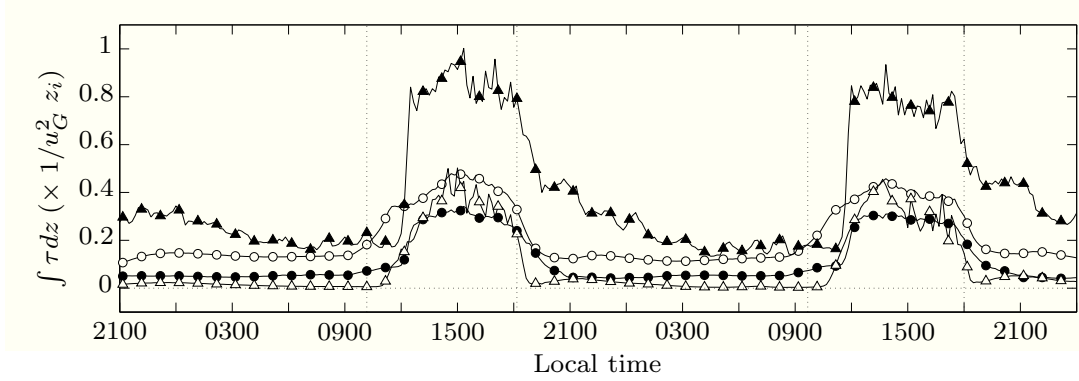


Figure 2.7 – Momentum flux integrated between $z = \Delta_z/2$ and $z_h - D/2$ (marked as circles) and between $z = z_h + D/2$ and $2z_h$ (marked as triangles). The noWT and WT24 simulations are represented by open and closed markers respectively. The four vertical lines mark the transition points at 1010 h and 1810 h on Day 2 and 0940 h and 1800 h on Day 3. Values are scaled by the geostrophic velocity and a reference boundary-layer height of 1000 m.

spatio-temporally varying flow direction. As each wind turbine corrects its yaw independent of the other turbines, this model permits us to simulate a more realistic wind farm with different orientations of each of the constituent wind turbines.

In Fig. 2.4, the height of the ABL during the course of the diurnal cycle is shown, where this is identified differently, according to the prevailing stratification. For unstable conditions the peak of the negative sensible heat flux in the entrainment region is used to identify the height of the ABL (or CBL during this period) [e.g. Mahrt and Lenschow, 1976]. For the stable period, we identify the top of the SBL as the height at which the vertical momentum flux falls to 10 percent of the surface stress in the noWT simulation and the value at top of the rotor disk in the WT24 simulation. Our justification is that in the SBL, turbulence is generated mechanically and the sensible heat flux simply reflects the profiles of the vertical momentum flux, sensible heat flux and vertical momentum flux being linked through the TKE budget equation. In the SBL, sensible heat flux acts to destroy turbulence and is balanced by the shear divergence. In the standard flat-terrain SBL, the shear generation is maximum at the surface whereas in the presence of the wind farm, this occurs at the top of the rotor disk. Derbyshire [1990] derived an analytical expression for determining the height of the nocturnal SBL,

$$h^2 = \sqrt{3} k R_f \frac{u_* L}{|f_c|}, \quad (2.2)$$

where k is the Von Karman constant, R_f is the flux Richardson number, u_* is the friction velocity, L is the Obukhov length as described earlier, and $|f_c|$ is the Coriolis parameter. Using these values from the LES data for a period between 0600 h and 0900 h on Day 2 gives a height of 158 m. This compares well with the height of SBL as 157 m for the same period presented in Fig. 2.4 and computed using the methodology adopted herein. The open symbols in Fig. 2.4 represent the noWT simulation and the closed symbols mark the WT24 counterpart. Note that the markers are present only to distinguish the two line plots showing the ABL

Chapter 2. Perturbations to the spatial and temporal characteristics of the diurnally-varying atmospheric boundary layer due to an extensive wind farm

height computed every 10 min based on the 10-min averaged statistics. The four vertical lines represent the transition points during the simulation described earlier. It is found that the height of the ABL is 175% larger in the WT24 simulation as compared to the noWT simulation during the stable period. On the other hand, the steady-state convective period shows a mere 5% increase due to the presence of the wind farm. However, as will be shown in the next section, during the unstable regime, it is the dynamics of the formation and growth of the CBL that are significantly perturbed by the presence of a large wind farm.

Figures 2.5 and 2.6 show the diurnal evolution of ABL for the noWT and the WT24 simulations respectively through subplots showcasing the bulk quantities of (a) magnitude of velocity ($|\bar{u}|$), (b) temperature (θ), (c) TKE, (d) vertical momentum flux (τ), and (e) sensible heat flux (H_s). These quantities are normalized using the geostrophic velocity and surface temperature; the corresponding ABL heights from Fig. 2.4 are super-imposed onto each subplot for reference. All figures contain four vertical lines to mark the transition points, and additionally a horizontal dotted line at hub-height is also marked for reference. The colours of these additional annotations are varied for improved visualization.

We limit our discussion to the period between the transition point at 1010 h on Day 2 and the transition point at 0940 h on Day 3, thus nearly covering an entire diurnal cycle. In the noWT simulation (Fig. 2.5), upon transition, the CBL is formed and begins to grow; this can be seen in the H_s subplot with a growing region of positive heat flux capped by an entrainment zone with negative heat flux. The buoyant thermal plumes generated at the surface act as contributors in the TKE budget and the excess turbulent energy is dissipated through increased Reynolds stresses. Thus, values of τ and TKE reflect the trend in H_s . The wind speeds during the unstable period are marked by being subgeostrophic and generally lower than at nighttime. This is due to the higher τ values in the CBL, and the dissipation of MKE. It is interesting to note that the computed height of the CBL neatly encompasses this low-velocity region. The partitioning of the total energy is therefore altered with higher TKE and lower MKE in the CBL as compared to the SBL. The growth of the CBL is ultimately constrained by the overlying capping inversion between the ABL and the free atmosphere and reaches a steady height at 1600 h, 2 h before the impending transition to the SBL. The SBL is marked by a sudden decrease in shear stress and TKE throughout the depth of the erstwhile CBL. The cooling surface results in negative H_s at the surface. Turbulence is generated by mechanical shear at the surface and it can be seen that their corresponding values are negligible throughout the ABL apart from a shallow region near the surface. It is worthwhile to note that the methodology used to identify the height of the SBL delineates the height below which the cooling from the surface extends quite clearly. The flow field above 100 m accelerates to super-geostrophic velocities just after 2100 h, and this high velocity region ultimately shrinks to a confined space just above 100 m beginning around 0300 h until 1000 h. This region is otherwise known as the low-level jet (LLJ), which collapses upon transition to the convective regime. The dynamics of the flow above the SBL are governed by a balance of geostrophic and Coriolis forces in the absence of any friction. This is the well-known inertial oscillation phenomenon that has been observed in various flat-terrain field campaigns [Blackadar, 1957, Stensrud, 1996, Banta et al., 2002].

Before proceeding further, it is pertinent to place these results in the context of the existing literature on the subject of the diurnal cycle over flat terrain under clear-sky conditions. The results of the noWT simulation show many notable features such as the initial linear growth of the CBL followed by a convex (faster) growth while being capped by an entrainment region [Wyngaard and Coté, 1974, Mahrt and Lenschow, 1976, Sun and Ogura, 1980], the rapid decay of shear stress and TKE throughout the depth of the ABL following the evening transition [Nieuwstadt and Brost, 1986, Sorbjan, 1997] and the inertial oscillations observed above the SBL giving rise to the LLJ in the late stable period [Blackadar, 1957]. In general the noWT simulation also shows consistency with LES results presented in Basu et al. [2008] and Kumar et al. [2010].

Figure 2.6 shows the spatio-temporal evolution of the ABL in the presence of a wind farm and the large-scale perturbations induced in relation to the noWT simulation in Fig. 2.5. Once again focusing on the period between 1010 h on Day 2 and the transition point at 0940 h on Day 3, it is immediately apparent that the formation and growth of the CBL is significantly different from the noWT simulation. The sensible heat flux has a slow growth until 1200 h at which time, there is a sudden increase in the growth of the CBL. It can also be seen that the momentum flux and TKE are much lower between the surface and hub-height than above effectively decoupling the mixing between the surface and the air aloft. At 1200 h, the sudden growth of the CBL occurs as the flux values as well as the TKE below the rotor disk increase sharply. The growth of the CBL itself follows a concave trend (decreasing rate of growth) as opposed to the convex shape of CBL growth (increasing rate of growth) in the noWT simulation. Velocities are sub-geostrophic, similar to the noWT simulation and encapsulated well by the computed height of the CBL. Upon transition to the SBL, the general trend in the velocity is similar to the noWT simulation with the main difference being that the LLJ is shifted upwards by the wind farm. The LLJ in the presence of the wind farm is observed to form above the rotor-disk region, with a more extensive vertical extent as compared to the noWT simulation. The differences between the WT24 and the noWT simulations are far more evident for the momentum flux and the TKE. It can be observed that a layer of high shear stress and TKE persists above the rotor-disk region throughout the SBL, reaching a constant thickness between 0600 h and 1000 h. In contrast, the momentum flux and TKE values below the rotor disk are reduced to negligible values rapidly upon transition and remain as such throughout the stable period. Thus the main source of turbulence in the presence of the wind farm during the stable period is at the top of the rotor disk with much weaker turbulence beneath the rotor disk. It is further interesting to note that due to the additional mixing induced by wind-turbine wakes, the negative heat-flux region extends deeper into the ABL and it is more diffused with significant oscillations in its vertical extent as compared to the noWT simulation.

The results of the WT24 simulation are similar to the SBL simulations of Lu and Porté-Agel [2011] with a decrease in turbulence levels below the rotor-disk region and the upward shift of the LLJ, as also reported in LES of finite-sized wind farms [Abkar et al., 2016] and WRF simulations [Fitch et al., 2013b]. The results for the quasi-steady CBL (for example, between 1500 h and 1800 h on Day 2), compare well with the trends shown by Lu and Porté-Agel [2015],

Chapter 2. Perturbations to the spatial and temporal characteristics of the diurnally-varying atmospheric boundary layer due to an extensive wind farm

namely, the slight increase in the height of the late CBL and a deeper entrainment region with relatively higher heat flux as compared to the noWT simulation.

Figure 2.7 focuses on the perturbation of the momentum-flux profiles due to a large wind farm in the regions above and below the rotor-disk region in comparison to the noWT simulation. The momentum flux (τ) is integrated vertically between $z = \Delta_z/2$ and $z_h - D/2$ (marked as circles and referred to as \mathcal{L}) and between $z = z_h + D/2$ and $2z_h$ (marked as triangles and referred to as \mathcal{H}). The noWT and WT24 simulations are represented by open and closed markers respectively, with transitions points marked by vertical dotted lines.

For the noWT simulation, \mathcal{H} is smaller than \mathcal{L} for the entire diurnal cycle ($0.03 \leq \mathcal{H}_{noWT}/\mathcal{L}_{noWT} \leq 0.9$) as expected. The upper limit of the \mathcal{H}/\mathcal{L} ratio is found only during the late convective period (between 1500 h and 1800 h). On the contrary, for the WT24 simulation, \mathcal{H} is larger than \mathcal{L} throughout the diurnal cycle ($1.1 \leq \mathcal{H}_{WT24}/\mathcal{L}_{WT24} \leq 9$). The upper limit of the ratio ($\mathcal{H}/\mathcal{L} \approx 9$) is found in the early stable period around 2100 h, and is due to the rapid decay of the near-surface stresses after the evening transition in combination with the slow decay of stresses above the rotor-disk region (see Fig. 2.6d). Interestingly, for both the steady-state SBL (between 0400 h and 0900 h) and the late CBL (between 1500 h and 1800 h), $\mathcal{H}_{WT24}/\mathcal{L}_{WT24} = 3$.

Perturbation of the near-surface stresses due to the wind farm is found to be significant with a reduction of 60% throughout the diurnal cycle. Near-surface mixing is the only mechanism available for propagating cooling from the surface upwards ($\mathcal{L}_{WT24}/\mathcal{L}_{noWT} \approx 0.4$). As we shall see in the following section, the perturbation induced by wind farms has a significant impact on (a) structure of the SBL, and (b) formation and growth of the CBL (Sect. 2.4.2).

2.4 Analysis

2.4.1 Mean Kinetic Energy Budget

The MKE budget terms (MKE is defined in Sect. 2.2.1) were computed for the period beginning at 2300 h on Day 1 and continued until 1900 h on the following day. The budget equation for MKE is as follows,

$$\begin{aligned}
 \frac{\partial(MKE)}{\partial t} = & \underbrace{f_c \langle \bar{v} \rangle u_G}_{\text{V}} + \underbrace{\langle \overline{f_x^{wt}} \rangle \langle \bar{u} \rangle + \langle \overline{f_y^{wt}} \rangle \langle \bar{v} \rangle + \langle \overline{f_z^{wt}} \rangle \langle \bar{w} \rangle}_{\text{I}} \\
 & - \underbrace{\left(\langle \bar{u} \rangle \frac{\partial \langle \bar{u}' w' \rangle}{\partial z} + \langle \bar{v} \rangle \frac{\partial \langle \bar{v}' w' \rangle}{\partial z} \right)}_{\text{II}} \\
 & - \underbrace{\left(\langle \bar{u} \rangle \frac{\partial \langle \bar{u}'' \bar{w}'' \rangle}{\partial z} + \langle \bar{v} \rangle \frac{\partial \langle \bar{v}'' \bar{w}'' \rangle}{\partial z} \right)}_{\text{III}}, \tag{2.3}
 \end{aligned}$$

where terms represent the loss of the MKE due to wind-turbine forces (term I), the contribution of MKE due to Reynolds fluxes (term II), dispersive stresses (term III), the geostrophic forcing of the simulation (term IV) and finally, the acceleration term or the residual of the balance of forces (term V). The buoyancy force is neglected since $\langle \overline{w} \rangle = 0$. As this analysis was performed to understand the balance of forces within the wake region of the wind farm in the bulk sense, Eq. 2.4.1 was integrated between $z_h - D/2$ and $z_h + D/2$. Note that in comparison to the standard MKE budget equation [see, for example, Finnigan, 2000] terms due to advection, SGS dissipation and pressure perturbation were found to be negligible upon vertical integration and are not shown. Furthermore the turbulent quantities are not reformulated into transport and dissipation terms since the transport term in general is the dominant term [Calaf et al., 2010]. The budget terms are normalized and shown in Fig. 2.8, where the two vertical lines represent the transition points at 1010 h and 1810 h. While Calaf et al. [2010] showed that the vertical momentum flux plays the dominant role in replenishment of MKE in the rotor-disk region, it can be seen that this is valid only for unstable conditions where term II is indeed found to be dominant (it is 70% of term I). On the other hand, during the stable regime, energy from the geostrophic forcing is as important as the Reynolds flux term in balancing the MKE lost due to the presence of the wind-farm with each contributing 57% and 35% respectively in the late stable period beginning 0400 h until 0900 h. The relatively higher importance of the geostrophic forcing within the SBL as opposed to the CBL implies that perturbations to mesoscale flows affect wind-farm operations more strongly during nighttime stable conditions than during daytime convective conditions. The dispersive stress that is associated with the presence of wakes in the rotor-disk region is surprisingly negligible in the total rotor-disk region throughout the diurnal cycle with the exception of the unstable period. The MKE lost due to the wind farm remains nearly constant during the stable period and increases during the unstable period to almost double the value. However the increase occurs very rapidly at 1200 h, almost 2 h after the transition point at 1010 h. We explore the reason for this delay below.

2.4.2 Formation and Growth of the CBL

Since we have imposed a similar temperature signal at the surface for both noWT and WT24 simulations, we can investigate the impact of the perturbed stress profile due to the wind farm on the formation and growth of the CBL. Here, we restate significant moments during the diurnal cycle: we denote ‘sunrise’ as the time when the imposed temperature at the surface (Fig. 2.1d) begins to rise after reaching a minimum. This occurs at 0920 h and is similar for both noWT and WT24 simulations. The transition to the CBL is identified as the time at which the sensible heat flux at the surface changes from negative to positive. We note that there is a 20-min difference between the noWT and the WT24 simulations, with the transition occurring at 1010 h and 1030 h respectively.

In Fig. 2.9, subplots (a)-(c) show the profiles of temperature (θ), momentum flux (τ) and sensible heat flux (H_s) respectively for the noWT simulation. Subplots (d)-(e) are the respective counterparts for the WT24 simulation. We begin our analysis 30 min before sunrise (at 0850 h)

Chapter 2. Perturbations to the spatial and temporal characteristics of the diurnally-varying atmospheric boundary layer due to an extensive wind farm

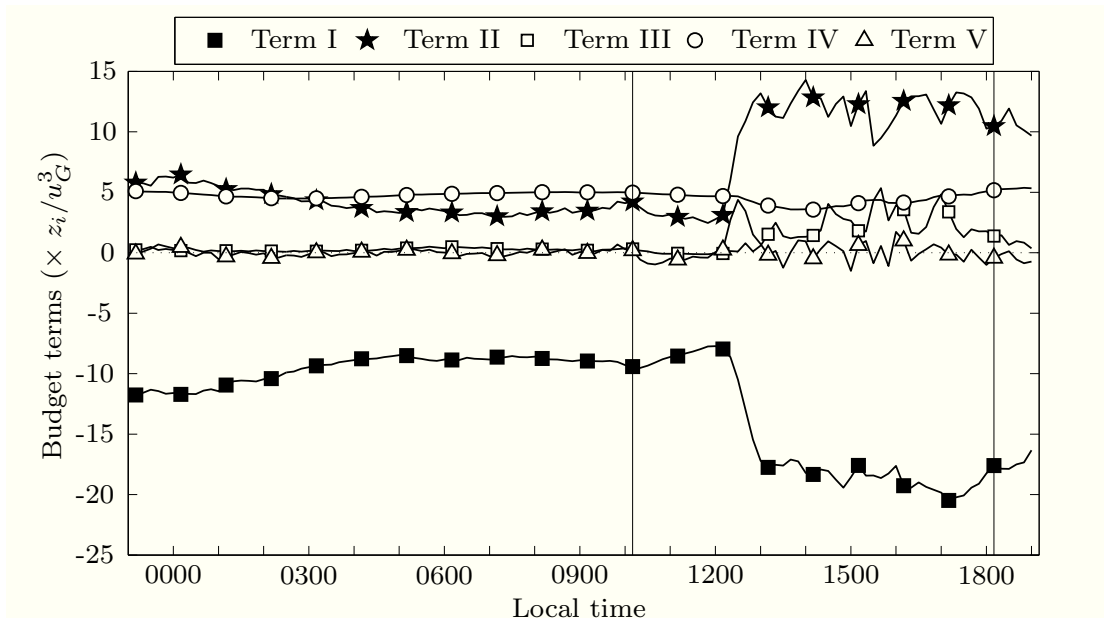


Figure 2.8 – MKE budget during a diurnal cycle: term I: loss of the MKE due to wind-turbine forces, term II: contribution of MKE due to Reynolds fluxes, term III: dispersive stresses and term IV: geostrophic forcing of the simulation. Term V shows the acceleration term or the residual. All values are scaled using a reference boundary-layer height of 1000 m and the geostrophic velocity. The two vertical lines mark the transition points at 1010 h on Day 2 and 1810 h Day 2.

and focus only on the early growth of the CBL.

The 0850 h profiles represent the quasi-steady, late stable period. In the standard flat-terrain scenario, the SBL can be considered to be a purely surface-driven phenomenon with the surface acting as a thermal sink. Mechanically-generated turbulence and associated mixing (momentum flux) due to shear at the rough wall are the only available mechanisms for extending the cooling effect (referred to as the ‘cooling wave’ in the literature) deeper into the atmosphere. This concept is well-described by the profiles at 0850 h with the cooling extending up to a height of 300 m. At this height, the shear stress and the sensible heat flux decay to negligible values as compared to their reference surface values. The shape of the temperature profile, with the temperature gradient increasing with increasing height, provides further evidence of maximum mixing at the surface that decreases with height.

In the presence of the wind farm, turbulence and momentum flux are maximum at the top of the rotor disk rather than at the surface. In fact, as already described in Fig. 2.7, the integrated momentum flux in the first 50 m above the surface in the WT24 simulation is only 40% of that in the noWT simulation (recall that $\mathcal{L}_{WT24}/\mathcal{L}_{noWT} \approx 0.4$). As a consequence, the cooling effect originating at the surface is much reduced in the first 50 m of the WT24 simulation as compared to the noWT simulation. The profiles for the WT24 simulation at 0850 h reaffirm the ‘lack of cooling’, with the mean temperature of the first 50 m being 0.8 K higher than in the noWT simulation and a difference of 2.6 K at 50-m height (i.e. the bottom of the rotor-disk

region). This ultimately results in a stronger stratification beneath the rotor-disk region ($\partial\theta/\partial z|_{WT24} = 0.1 \text{ Km}^{-1}$, $\partial\theta/\partial z|_{noWT} = 0.03 \text{ Km}^{-1}$). Many previous studies [Roy and Traiteur, 2010, Lu and Porté-Agel, 2011, Fitch et al., 2013b] have described a similar ‘warming’ near the surface. A recent study by Armstrong et al. [2016] found ‘warming’ at scales comparable to the turbine rotor-diameter. However, for the sake of clarity, it would perhaps be more suitable to state this phenomenon as ‘lack of cooling’.

In addition, the flow above the wind farm is characterized by a negative heat flux region that extends up to a height of 500 m in the atmosphere, 200 m higher than for the noWT simulation. This is a direct consequence of the enhanced mixing available above the wind farm with the integrated momentum flux for the WT24 simulation being much larger than the noWT simulation ($\mathcal{H}_{WT24}/\mathcal{H}_{noWT} = 20$). To summarise the late SBL profile, the cooling of the ABL during stable conditions occurs differently with and without wind farms. For the WT24 simulation, there is reduced cooling between the surface and the rotor-disk region, and above the rotor-disk region, the cooling effect extends deeper into the atmosphere. Instead, in the noWT simulation, the cooling is maximum near the surface and progressively decreases with height. These differences are a direct reflection of the perturbed stress profile of the WT24 simulation.

Upon sunrise, the surface temperature rises equally in both the noWT and the WT24 simulation. The 1020 h profile for the noWT simulation shows a small positive sensible heat flux at the surface (transition occurs at 1010 h). At 1050 h, the initial stratification is essentially overcome with the surface temperature significantly warmer than the overlying air and the shear stress begins to increase at the surface. In a matter of 30 min, between 1050 h and 1120 h, there is an approximately 30% increase in shear at the surface and in the following period remains constant at this value while the CBL grows. The 1320 h profile of the momentum flux shows an interesting feature with two definite linear trends, one extending from the surface to 230 m and the other from thereon up to 400 m. This corresponds identically to regions of positive sensible heat flux and the negative sensible heat flux also termed as the entrainment region.

On the other hand, the much stronger stratification near the surface due to the presence of the wind farm has a significant impact of the formation and growth of the CBL. At the outset, the transition event is delayed by 20 min as compared to the noWT simulation. Furthermore, upon transition, much of the heating is limited to below the hub-height and occurs exclusively through surface driven thermals as opposed to the noWT simulation where the heating occurs through both the surface driven thermals and entrainment of warmer air from the residual region above. The overlying stratification is finally overcome between 1150 h and 1220 h (almost 2.5 h later in comparison with the noWT simulation). During the same 30 min, there is an incredible 200% increase in shear stress at the top of the rotor disk. Hereafter, the CBL grows rapidly with a deeper entrainment region as evidenced by the profiles of sensible heat flux. The deeper entrainment region is a signature of the erstwhile SBL which due to enhanced mixing induced by the wind farm, extends deeper into the atmosphere.

A comparison between the entrainment region associated with the growing CBL for the

Chapter 2. Perturbations to the spatial and temporal characteristics of the diurnally-varying atmospheric boundary layer due to an extensive wind farm

noWT and WT24 simulations is made in Figs. 2.10a,b respectively. The entrainment region is identified from the profiles of H_s in Figs. 2.9c,f as the region with negative H_s (while the surface H_s is positive) and is shaded grey. The region of the ABL between the surface and the lower edge is understood to be primarily heated by the warming surface. The upper edge of the entrainment region is difficult to identify in the late convective period, when the upper edge of the entrainment region reaches the capping inversion. The presence of the wind farms further complicates its identification as the enhanced mixing causes the sensible heat flux to decay slower vertically and never reach zero; in certain cases up to the height of the capping inversion even in the late stable period. We used the evolution of the mean temperature gradient ($\partial\langle\bar{\theta}\rangle/\partial z$) to identify the top of the entrainment region.

The triangle symbols mark the height where the maximum value of absolute H_s is found in the entrainment region. This is also denoted as the height of the CBL used in Fig. 2.3. Notice that the CBL grows linearly for the noWT simulation with the width of the entrainment region being nearly constant (≈ 120 m) throughout the growth period. On the other hand, the growth of the CBL in the WT24 simulation is perturbed and can be considered as following a two stage growth. The first stage consists of the period between the transition and 1200 h. It is characterised by two observations. Firstly, the growth of the positive H_s region is markedly slower with respect to the noWT simulation - this is a consequence of the stronger stratification in the WT24 simulation at the end of the stable period. Secondly, the height of the CBL remains nearly fixed at hub-height and begins to rise only at 1200 h. Onset of the second stage of CBL growth appears to be when the positive H_s region reaches the rotor-disk region upon which, the CBL growth is accelerated to grow more rapidly than the noWT simulation. It is surmised that this increase in the rate of growth is due to additional mixing in the wake region of the wind farm. Also note that the width of the entrainment region is higher in the WT24 simulation through out the growth period (width after 1200 h is ≈ 250 m, 130 m larger than for the noWT simulation).

We summarise the effect of wind farms on the formation and growth of the CBL as follows: as a consequence of lower mixing below the rotor-disk region causing significantly stronger stratification in the late stable period, the time-lag between sunrise and transition is slightly increased (20 min). Upon transition, the growth of the CBL follows a two-stage process: Initially, there is no growth as the stratification is overcome by slowly growing positive H_s region, following which the CBL grows at a rapid rate aided by additional mixing induced by the wind farms. The trigger for the onset of the second stage is the thermal plumes from the surface entering the wake region of the wind farm.

2.4.3 Phenomenology of the Low-level Jet

In this section we describe the formation of the low-level jet (LLJ) and the role of wind farms in modulating its formation. The LLJ is a loosely defined term for any maximum found in the wind profile that is shallow in the vertical but is found to extend over a wide horizontal area. LLJs are found in diverse flow scenarios such as steep and shallow sloping terrain [Shapiro and Fedorovich, 2009, Oldroyd et al., 2014], the Great Plains in the United States [Whiteman et al.,

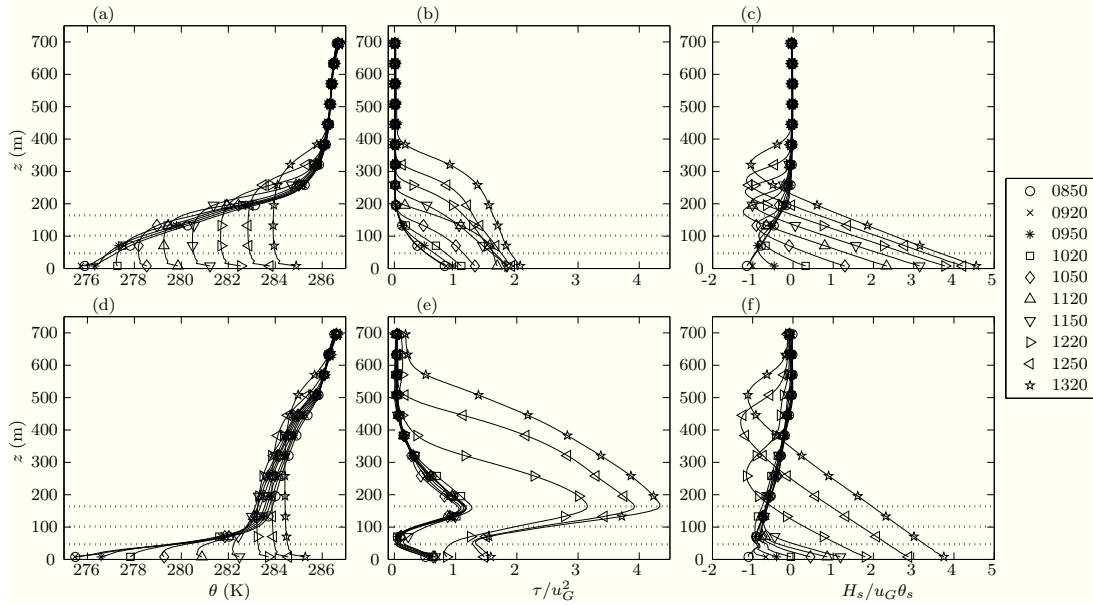


Figure 2.9 – Formation and growth of the CBL. Subplots (a)-(c) show the profiles of temperature, net momentum flux ($\times 10^3$) and sensible heat flux ($\times 10^3$) respectively for the noWT simulation. Subplots (d)-(e) are the respective counterparts for the WT24 simulation. Each subplot contains profiles 30 min apart beginning at 0850 h on Day 2 and continuing until 1320 h on Day 2. Geostrophic velocity and surface temperature are used as normalization scales. The three horizontal dotted lines on each subplot mark the top, bottom and hub-height of the wind turbines.

1997, Banta et al., 2002], Antarctica [Chiba and Kobayashi, 1986]. The LLJ is an important meteorological phenomenon as it influences nocturnal scalar transport, ventilation of urban canopies and wind farm operations among other aspects [Stensrud, 1996].

In this study, we limit our focus to the Blackadar-type nocturnal LLJ [Blackadar, 1957] that forms over flat terrain at nighttime under clear-sky conditions. This type of LLJ is formed when the flow between the top of the SBL [$\mathcal{O}(100\text{m})$] and the overlying capping inversion [$\mathcal{O}(1000\text{m})$] experiences a complete decay in the momentum fluxes (see, for example, Fig. 2.9b, 0850 h profile). In this region, the flow is essentially non-turbulent and undergoes inertial oscillations due to a balance between the geostrophic and Coriolis forces [Wyngaard, 2010]. Within the SBL, the divergence of stress balances the geostrophic and Coriolis forcing and hence there is no time evolution in the flow. The peak of the LLJ is found at the interface between the ‘stationary’ SBL layer and the overlying ‘oscillating’ inviscid layer. In the noWT simulation, the jet peak occurs at 156 m and for the WT24 simulation, it occurs at 400 m, approximately 250 m higher than the noWT simulation. This is illustrated in Fig. 2.11 in detail. Figure 2.11a,c show the $\langle \bar{u} \rangle$ (closed symbols) and $\langle \bar{v} \rangle$ (open symbols) for the noWT and WT24 simulations respectively. Figure 2.11b,d show the bulk quantities τ_x (closed symbols) and τ_y (open symbols) for the corresponding cases (see Section 2.2.2 for formulation of bulk statistics). The profiles presented span the latter half of the stable period between 0300 h and 0800 h. As in previous figures, the three horizontal regions represent the rotor-disk region.

Chapter 2. Perturbations to the spatial and temporal characteristics of the diurnally-varying atmospheric boundary layer due to an extensive wind farm

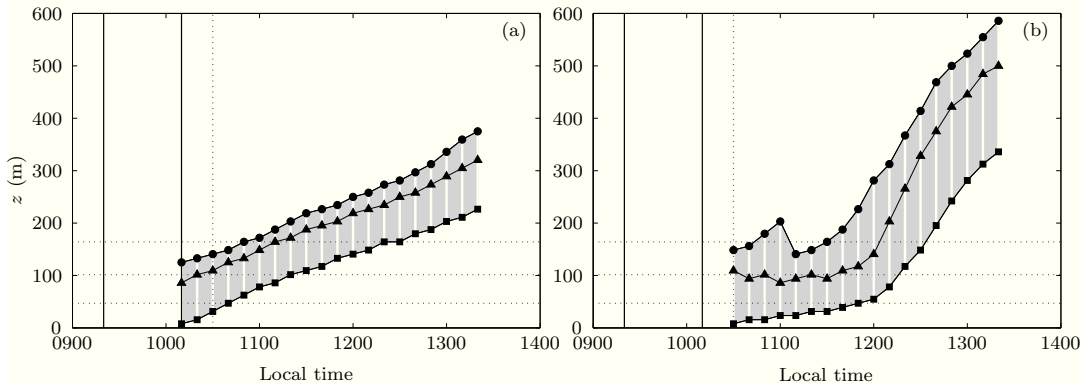


Figure 2.10 – Entrainment region for (a) the noWT simulation and (b) WT24 simulation. The lower edge of the shaded region (marked by square symbols) represents the height up to which the ABL is subjected to a positive H_s . The triangle symbols mark the height where the maximum value of absolute H_s is found in the entrainment region. The upper edge of the entrainment region, marked by circular symbols is the height where the heat flux becomes zero once again. Each subplot contains 3 vertical lines, which beginning from the left represent the sunrise at 0920 h (solid), morning transition for noWT simulation at 1010 h (solid) and for the WT24 simulation at 1030 h (dotted) respectively. The three horizontal dotted lines represent the rotor-disk region of the wind farm.

The effect of wind farms on LLJs has been documented recently in Fitch et al. [2013b] and Abkar et al. [2016]. In both of these works, a finite-size wind farm was simulated as opposed to the infinite farm in this study. Fitch et al. [2013b] found that the LLJ developed upstream of the wind farm is depleted by the first couple of rows. In fact, they showed that due to the effect of the LLJ, the upstream wind turbines generate much more power at night as compared to the wind turbines deep within the wind farm. A similar scenario was also observed by Abkar et al. [2016]. Additionally, their work showed that the LLJ was shifted upwards and is re-generated above the wind farm; much like in the present study. To reconcile our infinite wind-farm results with these works, a solitary wind-turbine was placed in the diurnal ABL simulation. Due to the effect of the periodic boundary conditions, this in effect simulates an infinite wind farm with extremely large spacing. This simulation is denoted as WT1 with $s_x, s_y = 1000\pi \text{ m} = 31.5D$ in comparison to $s_x = 7D, s_y = 5D$ for the WT24 simulation and $s_x, s_y = 1000\text{m} = 10D$ for the Fitch et al. [2013b] case.

Figure 2.12 shows an illustration of the WT1 simulation during the LLJ event. From the 10-min averaged velocity field, a vertical slice passing through the centre of the wind turbine is extracted. It can be clearly seen that the LLJ affects the wind turbine and persists continuously downstream of the wind turbine as well. In fact, the mean field is perturbed quasi-linearly as the wake is simply super-imposed on the mean field. An implication of this fact is shown in Fig. 2.13 where the mean 10-min averaged power of a wind turbine in the WT24 simulation (blue line) is compared with the single wind turbine in the WT1 simulation (black line) during the course of the diurnal cycle. The power (P) is computed as $P = \sum r F_r \omega$, where F_r is the tangential force at a point at distance r from the centre of the rotor disk, ω is the angular

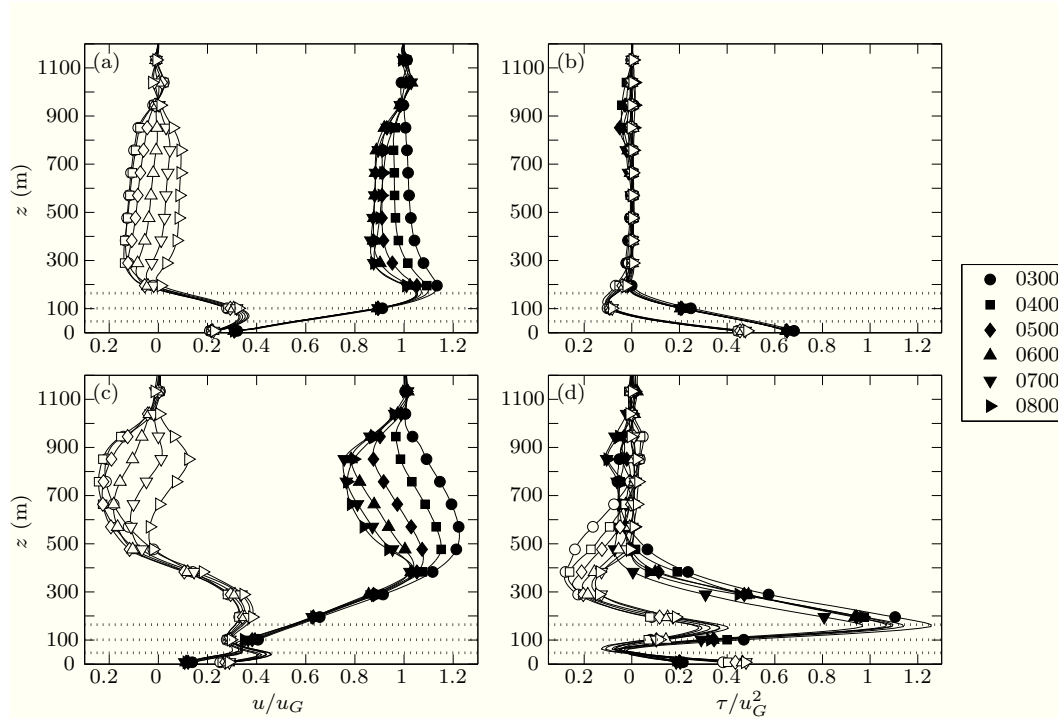


Figure 2.11 – Formation of the LLJ: Subplots (a) and (c) show the $\langle \bar{u} \rangle$ (closed symbols) and $\langle \bar{v} \rangle$ (open symbols) for the noWT and WT24 simulations respectively. Subplots (b) and (d) show the bulk quantities τ_x (closed symbols) and τ_y (open symbols) for the corresponding cases (see sect. 2.2.2 for formulation of bulk statistics). The profiles presented span the latter half of the stable period between 0300 h and 0800 h on Day 2. The three horizontal lines represent the rotor-disk region. All values are normalized using geostrophic velocity. The stress values are scaled by a factor of 10^{-3} .

velocity of the wind-turbine and the summation is for integrating over the entire rotor disk [see Sharma et al., 2015, for a detailed description of the wind turbine parametrisation]. Note that in the WT1 simulation, due to extremely low loading of the surface, the wind speeds are higher and as a consequence, the power output. However, the more interesting observation is that in the WT1 simulation, the stable period has higher ($\approx 40\%$ more) power output in comparison to the unstable period whereas in the WT24 simulation, this trend is opposite with the power output being twice as large as that during the stable period. This is a direct result of the fact that at nighttime, the WT1 simulation is able to extract power from the LLJ while in the WT24 simulation, the LLJ forms above the rotor-disk region. The comparison between WT1 and WT24 in addition to the results presented in Fitch et al. [2013b] and Abkar and Porté-Agel [2015] hints towards a high dependence of wind-farm power output on loading during stably stratified conditions.

2.4.4 Effective Roughness Lengths of a wind farm during a diurnally varying ABL

Over the past few years different works have proposed formulations for a wind-farm induced surface roughness under neutral stratification [Frandsen, 1992, Calaf et al., 2010, Stevens

Chapter 2. Perturbations to the spatial and temporal characteristics of the diurnally-varying atmospheric boundary layer due to an extensive wind farm

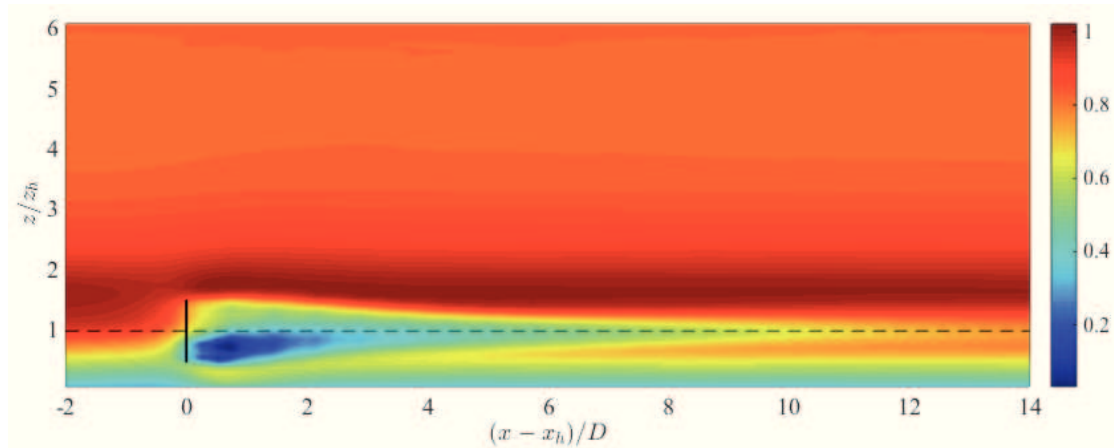


Figure 2.12 – Illustration of the LLJ impacting the wind turbine in the WT1 simulation. A vertical slice passing through the rotor disk of the 10-min averaged normalised velocity magnitude field. The horizontal and vertical axes are scaled using the rotor diameter (D) and the hub-height (z_h), respectively.

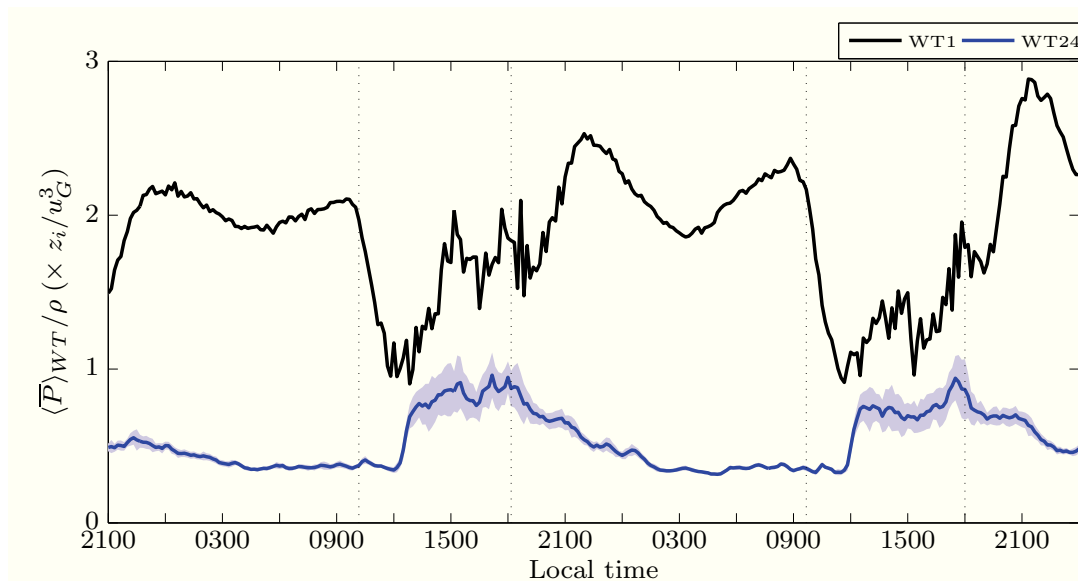


Figure 2.13 – Temporal evolution of the normalized available power for extraction at the wind-turbine rotor disk. The single black line represents the WT1 simulation and the blue line represents the mean for the WT24 simulation. The shaded blue region illustrates the standard deviation for the WT24 simulation. The power values are scaled by a factor of 10^3 . The vertical lines represent the transition points. The four vertical lines mark the transition points at 1010 h and 1810 h on Day 2 and 0940 h and 1800 h on Day 3.

et al., 2014]. Some of these formulations have been used within different climate studies [Keith et al., 2004, Kirk-Davidoff and Keith, 2008, Barrie and Kirk-Davidoff, 2010, Wang and Prinn, 2010] to study the potential impact of large scale wind energy deployment on global atmospheric circulation. More recently, improved parametrizations accounting for the effect of atmospheric stratification have also been developed [Peña and Rathmann, 2014, Sescu and Meneveau, 2015]. In this section we further explore the induced change on the wind-farm induced surface-roughness due to the time-varying atmospheric stratification typically found in a diurnal cycle. Our aim is to highlight the possible pitfall of using the wind-farm induced surface-roughness values computed assuming neutral stratification, in GCMs.

For the standard flat-terrain boundary layer, the mean velocity profile for stratified conditions can be expressed as

$$\frac{\langle \bar{u} \rangle(z)}{u_{\star}} = \frac{1}{\kappa} \left[\ln \left(\frac{z}{z_0} \right) + \beta \right] \quad (2.4)$$

where β is the stability correction function (with $\beta = 0$, signifying neutral conditions), and z_0 is the surface roughness length defined by the aerodynamic nature of the surface. Upon manipulation of the above equation, it is possible to obtain an expression for an equivalent effective roughness length that includes the effect of atmospheric stratification, $z_{0,eff}$, such as

$$z_{0,eff} = z_0 e^{-\beta} = z \exp \left[-\langle \bar{u} \rangle \kappa / u_{\star} \right]. \quad (2.5)$$

Note that for the case of $\beta = 0$, the equation recovers the expected value for the neutral case, $z_{0,eff} = z_0$. This approach of including the effect of stratification in the surface roughness formulation can be further expanded to the case where a large wind farm is present. Therefore the counterpart of Eq. 2.4 for flows over wind farms can be written as follows,

$$\begin{aligned} \frac{\langle \bar{u} \rangle(z)}{u_{\star, wf}} &= \frac{1}{\kappa} \left[\ln \left(\frac{z}{z_{wf}} \right) + \beta^{wf} \right] \\ &= \frac{1}{\kappa} \left[\ln \left(\frac{z}{z_{wf} e^{-\beta_{wf}}} \right) \right] \\ &= \frac{1}{\kappa} \left[\ln \left(\frac{z}{z_{wf, eff}} \right) \right], \end{aligned} \quad (2.6)$$

for $z \geq z_h + D/2$, where β^{wf} is an equivalent stability correction function for the wind farm and $z_{wf, eff}$ represents the effective wind-farm roughness for stratified conditions. Again, upon manipulation it is possible to obtain an expression for $z_{wf, eff}$ as follows

$$z_{wf, eff} = z \exp \left[\langle \bar{u} \rangle \kappa / u_{\star, wf} \right], \quad (2.7)$$

for $z \geq z_h + D/2$. Equations 2.5 and 2.7 are used to compute the corresponding values of effective roughness using data from the LES. The effective roughness calculation requires a choice of height at which reference velocity values are extracted from. In the present case, the

Chapter 2. Perturbations to the spatial and temporal characteristics of the diurnally-varying atmospheric boundary layer due to an extensive wind farm

heights of 3.9 m (the first grid point above the surface) and 200 m ($2z_h$) are chosen for the noWT and the WT24 simulations respectively. Note that this is an unusual way to formulate the modified surface roughness because it directly includes the effect of atmospheric stability, and hence becomes height dependent. However, because the stability correction functions used become constant with height from $|z/L| > 2$ to 3 ($L \approx 40$ m height in the presented diurnal cycle), the actual value of the wind-farm induced surface roughness remains effectively height-independent. Additional calculations using data from different heights were performed and results (not shown here) confirmed this fact. The vertical momentum flux values were taken at the surface and the top of the rotor-disk region for noWT and WT24 simulations respectively. The computed effective roughness values are normalised by the respective neutral roughness values of z_0 (for the noWT simulation, imposed as 0.03 m) and z_{wf} (computed for the WT24 simulation to be equal to 2.4 m) and shown in Fig. 2.14. The corresponding wind-farm surface roughness for neutral conditions (z_{wf}) has been obtained using Calaf et al. [2010]’s expression based on the geometry of the wind farm (streamwise and spanwise spacing), therein referred as $z_{0,hi}$. Note that this normalization helps in identifying the deviations in the new surface roughness (Eqs. 2.5 and 2.7) from the neutrally stratified conditions, with values > 1 , signifying ‘high roughness’ unstable conditions and < 1 signifying ‘low roughness’ stable conditions.

As expected, the normalised effective roughness is equal to 1 for the noWT simulation at the transition points (marked by four vertical dotted lines). The results for the WT24 simulation are far more surprising. The effect of the delayed formation and growth of the CBL is seen as the effective roughness increases to values > 1 at 1200 h, two hours after the transition. The transition from unstable to stable conditions on the other hand occurs approximately at the same time. However, during the stable period, the effective roughness drops by several orders of magnitude. The average effective roughness ($\overline{z_{0,eff}}$) during a 24-h period beginning at 0000 h on Day 2 for the noWT simulation was computed as 0.024 m (80% of z_0) whereas for the WT24 simulation, $\overline{z_{wf,eff}}$, it was found to be equal to 0.96 m (40% of z_{wf}). The extended stable period during the simulation as imposed by the adopted temperature signal at the surface is represented well by the fact that in both the noWT and WT24 simulations, the effective roughness values are found to be smaller than the reference value for neutral stratification. However, the decrease in the WT24 simulation is markedly larger. This result is pertinent for researchers using enhanced surface roughness representation for terrestrial wind farms in GCM simulations and illustrates the need for using surface roughness parametrizations that not only include the effect of wind farms but also the time-varying atmospheric stratification.

2.5 Summary and Conclusions

We studied the impact of an extremely large wind farm on the spatio-temporal structure of a diurnally-varying ABL. Towards this end, computational experiments using LES were performed for cases with and without wind turbines (denoted as WT24 and noWT respectively) during a diurnal cycle forced with data from the CASES-99 field campaign. The noWT simulation was used for validating the computational set-up through comparison with the existing literature. In addition, it served as the baseline case to delineate the perturbations

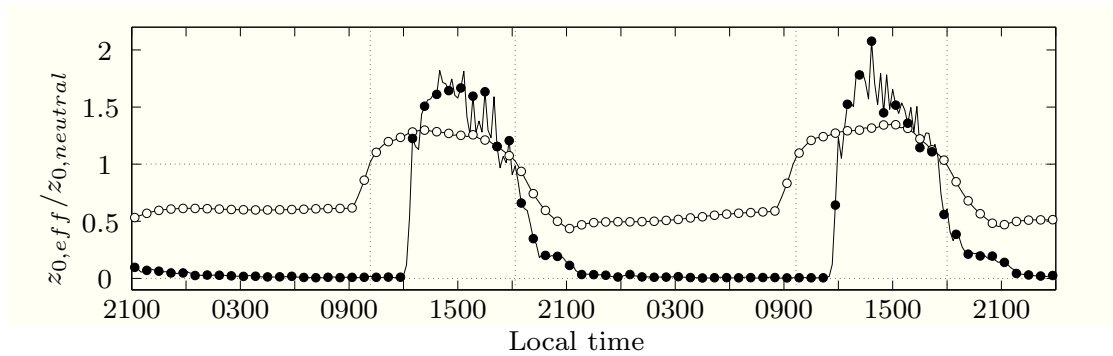


Figure 2.14 – Temporal evolution of the effective roughness for the noWT simulation ($z_{0,eff}$, open markers) and the WT24 simulation ($z_{wf,eff}$), closed markers. Values are normalized by the the corresponding roughness lengths for neutral conditions (z_0 and z_{wf}). The four vertical lines mark the transition points at 1010 h and 1810 h on Day 2 and 0940 h and 1800 h on Day 3.

induced by wind farms.

The WT24 simulation reaffirmed previous results, namely, the formation of the LLJ above the wind farm, depletion of turbulence and mixing beneath the rotor-disk region and deeper and stronger entrainment region in the quasi-steady CBL in the presence of wind farms in comparison to the noWT simulation.

New insights and their implications for the wind-energy community are summarized as follows. The MKE budget revealed the important role played by large-scale forcing (the geostrophic flow in our case) for wind-farm operations during stably stratified conditions as opposed to convective conditions where their effect was less significant. This implies that wind-farm operators need to be mindful of perturbations in the mesoscale flow during nighttime operations. Further, the daytime (unstable conditions) power output was found to be almost twice as large as that at nighttime (stable conditions).

Operating the wind farm during the stably stratified period produced two major perturbations, firstly, the LLJ was shifted upwards and the wind farm was unable to benefit from the high wind speeds found in the LLJ peak (this resulted in lower power output at night). Secondly, the operation of the wind farm caused a stronger stratification beneath the rotor-disk region and consequently, a significant timelag was found (2 h) for the formation and growth of the CBL. This phenomenon results in a delay in achieving the higher power output available during daytime. On the other hand, through an ancillary simulation with very low loading (WT1), we found that these perturbations can be mitigated, particularly with respect to the LLJ. Thus, it may be advantageous for wind-farm operators to optimize their operation and maintenance schedules by lowering the wind farm loading at nighttime. This would result in the wind farm being able to extract kinetic energy from the inertial oscillations and the LLJ that would now occur at a lower height. Secondly, a weaker stratification allows the CBL to grow more rapidly upon transition and significantly reduce the timelag between low-power nighttime conditions and high-power daytime conditions. Later, the loading of the wind farm could be increased as soon as the CBL top reaches the rotor-disk region. An additional perturbation induced by large

Chapter 2. Perturbations to the spatial and temporal characteristics of the diurnally-varying atmospheric boundary layer due to an extensive wind farm

wind farms is the increase in the vertical extent of the entrainment region (108% increase) capping the CBL along with stronger entrainment fluxes (78% increase).

The final contribution has been to show that the diurnally-averaged wind-farm effective roughness is significantly lower (40% in our case) than the effective roughness computed for neutral conditions. Specifically, $z_{wf,eff}$ ranges between a low value of 0.04 m (found during the stable stratification) and 3.6 m (during the unstable conditions). Therefore, care should be taken when using an effective surface roughness parametrization within GCMs to study the impact of large-scale wind-farm deployment on climate dynamics. The theoretical formulation for effective roughness during neutral conditions as representative of the diurnally-averaged value may be inappropriate.

In the next chapter, a finite-sized wind farm is considered with the aim of understanding flow development as a function of the downstream distance from the leading edge of the wind farm. The influence of the wind farm geometry on this evolution is also analysed. Furthermore, common wind farm models used in the industry are applied and compared to the LES generated flow database and shortcomings of these models is highlighted.

Acknowledgements

The work was made possible by support received through the Swiss National Science Foundation (project no. 200021134892/1 and 20020 125092), ETH Domain Centre for Competence in Environmental Sustainability, NSERC Discovery Grant (MBP), Swiss National Supercomputing Center (CSCS), Scientific IT and Application Support (SCITAS) group at EPFL, University of Utah and University of British Columbia.

Bibliography

- Mahdi Abkar and Fernando Porté-Agel. The effect of free-atmosphere stratification on boundary-layer flow and power output from very large wind farms. *Energies*, 6:2338–2361, 2013. doi: 10.3390/en6052338.
- Mahdi Abkar and Fernando Porté-Agel. Influence of atmospheric stability on wind-turbine wakes : A large-eddy simulation study. *Phys. Fluids*, 27(035104):1–19, 2015. doi: 10.1063/1.4913695.
- Mahdi Abkar and Fernando Porté-Agel. A new wind-farm parameterization for large-scale atmospheric models. *J. Renewable Sustainable Energy*, 7(1):013121, 2015.
- Mahdi Abkar, Ahmad Sharifi, and Fernando Porté-Agel. Wake flow in a wind farm during a diurnal cycle. *J. Turbul.*, pages 1–22, 2016.
- Matthew L Aitken, Branko Kosović, Jeffrey D Mirocha, and Julie K Lundquist. Large eddy simulation of wind turbine wake dynamics in the stable boundary layer using the weather research and forecasting model. *J. Renewable Sustainable Energy*, 6(3):033137, 2014.
- John D. Albertson and Marc B. Parlange. Natural integration of scalar fluxes from complex terrain. *Water Resour. Res.*, 23:239–252, 1999a.
- John D. Albertson and Marc B. Parlange. Surface length-scales and shear stress: Implications for land-atmosphere interaction over complex terrain. *Water Resour. Res.*, 35:2121–2131, 1999b.
- Alona Armstrong, Ralph R Burton, Susan E Lee, Stephen Mobbs, Nicholas Ostle, Victoria Smith, Susan Waldron, and Jeanette Whitaker. Ground-level climate at a peatland wind farm in scotland is affected by wind turbine operation. *Environmental Research Letters*, 11(4):044024, 2016. URL <http://stacks.iop.org/1748-9326/11/i=4/a=044024>.
- R. W. Baker and S. N. Walker. Wake measurements behind a large horizontal axis wind turbine generator. *Sol. Energy*, 33(1):5–12, 1984. doi: doi:10.1016/0038-092X(84)90110-5.

Bibliography

- RM Banta, RK Newsom, JK Lundquist, YL Pichugina, RL Coulter, and L Mahrt. Nocturnal low-level jet characteristics over Kansas during cases-99. *Boundary-Layer Meteorol.*, 105(2): 221–252, 2002.
- DB Barrie and DB Kirk-Davidoff. Weather response to a large wind turbine array. *Atmos. Chem. Phys.*, 10(2):769–775, 2010.
- R. J. Barthelme and L.E. Jensen. Evaluation of wind farm efficiency and wind turbine wakes at the Nysted offshore wind farm. *Wind Energy*, 13:573–586, 2010.
- R J Barthelme, O Rathmann, S T Frandsen, K S Hansen, E Politis, J Prospathopoulos, K Rados, D Cabezón, W Schlez, J Phillips, a Neubert, J G Schepers, and S P Van Der Pijl. Modelling and measurements of wakes in large wind farms. *J. Phys. Conf. Ser.*, 75:012049, 2007. doi: 10.1088/1742-6596/75/1/012049.
- R. J. Barthelme, K. Hansen, S. T. Frandsen, O. Rathmann, J. G. Schepers, W. Schlez, J. Phillips, K. Rados, a. Zervos, E. S. Politis, and P. K. Chaviaropoulos. Modelling and measuring flow and wind turbine wakes in large wind farms offshore. *Wind Energy*, 12(June):431–444, 2009. doi: 10.1002/we.348.
- R. J. Barthelme, S. C. Pryor, S. T. Frandsen, K. S. Hansen, J. G. Schepers, K. Rados, W. Schlez, a. Neubert, L. E. Jensen, and S. Neckelmann. Quantifying the impact of wind turbine wakes on power output at offshore wind farms. *J. Atmos. Ocean Technol.*, 27(8):1302–1317, 2010. doi: 10.1175/2010JTECHA1398.1.
- Sukanta Basu, Jean-François Vinuesa, and Andrew Swift. Dynamic les modeling of a diurnal cycle. *J. Appl. Meteorol. Clim.*, 47(4):1156–1174, 2008.
- Kiran Bhaganagar and Mithu Debnath. The effects of mean atmospheric forcings of the stable atmospheric boundary layer on wind turbine wake. *J. Renewable Sustainable Energy*, 7(1): 013124, 2015.
- Alfred K Blackadar. Boundary layer wind maxima and their significance for the growth of nocturnal inversions. *Bull. Amer. Meteorol. Soc.*, 38(5):283–290, 1957.
- E. Bou-Zeid, C. Meneveau, and Marc B. Parlange. A scale-dependent lagrangian dynamic model for large-eddy simulation of complex turbulent flows. *Phys. Fluids*, 17:1–18, 2005.
- W Brutsaert, JHC Gash, and Marc B. Parlange. Neutral humidity profiles in the boundary layer and regional evaporation from sparse pine forest. *Ann. Geophys.*, 7:623–630, 1989.
- Wilfried Brutsaert. Stability correction functions for the mean wind speed and temperature in the unstable surface layer. *Geophys. Res. Lett.*, 19(5):469–472, 1992. ISSN 1944-8007. doi: 10.1029/92GL00084. URL <http://dx.doi.org/10.1029/92GL00084>.
- Raúl Bayoán Cal, José Lebrón, Luciano Castillo, Hyung Suk Kang, and Charles Meneveau. Experimental study of the horizontally averaged flow structure in a model wind-turbine array boundary layer. *J. Renewable Sustainable Energy*, 2(1):013106, 2010.

- M. Calaf, J. Meyers, and C. Meneveau. Large eddy simulation study of fully developed wind-turbine array boundary layers. *Phys. Fluids*, 22(015110):1–16, 2010.
- M. Calaf, M. B. Parlange, and C. Meneveau. Large eddy simulation of scalar transport in fully developed wind-turbine array boundary layers. *Phys. Fluids*, 23(126603):1–16, 2011.
- Marc Calaf, Chad Higgins, and Marc B. Parlange. Large wind farms and the scalar flux over an heterogeneously rough land surface. *Boundary-Layer Meteorol.*, 153(3):471–495, 2014.
- Claudio Canuto, M. Yousuff Hussaini, Alfio Quarteroni, and Thomas A. Zang. *Fundamentals of Spectral Methods for PDEs*, pages 80–85. Springer Berlin Heidelberg, Berlin, Heidelberg, 1988. ISBN 978-3-642-84108-8.
- Osamu Chiba and Shun’ichi Kobayashi. A study of the structure of low-level katabatic winds at mizuho station, east antarctica. *Boundary-Layer Meteorol.*, 37(4):343–355, 1986.
- Matthew J. Churchfield, Sang Lee, John Michalakes, and Patrick J. Moriarty. A numerical study of the effects of atmospheric and wake turbulence on wind turbine dynamics. *J. Turbul.*, 13 (February 2015):N14, 2012. doi: 10.1080/14685248.2012.668191.
- Stephen H Derbyshire. Nieuwstadt’s stable boundary layer revisited. *Q. J. R. Meteorol. Soc.*, 116(491):127–158, 1990.
- Stefan Emeis and Sten Frandsen. Reduction of horizontal wind speed in a boundary layer with obstacles. *Boundary-Layer Meteorol.*, 64(1980):297–305, 1993. doi: 10.1007/BF00708968.
- John Finnigan. Turbulence in plant canopies. *Annu. Rev. Fluid Mech.*, 32(1):519–571, 2000.
- A. C. Fitch, J. B. Olson, J. K. Lundquist, J. Dudhia, A. K. Gupta, J. Michalakes, and I. Barstad. Local and mesoscale impacts of wind farms as parametrized in a mesoscale nwp model. *Mon. Weather Rev.*, 140:3017–38, 2013a.
- Anna C Fitch, Joseph B Olson, Julie K Lundquist, Jimy Dudhia, Alok K Gupta, John Michalakes, and Idar Barstad. Local and mesoscale impacts of wind farms as parameterized in a mesoscale nwp model. *Mon. Weather. Rev.*, 140(9):3017–3038, 2012.
- Anna C Fitch, Julie K Lundquist, and Joseph B Olson. Mesoscale influences of wind farms throughout a diurnal cycle. *Mon. Weather. Rev.*, 141(7):2173–2198, 2013b.
- S. Frandsen. On the wind speed reduction in the center of large clusters of wind turbines. *J. Wind Eng. Ind. Aerodyn.*, 39:251–265, 1992.
- Sten Frandsen, Rebecca Barthelmie, Sara Pryor, Ole Rathmann, Søren Larsen, Jørgen Højstrup, and Morten Thøgersen. Analytical modelling of wind speed deficit in large offshore wind farms. *Wind Energy*, 9:39–53, 2006. doi: 10.1002/we.189.
- M. Frigo and S.G. Johnson. The design and implementation of fftw3. *Proc of the IEEE*, 93(2): 216–231, 2005.

Bibliography

- M. G. Giometto, A. Christen, C. Meneveau, J. Fang, M. Krafczyk, and M. B. Parlange. Spatial characteristics of roughness sublayer mean flow and turbulence over a realistic urban surface. *Boundary-Layer Meteorol*, pages 1–28, 2016. ISSN 1573-1472. doi: 10.1007/s10546-016-0157-6. URL <http://dx.doi.org/10.1007/s10546-016-0157-6>.
- PE. Hancock and F. Pascheke. Wind tunnel simulations of wind turbine wake interactions in neutral and stratified wind flow. In *10th EMS annual meeting, 10th European Conference on Applications of Meteorology (ECAM)*, Sep 13-17 2010.
- C Higgins, Kellie Vache, Marc Calaf, Elnaz Hassanpour, and Marc B. Parlange. Wind turbines and water in irrigated areas. *Agric. Water Manage.*, 152:299–300, 2015. ISSN 03783774. doi: 10.1016/j.agwat.2014.11.016. URL <http://linkinghub.elsevier.com/retrieve/pii/S0378377414003771>.
- M. Hultmark, M. Calaf, and M. B. Parlange. A new wall shear stress model for atmospheric boundary layer. *J. Atmos. Sci.*, 70:3460–3470, 2013.
- Giacomo Valerio Iungo and Fernando Porté-Agel. Volumetric LiDAR scanning of wind turbine wakes under convective and neutral atmospheric stability regimes. *J. Atmos. Ocean. Technol.*, 31(10):2035–2048, 2014. doi: 10.1175/JTECH-D-13-00252.1.
- N.O. Jensen. *A note on wind generator interaction*, pages 1—16. Risø-M; No.2411, 1983. ISBN 87-550-0971-9.
- I Katic, J Højstrup, and Niels Otto Jensen. A simple model for cluster efficiency. In *European Wind Energy Association Conference and Exhibition*, pages 407–410, 1986.
- R-E. Keck, M. Maré, M. J. Churchfield, S. Lee, G. Larsen, and H. A. Madsen. On atmospheric stability in the dynamic wake meandering model. *Wind Energy*, 17:1689–1710, 2014.
- D.W. Keith, J.F. DeCarolis, D.C. Denkenberger, D.H. Lenschow, S.L. Malyshev, S. Pacala, and P.J. Rasch. The influence of large-scale wind power on global climate. *Proc. Natl. Acad. Sci. USA*, 101(46):16115–16120, 2004.
- D. B. Kirk-Davidoff and D. W. Keith. On the climate impact of surface roughness anomalies. *J. Atmos. Sci.*, 65:2215–2234, 2008.
- Vijayant Kumar, Gunilla Svensson, AAM Holtslag, Charles Meneveau, and Marc B. Parlange. Impact of surface flux formulations and geostrophic forcing on large-eddy simulations of diurnal atmospheric boundary layer flow. *J. Appl. Meteorol. Clim.*, 49(7):1496–1516, 2010.
- H. Lu and F. Porté-Agel. Large-eddy simulation of a very large wind farm in a stable atmospheric boundary layer. *Phys. Fluids*, 23(065101):1–19, 2011.
- Hao Lu and Fernando Porté-Agel. On the impact of wind farms on a convective atmospheric boundary layer. *Boundary-Layer Meteorol.*, 157(1):81–96, 2015.

- M. Magnusson and A. S. Smedman. Influence of atmospheric stability on wind-turbine wakes. *Wind Energy*, 18:139–152, 1994.
- L Mahrt and DH Lenschow. Growth dynamics of the convectively mixed layer. *J. Atmos. Sci.*, 33(1):41–51, 1976.
- Corey D Markfort, Wei Zhang, and Fernando Porté-Agel. Turbulent flow and scalar transport through and over aligned and staggered wind farms. *J. Turbul.*, 13(1):N33, 2012.
- Charles Meneveau. The top-down model of wind farm boundary layers and its applications. *J. Turbul.*, 13:N7, 2012. doi: 10.1080/14685248.2012.663092.
- J. Meyers and C. Meneveau. Large eddy simulations of large wind-turbine arrays in the atmospheric boundary layer. *48th AIAA Aerospace Sciences Meeting Including the New Horizons Forum and Aerospace Exposition*, 4-7 January 2010.
- C. H. Moeng. A large-eddy simulation model for the study of planetary boundary-layer turbulence. *J. Atmos. Sci.*, 41(2052), 1984.
- A.S. Monin and A.M. Obukhov. Basic laws of turbulent mixing in the ground layer of the atmosphere. *Tr. Geofiz. Int. Akad. Nauk SSSR*, 151:163–187, 1954.
- FTM Nieuwstadt and RA Brost. The decay of convective turbulence. *J. Atmos. Sci.*, 43(6): 532–546, 1986.
- Holly J Oldroyd, Gabriel Katul, Eric R Pardyjak, and Marc B. Parlange. Momentum balance of katabatic flow on steep slopes covered with short vegetation. *Geophys. Res. Lett.*, 41(13): 4761–4768, 2014.
- Alfredo Peña and Ole Rathmann. Atmospheric stability-dependent infinite wind-farm models and the wake-decay coefficient. *Wind Energy*, 17(8):1269–1285, 2014.
- Fernando Porté-Agel, Yu-Ting Wu, and Chang-Hung Chen. A numerical study of the effects of wind direction on turbine wakes and power losses in a large wind farm. *Energies*, 6(10): 5297–5313, 2013. ISSN 1996-1073. doi: 10.3390/en6105297.
- Gregory S Poulos, William Blumen, David C Fritts, Julie K Lundquist, Jielun Sun, Sean P Burns, Carmen Nappo, Robert Banta, Rob Newsom, Joan Cuxart, et al. Cases-99: A comprehensive investigation of the stable nocturnal boundary layer. *Bull. Am. Meteorol. Soc.*, 83(4):555–581, 2002.
- A. Povitsky and P. J. Morris. A higher-order compact method in space and time based on parallel implementation of the thomas algorithm. *J. Comput. Phys.*, 161(1):182–203, 2000.
- S. Baidya Roy. Simulating impacts of wind farms on local hydrometeorology. *J. Wind Eng. Ind. Aerodyn.*, 99:491–498, 2011.

Bibliography

- S. Baidya Roy and J. J. Traiteur. Impacts of wind farms on surface air temperatures. *Proc. Nat. Acad. Sci. USA.*, 107(42):17899–17904, 2010.
- PB S. Lissaman. Energy effectiveness of arbitrary arrays of wind turbines. *Journal of Energy*, 3(6):323–328, 1979.
- Adrian Sescu and Charles Meneveau. Large-eddy simulation and single-column modeling of thermally stratified wind turbine arrays for fully developed, stationary atmospheric conditions. *J. Atmos. Oceanic Technol.*, 32(6):1144–1162, 2015.
- Alan Shapiro and Evgeni Fedorovich. Nocturnal low-level jet over a shallow slope. *Acta Geophys.*, 57(4):950–980, 2009.
- V. Sharma, M. Calaf, M. Lehning, and M. B. Parlange. An LES model for a time-adaptive wind turbine. *Wind Energy*, 2015. doi: 10.1002/we.1877.
- Hyeyum Hailey Shin and Song-You Hong. Intercomparison of planetary boundary-layer parametrizations in the WRF model for a single day from CASES-99. *Boundary-Layer Meteorol.*, 139(2):261–281, 2011.
- Zbigniew Sorbjan. Decay of convective turbulence revisited. *Boundary-Layer Meteorol.*, 82(3):503–517, 1997.
- David J Stensrud. Importance of low-level jets to climate: A review. *J. Clim.*, 9(8):1698–1711, 1996.
- Richard J. A. M. Stevens, Dennice F. Gayme, and Charles Meneveau. Large eddy simulation studies of the effects of alignment and wind farm length. *J. Renewable Sustainable Energy*, 6(2):023105, 2014.
- Wen-Yih Sun and Yoshi Ogura. Modeling the evolution of the convective planetary boundary layer. *J. Atmos. Sci.*, 37(7):1558–1572, 1980.
- Gunilla Svensson, AAM Holtslag, V Kumar, T Mauritsen, GJ Steeneveld, WM Angevine, E Bazile, A Beljaars, EIF de Bruijn, A Cheng, et al. Evaluation of the diurnal cycle in the atmospheric boundary layer over land as represented by a variety of single-column models: the second GABLS experiment. *Boundary-Layer Meteorol.*, 140(2):177–206, 2011.
- Yu-Heng Tseng, Charles Meneveau, and Marc B Parlange. Modeling flow around bluff bodies and predicting urban dispersion using large eddy simulation. *Environ. Sci. Technol.*, 40(8):2653–2662, 2006.
- Chien Wang and Ronald G Prinn. Potential climatic impacts and reliability of very large-scale wind farms. *Atmos. Chem. and Phys.*, 10(4):2053–2061, 2010.
- C David Whiteman, Xindi Bian, and Shiyuan Zhong. Low-level jet climatology from enhanced rawinsonde observations at a site in the southern great plains. *J. Appl. Meteorol.*, 36(10):1363–1376, 1997.

- Y-T. Wu and F. Porté-Agel. Large-eddy simulation of wind-turbine wakes: Evaluation of turbine parametrizations. *Boundary-Layer Meteorol.*, 138:345–366, 2011. doi: 10.1007/s10546-010-9569-x.
- John C Wyngaard. *Turbulence in the Atmosphere*, pages 270—280. Cambridge University Press, 2010.
- John C Wyngaard and OR Coté. The evolution of a convective planetary boundary layer—a higher-order-closure model study. *Boundary-Layer Meteorol.*, 7(3):289–308, 1974.
- Geng Xia, Liming Zhou, Jeffrey M Freedman, Somnath Baidya Roy, Ronald A Harris, and Matthew Charles Cervarich. A case study of effects of atmospheric boundary layer turbulence, wind speed, and stability on wind farm induced temperature changes using observations from a field campaign. *Clim. Dyn.*, pages 1–18, 2015.
- W. Zhang, C. D. Markfort, and F. Porté-Agel. Experimental study of the impact of large-scale wind farms on land-atmosphere exchanges. *Environ. Res. Lett.*, 8(015002):1–8, 2013. doi: 10.1088/1748-9326/8/1/015002.
- Liming Zhou, Yuhong Tian, Somnath Baidya Roy, Chris Thorncroft, Lance F Bosart, and Yuanlong Hu. Impacts of wind farms on land surface temperature. *Nat. Clim. Change*, 2(7): 539–543, 2012.

3 Evolution of flow characteristics through finite-sized wind farms and influence of turbine arrangement

An edited version of this chapter was published in the journal *Renewable Energy* by Elsevier Ltd. Copyright ©2017 Elsevier Ltd. All rights reserved

V. Sharma, G. Cortina, F. Margairaz, M.B. Parlange, M. Calaf, Evolution of flow characteristics through finite-sized wind farms and influence of turbine arrangement, *Renewable Energy*, Volume 115, 2018, Pages 1196-1208, ISSN 0960-1481, <https://doi.org/10.1016/j.renene.2017.08.075>.

To view the published open abstract, go to <http://dx.doi.org> and enter the DOI

V.S developed the numerical model, implemented it in the LES code, took part in the research design, performed simulations, analyzed the data and contributed to the writing of the paper

3.1 Introduction

Interaction between a wind-farm and the atmospheric boundary layer is a complex fluid dynamics problem where wind-turbines, acting as distributed drag elements decelerate the mean flow and enhances turbulence due to formation of wakes downstream of the turbines. These wakes interact with other turbines resulting in fluctuating wind loads on turbine structures, impact the land-atmosphere exchange of heat, moisture and other scalars, mix with other wakes in the wind farm non-linearly resulting in large-scale effects.

Research regarding the interaction between wind farms and the atmospheric flow has been developed through myriad types of approaches over the past decades. These include mast-measurements taken in existing wind farms, wind tunnel experiments, through the development of analytical models as well as numerical simulations. Each of these studies have been conducted using a varying set of simplifying assumptions; being motivated and targeted

Chapter 3. Evolution of flow characteristics through finite-sized wind farms and influence of turbine arrangement

towards different goals and end-users. The earliest wake models [Jensen, 1983] were tested and calibrated using limited point-measurements from offshore wind farms and wind tunnel experiments. On the other hand, in the numerical studies, mesoscale and global circulation models have been used wherein wind farms have been parametrized either as elevated sinks of mean kinetic energy and sources of turbulence or as enhanced surface roughness. A common feature of all these different approaches has been the low fidelity of the the turbulent flow-field information, either due to the lack of sufficient experimental data, limitations of measurement techniques, or simplified turbulence representation in numerical models.

A comparatively more recent development has been the use of large-eddy simulations (LES) to study the interaction of turbulent flow with a distributed array of wind turbines. The LES-based methodology has been successfully applied to a wide range of atmospheric boundary layer (ABL) problems. Within the context of ABL-wind farm interaction, inter-comparisons between LES data and wind-tunnel experiments [Cal et al., 2010] and field-data [Wu and Porté-Agel, 2013] have been very successful in demonstrating the competence of the LES-based framework. The LES technique has also been used to understand the influence of wind farms on the ABL at micro-meteorology scales. For example, in Chapter 2, perturbations due to the wind farm on a diurnally-evolving atmospheric boundary layer (ABL) were discussed, where it was discovered that wind farms increase the height of the ABL, particularly the structure of the stable boundary layer and low-level jet, the dynamics of the ‘morning’ transition and entrainment across the capping inversion topping the ABL.

Most of the initial LES-based work was performed in the idealized setting of an ‘infinite’ wind farm beginning with Calaf et al. [2010] and including Chapters 1 and 2 of this thesis. Increasing computational power has now made it feasible for LES of finite-sized wind farms to be performed. In this chapter we describe the results of a suite of LES of finite-sized wind farms. The objective of this study is to provide an accurate measure of three diagnostic variables traditionally used in wind-energy models, namely, the wind-farm induced effective roughness length ($z_{0,eff}$), the wake-induced eddy viscosity (ν_w^*), and the wake-expansion coefficient (k_w). The wind-farm induced effective surface roughness ($z_{0,eff}$), is used in weather and climate-scale studies as an efficient parametrization to include the effect of wind farms on large-scale meteorology [Keith et al., 2004, Kirk-Davidoff and Keith, 2008, Barrie and Kirk-Davidoff, 2010, Wang and Prinn, 2010]. The wake viscosity (ν_w^*), is used in eddy-viscosity based RANS models for wind-farm design and analysis [Ainslie, 1988, Larsen et al., 2008]. These types of models are in general more accurate than pure wake models, but require parametrizations to account for mixing induced by wind-turbine wakes to better represent the wake-wake interactions, the wake recovery etc. The simplest of such parametrizations is to include additional ‘wake’ viscosity in the eddy-viscosity closure. Finally, the wake-expansion coefficient (k_w) is a necessary parameter that needs to be provided to run classic wake-models such as the Jensen and the Katic-Park models [Jensen, 1983, Katic et al., 1986] for single-wake interaction and further extended using a technique originally from S. Lissaman [1979] for multiple-wake and ground-wake interactions. While these models provide a crude representation of turbine-wake and wake-wake interactions, they continue to be used within

the wind-energy industry. An added motivation for using these three diagnostic variables is that a significant amount of information on the mean-flow and turbulence statistics is neatly distilled into these three variables.

Particular emphasis is placed on understanding how these three quantities evolve downstream of the leading edge of the wind farms and the influence of the wind-farm arrangement in modulating this evolution. For this purpose, five different wind farm configurations have been considered with different streamwise and spanwise spacings. As a first approximation, only the case of a neutrally stratified boundary layer is considered, which is representative of regions with high wind speeds as well as offshore regions. A study with a firm focus on diagnosing these quantities based on LES data has not been performed to the best of our knowledge.

The following section describes the theoretical framework adopted for this study and the methodology used to compute the aforementioned diagnostic variables using LES-data. Section 3.3 provides a detailed description of the suite of simulations. In Sect. 3.4, results are presented and discussed. Finally in Sect. 3.5 the results are summarized and conclusions are provided.

3.2 Theoretical framework

In this section, we provide a brief review of the theory related to the diagnostic variables studied in this work, i.e., the wind-farm induced effective surface roughness ($z_{0,eff}$), the wake viscosity (ν_w^*) and the wake-expansion coefficient (k_w).

3.2.1 Wake models and the wake-expansion coefficient

The wake-expansion coefficient is a necessary parameter for wake models to simulate the flow within a wind farm. We begin the discussion by describing the Jensen wake model, which prescribes the flow velocity in the wake of a turbine as,

$$u = u_0 \left(1 - \frac{1 - \sqrt{1 - C_T}}{(1 + k_w x/R)^2} \right) = u_0 \left(1 - \frac{2a}{(1 + k_w x/R)^2} \right). \quad (3.1)$$

This relationship is derived by applying conservation of mass to the flow around a turbine. In the above expression, u_0 is the inflow velocity into a wind-turbine, x is the distance downstream of the wind turbine, C_T is the thrust coefficient, k_w is the wake-expansion coefficient, a is the induction factor and R is the radius of the rotor disk. The Jensen model makes a distinction between ‘wake’ and ‘non-wake’ region downstream of a rotor-disk based on geometrical considerations. Limiting the explanation to the horizontal plane at hub-height, the wake region is described mathematically as,

$$|y - y_0 - R| < k_w (x - x_0), \quad (3.2)$$

Chapter 3. Evolution of flow characteristics through finite-sized wind farms and influence of turbine arrangement

where (x_0, y_0) are the streamwise and spanwise coordinates of the hub of the wind turbine. Thus, Eq. 3.1 can be used to compute the flow in the limited region satisfying Eq. 3.2. The velocity deficit $\delta u = u_0 - u$, due to a solitary wind turbine can be then expressed as,

$$\frac{\delta u}{u_0} = \frac{2a}{(1 + k_w(x - x_0)/R)^2}. \quad (3.3)$$

This model was extended by Katic et al. [1986] to describe a more general scenario of a wind farm, where multiple turbine wakes overlap and interact with each other as well as other turbines. The extension was based on the assumption that the presence of multiple wakes in the flow can be accounted for by considering a superimposition of their resultant kinetic energy deficit (as opposed to velocity deficits) at any location in the flow field. Thus, the expression for velocity deficit in this case is expressed as

$$\frac{\delta u(x, y)}{u_0} = \frac{2a}{\sqrt{\sum_{j \in T} [1 + k_w(x - x_j)/R]^4}}, \quad (3.4)$$

where, T is the set of all the turbines upstream of the point (x, y) , for which Eq. 3.2 is satisfied, including turbines from adjacent columns and the so-called “ghost-turbines” or imaginary turbines included to account for the interaction of wakes with the ground [S. Lissaman, 1979]. The imaginary turbines are located at $z = -z_h$ while having the same streamwise and spanwise coordinates as their real counterparts.

From Eq. 3.4, it is clear that given the values of k_w for each wind turbine, the entire wind farm flow can be computed in a very short amount of time. In the past, a fixed value for the wake-expansion coefficient was used for all turbines. This value was found by fitting experimental data to the above mentioned model. Jensen [1983] proposed $k_w = 0.1$ in his original formulation based on mast-measurements from offshore wind farms. Later on, Frandsen [1992] - based on theoretical considerations of linking wake growth to atmospheric turbulence derived an expression for $k_w = \kappa / \ln(z_h/z_0)$, which upon substitution of the corresponding parameters of the current study ($\kappa = 0.4$, $z_h = 100 \text{ m}$ and $z_0 = 0.1 \text{ m}$) provides $k_w = 0.058$. Recent LES based studies by Stevens et al. [2015] and Bokharaie et al. [2016] have hinted towards the possibility that the k_w parameter may in fact evolve with distance downstream from the leading edge of the wind farm when comparing simulation results with measurements from offshore wind farms. In this study, we use the LES-data to calculate the k_w values for each row of the wind farm. This is achieved through a row-by-row optimization procedure, which numerically determines the most appropriate k_w value for each row. At each row, the error between the LES data and that predicted by the Katic/Park model is minimized in the root-mean-square sense. More specifically, the optimization is performed by extracting the centre-line velocities behind each turbine from the LES data, and matching those from the wake model between $2D$ and $6D$ distances downstream of each rotor disk. It is assumed that all turbines in a row have the same k_w value. This is justified by the fact that the flow is neutrally buoyant, and is perfectly aligned in the streamwise direction, while the spanwise direction is periodic resulting in an infinite wind farm in that direction.

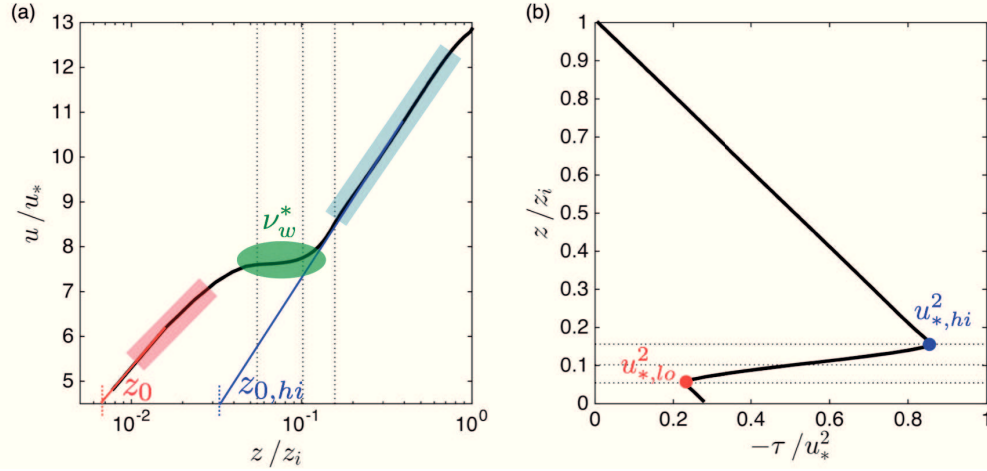


Figure 3.1 – Fully-developed flow in the presence of a wind-farm: characteristic (a) velocity and (b) shear stress profiles (in normalized units). Note that u_* and z_i are used as the normalizing velocity and length scales respectively. The dotted lines, vertical in (a) and horizontal in (b) represent the rotor-disk region. In subplot (a), the intercepts of the velocity profile below and above the rotor-disk with the x-axis are the surface roughness of the underlying surface and the effective surface roughness of the wind-farm respectively. In subplot (b), the momentum flux at the bottom and the top of the rotor-disk region is denoted as $u_{*,lo}^2$ and $u_{*,hi}^2$ respectively.

3.2.2 Wind-farm induced effective surface roughness and wake-viscosity

If the wind-farm extends over a sufficiently large spatial extent, it is expected that deep within the wind farm, far from the leading edge, the entire boundary layer is in equilibrium with the drag induced by the wind turbines and there is no advection in the flow. In this case, the flow is deemed as being ‘fully-developed’, i.e., up-stream conditions have a negligible influence on the flow. An analytical model describing the fully-developed flow regime was first introduced by Frandsen et al. [2006] and later refined by Calaf et al. [2010], Meneveau [2012] and Yang et al. [2012]. In these analytical models, the streamwise velocity and shear stresses are modelled in a height-dependent one-dimensional framework, as shown in Fig. 3.1. From the LES results of Calaf et al. [2010], it was observed that the flow is neatly divided into three vertical regions. The lowest region extending from the ground to the bottom of the rotor-disk region consists of the surface layer of the standard ABL as evidenced by the logarithmic velocity profile. This region is characterized by lower stresses in comparison to the unperturbed ABL. The middle-layer is the rotor-disk region of the wind farm and is characterized by the dominating presence of the wind-turbine wakes. The presence of wakes causes enhanced mixing of the flow and results in a flattening of the velocity profile (see the green-shaded region Fig. 3.1(a)). This enhanced mixing can be modelled by considering an enhanced eddy viscosity within the wake region which is termed as the wake viscosity (ν_w). Based on the ‘eddy-viscosity’ concept, the mean streamwise velocity gradient can be related to the momentum flux through the rotor-disk region ($z_h - D/2 < z < z_h + D/2$) as follows,

$$\left(1 + \frac{\nu_w}{\kappa z u_*}\right) \frac{d\langle \bar{u} \rangle}{dz} = \frac{u_*}{\kappa z}. \quad (3.5)$$

Chapter 3. Evolution of flow characteristics through finite-sized wind farms and influence of turbine arrangement

Here, the wake viscosity (ν_w) is the additional viscosity induced by the turbines and it is assumed to be superimposed upon the background turbulent flow eddy-viscosity (described as $\kappa z u_*$) which scales as the distance from the surface. The wake viscosity is further non-dimensionalised and denoted as ν_w^* , and is computed as $\nu_w / \kappa z u_*$. The angular brackets denote spatial averaging in the horizontal directions. In the case of wind farms, it is common for the spatial extent of the averaging to be equal to the streamwise and spanwise spacing [Belcher et al., 2003]. The spatial averaging operation implies that the momentum flux calculation includes the contribution of the dispersive stress terms along with the traditional Reynolds stress terms [Raupach and Shaw, 1982]. The momentum flux calculation additionally includes the SGS flux terms when using LES data.

For the region above the rotor-disk region of the wind-farm, the flow recovers a logarithmic profile with a steeper slope. The shear stress has a maximum value at the top of the rotor-disk region, denoted as $u_{*,hi}$. The shear stress then decays linearly in accordance with the imposed uniform pressure gradient (see Fig. 3.1(b)). Therefore, the velocity profile in this region can be modelled based on $u_{*,hi}$, and the wind-farm induced effective surface roughness $z_{0,eff}$.

$$\frac{\langle \bar{u} \rangle (z)}{u_{*,hi}} = \frac{1}{\kappa} \ln \left(\frac{z}{z_{0,eff}} \right), \quad (3.6)$$

where $z > z_h + D/2$. Note that $z_{0,eff}$ and $z_{0,hi}$ are used interchangeably in this article to denote the wind-farm induced effective surface roughness. In the works of Frandsen et al. [2006], Calaf et al. [2010], Meneveau [2012] and Yang et al. [2012], analytical expressions were derived for $z_{0,eff}$ and ν_w^* as functions of wind-farm arrangement (i.e., streamwise and spanwise spacing), the diameter of the wind-turbine rotor-disk and the hub-height. A prerequisite for the derivations however, was the restrictive condition of zero advection, which is indeed satisfied in the fully-developed regime of the flow. Analytical expressions for these quantities are not available for the developing region of the wind-farm where advection is expected to be important. In this study, these quantities are extracted directly from the LES-generated datasets.

3.2.3 Extension to finite-sized wind farms

To extend the theoretical framework of the fully-developed flow regime described in the previous paragraphs to a more realistic scenario of a finite-sized wind farm, effects of advection across the leading edge of the wind farm, and development of an internal boundary layer over the wind-farm must be included. Figure 3.2 provides a simple schematic of the interaction between the incoming flow, upstream of the leading edge of the wind-farm and the downstream evolution of the flow, under the action of an enhanced drag induced by the turbines. The upstream flow in the standard neutral ABL is characterized by friction velocity (u_*), surface roughness (z_0) and the resultant velocity profile ($\bar{U}(z)$).

Beginning from the leading edge of the wind farm, the flow is divided horizontally into two main regions. In the first region, denoted as the ‘Adjustment Zone’, the flow decelerates under

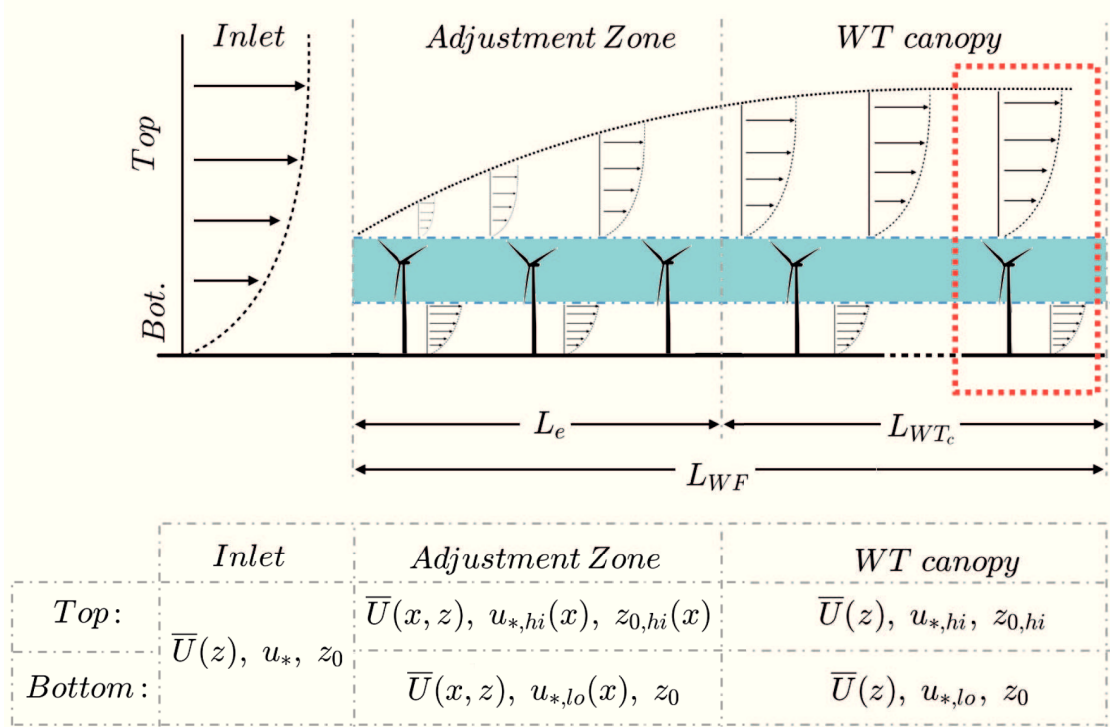


Figure 3.2 – Schematic representation of the mean flow adjustment in a finite size wind farm.

the action of the drag force applied by the wind-turbine blades, accompanied by increasing Reynolds stresses at the top of the rotor-disk. This region is characterized by mean-flow and turbulence statistics which are a function of the downstream distance from the leading edge of the wind farm ($\bar{U}(x, z), u_{*,hi}(x), u_{*,lo}(x), z_{0,hi}(x)$). After a certain distance L_e downstream from the leading edge of the wind farm, the flow is found to no longer decelerate, with the drag being balanced completely by the vertical entrainment of mean kinetic energy. This region of the wind farm is denoted as ‘WT canopy’ and extends up to the trailing edge of the wind farm. Thus within the region marked by red in Fig. 3.2, we expect the velocity and stress profiles to be similar to those in Fig. 3.1.

Concurrently, the flow is also partitioned vertically, similar to the 1-D framework described in the previous section. The region above the top of the rotor-disk is denoted as ‘Top’ and the flow is characterized by an evolving friction velocity $u_{*,hi}(x)$ and effective surface roughness $z_{0,hi}(x)$. On the other other hand, the flow below the rotor-disk region, denoted as ‘Bottom’ is described by an evolving friction velocity $u_{*,lo}(x)$ and the fixed roughness length of the underlying surface (z_0). The evolution of both the ‘Top’ and ‘Bottom’ quantities ceases in the ‘WT canopy’ region of the flow. The quantities describing the flow in this theoretical framework are described in the table accompanying Fig. 3.2. Thus, the 1-D framework of the wind-farm induced perturbation in the fully-developed regime is now extended to two-dimensions.

A simple re-arrangement of Eq. (3.6), and expanding the analysis to two dimensions by con-

Chapter 3. Evolution of flow characteristics through finite-sized wind farms and influence of turbine arrangement

sidering the quantities as functions of streamwise distance (x) and height (z) results in,

$$z_{0,hi}(x) = z \exp \left[- \langle u(x, z) \rangle \kappa / u_{*,hi}(x, z) \right]. \quad (3.7)$$

Thus, inputting values of $u(x, z)$ and $u_{*,hi}$ from LES-data (post-processing of LES-generated flow fields is described in Section 3.3.1), $z_{0,hi}$ can be computed. In a similar fashion, $v_w^*(x)$ can be computed from LES data using a rearranged form of Eq. (3.5). Here, we use the stress values at the top of the rotor-disk while the velocity gradient is computed at hub-height, similar to the procedure adopted by Calaf et al. [2010]. Thus, the expression for $v_w^*(x)$ can be written as,

$$v_w^*(x) = \frac{u_{*,hi}(x)}{\kappa z (d\langle u \rangle / dz|_{z=z_h})(x)} - 1. \quad (3.8)$$

Calaf et al. [2010] additionally provided an analytical expression for the wake viscosity in fully-developed flow conditions as a function of the wind farm geometry. For a wind farm with spacings in the streamwise and the lateral directions as $s_x D$ and $s_y D$ respectively, the wake viscosity can computed as,

$$v_w^* = 28 \sqrt{0.5 * c_{ft}}, \quad (3.9)$$

where the friction coefficient is defined as $c_{ft} = \pi C_T / 4 s_x s_y$.

It is important to note that the simplistic representation of flow in Fig. 3.2 has several subtle assumptions. Firstly, it is assumed that the mean-flow and turbulence statistics evolve at a similar rate, while in reality, mean flow and higher-order moments take progressively increasing time to reach equilibrium. A similar assumption is made with respect to flow equilibrium at different heights.

3.3 Large eddy simulation and study cases

3.3.1 Simulation Details

A set of different LES cases has been considered. The LES solver is based on pseudo-spectral methods, with Fourier transform based differentiation in the horizontal direction and second-order finite-differences in the vertical direction to solve the equations of conservation of mass (continuity) and momentum (Navier-Stokes, NS) of an incompressible flow. The time integration is performed using the second-order Adams-Bashforth scheme. As is intrinsic to the LES methodology, only the large, energy-containing eddies are resolved, and the smaller ones are parametrized using a subgrid-scale model.

In the LES performed for this study, the flow is forced with a constant pressure gradient in the streamwise direction, such that at the top of the domain, or boundary-layer height ($z_i = 1000\text{m}$), it is approximately equivalent to a geostrophic wind forcing of $\approx 10 \text{ m/s}$. For this purpose, a momentum surface roughness $z_0 = 0.1 \text{ m}$ is imposed, which is a representative value for onshore wind farms. To include the effect of the wind turbines, a drag-force term is included on the right hand-side of the NS equations. The drag-force parametrization utilized

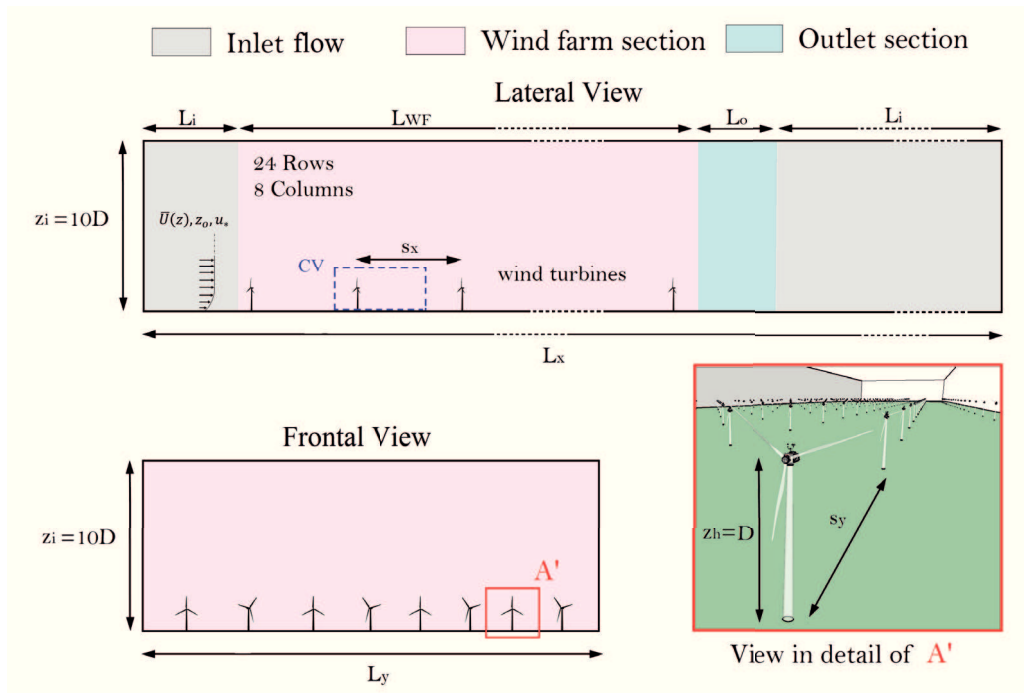


Figure 3.3 – Schematic representation of the base case wind farm configuration. Top sub-figure: Lateral view of the wind farm configuration in the streamwise direction. Bottom left: Frontal view of the wind farm. Bottom right: Detail view of the highlighted A' region in the bottom left sub-figure.

is the actuator-disk with rotation approach of Meyers and Meneveau [2010]. For the purpose of this study a large numerical domain is needed, such that it fits a large wind farm, and it provides enough physical space for the flow to fully recover. Because of the spectral approach used in the horizontal directions, the flow is periodic between the inlet and outlet regions, as well as in the lateral directions.

The wind farm is set such to respect the lateral periodicity, hence the wind farm is in practice infinite in the spanwise direction. However, the wind farm is finite in the streamwise direction and occupies only 18% of the streamwise length of the computational domain. As we shall see in the results section, despite the inherent periodicity of the simulation technique, the streamwise length of the domain is sufficient for the flow to completely recover to the unperturbed ABL flow both for mean and turbulent statistics. Note that the flow is aligned with the finite-size direction of the wind farm, hence the infinite lateral size of the farm excludes the study of the lateral wind farm effects.

Each one of the cases performed consists of a numerical domain of size $(32\pi \times \pi \times 1)z_i$, in the streamwise, spanwise and vertical directions, respectively. To be able to reproduce the wind turbines with a reasonable accuracy, and capture the mid- and far-wake regions accurately, a numerical grid consisting of $4096 \times 128 \times 128$ grid-points was used, providing a numerical resolution of $24.5 \text{ m} \times 24.5 \text{ m} \times 7.85 \text{ m}$. This numerical configuration constitutes the most intensive channel flow as well as LES based wind farm study to date. For further details of the

Chapter 3. Evolution of flow characteristics through finite-sized wind farms and influence of turbine arrangement

Cases	AL-1	AL-2	AL-3	AL-4	ST
Spacing	s_x, s_y	$s_x, 2s_y$	$2s_x, s_y$	$2s_x, 2s_y$	s_x, s_y

Table 3.1 – Overview of study cases

numerical approach used, please refer to Chapter 1.

To illustrate the relevance of wind turbines' arrangement within a wind farm on the flow evolution and the diagnostic variables described in the introduction, a set of 5 different wind farm configurations have been considered. The 'baseline' simulation consists of a wind farm composed of 24 rows of turbines, each row with 8 turbines, all aligned and with spacings of $s_x \approx 8D$ and $s_y \approx 4D$ (henceforth referred to as AL-1). Three additional aligned cases have been considered; one configuration with s_x and $2s_y$ spacing (AL-2), and two configurations with turbines arranged with a $2s_x$ spacing and with corresponding s_y and $2s_y$ spanwise separations (AL-3 and AL-4 respectively). Finally, an additional case with staggered rows of turbines (ST) has been considered and serves as a counterpart of the AL-1 aligned case. The configurations are summarized for future reference in table 3.1. Note that all wind farms have the same streamwise length (L), hence those wind farm configurations with $2s_x$ spacing between turbines are only composed of 12 rows of turbines, instead of 24. The numerical setup for the AL-1 case is represented in Fig. 3.3.

All five cases are integrated for a million time-steps representing $T_* = T u_* / z_i = 450$ non-dimensional time-units and an additional 200,000 steps are simulated to calculate mean and second-order turbulence statistics (which corresponds to $T_* = 27$).

3.3.2 Post-processing of LES output

The velocity fields $\alpha, \beta \in \{u, v, w\}$, simulated during the LES cases described above are first time-averaged for each point of the three-dimensional grid. In accordance to the two-dimensional framework discussed in Section 3.2.3, the time-averaged quantities are further averaged along the cross-stream direction (represented by $\langle \rangle$). The correlation terms arising from these averaging operation are the Reynolds flux terms and the dispersive stress terms resulting in $\langle \alpha' \beta' \rangle$ and $\langle \bar{\alpha}'' \bar{\beta}'' \rangle$ respectively. The most important of these second-order statistics for this study are the vertical momentum fluxes. Correspondingly, the friction velocities $\{u_{*,hi}(x), u_{*,lo}(x)\}$ are given by $\sqrt{\langle \overline{u'w'} \rangle + \langle \overline{u''w''} \rangle + \langle \tau_{xz}^{sgs} \rangle}$ ($x, z = z_h + D/2, z_h - D/2$), where τ_{xz}^{sgs} is the vertical subgrid-scale flux.

3.4 Results

3.4.1 Evolution of Mean and Turbulent Flow Quantities

We begin the analysis of the LES data with an illustration of the time-averaged streamwise velocity (u) at hub-height shown in Fig. 3.4, for the five simulation cases (presented in table 3.1). The velocity values are normalized by the unperturbed velocity far upstream of the wind farm. Sub-plot (a) corresponds to the aligned reference case (AL-1) with the subsequent subplots

(top to bottom) showing the AL-2, AL-3, AL-4 and ST cases respectively. In the reference case AL-1, it is interesting to observe the evolution of the wind-turbine wakes. The first row shows the characteristic ‘single-column’ wake regime where wakes of the adjacent turbines (same row) do not interact with each other. The wakes in the first row are quite narrow and the lateral expansion of wakes increases with each successive row. The wakes ultimately merge and occupy the inter-column spacing at approximately $0.6 L_{WF}$ (corresponding to row 15). In the AL-2 case, the mean flow velocity is higher and the inter-turbine high-momentum streaks are more prominent than for the AL-1 case. This is expected given the larger spanwise spacing of the turbines. This also results in a reduction of the lateral interaction between turbines of adjacent columns as compared to the AL-1 case. In the AL-2 case, there is also a weaker momentum deficit in the wake region, sign of an enhanced wake recovery. As a result of the larger streamwise spacing in the AL-3 case, wakes seem to fully or quasi-fully recover before reaching the following turbine. In this case, while the wakes have a longer streamwise distance to recover and hence become more elongated, there seems to exist a slightly more intense lateral wake interaction as compared to the AL-2 case. In case AL-4, turbines have the largest spacing in both the stream-wise and span-wise directions and thus minimum inter-turbine interaction is observed, especially between adjacent wind turbines. The presence of the downstream turbines still causes the wakes to expand laterally but not sufficiently to merge with the adjacent wakes. Given the large spanwise spacing, it is easy to identify a large velocity deficit that encompasses each column of wind turbines (see Fig. 3.4(d)). The flow-field of the staggered case is shown in the final subplot. Due to the unique nature of the turbine arrangement, there are no inter-column high-momentum streaks and it can be qualitatively observed that the flow reaches the fully waked regime earlier as compared to the AL-1 case.

To better quantify the differences in mean wind velocity between the different study cases, Fig. 3.5a shows the spanwise as well as rotor-disk averaged mean streamwise velocity as a function of downstream distance, for the five study cases. The velocities are normalized by the corresponding wind farm inflow velocity for better comparison between the five cases. Dotted lines are included to highlight the location of the wind farm rows. The oscillatory trends in Fig. 3.5 show the induced wakes and the subsequent recovery downstream of each row of turbines. Note that the high-momentum regions between the wind-turbine columns are included in the averaging operation. This inclusion is necessary to understand how the entire hub-region of the wind farm, and not just the wind-turbine columns, achieve equilibrium.

There are two quantities of interest here, namely, (1) the rate, and (2) the magnitude of deceleration of the mean flow (or deficit) induced by the wind farm. It is immediately clear that the ST case shows the most rapid and extensive deceleration of the mean flow with a 23% deficit developing between the first and eighth row of turbines (corresponding to $\approx 0.4 L_{WF}$). The least ‘dense’ wind farm, AL-4 shows a maximum deficit of 8% at the downstream edge of the wind farm. As expected, this is the smallest deficit induced amongst the five study cases. The ST and AL-4 cases mark the upper and lower bound of the wind-farm induced perturbation to the mean flow. Interestingly, the aligned counterpart of the ST case, AL-1,

Chapter 3. Evolution of flow characteristics through finite-sized wind farms and influence of turbine arrangement

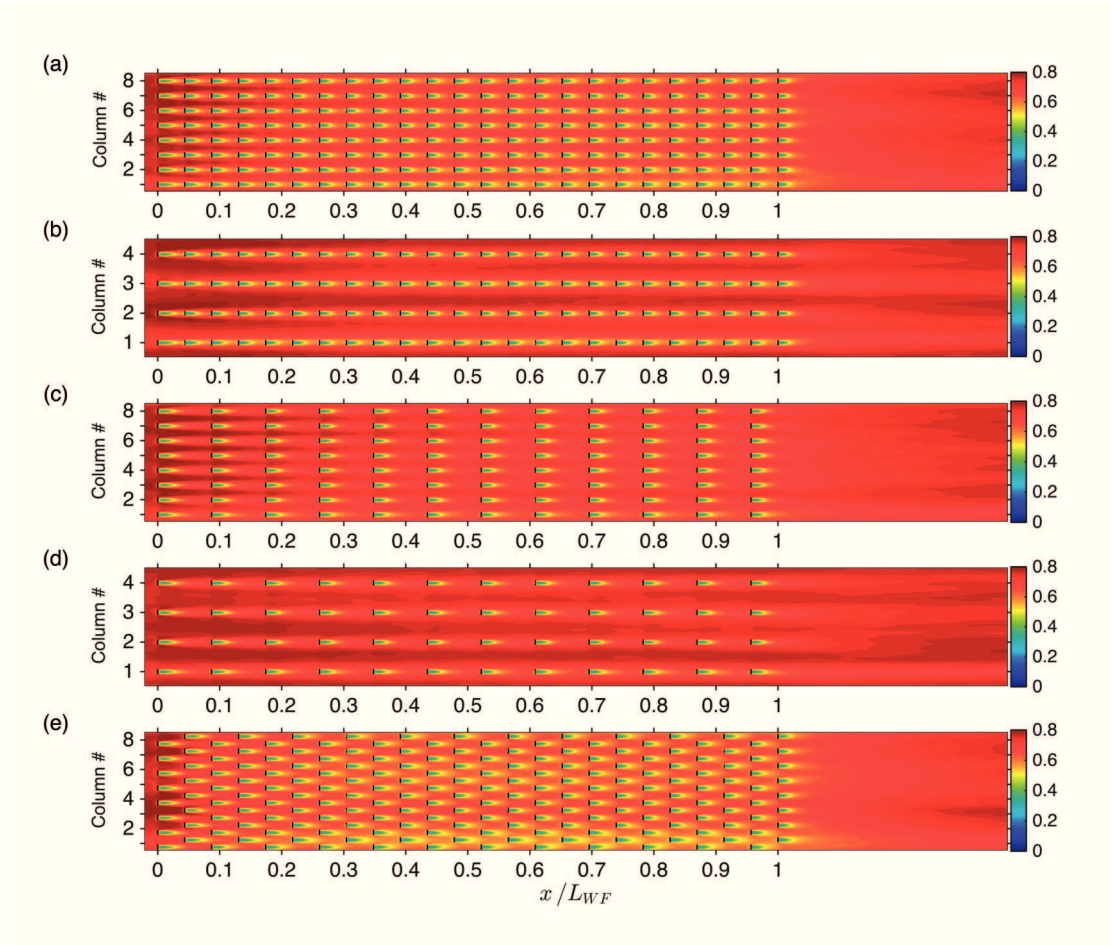


Figure 3.4 – Mean wind velocity for the finite-size wind-farm configurations described in table 3.1. (a) the AL-1 , (b) AL-2, (c) AL-3, (d) AL-4, and (e) the ST cases, respectively. The velocity values are normalized by the far upstream velocity. Note that the figure represents only 25% of the full numerical domain.

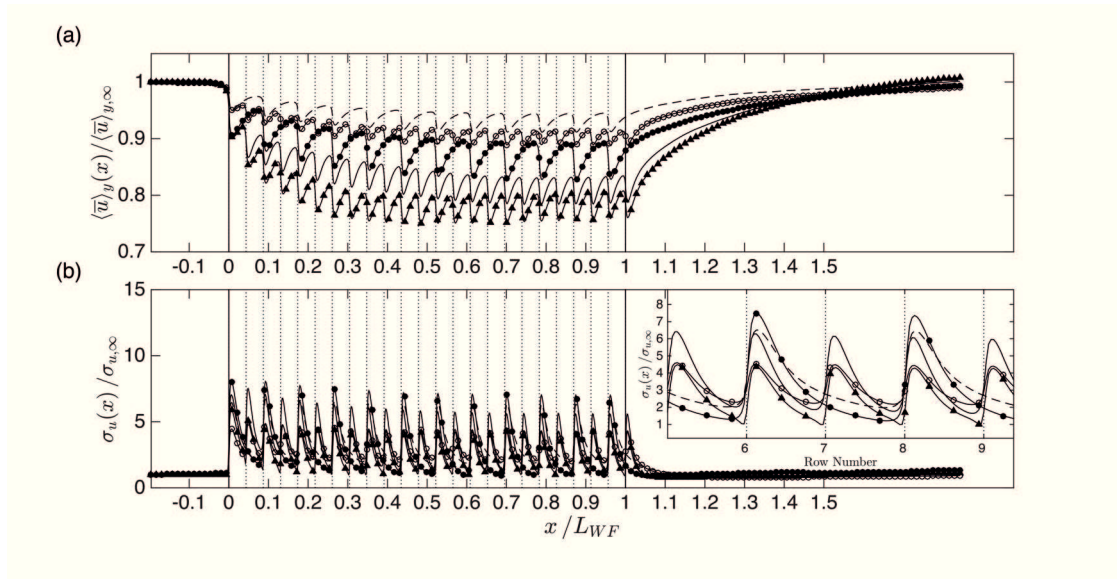


Figure 3.5 – (a) Spanwise averaged mean wind velocity as a function of downstream distance within the wind farm. (b) Spanwise standard deviation of the mean wind velocity as a function of downstream distance within the wind farm. Solid-line with triangles represents the ST case, solid line the AL-1 case, solid-line with filled circles the AL-3 case, and with hollow circles the AL-2 case. Finally, dashed-line represents the AL-4 case.

shows a slightly lower deficit than the ST case with a maximum deficit of 19%. Moreover, the velocity achieves steady state at $\approx 0.6 L_{WF}$, further downstream than the corresponding distance for the ST-case. Taking AL-1 as the ‘baseline’ case, we can analyse the effect of increasing the spanwise and streamwise spacing by comparing the rate and amount of deficit of the AL-2 and AL-3 cases. Increasing the spanwise spacing from s_y to $2s_y$ seems to result in a greater effect than increasing the streamwise spacing from s_x to $2s_x$. The AL-2 case shows a 10% maximum deficit as compared to the 15% deficit found in the AL-3 case. On the other hand, the AL-2 case reaches steady-state velocity at $\approx 0.7 L_{WF}$, while for the AL-3 and AL-4 cases, the corresponding value is $\approx 0.85 L_{WF}$.

Two additional points are of interest here; first, it is interesting to note that cases with the same spanwise spacing show the same deficit at the first row of the wind-farm, and at the entrance region of the wind-farm, the stream-wise spacing does not seem to play a role. Second, Fig. 3.5a also shows the recovery of the ‘global’ wind-farm velocity-deficit (downstream of the trailing edge of the wind farm) with all the five cases recovering approximately 90% of the deficit within $0.5 L_{WF}$. Thus, more the loading of the wind farm, more is the deficit induced as expected, but remarkably, faster is the recovery of the ‘global’ wake as well.

Figure 3.5b shows the spanwise standard deviation of the streamwise velocity as a function of downstream distance from the leading edge of the wind farm. This figure essentially shows the evolution of spanwise heterogeneity in the rotor-disk region of the flow. Similar to Fig. 3.5a, the values are normalized by the same quantity computed far upstream of the wind farms. The principal reason for the heterogeneity is due to the presence of wind-turbine wakes and

Chapter 3. Evolution of flow characteristics through finite-sized wind farms and influence of turbine arrangement

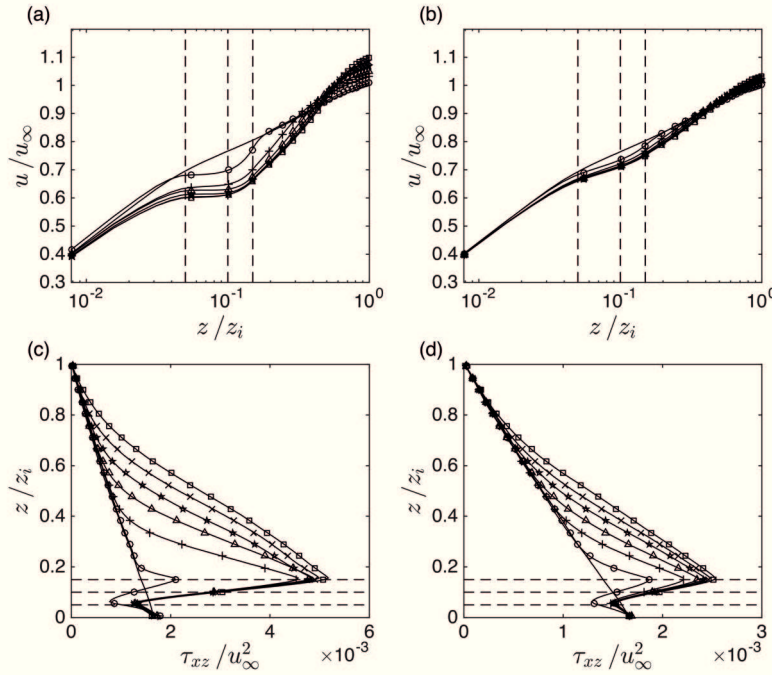


Figure 3.6 – Vertical profiles of mean wind velocity (a and b), and shear stress (c and d). Each profile represents a different downstream distance within the wind farm, with the solid line representing the far upstream, unperturbed flow. The following profiles are at the entrance of the wind farm $0L_{WF}$ (hollow circles), at $0.2L_{WF}$ (crosses), $0.35L_{WF}$ (triangles), $0.5L_{WF}$ (stars), $0.7L_{WF}$ (crosses), and $0.9L_{WF}$ (squares) downstream within the wind farm.

the high-momentum streaks in the inter-column spacing.

In general, the values show little evolution through the wind farm. The most significant trends are to be found instead within inter-row spacing. This can be seen in the inset in Fig. 3.5b. Interestingly, the heterogeneity peaks at approximately the same distance $\approx 1D$ downstream of a row of turbines, for all of the five cases. The AL-1 and AL-4 cases have the same maximum value as do the AL-2 and ST cases with the former group's value being larger. The maximum heterogeneity is surprisingly found in the AL-3 case.

Figure 3.6 presents vertical profiles of the mean wind velocity (subplots a and b) using a semi-logarithmic representation, and subplots c and d present vertical profiles of shear stress, for two representative cases, AL-1 and AL-4. It is immediately clear that the vertical profiles are similar to the canonical vertical profiles of these quantities shown earlier in Fig. 3.1. The velocity profiles present a logarithmic shape between the surface and the bottom of the rotor-disk, with a strong perturbation above. This lower section of the velocity profile is characterized by the ground surface roughness (z_0), and the near-surface friction velocity ($u_{*,l0}$), as mentioned earlier in Sect. 3.2. Above this region, profiles show a strong perturbation throughout the rotor-disk region, with a progressive enhanced deficit with distance downstream in the wind farm. Above the rotor-disk region, a modified logarithmic velocity region progressively

forms. This region is characterized by an enhanced roughness ($z_{0,hi}$) and mixing ($u_{*,hi}$), which increase with downstream distance. Further up, this modified logarithmic profile connects with the outer, unperturbed velocity field, characterized by the upstream wind farm surface characteristics (surface roughness, z_0 and friction velocity, u_* , see Fig. 3.2 for further details).

For case AL-1, a progressive decrease in the mean wind speed is observed around the turbine rotor-disk region, with little difference observed from distance $0.5L_{WF}$ onwards. On the contrary, for the ‘least-dense’ wind-farm canopy, the profile adjusts fast and does not present much variation further on. Also the vertical profiles of shear stress (subplots c and d), present a similar vertical structure to that observed in Calaf et al. [2010], with a slight reduction below the rotor-disk and a strong increase above. Similar to the velocity profiles, case AL-1 presents a progressive increase in shear above the rotor-disk down to profile $0.5L_{WF}$, with an almost constant value thereon. On the other hand, case AL-4 presents an almost constant increase in shear above the rotor-disk area throughout all profiles. Below the rotor disk, the shear decays sharply in the entrance region of the wind farm ($0.2L_{WF}$), presenting an almost constant value thereon.

The detailed downstream evolution of the friction velocities at the top ($u_{*,hi}$) and bottom ($u_{*,lo}$) of the rotor-disk are illustrated in Fig. 3.7. The friction velocity at the top of the rotor-disk increases with the downstream distance from the leading edge of the wind farm, progressively reaching a ‘saturation’ value which is a function of the loading of the wind farm. The maximum and minimum saturation values are found for the ST and the AL-4 cases respectively, showing a difference between cases of $\sim 40\%$. The bottom friction velocity illustrates a much more reduced variation between cases ($\sim 9\%$), with an initial reduction in magnitude for cases ST (22%, between first and third row), AL-1 (9%, between first and second row), and AL-2 (3%, between the first and second row). It is interesting to note that, in general, LES results seem to indicate that increasing the wind farm loading results in increase of $u_{*,hi}$ values and a decrease of $u_{*,lo}$ values.

It is also interesting to analyse the progressive increase in friction velocity above the rotor-disk, as a function of downstream turbine row. Note, for example that for cases ST and AL-1, there exists an increase of about 60% between the first and the 17th row of turbines ($0.7L_{WF}$). This increase is followed by a saturation region, from whereon the turbulent mixing above the rotor-disk remains fairly constant. This could be indicative of the flow having reached a fully-developed regime (this will be further discussed later). On the contrary, results of the least-dense wind farm, i.e, the AL-4 case, does not reach convergence. The friction velocity above the rotor-disk increases nearly 13% between the entrance region and $0.3L_{WF}$ downstream, thereon illustrating a weak linear increase of $\sim 5\%$. Cases AL-2 and AL-3 present an intermediate behaviour, with case AL-2 reaching a saturation value beyond $0.8L_{WF}$. From these results, it is clear that the streamwise turbine spacing plays an important role in reaching saturation of the turbulent mixing above the rotor disk. This means that beyond a certain streamwise wind farm packing, turbines can not induce stronger mixing, and hence limit the process of wake recovery. In parallel, the two cases with larger streamwise spacing ($2s_x$, AL-3 and AL-4), while presenting different absolute values in turbulent mixing above the

Chapter 3. Evolution of flow characteristics through finite-sized wind farms and influence of turbine arrangement

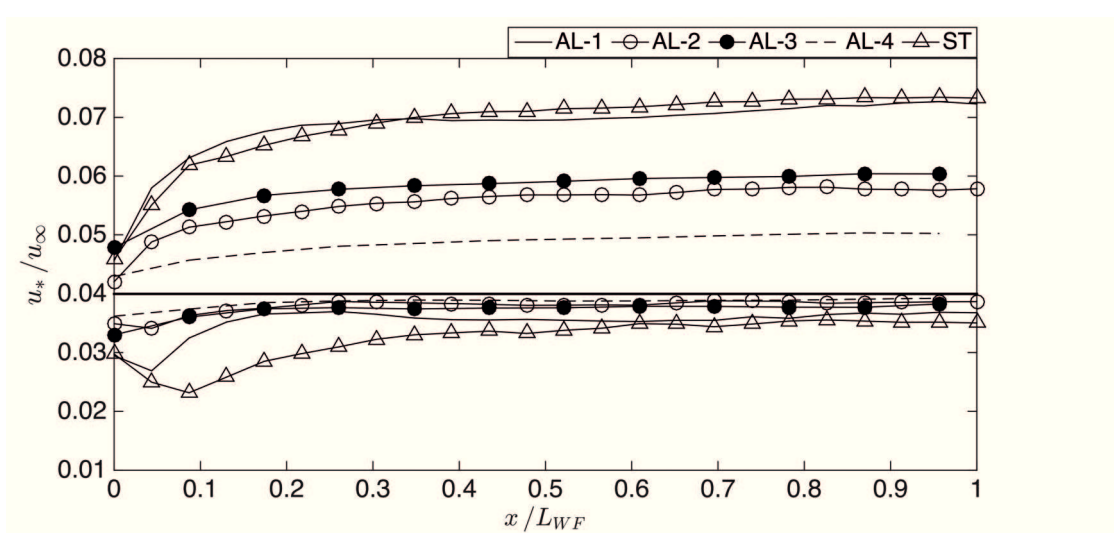


Figure 3.7 – Downstream evolution of the friction velocities at the top ($u_{*,hi}$) and bottom ($u_{*,lo}$) of the rotor-disk area in the five wind-farm cases. All trends above 0.04 are for $u_{*,hi}$ while the remainder represent $u_{*,lo}$.

rotor-disk, present the same trend, with a very similar quasi-linear growth beyond the fourth row ($\sim 0.25 L_{WF}$). Between these two cases, differences in $u_{*,hi}$ growth are observed between the first three rows, with a stronger increase in the AL-3 case as one would expect, given the reduced spacing in the spanwise direction. With respect to the downstream evolution of the turbulent mixing below the rotor disk ($u_{*,lo}$), it can be observed that beyond $0.6 L_{WF}$ very small differences are observed between the different cases ($< 10\%$). Interestingly, for cases ST and AL-1 an initial strong decrease occurs followed by a recovery around the third row for the AL-1 case, and the 9th row for the ST case. A weaker initial decrease also occurs for case AL-2, which is recovered after the third row of turbines. This initial weakening of turbulent mixing below the rotor-disk is believed to be due to the strong initial absorption of momentum by the turbines. Initially, all source of mean kinetic energy (MKE) is due to horizontal advection, which is mostly absorbed by the turbine. As the flow evolves within the wind farm, part of the MKE is now also lost into turbulence, and hence recovering the turbulent mixing below the rotor-disk. Note that the two cases with larger streamwise spacing (AL-3 and AL-4) don't present this initial decrease in turbulent mixing.

3.4.2 The wind-farm induced effective surface roughness

Following the framework presented in Sect. 3.2, the wind turbine array induced effective surface roughness is presented in Fig. 3.8. This variable has been computed using the velocity field values at a height twice the hub-height ($z = 2z_h$), using the logarithmic profile fit described in Eq. (3.7), similar to the approach used in Calaf et al. [2010]. From the results presented in Fig. 3.8 it is clear that both cases, AL-1 and ST, present a similar behaviour, with a strong increase (22 times) over the first ten rows of turbines ($0.4 L_{WF}$), a more gentle slope (28% increase) from there on until row 19 ($0.8 L_{WF}$), and a nearly constant regime till the end of the wind farm (only 1% increase). The effective surface roughness obtained for both

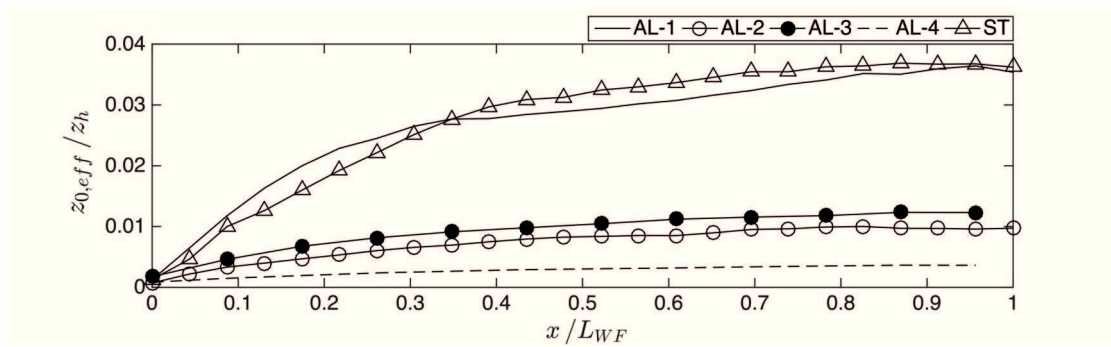


Figure 3.8 – Wind farm downstream evolution of the wind-farm induced surface roughness.

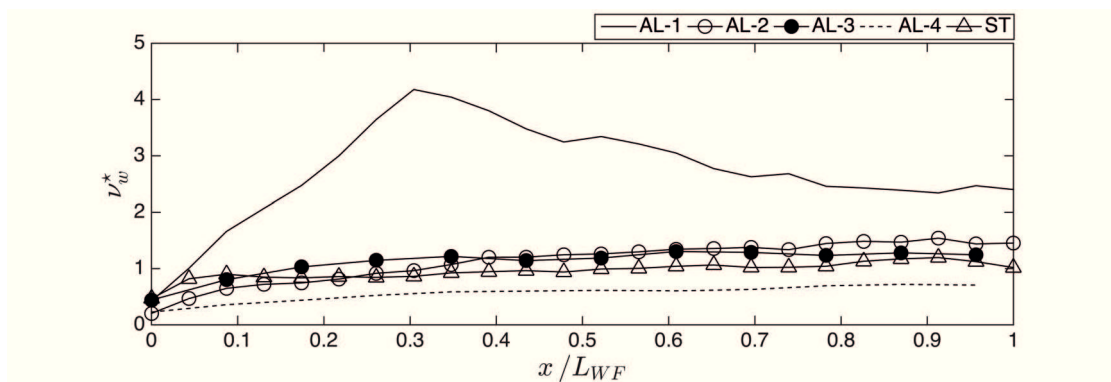


Figure 3.9 – Wind farm downstream evolution of the wind-farm induced wake viscosity v_w^* . This is a non-dimensional variable first introduced in Calaf et al. [2010].

cases (AL-1 and ST) at the end of the wind farm (3.6 m and 3.7 m respectively) is 86% of the analytically obtained value of 4.2 m for fully-developed flow conditions using Calaf et al. [2010]’s expression. This result is indicative once again that beyond the downstream distance $0.8 L_{WF}$, the flow reaches a fully-developed state. In a similar fashion, case AL-2 also presents a constant regime beyond downstream distance $0.8 L_{WF}$, with only a 0.5% increase. In this case the induced surface roughness takes a value of 1.2 m, 3 times lower compared to the previous two cases. Similar to the upper friction velocity trend presented in Fig. 3.7, cases AL-3 and AL-4 present an almost constant increase in effective surface roughness as a function of downstream distance with a 10% increase beyond $0.8 L_{WF}$, signifying that in this case the flow doesn’t reach a fully-developed regime. This was qualitatively shown in Fig. 3.4.

In relation to these results, Fig. 3.9 presents the downstream evolution of the wake induced eddy-viscosity (v_w^*). This magnitude has been computed using Eq. (3.8), defined by an informal extension of similarity theory to the wind turbine array boundary layer, as introduced in previous works by Calaf et al. [2010], Meneveau [2012], and reviewed in Sect. 3.2. Its usefulness lies in the fact that it provides an estimate of the enhanced mixing within the wind farm due to the presence of the wakes. From the results for the AL-1 case, it can be observed that beyond the wind farm downstream distance of $0.8 L_{WF}$, the flow presents a constant wind turbine wake induced eddy-viscosity. This matches well the results of the top friction velocity and the induced surface roughness as shown in Figs.3.6 and 3.7, respectively.

Chapter 3. Evolution of flow characteristics through finite-sized wind farms and influence of turbine arrangement

It is also interesting to note that the value obtained for this case ($v_w^* = 2.4$), is approximately 87% of the analytically computed value of 2.74 (using Equation 3.9). The trend for the AL-1 case shows a sharp increase in the wake-viscosity, reaching a maximum value at $0.3 L_{WF}$. This feature is very different from the rest of the simulated cases. It is hypothesized that this is the result of a rapid growth of the internal boundary layer in the AL-1 case (which incidentally is the most-dense configuration) and its interaction with the top of the ABL. Results for case AL-2 illustrates a constant regime also beyond downstream distance $0.8 L_{WF}$, with a value approximately half of that of case AL-1. In this case, the staggered configuration presents a more variable pattern beyond downstream distance $0.8 L_{WF}$.

Overall, the change in absolute value is small and it might be explained by the intrinsic heterogeneity of this configuration in comparison to the perfectly aligned cases. Once again, similar to the induced surface roughness and the upper friction velocity, cases AL-3 and AL-4 illustrate a weak constant growth pattern. This is explained by the fact that at none of the downstream distances these configurations reach a fully-developed state within the wake region, nor with the surrounding channelled flow. Note specially the weakest ‘viscosity’ presented by case AL-4, due to the large inter-turbine spacing.

3.4.3 The wake-expansion coefficient

As described in Sect. 3.2, a row-by-row optimization procedure is utilized for numerically determining the k_w value at each row of the wind farm using LES data. The optimized k_w values are shown in Fig. 3.10 for all 5 cases. For each of the cases, a k_w value of 0.017 is determined for the first row of the wind farm. This value is lower than that reported in literature and usually used in the industry (i.e. 0.058, based on Frandsen [1992]’s model). It is interesting to note that the 5 cases can be divided into two groups related to their corresponding streamwise spacing. The AL-1 and AL-2 cases (having streamwise spacing of s_x) show a very similar trend, with a 6 times increase in the k_w value for the second row of the wind farm ($k_w = 0.07$) followed by a rapid decay within 4 rows to reach a steady state value of ~ 0.05 . The remaining three cases of AL-3, AL-4 and ST (having the same streamwise spacing of $2 s_x$) also share a common trend with a ‘steady-state’ value of 0.037, achieved by AL-3 and AL-4 at the third row and ST at row 15.

The wake-expansion coefficient also determines the width of the wake as described in Eq. (3.2). The dominance of the streamwise spacing in modulating the values of the wake-expansion coefficient is striking, with larger streamwise spacing resulting in narrower wakes, as can be intuitively guessed. However, the spanwise spacing seems to play little role in affecting the expansion of wakes. It must be noted that in this study, the minimum spanwise spacing is $\sim 3.5D$. In wind farms with even higher spanwise loading, influence of adjacent wind turbine columns may be more pronounced. More simulations and field-data is needed in this regard.

Lastly, Fig. 3.11 shows the result of the optimization procedure by comparing the centre-line velocities (averaged over all the columns of the wind farm) between LES-data (shown in solid black lines), the wake model (shown with dashed-line and markers) using optimal k_w values

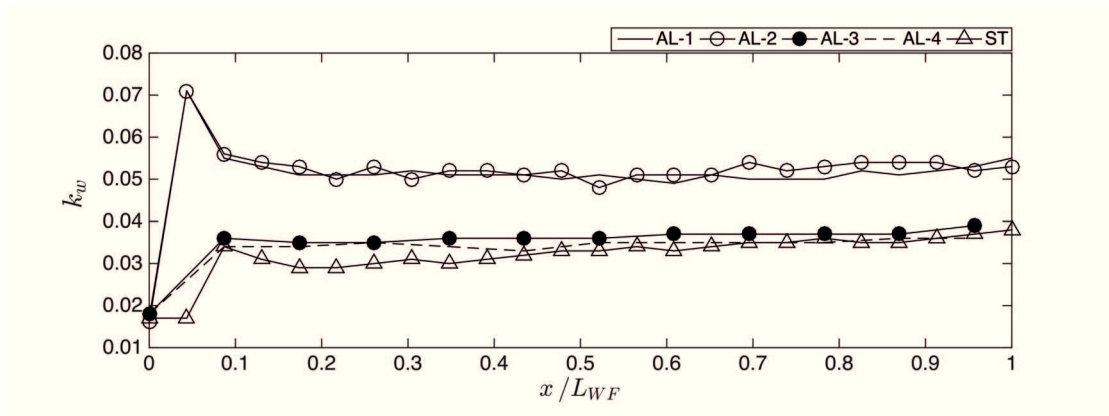


Figure 3.10 – Wind farm downstream evolution of the wake-expansion coefficient k_w .

and the wake model using a fixed k_w value of 0.058 (shown with solid red lines). It can be seen that the optimization procedure works reasonably well and the wake model with the optimized k_w values matches the LES-data better than that with a fixed k_w value, especially in the far-wake region. This improvement is more pronounced for cases AL-3, AL-4 and ST that have a larger streamwise spacing.

3.5 Discussion and Conclusions

A suite of five numerical simulations of finite-sized wind farms with different streamwise and spanwise spacings were performed for a neutrally stratified ABL flow using LES. From the resultant dataset, three diagnostic quantities were computed, namely, the wind-farm induced effective surface roughness ($z_{0,eff}$), the wake viscosity (ν_w^*) and the wake-expansion coefficient (k_w).

Analysis of the mean flow within the rotor-disk region showed that the cases with streamwise spacing of s_x (AL-1 and AL-2) reach ‘steady-state’ conditions at $\approx 0.6L_{WF}$, corresponding to the 15th row of the wind-farm. The corresponding distance for cases with $2s_x$ spacing (AL-3 and AL-4) was found to be $\approx 0.9L_{WF}$.

The wind-farm induced effective surface roughness was observed to increase monotonically for each of the five cases with rapid increase within the first few rows of the wind farm. The maximum effective roughness values achieved in the wind farm were directly proportional to the wind farm loading as expected. However, upon using trends of $z_{0,eff}$ for identifying achievement of flow equilibrium, it was found that only the cases AL-1, AL-2 and ST achieve fully developed flow at $0.8L_{WF}$. It was shown that the effective roughness value beyond this distance was approximately constant at 3.6 m for the AL-1 and ST case, which is 86% of the analytically determined value of 4.2 m for these configurations. For the remaining cases of AL-3 and AL-4, the length of the wind farm was found to be insufficient to reach fully-developed conditions.

The wake viscosity values followed trends similar to those of $z_{0,eff}$ in the fact that for the AL-1, AL-2 and ST cases, values were found to be nearly constant beyond $0.8L_{WF}$ and approach the

Chapter 3. Evolution of flow characteristics through finite-sized wind farms and influence of turbine arrangement

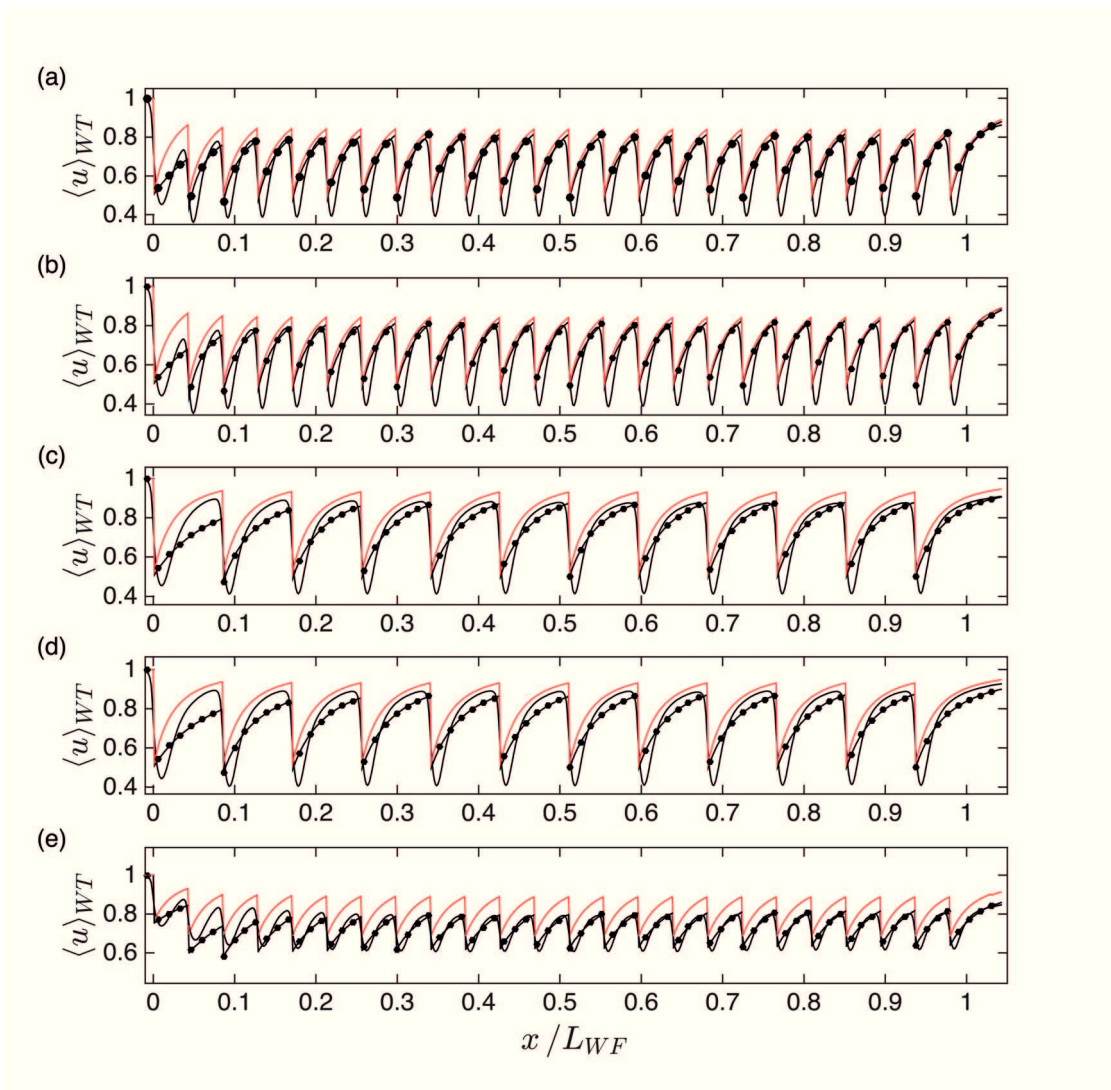


Figure 3.11 – Intercomparison of average center-line streamwise velocity between LES data (solid lines), wake model based on row-wise optimized k_w values shown in Fig.3.10 (solid lines with filled circles) and wake model using fixed k_w value of 0.058 for all rows (red line). Subplots (a)-(e) shows results for cases AL-1, AL-2, AL-3, AL-4 and ST respectively.

analytically predicted values for fully-developed flow conditions.

The values for the wake-expansion coefficient (k_w) were computed using an optimization procedure such that at each row of the wind farm, the error between the center-line velocities behind turbines extracted from the LES data and that predicted by the Katic/Park model is minimized in the root-mean-square sense. The resulting trends showed that configurations with the same streamwise spacing but different spanwise spacing were grouped together (trends for AL-1 and AL-2 overlap as do the trends of AL-3 and AL-4). This illustrates the dominant role of the streamwise spacing in modulating the wake recovery. The staggered case effectively has a $2 s_x$ streamwise spacing and the k_w values match those of AL-3 and AL-4.

We would like to discuss two important principles at this point. Firstly, in this study, identification of fully-developed flow is based on both mean-flow as well as second-order turbulent statistics. However, the mean-flow reaches equilibrium earlier compared to turbulence. On the other hand, the three diagnostic variables depend on both the mean flow as well as momentum flux values and thus their trends are dependent on how turbulence evolves as a function of the downstream distance within the wind farm. Therefore, the equilibrium distance is found further downstream when using turbulence statistics instead of only the mean flow. Secondly, we would like to highlight the fact that two of the diagnostic variables, namely $z_{0,eff}$ and v_{WF}^* are based on area-averaged statistics. This means that the contribution of the high-momentum streaks between the turbine columns is included in the analysis and thus the influence of streamwise and spanwise spacing on the flow is more difficult to identify. However, results in this study hint towards the fact that streamwise spacing strongly modulates the downstream distance within the wind farm at which the flow reaches equilibrium. On the other hand, the wake-expansion coefficient (k_w) is computed using only the center-line velocities behind each turbine, not including the effect of the inter-column regions. As a result, the effect of streamwise and spanwise spacing is clearly highlighted in this case.

In Appendix B, a mean-kinetic energy budgets of the ABL simulations described in this chapter are presented. The purpose of that study is to identify the flow adjustment and evolution using appropriately identified terms of the MKE budget equation. The results presented therein provide additional support to those described in this chapter.

In closing, we believe that the values obtained for the three diagnostic variables will be a valuable point of reference for the wind-energy community given that they are used in various numerical parametrizations of diverse complexity, ranging from weather and climate models to wind farm design tools used in industry. Future efforts shall explore in further detail: the reasons why the streamwise spacing seems to play a dominant role in flow-adjustment as compared to the spanwise spacing; the effects of mis-alignment between the mean wind direction and the wind-farm pattern; and the effect of atmospheric stability on the diagnostic variables.

Chapter 3. Evolution of flow characteristics through finite-sized wind farms and influence of turbine arrangement

Acknowledgements

The work was made possible by support received through the Swiss National Science Foundation (project no. 200021134892/1 and 20020 125092), ETH Domain Centre for Competence in Environmental Sustainability, NSERC Discovery Grant (MBP), Swiss National Supercomputing Center (CSCS), Scientific IT and Application Support (SCITAS) group at EPFL, University of Utah and University of British Columbia.

Bibliography

- J.F. Ainslie. Calculating the flowfield in the wake of wind turbines. *J. Wind Eng. Ind. Aerodyn.*, 27(1):213 – 224, 1988.
- DB Barrie and DB Kirk-Davidoff. Weather response to a large wind turbine array. *Atmos. Chem. Phys.*, 10(2):769–775, 2010.
- S. E. Belcher, N. Jerram, and J. C. R. Hunt. Adjustment of a turbulent boundary layer to a canopy of roughness elements. *J. Fluid Mech.*, 488:369–398, 7 2003.
- V. S. Bokharaie, P. Bauweraerts, and J. Meyers. Wind-farm layout optimisation using a hybrid Jensen's approach. *Wind Energy Science Discussions*, 2016:1–23, 2016.
- Raúl Bayoán Cal, José Lebrón, Luciano Castillo, Hyung Suk Kang, and Charles Meneveau. Experimental study of the horizontally averaged flow structure in a model wind-turbine array boundary layer. *Journal of Renewable and Sustainable Energy*, 2(1), 2010.
- M. Calaf, C. Meneveau, and J. Meyers. Large eddy simulation study of fully developed wind-turbine array boundary layers. *Phys. Fluids*, 22(015110):1–16, 2010.
- Sten Frandsen. On the wind speed reduction in the center of large clusters of wind turbines. *J. Wind Eng. Ind. Aerodyn.*, 39(1):251 – 265, 1992.
- Sten Frandsen, Rebecca Barthelmie, Sara Pryor, Ole Rathmann, Søren Larsen, Jørgen Højstrup, and Morten Thøgersen. Analytical modelling of wind speed deficit in large offshore wind farms. *Wind Energy*, 9:39–53, 2006.
- N.O. Jensen. *A note on wind generator interaction*, pages 1—16. Risø-M; No.2411, 1983. ISBN 87-550-0971-9.
- I Katic, J Højstrup, and Niels Otto Jensen. A simple model for cluster efficiency. In *European Wind Energy Association Conference and Exhibition*, pages 407–410, 1986.

Bibliography

- D.W. Keith, J.F. DeCarolis, D.C. Denkenberger, D.H. Lenschow, S.L. Malyshev, S. Pacala, and P.J. Rasch. The influence of large-scale wind power on global climate. *Proc. Natl. Acad. Sci. USA*, 101(46):16115–16120, 2004.
- D. B. Kirk-Davidoff and D. W. Keith. On the climate impact of surface roughness anomalies. *J. Atmos. Sci.*, 65:2215–2234, 2008.
- Gunner C. Larsen, Helge Aa. Madsen, Kenneth Thomsen, and Torben J. Larsen. Wake meandering: a pragmatic approach. *Wind Energy*, 11(4):377–395, 2008.
- Charles Meneveau. The top-down model of wind farm boundary layers and its applications. *J. Turbul.*, 13:N7, 2012.
- J. Meyers and C. Meneveau. Large eddy simulations of large wind-turbine arrays in the atmospheric boundary layer. *48th AIAA Aerospace Sciences Meeting Including the New Horizons Forum and Aerospace Exposition*, 4-7 January 2010.
- M. R. Raupach and R. H. Shaw. Averaging procedures for flow within vegetation canopies. *Boundary-Layer Meteorol.*, 22(1):79–90, 1982.
- PB S. Lissaman. Energy effectiveness of arbitrary arrays of wind turbines. *J. Energy*, 3(6): 323–328, 1979.
- Richard J. A. M. Stevens, Dennice F. Gayme, and Charles Meneveau. Coupled wake boundary layer model of wind-farms. *J. Renewable Sustainable Energy*, 7(2), 2015.
- Chien Wang and Ronald G Prinn. Potential climatic impacts and reliability of very large-scale wind farms. *Atmos. Chem. and Phys.*, 10(4):2053–2061, 2010.
- Yu-Ting Wu and Fernando Porté-Agel. Simulation of Turbulent Flow Inside and Above Wind Farms: Model Validation and Layout Effects. *Boundary-Layer Meteorol.*, 146(2):181–205, 2013.
- Xiaolei Yang, Seokkoo Kang, and Fotis Sotiropoulos. Computational study and modeling of turbine spacing effects in infinite aligned wind farms. *Phys. Fluids*, 24(11), 2012.

Part II

4 Large-eddy simulation of drifting and blowing snow

An edited version of this chapter has been submitted for publication to the journal *The Cryosphere*.

Sharma, V., Comola, F., Lehning, M., On the suitability of the Thorpe-Mason model for calculating sublimation of saltating snow, Submitted

4.1 Introduction

A detailed description of the LES model for simulating sublimation of drifting and blowing snow is provided in this chapter. The Navier-Stokes equations are solved in the Eulerian frame of reference along with advection-diffusion equations for temperature and specific humidity that include the source/sink terms to account for the interaction of the flow with the particles. The lower boundary of the flow consists of an erodible snow surface that acts as a source of lagrangian particles that enter the flow due to aerodynamic, rebound and splash entrainment. The entrainment mechanisms are modelled using stochastic parametrizations derived from theory and implemented in the LES model. The particles' motion is solved using Newton's equations of motion in the lagrangian frame of reference. Two models for sublimation of ice grains are implemented with one being the classic Thorpe and Mason Model (1966) while the other is the heat and mass balance equations of individual ice grains.

4.2 Flow equations

The large-eddy simulation (LES) technique solves three-dimensional filtered Navier-Stokes (N-S) equations in rotational form for an incompressible flow in hydrostatic equilibrium along with the continuity equation. Advection-diffusion equations for temperature and specific

humidity are solved and resulting buoyancy forces are added to the N-S equations using the Boussinesq approximation. The equations solved (presented using Einstein's convention) are as follows.

$$\partial_t \tilde{u}_i + \tilde{u}_j (\partial_j \tilde{u}_i - \partial_i \tilde{u}_j) = -\frac{1}{\rho_f} \partial_i \widetilde{p_\infty} \delta_{i,1} - \frac{1}{\rho_f} \partial_i \widetilde{p^*} - \partial_j \tilde{\tau}_{ij} + g \left(\frac{\tilde{\theta}_v - \langle \tilde{\theta}_v \rangle}{\langle \tilde{\theta}_v \rangle} \right) \delta_{i,3} + \frac{1}{\rho_f} S_i^m, \quad (4.1)$$

$$\partial_i \tilde{u}_i = 0, \quad (4.2)$$

$$\partial_t \tilde{\theta} + \tilde{u}_j \partial_j \tilde{\theta} = -\partial_j \tilde{\pi}_j + \frac{1}{\rho_f c_{p,f}} (S^h), \quad (4.3)$$

$$\partial_t \tilde{q} + \tilde{u}_j \partial_j \tilde{q} = -\partial_j \tilde{\Omega}_j + S^q, \quad (4.4)$$

$$\tilde{\theta}_v = \tilde{\theta} (1 + 0.61 \tilde{q}). \quad (4.5)$$

In the above equations, u_i are the three velocity components, θ and θ_v are the potential and virtual potential temperature respectively and q is the specific humidity. The overhead tildes ($\tilde{}$) represent quantities filtered via spectral cutoff while the brackets ($\langle \rangle$) represent horizontal averaging. Note that in this study, since we are simulating the atmospheric surface layer, temperature and potential temperature are considered to be the same. The modified pressure term \tilde{p}^* consists of static pressure (p), filtered kinetic energy ($0.5 \tilde{u}_i \tilde{u}_i$) and the trace of the subgrid-scale tensor ($\tau_{kk}/3$). The first term on the R.H.S of Equation 1 is the large-scale pressure gradient that is imposed to drive the simulation. Terms $\tilde{\tau}$, $\tilde{\pi}$, $\tilde{\Omega}$ represent the subgrid-scale (SGS) fluxes for momentum, heat and specific humidity respectively. The source/sink terms S_i^m , S^h and S^q are included to incorporate the effect of sublimating particles being transported by the wind on the flow dynamics and thermodynamics. Particles exert drag on the flow and exchange heat and mass due to sublimation/deposition. In accordance with the incompressible assumption, we consider the density of the fluid ρ_f to remain constant. The specific heat capacity of air $c_{p,f}$ is considered to be constant irrespective of the value of specific humidity.

4.2.1 SGS model

The deviatoric part of the SGS flux tensor for momentum is computed using a dynamic Smagorinsky-type model, while the scalar SGS fluxes are related to the momentum fluxes using fixed turbulent Prandtl (Pr) and Schmidt (Sc) numbers. The equations used for SGS fluxes are

$$\tau_{ij} = -2\nu_T \widetilde{S}_{ij} = -2c_s^2 \Delta^2 |\widetilde{S}| \widetilde{S}_{ij}, \quad (4.6)$$

$$\pi_j = -\frac{\nu_T}{Pr} \partial_j \tilde{\theta}, \quad (4.7)$$

$$\Omega_j = -\frac{\nu_T}{Sc} \partial_j \tilde{q}, \quad (4.8)$$

where, ν_t is the turbulent viscosity of air which is parametrized using a *Smagorinsky-type eddy-viscosity* approach. In this approach, ν_T is considered to be equal to the product of a length scale $c_s \Delta$ times a velocity scale $c_s \Delta |\widetilde{S}_{ij}|$. \widetilde{S}_{ij} is symmetric part of the strain rate tensor and $|\widetilde{S}_{ij}| = \sqrt{2 \widetilde{S}_{ij} \widetilde{S}_{ij}}$ is the Galilean invariant estimate of \widetilde{S}_{ij} . The Smagorinsky coefficient, c_s is estimated dynamically using resolved velocity values through applying the Germano identity along trajectories of lagrangian fluid particles. This approach, known as the *Lagrangian Scale-Dependent Dynamic Smagorinsky (LASD)* SGS model was developed by Bou-Zeid et al. [2005], where detailed derivations and applications for LES can be found.

4.2.2 Lower-boundary condition for Eulerian quantities

For the surface boundary conditions for velocity, a non-slip condition is imposed for the vertical velocity and for the horizontal components of the momentum equation an equivalent shear stress is imposed using the log-law with correction for the presence of particles between the surface and the first grid point based on Shao and Li [1999],

$$\tau_{i,3}(x, y, z_1) = \left[\frac{\sqrt{(\widehat{u}_1^2 + \widehat{u}_2^2)}}{\ln(z_1/z_0)} \right]^2 \mathbf{n}_i + \frac{1}{\rho_f} S_i^m(x, y, z_1) z_1, \quad (4.9)$$

where i represents the direction in the plane parallel to the surface ($i = 1, 2$), and \mathbf{n}_i is a unitary directional vector defined as: $\mathbf{n}_i = \widehat{u}_i / \sqrt{\widehat{u}_1^2 + \widehat{u}_2^2}$. The shear stress is imposed at $z_1 = \Delta z / 2$. Recall that $(1/\rho_f) S_i^m$ is the sink of momentum due to drag forces from the flow-particle interaction. In the case with no particles, the stress term reconciles with the standard log law whereas in the presence of the particles, the stress at the surface decreases (S_i^m is negative). The $(\widehat{\quad})$ operator represents a double filtering operation (at 2Δ grid spacing) on horizontal components of the flow, which is equivalent to a local average. The surface roughness is constant over the entire numerical domain and has a value of $z_0 = 10^{-5} m$. For the numerical integration of the momentum equation, the vertical derivatives of the horizontal velocity components are also needed. These are parametrised at the first grid point also using Monin-Obukhov similarity theory,

$$\partial_3 \widetilde{u}_i(x, y, z_1) = \left(\frac{\sqrt{\tau_{i,3}}}{\kappa z_1} \right) \mathbf{n}_i, \quad (4.10)$$

with $\tau = \sqrt{\tau_{1,3}^2 + \tau_{2,3}^2}$ and κ is the von Karman constant = 0.4. The kinematic sensible $(\overline{w'\theta'})$ and latent $(\overline{w'q'})$ heat fluxes are zero.

4.3 Surface-flow coupling

Ice grains lying on the surface enter into the overlying, usually turbulent fluid through mechanisms of aerodynamic, rebound and splash entrainment from the surface. These mechanisms and the accompanying models used in this work are described in detail in the following para-

graphs. There are some common elements in these models. All particles are assumed to enter the flow at a height of $h_{init} = 4 \langle d_p \rangle$ above the surface. Each of these models provides the number of particles per unit area that enter into the flow, along with the initial conditions for both velocity magnitude and direction for the lagrangian particle.

4.3.1 Aerodynamic entrainment

Initiation of aeolian transport of particles occurs due to entrainment of particles by the fluid when the stress at the surface $\tau_{f,surface}$ increases above a threshold value ($\tau_{threshold}$) and particles from the surface are dislodged to relieve stress at the surface. Bagnold [1941] derived an expression for the threshold stress as

$$\tau_{threshold} = A^2 g \langle d_p \rangle (\rho_p - \rho_f) \quad (4.11)$$

where g is the acceleration due to gravity, $\langle d_p \rangle$ is the mean particle diameter of all particles present on the surface, ρ_p and ρ_f are the density of the particles and the fluid respectively. The coefficient A is an empirical parameter taken to be equal to 0.2 based on wind tunnel experiments of drifting and blowing snow by Clifton et al. [2006].

From each computational grid point on the surface, the number of particles entering the fluid due to aerodynamic entrainment at each time-step can then be computed using the expression of Anderson and Haff [1991] as

$$N_{ae} = \frac{C_e}{8\pi \langle d_p \rangle^2} (\tau_{f,surface} - \tau_{threshold}) \Delta x \Delta y \Delta t, \quad (4.12)$$

where C_e is an empirically derived constant of proportionality (equal to 1.5, according to Doorschot and Lehning [2002], Groot Zwaafink et al. [2014] and Δx and Δy are the grid step sizes in the streamwise and cross-stream directions respectively and Δt is the simulation time-step. Once the number of particles has been calculated, for each particle entrained into the flow, the diameter is sampled from the log-normal distribution of the particle size distribution (characterized by the $\langle d_p \rangle$ and σ_{d_p}). The particle is initialized at height h_{init} and provided with an initial velocity magnitude sampled from a log-normal distribution characterized by mean velocity of $3.5u_*$ and a standard deviation of $2.5u_*$. The ejection angle is sampled from a lognormal distribution with a mean angle as a function of mean particle diameter as follows,

$$\langle \alpha_{ae,ejection} \rangle = 75 - 55 \left(1 - \exp \frac{-\langle d_p \rangle}{175 \times 10^{-6}} \right). \quad (4.13)$$

Thus, at any given time-step, based on the stress at the wall, the number of particles entering the fluid along with the initial position and velocity can be simulated.

4.3.2 Rebound and splash entrainment

A particle, once entrained within the turbulent fluid, may impact the bed upon which it may rebound back into the fluid (known as *rebound* entrainment) as well as dislodge particles present in the bed that get entrained into the fluid as well (known as *splash* entrainment).

Consider a particle with diameter d_i that impacts the bed with velocity magnitude v_i at a vertical impact angle of α_i . The probability that the particle shall rebound following impact (P_r) is given by Anderson and Haff [1991]

$$P_r = P_m (1 - e^{-\gamma v_i}) \quad (4.14)$$

where P_m is the maximum probability that is assumed to be equal to 0.9 for snow [Groot Zwaafink et al., 2011] and γ is a empirical coefficient equal to 2 according to Anderson and Haff [1991]. Once the particle rebounds, its velocity must be re-initialized. The rebound velocity magnitude v_r is taken to be half of v_i . The vertical rebound angle (α_r) is sampled from an exponential distribution of mean angle equal to 45° following [Kok and Renno, 2009]. The particle is assumed to remain in the same vertical plane before and after the collision for simplicity.

As mentioned earlier, the impacting particle may break inter-particle bonds present in the snowbed and dislodge additional additional particles into the overlying turbulent flow. The number of particles dislodged $N_{splash} = \min(N_E, N_M)$, where,

$$N_E = \frac{(1 - P_r \epsilon_r - \epsilon_f) d_i^3 v_i^2}{2 \langle v \rangle^2 \left(\langle d \rangle + \frac{\sigma_d^2}{\langle d \rangle} \right)^3 \left(1 + r_E \sqrt{5 \left[1 + \left(\frac{\sigma_d}{\langle d \rangle} \right)^2 \right]^9 - 5} \right) + 2\phi}, \quad (4.15)$$

$$N_M = \frac{(1 - P_r \mu_r - \mu_f) d_i^3 v_i \cos \alpha_i}{\langle v \rangle \left(\langle d \rangle + \frac{\sigma_d^2}{\langle d \rangle} \right)^3 \left(\langle \cos \alpha \rangle \langle \cos \beta \rangle + r_M \sqrt{\left[1 + \left(\frac{\sigma_d}{\langle d \rangle} \right)^2 \right]^9 - 1} \right)} \quad (4.16)$$

In the above equations, P_r is the probability of rebound of the impacting grain, calculated using Equation (4.14); ϵ_f and ϵ_r are the fractions of impact energy lost to the bed due to friction and that retained by the rebounding particle respectively. The corresponding fractions of impact momentum are denoted as μ_f and μ_r respectively. The mean and standard deviation of the ejecta's diameter are represented by $\langle d \rangle$ and σ_d . $\langle v \rangle$ is the mean velocity of the ejecta with α and β being the vertical and horizontal ejection angles of ejected particles. Cohesion of the snow bed is represented by ϕ . Correlation coefficient between the ejected mass m and velocity v^2 is r_E while r_M is the corresponding correlation coefficient between m and v .

The splashed particles are initialized at a height similar to the aerodynamically entrained particles at the height of h_{init} . The initial velocity magnitude is assumed to follow an exponential distribution with a mean value of $0.25 v_i^{0.3}$. The vertical entrainment angle α is chosen as a random number that is drawn from an exponential distribution with a mean value of 50° . The horizontal splash angle β_n is sampled from a Gaussian distribution with a mean value of the

horizontal angle of the impacting particle and a standard deviation of 15° .

Models for splash entrainment are derived by Comola and Lehning [2017] and similar models have previously been implemented by Groot Zwaafink et al. [2014]. Additional references can be found in these works.

4.4 Dynamics of particles in flow

Once the ice grain is entrained within the turbulent flow, its fate is determined by solving the equations of motion. The only forces we included in our calculations are drag forces and gravity. The drag forces are computed by considering the ice grains to be spherical and use well-known bulk parametrizations of drag on a sphere in a turbulent flow [Clift et al., 1978]. The equations for motion are as follows

$$\frac{d u_{p,i}}{d t} = \left(1 + 0.15 Re_p^{0.687}\right) \frac{1}{t_p} (\tilde{u}_i + u_{sgs,i} - u_{p,i}) - g \delta_{i,3} , \quad (4.17)$$

$$t_p = \rho_p d_p^2 / 18 \rho_f \nu_a , \quad (4.18)$$

where, $u_{p,i}$ are the velocity components of the particle, \tilde{u}_i is the filtered velocity solved in Equation 4.1, Re_p is the particle Reynolds number (defined later), ν_a is the kinematic viscosity of air and $u_{sgs,i}$ is the SGS fluid velocity computed along the path of the particle's motion. We use the equation for SGS velocities from Weil et al. [2004] as follow,

$$d u_{sgs,i} = -f \frac{u_{sgs,i}}{T_f} dt + \frac{1}{2} \left(\frac{1}{\sigma^2} \frac{d\sigma^2}{dt} u_{sgs,i} + \frac{\partial \sigma^2}{\partial x_i} \right) dt + \left(f \frac{2\sigma^2}{T_f} \right)^{1/2} d\xi_i , \quad (4.19)$$

where $\sigma^2 = 2e/3$ is the variance of the SGS velocity, which is directly proportional to the SGS turbulence kinetic energy (TKE) e . The fraction of TKE present in subgrid scales is represented by f . $d\xi_i$ is a normally distributed random number with zero mean and a variance of dt . The velocity autocorrelation timescale ($T_f = 2\sigma^2/C_o e$) is used to consider the effect of heavy particles as opposed to purely lagrangian particles without inertia.

The mass exchange between the ice grain and the surrounding fluid is driven by the difference between the vapour density at the surface of the particle (which is considered to be saturated) and the vapour density in the fluid at the particle location. We assume that the total density of the fluid ρ_f is constant and thus can directly write the mass balance equation as a function of specific humidity as follows

$$\begin{aligned} \frac{dm_p}{dt} &= \pi \mathcal{D} d_p \rho_f (\tilde{q} - q_{p,surface}) Sh, \\ q_{p,surface} &= \frac{M_W}{R_u T_p \rho_f} e_{s,a} \exp \left[\frac{L_s M_w}{R_u} \left(\frac{1}{T_f} - \frac{1}{T_p} \right) \right], \\ e_{s,a}(T_f) &= 611.15 \exp \left[\left(23.036 - \frac{T_f - 273.15}{333.7} \right) \left(\frac{T_f - 273.15}{6.67 + T_f} \right) \right]. \end{aligned} \quad (4.20)$$

In above equation, m_p is the mass of the particle, \mathcal{D} is the diffusion coefficient of vapour in air, \tilde{q} is the filtered specific humidity computed using Equation (4.4), Sh is the Sherwood number (described later) and $q_{p,surface}$ is the specific humidity at the surface, which is computed using the ideal gas law and the Clausius-Clayperon equation, integrated between the particle surface and the mass-boundary layer. M_W is the molecular weight of water, R_u is the universal gas constant and L_s is the latent heat of sublimation. The saturation vapour pressure with respect to ice, $e_{s,a}$ is computed using the Arden-Buck equation for ice.

The temperature of the particle evolves according to a balance between the latent heat due to mass exchange and the convective heat transfer between the ice grain and the surrounding fluid and can be expressed as,

$$c_i m_p \frac{dT_p}{dt} = L_s \frac{dm_p}{dt} + \pi \mathcal{K} d_p (\tilde{\theta} - T_p) \mathcal{N}u, \quad (4.21)$$

where c_i is the specific heat capacity of ice, \mathcal{K} is the thermal conductivity of the air, $\tilde{\theta}$ is the filtered potential temperature obtained by solving Equation (4.3) and $\mathcal{N}u$ is the Nusselt number.

The effect of turbulence on momentum, heat and mass transfer is neatly encompassed in three non-dimensional parameters, namely the Reynolds, Nusselt and Sherwood numbers respectively. We use the following expressions to calculate these numbers.

$$Re_p = \frac{d |\tilde{u}_{rel}|}{\nu_{air}}, \quad (4.22)$$

$$\mathcal{N}u = 1.79 + 0.606 Re_p^{1/2} Pr^{1/3}, \quad (4.23)$$

$$Sh = 1.79 + 0.606 Re_p^{1/2} Sc^{1/3}, \quad (4.24)$$

The coupling between the particles and the flow occurs through the source/sink terms in equations for momentum (Equation 4.1, S_m), temperature (Equation 4.3, S^h) and specific humidity (Equation 4.4, S^q). Consider a particle lying at a point within in the fluid. The eight closest points of the LES discretized grid shall necessarily form a cube considering that we use a structured Cartesian grid. The point force due to drag upon the particle is simply extrapolated onto these eight points using inverse distance weighting. The total force at any LES grid point is a summation of all such extrapolated forces. If an LES grid point has N_p particles contributing to the total force at it's location, the source/sink terms can be simply

represented as

$$\begin{aligned}
 S_i^m &= - \sum_{\beta=1}^{N_p} \frac{w_\beta}{\Delta V} \left(m_p \frac{du_{p,i}}{dt} + \frac{dm_p}{dt} u_{p,i} \right)_\beta , \\
 S^h &= - \sum_{\beta=1}^{N_p} \frac{w_\beta}{\Delta V} (\pi \mathcal{K} d_p (\tilde{\theta} - T_p) \mathcal{N} u)_\beta , \\
 S^q &= - \sum_{\beta=1}^{N_p} \frac{w_\beta}{\Delta V} \frac{1}{\rho_f} \left(\frac{dm_p}{dt} \right)_\beta .
 \end{aligned} \tag{4.25}$$

In the above equation, w_β is the weight for the extrapolation operation computed using inverse distance weighting.

4.5 Numerics

The flow equations (Equations 4.1, 4.3 and 4.4) are solved in the Eulerian frame of reference using a pseudo-spectral collocation method in the same fashion as that introduced by Moeng [1984] and Albertson and Parlange [1999]. In this approach, the horizontal gradient operations are computed using fourier methods while vertical gradients are computed using second order finite differences. Because of the fourier based methods in both horizontal directions, the domain is fully periodic and no lateral boundary conditions are needed, and hence, the domain size tends to infinity in practical effects. The use of fourier methods is quite useful for SGS modelling is because allows the direct use of spectral cut-off for filtering the flow quantities. The horizontal grid is uniform with equal discretizations in the both the streamwise and cross-stream directions. In the vertical direction we use hyperbolic tangent function based grid stretching. This to insure that there are sufficient grid points within the saltation region. Incompressibility is enforced through a prediction-correction approach where the velocity is marched in time and the poisson equation is used to solve for the dynamic pressure field. To maintain proper consistency in numerics for solving the poisson equation, the vertical grid is staggered to ensure second-order accuracy.

Integration in time is done using a second-order Adams-Bashforth scheme. In addition, the non-linear convective terms are dealised with the 3/2 rule [Canuto et al., 1988]. The code is fully parallelised using Message Passing Interface (MPI), and the FFTW library [Frigo and Johnson, 2005] is employed for the Fourier transforms. The pressure solver is based on the pipeline Thomas algorithm [Povitsky and Morris, 2000] and is used to enforce incompressibility implied by Equation 2.

The equation of motion for particles (Equation 4.17) along with equations for heat and mass budgets (Equation 4.20 and 4.21) are solved using a simple first-order time stepping using forward Euler method. At each timestep, information from the Eulerian LES grid is translated to locations of the lagrangian particles using simple linear interpolation. The source/sink terms due to the flow-particle coupling are translated back to the Eulerian frame of reference using linear extrapolation as described in Equation 4.25.

All simulations in this study are driven by an imposed large-scale pressure gradient $\mathcal{P} = -(1/\rho_f)\partial\widetilde{p}_\infty/\partial x$ in the streamwise direction. This quantity is kept constant throughout the simulation. Upon choosing values of the surface friction velocity u_* , the imposed pressure gradient can be computed as $\mathcal{P} = u_*^2/L_z$, where L_z is the vertical extent of the computational domain.

4.6 Conclusions

This chapter is a comprehensive description of the LES code used for simulations of drifting and blowing snow. It includes all the details of the fluid solver, the stochastic models used to parametrize the entrainment processes at the erodible snow surface as well the equations of particle dynamics, including thermodynamics. The LES model presented in this chapter is used the following chapter to investigate sublimation of saltating snow grains.

Bibliography

- J.D. Albertson and M.B. Parlange. Natural integration of scalar fluxes from complex terrain. *Water Resour. Res.*, 23:239–252, 1999.
- RS Anderson and PK Haff. Wind modification and bed response during saltation of sand in air. In *Aeolian Grain Transport 1*, pages 21–51. Springer, 1991.
- Ralph Alger Bagnold. *The physics of blown sand and desert dunes*. New York: Methuen, 1941.
- Elie Bou-Zeid, Charles Meneveau, and Marc Parlange. A scale-dependent lagrangian dynamic model for large eddy simulation of complex turbulent flows. *Physics of Fluids*, 17(2):025105, 2005. doi: 10.1063/1.1839152. URL <http://dx.doi.org/10.1063/1.1839152>.
- C. Canuto, M.Y. Hussaini, A. Quarteroni, and T.A. Zang. *Spectral Methods in Fluid Dynamics*. Springer-Verlag, Berlin, 1988.
- R Clift, JR Grace, ME Weber, and Drops Bubbles. Particles. *Academic, New York*, pages 171–202, 1978.
- Andrew Clifton, Jean-Daniel Rüedi, and Michael Lehning. Snow saltation threshold measurements in a drifting-snow wind tunnel. *Journal of Glaciology*, 52(179):585–596, 2006.
- Francesco Comola and Michael Lehning. Energy- and momentum-conserving model of splash entrainment in sand and snow saltation. *Geophysical Research Letters*, 44(3):1601–1609, 2017. ISSN 1944-8007. doi: 10.1002/2016GL071822. URL <http://dx.doi.org/10.1002/2016GL071822>. 2016GL071822.
- Judith J. J. Doorschot and Michael Lehning. Equilibrium saltation: Mass fluxes, aerodynamic entrainment, and dependence on grain properties. *Boundary-Layer Meteorology*, 104(1): 111–130, Jul 2002. ISSN 1573-1472. doi: 10.1023/A:1015516420286. URL <https://doi.org/10.1023/A:1015516420286>.
- M. Frigo and S.G. Johnson. The design and implementation of fftw3. *Proceedings of the IEEE*, 93(2):216–231, 2005.

Bibliography

- C. D. Groot Zwaaftink, H. Löwe, R. Mott, M. Bavay, and M. Lehning. Drifting snow sublimation: A high-resolution 3-d model with temperature and moisture feedbacks. *Journal of Geophysical Research: Atmospheres*, 116(D16):n/a–n/a, 2011. ISSN 2156-2202. doi: 10.1029/2011JD015754. URL <http://dx.doi.org/10.1029/2011JD015754>. D16107.
- C. D. Groot Zwaaftink, M. Diebold, S. Horender, J. Overney, G. Lieberherr, M. B. Parlange, and M. Lehning. Modelling small-scale drifting snow with a lagrangian stochastic model based on large-eddy simulations. *Boundary-Layer Meteorology*, 153(1):117–139, Oct 2014. ISSN 1573-1472. doi: 10.1007/s10546-014-9934-2. URL <https://doi.org/10.1007/s10546-014-9934-2>.
- Jasper F. Kok and Nilton O. Renno. A comprehensive numerical model of steady state saltation (comsalt). *Journal of Geophysical Research: Atmospheres*, 114(D17):n/a–n/a, 2009. ISSN 2156-2202. doi: 10.1029/2009JD011702. URL <http://dx.doi.org/10.1029/2009JD011702>. D17204.
- C. H. Moeng. A large-eddy simulation model for the study of planetary boundary-layer turbulence. *J. Atmos. Sci.*, 41(2052), 1984.
- A. Povitsky and P. J. Morris. A higher-order compact method in space and time based on parallel implementation of the thomas algorithm. *J. Comput. Phys.*, 161(1):182–203, 2000.
- Yaping Shao and An Li. Numerical modelling of saltation in the atmospheric surface layer. *Boundary-Layer Meteorology*, 91(2):199–225, May 1999. ISSN 1573-1472. doi: 10.1023/A:1001816013475. URL <https://doi.org/10.1023/A:1001816013475>.
- Jeffrey C. Weil, Peter P. Sullivan, and Chin-Hoh Moeng. The use of large-eddy simulations in lagrangian particle dispersion models. *Journal of the Atmospheric Sciences*, 61(23):2877–2887, 2004. doi: 10.1175/JAS-3302.1. URL <https://doi.org/10.1175/JAS-3302.1>.

5 On the suitability of the Thorpe-Mason model for calculating sublimation of saltating snow

An edited version of this chapter has been submitted for publication to the journal *The Cryosphere*.

Sharma, V., Comola, F., Lehning, M., On the suitability of the Thorpe-Mason model for calculating sublimation of saltating snow, Submitted

V.S developed the numerical model, implemented it in the LES code, took part in the research design, performed simulations, analyzed the data and contributed to the writing of the paper

5.1 Introduction

Sublimation of drifting and blowing snow has been recognized as an important component of the mass budget of polar and alpine regions [Liston and Sturm, 2004, van den Broeke et al., 2006, Lenaerts et al., 2012, Vionnet et al., 2014]. Field observations and modelling efforts focused on Antarctica have highlighted the fact that precipitation and sublimation losses are the dominant terms of the mass budget in the katabatic flow region as well as the coastal plains [van den Broeke et al., 2006]. Even though precipitation is challenging to measure accurately, methods to measure it exist, for example, using radar [Grazioli et al., 2017] or snow depth change [Vögeli et al., 2016]. In comparison, sublimation losses are even harder to measure and can only be calculated implicitly; using measurements of wind speed, temperature and humidity. Thus, in regions where sublimation loss is a dominant term of the mass balance, it is also a major source of error. This error ultimately results in errors in the mass accumulation of ice on Antarctica, which is a crucial quantity for understanding sea-level rise and climate change [Rémy and Frezzotti, 2006, Rignot et al., 2011, Lenaerts et al., 2012].

Chapter 5. On the suitability of the Thorpe-Mason model for calculating sublimation of saltating snow

Aeolian transport of snow can be classified into two modes, namely, saltation and suspension. Saltation consists of particles being transported along the surface via short, ballistic trajectories with heights less than 10 cm and involves mechanisms of aerodynamic entrainment along with rebound and splashing of ice grains [Doorschot and Lehning, 2002, Comola and Lehning, 2017]. Suspension on the other hand refers to transport of small ice grains at higher elevations and over large distances without contact with the surface. Current calculations of sublimation losses are largely restricted to losses from ice grains in suspension. This is true for both field studies, where sublimation losses are calculated using measurements, usually at the height of $\mathcal{O}(1\text{ m})$, and in mesoscale modelling studies, where the computational grids and time-steps are too large to resolve flow dynamics at saltation length and time scales. Mass loss in the saltation layer is hard to measure and is neglected based on the justification that the saltation layer is saturated. However, recent studies using high-resolution large-eddy simulations [Dai and Huang, 2014] show that sublimation losses in the saltation layer are not negligible, particularly for wind speeds close to the threshold velocities for aeolian transport, wherein a majority of aeolian snow transport occurs via saltation rather than suspension.

The coupled heat and mass balance equations of a single ice particle immersed in turbulent flow are

$$c_i m_p \frac{dT_p}{dt} = L_s \frac{dm_p}{dt} + \pi \mathcal{K} d_p (T_{a,\infty} - T_p) \mathcal{N}u, \quad (5.1)$$

$$\frac{dm_p}{dt} = \pi \mathcal{D} d_p (\rho_{w,\infty} - \rho_{w,p}) Sh, \quad (5.2)$$

where, m_p , T_p and d_p are the mass, temperature and diameter of the particle respectively that vary with time, c_i is the specific heat capacity of ice, L_s is the latent heat of sublimation, \mathcal{K} is the thermal conductivity of moist air and \mathcal{D} is the mass diffusivity of water vapor in air. Transfer of heat and mass is driven by differences of temperature and vapor density between the particle surface ($T_p, \rho_{w,p}$) and the surrounding fluid ($T_{a,\infty}, \rho_{w,\infty}$) and enhanced by turbulence, the effect of which is parametrized by the Nusselt ($\mathcal{N}u$) and Sherwood (Sh) numbers respectively. $\mathcal{N}u$ and Sh are related to the relative speed ($|\vec{u}_{rel}|$) between the air and the particle via the particle Reynolds number (Re_p) as

$$Re_p = \frac{d|\vec{u}_{rel}|}{\nu_{air}}; \mathcal{N}u = 1.79 + 0.606 Re_p^{1/2} Pr^{1/3}; Sh = 1.79 + 0.606 Re_p^{1/2} Sc^{1/3}, \quad (5.3)$$

where ν_{air} is the kinematic viscosity of air and Pr and Sc are the Prandtl and Schmidt numbers respectively.

Thorpe and Mason [1966] solved the above coupled equations (5.1) and (5.2) by, (a) neglecting the thermal inertia of the ice particle, thus effectively stating that all the heat necessary for sublimation is supplied by the air, and (b) considering the temperature difference between the particle and surrounding air to be *small*, thereby allowing for Taylor series expansion of the Clausius-Clapeyron Equation and neglecting higher-order terms, resulting in their

formulation for the mass loss term as,

$$\frac{dm_p}{dt} = \pi d_p (\sigma_* - 1) / \left(\frac{L_s}{\mathcal{K} T_{a,\infty} \mathcal{N}u} \left(\frac{L_s M}{R T_{a,\infty}} - 1 \right) + \frac{1}{\mathcal{D} \rho_s(T_{a,\infty}) Sh} \right), \quad (5.4)$$

where $\rho_s(T_{a,\infty})$ is the saturation vapor density of air surrounding the particle, saturation $\sigma_* = \rho_{w,\infty} / \rho_s(T_{a,\infty})$, M is the molecular weight of water and R is the universal gas constant. The above formulation has been used extensively to analyse data collected in the field [Mann et al., 2000], wind tunnel experiments [Wever et al., 2009], and numerical simulations of drifting and blowing snow [D ery and Yau, 2002, Groot Zwaaftink et al., 2011, 2014, Vionnet et al., 2014]. In the modelling studies, the mass loss term is computed using Equation 5.4 and is added, with proper normalisation, to the advection-diffusion equation of specific humidity while the latent heat of sublimation multiplied by the mass loss term is added to the corresponding equation for temperature [Groot Zwaaftink et al., 2011].

Two observations motivated us to investigate the suitability of the TM model for sublimation of saltating snow particles. Firstly, the TM model assumes that all the energy required for sublimation is supplied by the air. This assumption was tested by Dover [1993] who compared the potential rates of cooling of particles with that of the surrounding air due to sublimation. Using scale analysis, Dover [1993] formulated the quantity $\xi = 6 \rho_{air} c_{p,air} / \pi \rho_i c_i \bar{d}_p^3 N$, where \bar{d}_p is the mean particle diameter, N is the particle number density, ρ_i is the density of ice, and showed that for $\xi \gg 1$, it can be accurately considered that the heat necessary for sublimation comes from the air. For standard values for an ice particle in suspension, $\bar{d}_p = 50 \mu m$ and $N \sim \mathcal{O}(10^6)$, this condition is easily met ($\xi \sim \mathcal{O}(10^3)$). However, if we input values typical for saltation, i.e., $\bar{d}_p = 200 \mu m$ and $N \sim \mathcal{O}(10^8)$, $\xi \sim \mathcal{O}(1)$, and the condition is not met. Thus, for sublimation of saltating particles, it is important to consider the thermal inertia of the particles. A similar conclusion was reached in other modelling studies on topics of heat and mass exchange between disperse particulate matter in turbulent flow such as small water droplets in heat exchangers [Russo et al., 2014] and sea-sprays [Helgans and Richter, 2016].

Secondly, Equation 5.4 computes mass loss as being directly proportional to σ_* and neglects the temperature difference between the particle and air. Equation 5.4 thus predicts a mass loss even in extremely high saturation conditions, whereas immediate deposition of water vapor would occur on a particle even slightly colder than the air. Indeed, some field experiments have reported deposition as opposed to sublimation which was expected, on the basis of the measured under-saturation of the environment, particularly near coastal polar regions [Sturm et al., 2002]. A simple everyday observation illustrates this fact clearly; There is immediate deposition of vapour and formation of small droplets on the surface of a cold bottle of beer even in room conditions with moderate humidity!

Motivated by the observations described above, in this chapter, we describe four numerical experiments where we compare differences between the fully numerical and the Thorpe and Mason [1966] solutions (referred to as NUM and TM approaches respectively). In Experiment I and II, we numerically solve equations (5.1) and (5.2) and compare the results with Equa-

Chapter 5. On the suitability of the Thorpe-Mason model for calculating sublimation of saltating snow

tion (5.4) for physically plausible values of a saltating ice particle. Results of these tests are presented in Sect. 5.2. High-resolution large-eddy simulations (LES) of saltating snow are performed for a range of environmental conditions to compute the differences between the NUM and TM approaches in realistic wind-driven saltating events. These results are presented in Sect. 5.3. A summary of the chapter is made in Sect. 5.4

5.2 Comparison between NUM and TM solutions: EXPERIMENT I and II

We consider an idealised scenario where a spherical ice particle is held still in a turbulent air flow with constant mean speed, temperature and under-saturation. This scenario is similar to the wind-tunnel study performed by Thorpe and Mason [1966] who measured mass loss of solitary ice grains suspended on fine fibres. While it can be expected that the environmental conditions will vary along the trajectory of a ice particle undergoing saltation or suspension, it is nevertheless useful to perform this analysis as it reveals important characteristics of the heat and mass evolution of a ice particle during sublimation and about the TM model.

For the NUM approach, Equations (5.1) and (5.2) are solved using a simple first-order finite-differencing scheme. The initial particle diameter is $200\ \mu\text{m}$ and the air-flow temperature is 263.15K . We use a constant air speed of $5\ \text{m/s}$ resulting in $Re_p = 80$, $Nu = 6.7$ and $Sh = 6.5$ (using Equation 5.3). The values used here are typical of a saltating ice particle. In Experiment I, we study the heat and mass output from a sublimating ice grain as a function of time. In the first case, we consider the effect of three different values of air-flow saturation ($\sigma_* = 0.8, 0.9$ and 0.95) on differences between NUM and TM solutions. In this case, the initial particle temperature is taken to be the same as the air-flow temperature for the NUM approach. Results are shown in Fig. 5.1(a-c), with subfigure (a) showing the mass output rate, F_M and subfigure (b) showing the heat output rate, F_Q . Note that in this figure and subsequent figures, $+(-)$ signifies mass and heat gained (lost) by the air. It can be seen that the NUM solutions decay with time and reconcile with the steady-state TM solutions after a transient regime of about 0.3 sec. In subfigure (c), the errors ($Err(t) = (\int_0^t F_{NUM} dt / \int_0^t F_{TM} dt - 1) * 100$) for mass, Err_M and heat, Err_Q are shown. The errors reduce dramatically with time (for example, 15% at 0.3 seconds) and do not depend on the saturation of the air-flow. In the following case, similar simulations are performed with $\sigma_* = 0.95$ while the initial temperature difference between the particle and the air is varied as $T_p - T_{Air} = -2, -1, 1, 2\ \text{K}$. It is interesting to note that while the TM solution predicts sublimation of the particle (consistent with $\sigma > 0$), for cases with colder particles, the NUM solutions show that there is initially deposition on the particle, along with larger values of heat absorbed from the air. Correspondingly, in the cases with particles being warmer than the air, the mass loss is much higher in the NUM solution than that computed by the TM solution while the heat gain is also much higher. These higher differences are reflected in the Err_M and Err_Q curves in subfigure (f) where errors are found to be an order of magnitude higher than those in subfigure (c).

We define relaxation time ($\tau_{relaxation}$) as the time required for the NUM solution to reconcile

5.2. Comparison between NUM and TM solutions: EXPERIMENT I and II

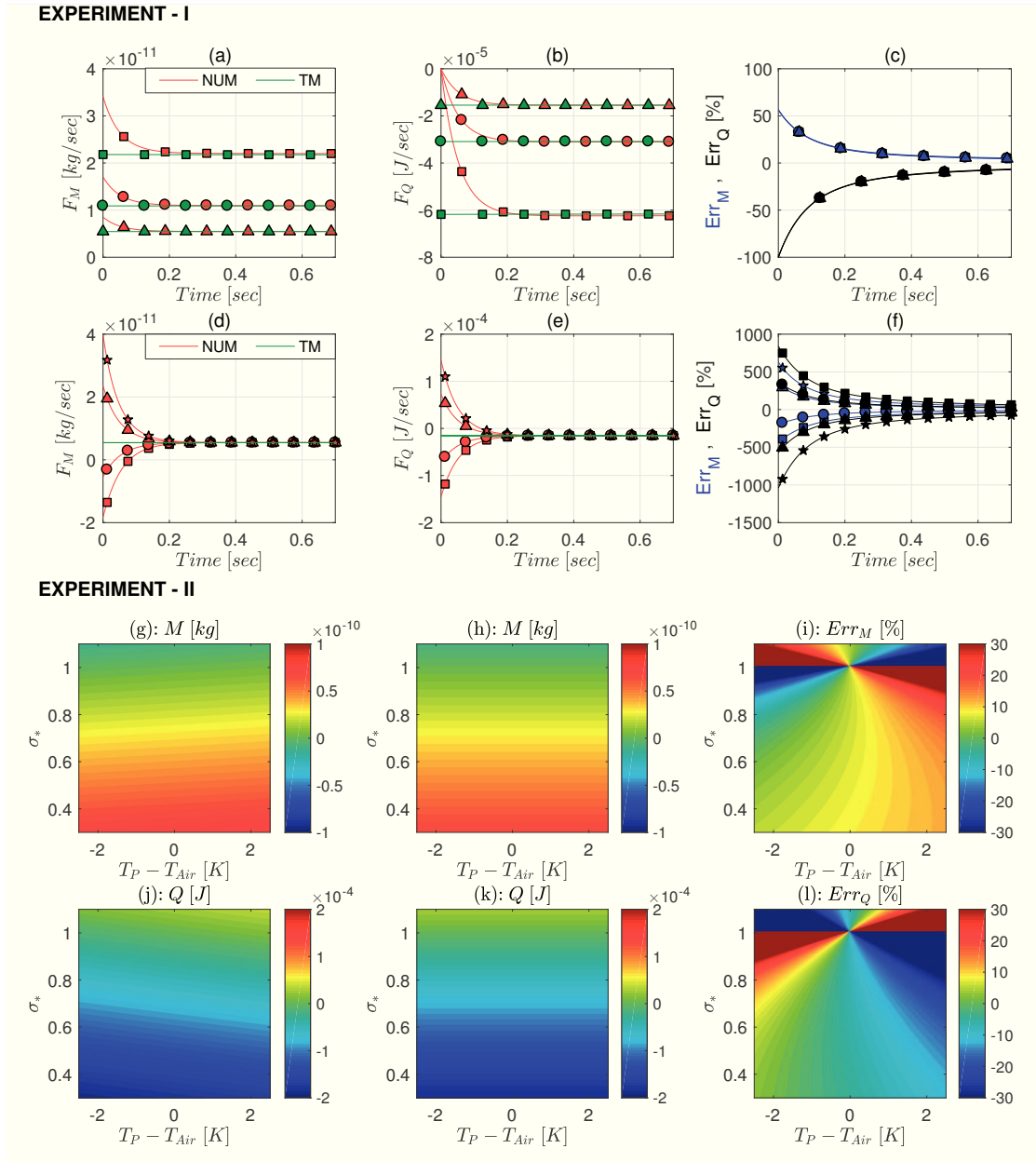


Figure 5.1 – TM and NUM solutions for a particle of $200 \mu m$ diameter in different environmental conditions. **Experiment I:** (a) Rate of mass and (b) heat output with (c) corresponding errors; $T_p - T_{a,\infty} = 0$, $\sigma_* = 0.8$ (squares), 0.9 (circles), 0.95 (triangles). (d-f) same as (a-c) with $\sigma_* = 0.95$; $T_p - T_{a,\infty} = -2K$ (squares), $-1K$ (circles), $1K$ (triangles), $2K$ (stars). **Experiment II:** Total mass output during 0.5 seconds by the (g) NUM and (h) TM solutions with (i) corresponding error for $\{0.3 \leq \sigma_* \leq 1.1, -2.5K \leq T_p - T_{Air} \leq 2.5K\}$. Similar plots for total heat output presented in (j-l).

Chapter 5. On the suitability of the Thorpe-Mason model for calculating sublimation of saltating snow

with the TM solution. The importance of this quantity lies in the fact that if the residence time of a saltating ice grain is shorter than $\tau_{relaxation}$, the TM approach is likely to be erroneous and the NUM approach would be required. It is intuitive that $\tau_{relaxation}$ increases with d_p on account of increasing inertia and decreases with $|\vec{u}_{rel}|$ due to more vigorous heat and mass transfer. Experiment I was repeated for values of d_p and $|\vec{u}_{rel}|$ ranging between (50 – 1000 μm) and (0 – 10 m/s) respectively. The upper-bound of the wind-speed range is quite high and it is extremely unlikely to find $|\vec{u}_{rel}| > 10 m/s$ in naturally-occurring aeolian transport. Numerical results indeed confirm our intuition and it is found that for any given value of $|\vec{u}_{rel}|$, $\tau_{relaxation}$ is found to be $\propto d_p^\alpha$, where $\alpha (\sim 1.65)$. Furthermore, $\tau_{relaxation}$ decreases monotonically with increasing $|\vec{u}_{rel}|$ for a given value of d_p . For $d_p = 200 \mu m$, the plausible values of $\tau_{relaxation}$ are found to lie between 0.28 and 1.5 seconds (for $|\vec{u}_{rel}| = 10$ and 0 m/s respectively). Plots of $\tau_{relaxation}$ are highly relevant to discussion in Sect. 5.3 and presented there.

Following results of Experiment I, in Experiment II, we explore the parameter space of $(\sigma_*, T_P - T_{Air})$ and compute the total mass ($M = \int_0^t F_M dt$) and total heat ($Q = \int_0^t F_Q dt$) output by a sublimating ice grain for a finite time of $t = 0.5$ seconds. Results shown in Fig. 5.1 subfigures g and h provide a comparison of the total mass lost using the NUM and TM solutions respectively and the corresponding error is shown in subfigure i. Similar figures are presented for the total heat lost/gained by the air in subfigures (j-l). The inclusion of the inertial terms essentially causes the contours to be sloped for the NUM solution while the TM solutions do not depend on $T_P - T_{Air}$ as expected. The error between the NUM and TM solutions are accentuated at high saturation regimes, with errors larger than 30 % for $\sigma_* > 0.8$.

In summary, Experiments I and II highlight the fact that during the sublimation of an ice grain, there exists a finite, well-defined transient regime before the NUM solutions match the steady-state TM solutions. Furthermore, the NUM and TM solutions diverge rapidly with slight temperature differences between the particle and the air and with increasing σ_* (which is a cause of concern since in snow-covered environments, the air usually is highly saturated). The results described above prompt an interesting question: are the residence times of saltating ice particles comparable to $\tau_{relaxation}$? We use large-eddy simulations to answer this question in the following section.

5.3 Large-eddy simulations of saltating snow

5.3.1 Experiment III and IV: simulation details

To further understand the implications of the differences between the NUM and the TM approach, we performed LES of the atmospheric surface layer with an erodible snow surface as the lower boundary. We describe here only the main details of the LES that are relevant to our discussion. Full model description along with equations are described in Chapter 4. The LES solves filtered Eulerian equations for momentum, temperature and specific humidity on a computational domain of $6.4 m \times 6.4 m \times 6.4 m$. Ice grains in the flow are considered to be spherical and their equations of motion are solved in the Lagrangian frame of reference with only gravitational and turbulent form drag forces included. Since the particle velocities are

5.3. Large-eddy simulations of saltating snow

known, $|\vec{u}_{rel}|$ is calculated explicitly and used to compute Re_p , $\mathcal{N}u$ and Sh . The horizontal boundaries of the domain are periodic and the lower boundary condition (LBC) for velocity uses flux parametrizations based on Monin-Obukhov similarity theory, additionally corrected for flux partition between fluid and particles between the wall and the first flow grid point [Raupach, 1991, Shao and Li, 1999]. The LBC for scalars are flux-free and thus the only source/sink of heat and water vapour in the simulations is through the interaction of the flow with the saltating particles. The snow surface consists of particles with a log-normal size distribution with a mean particle diameter of 200 μm and standard-deviation of 100 μm . The coupling between the erodible snow-bed and the atmosphere is modelled through statistical models for aerodynamic entrainment [Anderson and Haff, 1988], splashing and rebounding of particle grains [Kok and Renno, 2009], which have been updated recently by Comola and Lehning [2017] to include the effects of cohesion and heterogeneous particle sizes. All simulations are performed on a grid of 64 x 64 x 128 grid points with a uniform grid in the horizontal directions and a stretched grid in the vertical. A stationary turbulent flow is allowed to first develop, following which, the snow surface is allowed to be eroded by the air. The physical constants and the numerical setup are detailed in Table 5.1 and 5.2 respectively.

Table 5.1 – Important Physical Parameters and Constants

Parameter	Symbol [Units]	Value
Latent heat of sublimation	L_s [J kg ⁻¹]	2835.49×10^3
Prandtl number	Pr [-]	0.72
Schmidt number	Sc [-]	0.63
Molecular Weight of Water	M_w [kg mol ⁻¹]	0.018015
Density of ice	ρ_p [kg m ⁻³]	918.4
Density of air	ρ_f [kg m ⁻³]	1.34
Specific heat capacity of air	$c_{p,f}$ [J kg ⁻¹ K ⁻¹]	1.005×10^3
Specific heat capacity of ice	c_i [J kg ⁻¹ K ⁻¹]	2.0357×10^3
Roughness length	z_0 [m]	1.0×10^{-5}
Cohesion Strength	ϕ [J]	10^{-10}
Diffusivity of vapor in air	\mathcal{D} [m ² s ⁻¹]	1.96×10^{-5}
Thermal conductivity of air	\mathcal{K} [W m ⁻¹ K ⁻¹]	0.023
Universal Gas Constant	R_u [J mol ⁻¹ K ⁻¹]	8.314
Kinematic Viscosity of air	ν_a [m ² s ⁻¹]	1.24×10^{-5}

For the TM approach, Equation 5.4 is used to compute the specific humidity and (by multiplying with the latent heat of sublimation) heat forcing due to each ice grain in the flow. On the other hand, for the NUM approach, Equations (5.1) and (5.2) are solved and only the turbulent transfer of heat between the air and the particle (second term in R.H.S of Equation 5.1) acts as a heat forcing on the flow. An implication of the NUM approach is that the particle temperature evolves during the ice-grain's motion and this necessitates providing an initial condition for the particle temperature ($T_{p,IC}$).

Chapter 5. On the suitability of the Thorpe-Mason model for calculating sublimation of saltating snow

Table 5.2 – Details of the numerical setup

Parameter	Symbol [Units]	Value
Streamwise extent of domain	L_x [m]	6.4
Cross-stream extent of domain	L_y [m]	6.4
Vertical extent of domain	L_z [m]	6.4
Grid points in horizontal directions	$\{nx, ny\}$ [-]	64
Grid points in vertical direction	nz [-]	128
Vertical grid stretching	$\{z_{min}, z_{max}\}$ [m]	{0.01, 0.1}
Time step	Δt [μs]	50
Total time	T [s]	1200

The principle aims of Experiment III are to firstly quantify particle residence times (PRT) and their dependence on wind speeds and relative humidities and secondly, compute the differences in the heat and mass output between the NUM and the TM approaches during realistic saltation of snow. PRT is defined as the total time the particle is air-borne and in motion, including multiple hops across the surface. Towards this goal, simulations are performed, each with a combination of initial surface stress, $u_* \in \{0.4, 0.6, 0.8\}$ and initial saturation, $\sigma_* \in \{0.3, 0.6, 0.9\}$. These values are classified as low (L), medium (M) and high (H) and the simulations are named as $U\alpha-R\beta$, where $(\alpha, \beta) \in \{L, M, H\}$. Each combination is simulated independently for the NUM and TM approaches resulting in a total of eighteen simulations. Experiment III is limited to simulating the *usual* case where the initial air temperature ($T_{Air,IC}$) is the same as $T_{p,IC}$.

Experiment IV is aimed at exploring the implications of differences between the two approaches in cases where $T_{Air,IC}$ is significantly different from $T_{p,IC}$. Such conditions can occur in nature during events such as marine-air intrusions, katabatic winds, spring-season saltation events and winter flows over sea-ice floes, where significant temperature differences between the air and snow-surface are likely. We repeat the low wind case of Experiment III with ($u_* = 0.4$) and choose the initial saturation to be 0.95, motivated by results in Experiment II where errors were found to increase with increasing saturation. Simulations (named as UL-T(γ), where $T_{Air,IC} - T_{p,IC} = \gamma$) are performed once again for each of two approaches with $\gamma \in \{\pm 1K, \pm 2.5K, \pm 5K\}$ resulting in a total of twelve simulations. In all simulations performed for Experiments III and IV, $T_{p,IC} = 263.15$ K. It is important to note that the initial condition for particle temperature ($T_{p,IC}$) is fixed throughout the simulation period, which essentially means that surface temperature is kept constant. This is consistent with the imposed zero flux of heat at the surface. This imposition will be justified *a-posteriori* in the following section.

5.3.2 Results

Particle residence times versus $\tau_{relaxation}$

As mentioned in the concluding lines of the Sect. 5.2, the quantity of interest is the PRT of saltating ice grains. In Fig. 5.2a, the mean and median PRT of five different simulations

5.3. Large-eddy simulations of saltating snow

of Experiment III are shown as a function of the particle diameter. Additionally, values of $\tau_{relaxation}$ computed in Experiment I for wind speeds ranging from 0 to 10 m/s are also shown in the shaded region. Recall that the shaded region represents all the plausible values of $\tau_{relaxation}$ in naturally-occurring aeolian transport. As examples, $\tau_{relaxation}$ trends for 3 wind speeds, 0, 1 and 10 m/s are shown and the power-law dependence can clearly be seen. It is found that $\tau_{relaxation}$ is comparable to the PRT of saltating grains with diameters between 125 and 225 μm . For 200 μm , the mean PRT is found to be 0.6 seconds while the median PRT is 0.2 seconds, which is outside the range of admissible values of $\tau_{relaxation}$. For particles larger than 225 μm , the PRTs are an order of magnitude smaller than plausible values of $\tau_{relaxation}$ and therefore the TM model is likely to provide wrong values of mass loss. On the other hand, lighter particles with diameters smaller than 100 μm have much longer PRTs and the TM model is therefore valid. This proves that while the TM model is applicable for a majority of particles in suspension, it is likely to cause errors for particles in saltation.

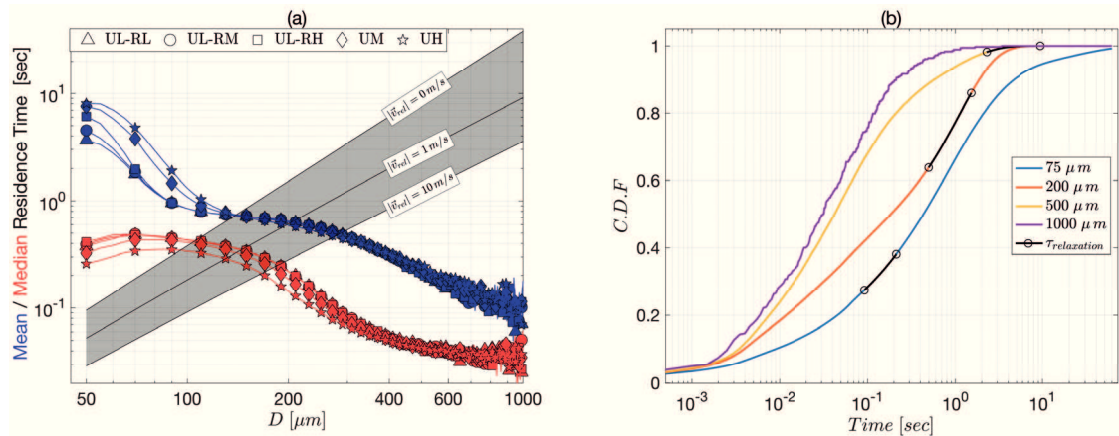


Figure 5.2 – (a) Mean and median particle residence time (PRT) as a function of particle diameter. The plausible values of $\tau_{relaxation}$ are represented by the shaded region with trends for three values of $|\vec{u}_{rel}|$ shown by straight lines. (b) Cumulative Distribution Functions of PRTs for four particle diameters along with range of plausible $\tau_{relaxation}$ values marked by overlying black curves

Results presented in Fig. 5.2a provides two additional insights. Firstly, it is quite interesting to note that particles larger than 100 μm have the same mean PRT irrespective of low, medium or high wind speeds. This means that the dynamics of the heavier particles are unaffected by larger-scale turbulence statistics, which is consistent with the notion of self-organized saltation, which has recently been shown by Paterna et al. [2016]. For particles smaller than 100 μm , the mean PRTs increases with wind speed. Secondly, the initial saturation does not seem to effect the PRT statistics for medium and high wind conditions and the UM- and UH- curves for different R values overlap (this is the reason only five PRTs are shown in Fig. 5.2a). In these cases turbulence is sufficient to rapidly mix any temperature anomaly due to sublimation throughout the surface layer. On the other hand, in low wind conditions (UL), low initial saturation results in more sublimation and cooling near the surface, resulting in suppression of vertical motions. This is reflected in the mean PRTs of particles smaller than 75

Chapter 5. On the suitability of the Thorpe-Mason model for calculating sublimation of saltating snow

μm , which decrease with decreasing initial σ_* .

The PRT distributions are found to be quasi-exponential with long tails, thus resulting in large differences in mean and median PRTs shown in Fig. 5.2a. These distributions are also strongly dependent on the particle diameter. As an illustration, in Fig. 5.2b, cumulative distributions of PRTs are shown for four particle diameters along with the corresponding range of plausible $\tau_{relaxation}$ values. For the mean particle diameter of $200 \mu m$, we find that between 65% to 85% of particles have PRTs shorter than $\tau_{relaxation}$, whereas for the $75 \mu m$ particles, at most 30% particles lie below the maximum $\tau_{relaxation}$ threshold. This reinforces the fact that applying the steady-state TM solution to sublimating ice-grains in saltation could be potentially erroneous.

Differences in total mass loss between NUM and TM models

We can directly assess the implications of differences in grain-scale sublimation between the two approaches on total mass loss rates during saltation at field scale. In Fig. 5.3, we compare the total 15-min averaged rate of mass loss computed in all cases in Experiment III (subfigure a) and Experiment IV (subfigure c) using the NUM and the TM approaches with corresponding errors shown in subfigures b and d respectively. Recalling the adopted convention of +(-) as gain(loss) of flow quantities, it can be seen in Experiment III, that sublimation increases with u_* and decreases with σ_* . The errors on the other hand increase with increasing values of both u_* and σ_* . The increase in error with u_* is mostly due to the fact that an increase in u_* proportionally increases the total mass entrained by air (see Supplementary Figure F1). The increase in error with increasing σ_* is in accordance with analysis done in Experiment II (see Fig. 5.2(i,l)) where it was shown that the NUM and TM solutions diverge with increasing saturation. The least error, 26% is found for case UL-RL (i.e., $u_*=0.4$, $\sigma_*=0.3$) while the largest error, 38% is found for UH-RH ($u_*=0.8$, $\sigma_*=0.9$). Overall, for all the simulation combinations, the NUM approach computes larger mass-loss than the TM approach.

Experiment IV highlights the effect of temperature difference between particle and air on sublimation. As shown in Fig. 5.3c, the mass output is found to be negative (deposition) for the NUM solutions when the air is warmer than the particles (i.e., cases UL-T(γ) with $\gamma > 0$). This is contrary to the TM solutions which indicate sublimation. In cases with $\gamma < 0$, the NUM approach shows a much higher sublimation rate than the TM solutions. This occurs firstly due to higher vapor pressure at the grain surface that results in enhanced vapor transport and secondly because the warmer particles heat the surrounding air via sensible heat exchange, causing the relative humidity to decrease. Errors increase dramatically from an already high 100% for UL-T(+1) to 800% for UL-T(+5). Simulations performed for medium and high wind cases in Experiment IV showed even higher errors, similar to results in Experiment III and are shown here).

The LES results do come with two caveats. Firstly, the scalar fluxes at the surface are neglected. This can be justified by considering that during drifting and blowing snow events, the friction velocity at the surface drops dramatically. This fact has been observed in both in experiments

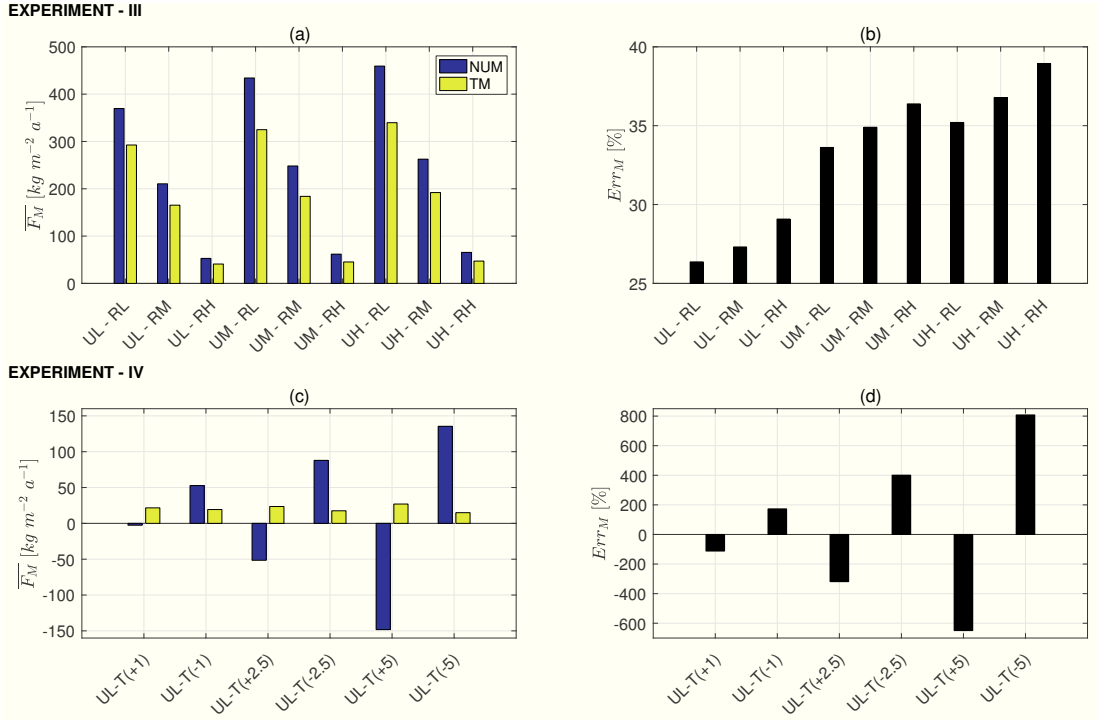


Figure 5.3 – Experiment III: (a) Average rate of mass loss during 15 minutes of saltation, (b) Error between NUM and TM solutions. Corresponding plots for Experiment IV in (c) and (d) respectively. Note that the units used for rate of mass loss are kilograms per unit area per unit year.

and in our current LESs (see Supplementary Figure F2). This implies that direct turbulent exchange between the surface and air is curtailed and instead, the dominant exchange occurs between air-borne particles and the air. This is nevertheless an important assertion that shall be more closely examined in future studies involving a full surface energy balance model. Secondly, we neglect collisions between particles in the saltation layer. While the effect of collisions has been shown to be important, incorporating their effects in the present work is not likely to affect our primary conclusion of the inadequacy of the TM approach for saltating snow.

5.4 Discussion and conclusion

In this chapter, we revisit the Thorpe and Mason [1966] model used to calculate sublimation of drifting and blowing snow and check its validity for saltating ice grains. We highlight the fact that solutions to unsteady heat and mass transfer equations (NUM solutions) converge to the steady-state TM model solutions after a *relaxation* time, denoted as $\tau_{relaxation}$ that has a power-law dependence on the particle diameter and is inversely proportional to the relative wind speed. Through extensive LESs of snow saltation, we compute the statistics of the PRTs as a function of their diameters and find them to be comparable to $\tau_{relaxation}$. This helps explain the difference between mass output when using the NUM model to the TM approach, also

Chapter 5. On the suitability of the Thorpe-Mason model for calculating sublimation of saltating snow

computed during the same LESs. The NUM approach computes higher sublimation losses ranging from 26% in low-wind, low saturation conditions to 38% in high-wind, high saturation conditions. Another set of numerical experiments explore the role of temperature differences between particle and air temperature in inducing differences between NUM and TM solutions. We find the effect to be extremely dramatic with errors of 100% for a temperature difference of 1 K with increasing errors for larger temperature perturbations. In general, the two solutions are found to diverge rapidly as the saturation tends towards 1.

Analogous to the role played by saltating grains in efficient momentum transfer to the underlying granular bed, the NUM approach can be considered as an efficient transfer of heat and mass between the flow and the underlying snow surface, albeit with a closer physical relationship between the thermodynamics of the snow surface and that of the air. Future efforts are geared towards including a high-fidelity snowpack thermodynamic model within the LES-Saltation framework to further study sublimation of drifting and blowing snow in a more realistic setting and to compare simulations with field observations.

Supplementary results

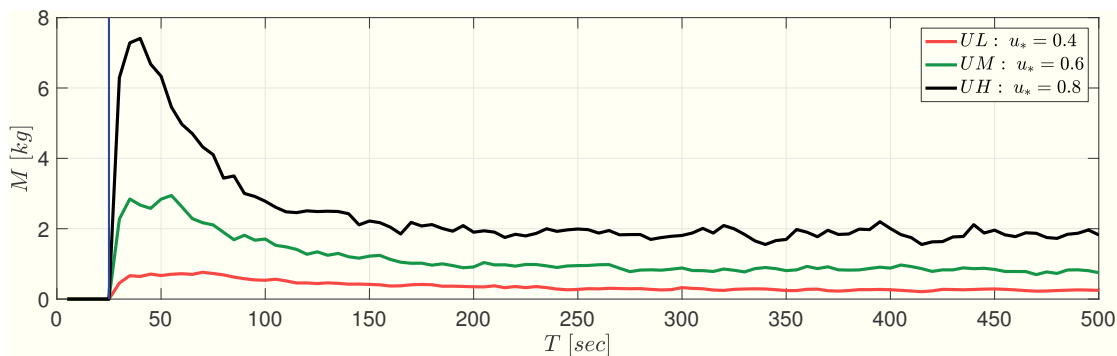


Figure F1 – The total mass of snow presented in the fluid at any given time of the simulation for three different forcing conditions. The vertical blue line denotes the commencement of surface erosion.

We present here two results that supplement the results presented in the main portion of the chapter. While these results are not critical to discussions presented in the chapter, they are nevertheless interesting in their own right and help justify certain assumptions used in the simulation setup.

Figure F1 shows evolution of the total air-borne mass of snow under three different forcing conditions. It shows that once surface erosion is allowed to occur, there is a rapid increase in the total mass present in the atmosphere, following which, it slowly decays to reach its asymptotic value at approximately 300 seconds. All the three forcings, marked by the three initial u_* values of 0.4 (UL), 0.6 (UM) and 0.8 (UH) show similar behaviour with larger mass entrained by the air with increasing u_* values as expected. The results in Fig. F1 explain the increase in errors in the mass-loss rate with increasing u_* values between the Nu-TM and TM

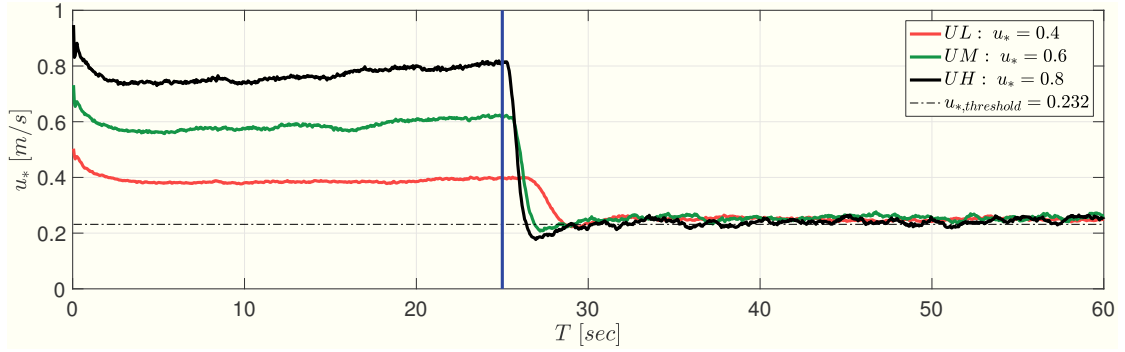


Figure F2 – Evolution of the friction velocity at the surface (u_*). The vertical blue line denotes the commencement of surface erosion which until this point in time has been artificially restricted.

approaches as discussed in Fig. 3 of the chapter.

In Fig. F2, the evolution of the surface friction velocity is shown as a function of time. The vertical blue line marks the beginning of surface erosion. It shows that irrespective of the forcing used to drive the flow, once saltation begins, the friction velocity at the surface drops to that of $u_{*,threshold}$. The value of $u_{*,threshold}$, computed using Equation 4.11 for $\tau_{threshold}$ and by considering that $u_{*,threshold} = \sqrt{\tau_{threshold}/\rho_f}$ is found to be equal to 0.232. The rate at which the surface friction velocity decays is dependent on the forcing used with larger forcing decaying more rapidly to the asymptotic value of $u_{*,threshold}$. This result is important since the surface friction velocity dictates the turbulent exchange between the surface and the overlying turbulent fluid. A drop in the surface friction velocity shows during drifting and blowing snow events, the heat and mass transfer between the surface and the atmosphere can be neglected as a first-order approximation and can be modelled using fixed stress values in more detailed studies.

Acknowledgments

We acknowledge the support of the Swiss National Science Foundation (Grant n. 200021-150146), the Swiss Super Computing Center (CSCS) for providing computational resources (Project: s633), ETH Domain Centre for Competence in Environmental and Sustainability (Project: Osper). We additionally thank Marco Giometto for providing the original version of the LES code and Tristan Brauchli, Annelen Kahl and Celine Labouesse for illuminating discussions and important suggestions in improving the manuscript.

Bibliography

- Robert S. Anderson and Peter K. Haff. Simulation of eolian saltation. *Science*, 241(4867): 820, Aug 12 1988. URL <https://search.proquest.com/docview/213543077?accountid=27198>. Copyright - Copyright American Association for the Advancement of Science Aug 12, 1988; Last updated - 2014-05-30; CODEN - SCIEAS.
- Francesco Comola and Michael Lehning. Energy- and momentum-conserving model of splash entrainment in sand and snow saltation. *Geophysical Research Letters*, 44(3):1601–1609, 2017. ISSN 1944-8007. doi: 10.1002/2016GL071822. URL <http://dx.doi.org/10.1002/2016GL071822>. 2016GL071822.
- Xiaoqing Dai and Ning Huang. Numerical simulation of drifting snow sublimation in the saltation layer. *Scientific reports*, 4:6611, 2014. ISSN 2045-2322. doi: 10.1038/srep06611. URL <http://www.pubmedcentral.nih.gov/articlerender.fcgi?artid=4196100&tool=pmcentrez&rendertype=abstract>.
- Stephen J. Déry and M. K. Yau. Large-scale mass balance effects of blowing snow and surface sublimation. *Journal of Geophysical Research Atmospheres*, 107(23), 2002. ISSN 01480227. doi: 10.1029/2001JD001251.
- Judith J. J. Doorschot and Michael Lehning. Equilibrium saltation: Mass fluxes, aerodynamic entrainment, and dependence on grain properties. *Boundary-Layer Meteorology*, 104(1): 111–130, Jul 2002. ISSN 1573-1472. doi: 10.1023/A:1015516420286. URL <https://doi.org/10.1023/A:1015516420286>.
- S.E. Dover. *Numerical Modelling of Blowing Snow*. PhD thesis, University of Leeds, 1993.
- Jacopo Grazioli, Jean-Baptiste Madeleine, Hubert Gallée, Richard M. Forbes, Christophe Genthon, Gerhard Krinner, and Alexis Berne. Katabatic winds diminish precipitation contribution to the antarctic ice mass balance. *Proceedings of the National Academy of Sciences*, 114(41):10858–10863, 2017. doi: 10.1073/pnas.1707633114. URL <http://www.pnas.org/content/114/41/10858.abstract>.

Bibliography

- C. D. Groot Zwaaftink, H. Löwe, R. Mott, M. Bavay, and M. Lehning. Drifting snow sublimation: A high-resolution 3-d model with temperature and moisture feedbacks. *Journal of Geophysical Research: Atmospheres*, 116(D16):n/a–n/a, 2011. ISSN 2156-2202. doi: 10.1029/2011JD015754. URL <http://dx.doi.org/10.1029/2011JD015754>. D16107.
- C. D. Groot Zwaaftink, M. Diebold, S. Horender, J. Overney, G. Lieberherr, M. B. Parlange, and M. Lehning. Modelling small-scale drifting snow with a lagrangian stochastic model based on large-eddy simulations. *Boundary-Layer Meteorology*, 153(1):117–139, Oct 2014. ISSN 1573-1472. doi: 10.1007/s10546-014-9934-2. URL <https://doi.org/10.1007/s10546-014-9934-2>.
- Brian Helgans and David H. Richter. Turbulent latent and sensible heat flux in the presence of evaporative droplets. *International Journal of Multiphase Flow*, 78:1 – 11, 2016. ISSN 0301-9322. doi: <https://doi.org/10.1016/j.ijmultiphaseflow.2015.09.010>. URL <http://www.sciencedirect.com/science/article/pii/S0301932215002086>.
- Jasper F. Kok and Nilton O. Renno. A comprehensive numerical model of steady state saltation (comsalt). *Journal of Geophysical Research: Atmospheres*, 114(D17):n/a–n/a, 2009. ISSN 2156-2202. doi: 10.1029/2009JD011702. URL <http://dx.doi.org/10.1029/2009JD011702>. D17204.
- J. T. M. Lenaerts, M. R. van den Broeke, S. J. Déry, E. van Meijgaard, W. J. van de Berg, Stephen P. Palm, and J. Sanz Rodrigo. Modeling drifting snow in Antarctica with a regional climate model: 1. Methods and model evaluation. *Journal of Geophysical Research: Atmospheres*, 117(D5):n/a–n/a, 2012. ISSN 01480227. doi: 10.1029/2011JD016145. URL <http://doi.wiley.com/10.1029/2011JD016145>.
- Glen E. Liston and M. Sturm. The role of winter sublimation in the Arctic moisture budget. *Nordic Hydrology*, 35(4-5):325–334, 2004. ISSN 00291277. doi: 10.1029/2001JD001251. URL ftp://ftp.cira.colostate.edu/ftp/Liston/papers/first_{ }author/2004.liston.NH.pdf.
- G. W. Mann, P. S. Anderson, and S. D. Mobbs. Profile measurements of blowing snow at halley, antarctica. *Journal of Geophysical Research: Atmospheres*, 105(D19):24491–24508, 2000. ISSN 2156-2202. doi: 10.1029/2000JD900247. URL <http://dx.doi.org/10.1029/2000JD900247>.
- E. Paterna, P. Crivelli, and M. Lehning. Decoupling of mass flux and turbulent wind fluctuations in drifting snow. *Geophysical Research Letters*, 43(9):4441–4447, 2016. ISSN 1944-8007. doi: 10.1002/2016GL068171. URL <http://dx.doi.org/10.1002/2016GL068171>. 2016GL068171.
- MR Raupach. Saltation layers, vegetation canopies and roughness lengths. *Acta Mechanica*, I, pages 83–96, 1991.
- Frédérique Rémy and Massimo Frezzotti. Antarctica ice sheet mass balance. *Comptes Rendus - Geoscience*, 338(14-15):1084–1097, 2006. ISSN 16310713. doi: 10.1016/j.crte.2006.05.009.
- E. Rignot, I. Velicogna, M. R. van den Broeke, A. Monaghan, and J. T. M. Lenaerts. Acceleration of the contribution of the greenland and antarctic ice sheets to sea level rise. *Geophysical*

- Research Letters*, 38(5):n/a–n/a, 2011. ISSN 1944-8007. doi: 10.1029/2011GL046583. URL <http://dx.doi.org/10.1029/2011GL046583>. L05503.
- E. Russo, J. G. M. Kuerten, C. W. M. van der Geld, and B. J. Geurts. Water droplet condensation and evaporation in turbulent channel flow. *Journal of Fluid Mechanics*, 749:666–700, 2014. doi: 10.1017/jfm.2014.239.
- Yaping Shao and An Li. Numerical modelling of saltation in the atmospheric surface layer. *Boundary-Layer Meteorology*, 91(2):199–225, May 1999. ISSN 1573-1472. doi: 10.1023/A:1001816013475. URL <https://doi.org/10.1023/A:1001816013475>.
- Matthew Sturm, Jon Holmgren, and Don K Perovich. Winter snow cover on the sea ice of the arctic ocean at the surface heat budget of the arctic ocean (sheba): Temporal evolution and spatial variability. *Journal of Geophysical Research: Oceans*, 107(C10), 2002.
- A. D. Thorpe and B. J. Mason. The evaporation of ice spheres and ice crystals. *British Journal of Applied Physics*, 17(4):541, 1966. ISSN 0508-3443. doi: 10.1088/0508-3443/17/4/316. URL <http://iopscience.iop.org/0508-3443/17/4/316>.
- Michiel van den Broeke, Willem Jan van de Berg, Erik van Meijgaard, and Carleen Reijmer. Identification of Antarctic ablation areas using a regional atmospheric climate model. *Journal of Geophysical Research*, 111(D18):D18110, 2006. ISSN 0148-0227. doi: 10.1029/2006JD007127. URL <http://doi.wiley.com/10.1029/2006JD007127>.
- V. Vionnet, E. Martin, V. Masson, G. Guyomarc’H, F. Naaim-Bouvet, A. Prokop, Y. Durand, and C. Lac. Simulation of wind-induced snow transport and sublimation in alpine terrain using a fully coupled snowpack/atmosphere model. *Cryosphere*, 8(2):395–415, 2014. ISSN 19940424. doi: 10.5194/tc-8-395-2014.
- Christian Vögeli, Michael Lehning, Nander Wever, and Mathias Bavay. Scaling precipitation input to spatially distributed hydrological models by measured snow distribution. *Frontiers in Earth Science*, 4:108, 2016. ISSN 2296-6463. doi: 10.3389/feart.2016.00108. URL <https://www.frontiersin.org/article/10.3389/feart.2016.00108>.
- N. Wever, M. Lehning, A. Clifton, J. D. Rüedi, K. Nishimura, M. Nemoto, S. Yamaguchi, and A. Sato. Verification of moisture budgets during drifting snow conditions in a cold wind tunnel. *Water Resources Research*, 45(7):1–14, 2009. ISSN 00431397. doi: 10.1029/2008WR007522.

Summary and Conclusions

Summary

In this thesis, numerical simulations of the atmospheric boundary layer (ABL) are performed using the large-eddy simulation (LES) methodology. First part of the thesis is focussed on understanding the interaction between the ABL with wind farms while the second part uses LES to elucidate the mechanisms involved in sublimation of drifting and blowing snow.

Most large-eddy simulation (LES) studies related to wind energy have been carried out either by using a fixed pressure gradient to ensure that mean wind direction is perpendicular to the wind turbine rotor disk, or by forcing the flow with a geostrophic wind and timely readjusting the turbines' orientation. This has not allowed for the study of wind farm characteristics with a time varying wind vector. In Chapter 1, a new LES model for time-adaptive wind turbines was introduced. The new algorithm enables the wind turbines to dynamically realign with the incoming wind vector and self-adjust the yaw orientation with the incoming wind vector similar to real wind turbines. The performance of the new model was tested first with a neutrally stratified atmospheric flow forced with a time varying geostrophic wind vector and a synthetic time-changing thermal atmospheric boundary layer (ABL) and an embedded wind farm. Results showed that there is significant potential power to be harvested during the unstable time periods at the cost of designing wind turbines capable of adapting to the enhanced variance of these periods. Stable periods were found to produce less power but are more constant over time with an enhanced lateral shear induced by an increased change in wind direction with height.

Next, in Chapter 2, the effect of extensive terrestrial wind farms on the spatio-temporal structure of a diurnally-evolving ABL were explored. Simulations were forced by a constant geostrophic velocity with time-varying surface boundary conditions derived from a selected period of the CASES-99 field campaign. Through analysis of the bulk statistics of the flow as a function of height and time, it was shown that extensive wind farms shift the inertial oscillations and the associated nocturnal low-level jet vertically upwards by approximately 200 m, cause a three times stronger stratification between the surface and the rotor-disk region,

Summary and Conclusions

and as a consequence, delay the formation and growth of the convective boundary layer (CBL) by approximately 2 h. These perturbations were found to have a direct impact on the potential power output of an extensive wind farm with the displacement of the low-level jet causing lower power output during the night as compared to the day. The low-power regime at night was shown to persist for almost 2 h beyond the morning transition due to the reduced growth of the CBL. Additionally, it was shown that the wind farm induced a deeper entrainment region with greater entrainment fluxes. Finally, it was found that the diurnally-averaged effective roughness length for wind farms is much lower than the reference value computed theoretically for neutral conditions.

Evolution of flow characteristics through finite-sized wind farms and the influence of the wind-farm configuration on modulating this evolution was explored in Chapter 3. The principal aim for the study was to identify regions of flow-adjustment and flow equilibrium within the wind farm. Towards this aim, a suite of five simulations of the neutral ABL with extremely long streamwise domains were performed with embedded finite-sized wind farms of different streamwise (s_x) and spanwise (s_y) spacing. Three diagnostic variables, namely, the wind-farm induced effective surface roughness, the wake viscosity and the wake-expansion coefficient were computed using the LES-generated database and were used to characterize the flow. Computation of the diagnostic variables is relevant to the wind-energy community in different contexts ranging from parametrization of wind farms in weather and climate models, to wind-farm design and optimization based on wake-models and eddy-viscosity type Reynolds-averaged Navier-Stokes solvers. Results showed that flow equilibrium was achieved in the ‘most dense’ configuration of $s_x \approx 8D$, $s_y \approx 5D$, where D is the diameter, at approximately the 19th row. Results also indicated that the streamwise spacing plays a dominant role determining the rate at which flow-adjustment is achieved within the wind farm.

In the second part of the thesis, LES of drifting and blowing snow were performed with the aim of calculating sublimation of saltating snow grains. Chapter 4 describes the LES model with Lagrangian particles in detail with descriptions of stochastic models used for coupling the flow with a erodible snow surface. The major additions to the code were the development of advection-diffusion equations for temperature and specific humidity along with the heat and mass transfer equations for the particulate phase. The Thorpe and Mason [1966] model for calculating the mass lost from a sublimating snow grain is the basis of all existing small and large-scale estimates of drifting snow sublimation and the associated snow mass balance of polar and alpine regions. In Chapter 5, this model was revisited to test its validity for calculating sublimation from saltating snow grains. It was shown that numerical solutions of the unsteady mass and heat balance equations of an individual snow grain reconcile well with the steady-state solution of the TM model, albeit after a transient regime. Using LES, it was found that the residence time of a typical saltating particle was shorter than the period of the transient regime, implying that using the steady state solution might be erroneous. For scenarios with equal air and surface temperatures, these errors were found to range from 26 % for low-wind low-saturation conditions to 38% for high-wind high-saturation conditions. With a small temperature perturbation of 1 K between the air and the snow surface, the errors due

to the TM model were already as high as 100% with errors increasing for larger temperature perturbations.

Conclusions, limitations and outlook

The first part of the thesis focusses on the interaction between a wind farm and the atmospheric boundary layer (ABL). Chapters 1 and 2 in particular were focussed on the scenario with a transient, diurnally-varying ABL as it responds to time-dependent surface boundary conditions. The new wind turbine model developed in Chapter 1 has proven to be a significant development and has been used for diverse problems. An example includes investigating the feasibility of *LIDAR* systems to diagnose upstream flow conditions for optimizing the yawing operation of turbines in a wind farm. Results from Chapter 2 indicate that wind farms can cause large-scale perturbations to both the vertical structure as well as the dynamics of the ABL. On one hand, results such as the upward displacement of the low-level jet and the increased power production during the daytime convective boundary layer are of immense importance to the wind energy industry as it provides crucial input for wind farm design and operations planning. It also makes it imperative for wind resource assessment operations to focus not only on pre-wind farm conditions but also on prediction of flow changes post-wind farm installation as the two scenarios might be significantly different. On the other hand, changes to the momentum fluxes and the effective roughness lengths during a diurnal cycle are of interest to micro-meteorologists looking to understand land-atmosphere interaction, the local water balance and dispersal of pollutants in the vicinity of a large wind farm. The influence of the wind farm at the top of the boundary layer is particularly surprising and indicates that wind farms could potentially have an influence on boundary layer clouds. In Appendix A, results of a preliminary study to understand the impact of a large wind farm on a stratocumulus cloud are provided.

Increasing computational resources have allowed for two distinct paths to emerge in the simulation of ABL flows with wind farms. Notice that Chapters 1 and 2 use a time-dependent surface temperature as a boundary condition with a dry ABL. Additionally the flow is over an idealized flat terrain. One approach is to increase the fidelity of components of the simulation setup that allow for more realistic ABL flows. This includes using, for example, a realistic topography, heterogeneous surface roughness values and an energy balance model for the underlying surface to compute the surface temperature.

The second path is to increase the fidelity of the wind farm parametrizations. In Chapters 1 and 2, we focussed on asymptotically large wind farms, which will be installed at least a few decades from now. A more realistic approach for the present and near future wind farms would be to simulate a finite-sized wind farm, a possibility that was explored in Chapter 3. Simulations of a transient ABL with a finite-sized wind farm remain computationally intensive at present. Models at the turbine scale need to improve as well and with increasing resolutions of the simulations in the near future, use of actuator-line and actuator-surface methods to parametrize the interaction between the ABL flow and a single wind turbine shall become fea-

Summary and Conclusions

sible. This would be a major improvement over the the actuator-disk approach that has been used in this thesis and shall open up the possibilities for capturing fluid-structure interactions at an unprecedented level of detail. The most prominent motivation for wind energy research remains expanding as well as optimizing the extraction of wind energy. However, this thesis and a few other works have demonstrated that along with the rapid growth in the installation of wind farms, attention needs to be paid to their implications on atmospheric circulation and attendant phenomena such as land-atmospheric interaction and cloud dynamics. This remains a promising area of research in the coming years.

The second part of the thesis describes the LES model for calculating sublimation of drifting and blowing snow (Chapter 4). The main result of this part of the thesis (Chapter 5) is the finding that the Thorpe and Mason [1966] model is unsuitable for calculating drifting snow sublimation in many cases. This is an important finding since all small and large-scale estimates of snow sublimation in air are based on the Thorpe and Mason model. This could potentially explain the wide range of values reported in the literature which are often contradictory. Accurate measurements of sublimation of drifting and blowing snow have proven to be quite difficult and shall remain so in the near future. Measurements are hindered as this important phenomenon takes place in challenging environments such as polar and alpine regions and the little that we know is a result of heroic efforts by intrepid scientists willing to work in the harsh conditions of cryospheric environments. Our lack of sufficient understanding is also a reflection of the complexity of the mechanisms giving rise to aeolian transport of snow in the first place, i.e. turbulence of the atmospheric flow, interaction of the entrained particles with the granular snow surface, and the fact that snow is highly dynamic material both mechanically as well as thermodynamically.

Thus, in the near future, researchers shall have to remain dependent on computational modelling to uncover further details on the mechanisms of drifting and blowing snow. However, this approach is no less challenging due to significant scale-separation between grain-scale interactions ($\mathcal{O}(10 - 100\mu m)$), grain-flow interactions ($\mathcal{O}(1 - 10cm)$) in the saltation regime and large-scale drifting and blowing snow ($\mathcal{O}(1 - 100m)$) involving suspension. Due to this scale separation, vastly different computational techniques ranging from *discrete-element modelling* (DEM) for the smallest scales to bulk snow transport models for the largest scales have been utilized. There is an urgent need for homogenization and upscaling of relevant equations and creating parametrizations for larger scales. Furthermore, our understanding of more exotic topics such as electrostatic and optical properties of drifting and blowing snow and their influence on surface mass and energy balance still remain deficient.

In conclusion, the work presented in this thesis makes a small contribution to our evolving understanding of two important areas of research in the context of climate change, namely, wind energy and sublimation of drifting and blowing snow. One part of the thesis has provided new evidence that wind farms cause significant perturbations to the ABL, such that the mere presence of the large wind farm can potentially alter the atmospheric flow at micro- and meso-scales. The second part of the thesis questions the current estimates of sublimation loss during aeolian transport of snow and gives evidence that much larger quantities of snow mass are

being lost due to sublimation than is currently accounted for. The thesis has also opened new topics for future research, particularly the influence of wind farms on clouds and the continuing exploration of snow sublimation processes, especially in harsh environments of the polar regions.

A Perturbation to a stratocumulus-topped boundary layer due to a very large wind farm

A.1 Introduction

In this appendix, preliminary results of LES of stratocumulus-topped boundary layers (STBL) with an immersed wind farm are presented. Stratocumulus is one of the most common cloud types found in the atmospheric boundary layer (ABL) [Wood, 2012] and have been shown to have a significant impact in modulating the global radiation and energy balance [Hartmann et al., 1992]. In spite of their ubiquitousness, they are quite challenging to account for in weather prediction and climate models, mostly due to their shallowness. This makes them *subgrid-scale* for the large-scale models.

These clouds are usually thin with thickness of $\mathcal{O}(100m)$ and are found near the top of the ABL if the lifting condensation level is below the capping inversion. If sufficient quantity of water condenses to form a layer of water droplets, radiative cooling at the top of the cloud is established and rapidly becomes the dominating process modulating the STBL. The radiative cooling increases the strength of the capping inversion while at the same time causing convection to occur between the top and the bottom of the cloud. These convective downdrafts can reach all the way to the earth's surface, keeping the sub-cloud layer well mixed. This is important because the source of moisture for the cloud comes from the surface. The same convective motions also cause mixing across the capping inversion, bring warmer and dryer air from aloft into the cloud. This process, known as cloud entrainment has a destabilizing effect on the cloud layer. It is necessary that the cloud-top entrainment is sufficiently weak so that the radiative cooling continues and the STBL remains well-mixed.

This study can be considered as a follow-up of the results presented in Chapter 2 where it was discovered that wind farms can have a significant impact at the top of the ABL and increase the depth of the capping inversion.

Appendix A. Perturbation to a stratocumulus-topped boundary layer due to a very large wind farm

A.2 Simulation details

The first research flight (RF O1) of the DYnamics and Chemistry Of Marine Stratocumulus (DYCOMS-II) field campaign [Stevens et al., 2003] was chosen because it is a conceptually simple, non-precipitating stratocumulus case and has been a subject of various LES studies [Moeng et al., 2005, Kirkpatrick et al., 2006, Yamaguchi and Randall, 2008] including a major LES intercomparison study [Stevens et al., 2005]. The open-source LES code for solving cloud dynamics, PyCLES, was adopted as the base flow solver [Pressel et al., 2015]. PyCLES solves the anelastic equations of motions and uniquely uses moist specific entropy and total water specific humidity as the thermodynamic prognostic variables based on the analytical work by Pauluis [2008]. This code was recently used to simulate the DYCOMS-II RF01 case and provided excellent agreement with the observations [Pressel et al., 2017]. PyCLES was modified to include the wind turbine model presented in Chapter 1.

All simulations are performed using a computational domain of size 3360 m in both the horizontal directions and 1500 m in the vertical direction. The resolution in the horizontal and vertical directions is 35 m and 5 m respectively. The domain is periodic in the horizontal directions. Three different wind farm setups with varying spacing and loading [Wind farm (S)parse, (D)ense and (V)ery (D)ense] are chosen and shown in Fig. A1 with the intention of understanding the effect of wind farm loading on the cloud perturbation, if any. Wind turbines have a hub-height as well as a diameter of 100 m respectively.

A spinup simulation is first performed for four hours of physical time following which the wind turbines are *switched on* and act as a momentum sink. The simulation is then continued for an additional eight hours. An additional simulation without wind farms is also performed and serves as a benchmark to highlight the influence of wind farms on the cloud.

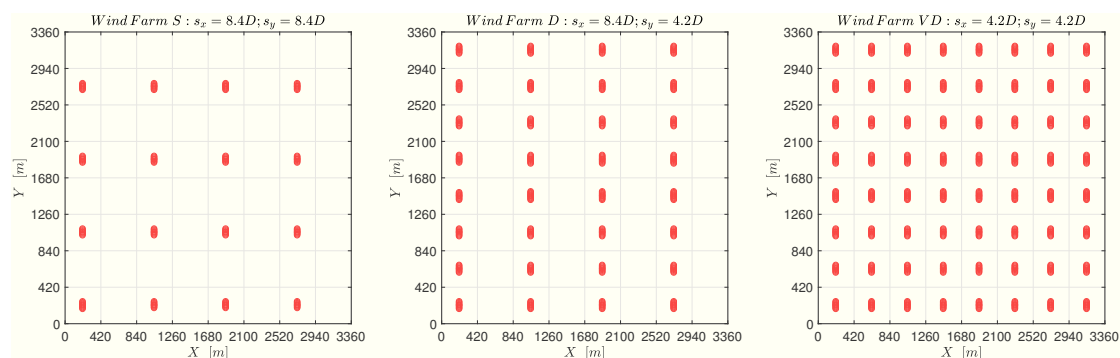


Figure A1 – Wind farm setups used in this study. A top view of the computational domain with the red dots marking the location of wind turbines.

A.3 Results

A.3.1 Perturbations to the cloud field

In this section, perturbations to the cloud layer caused due to the presence of the wind farms are presented. In Fig. A2(a), the cloud fraction is shown for the four cases as a function of time. Cloud fraction represents the percentage of surface area covered by the cloud layer. In observations during the DYCOMS-II campaign as well in the case without wind farms (NO WF), the cloud fraction remains close to one. However, in the presence of a wind farm, the cloud fraction is found to decrease proportionally to the loading of the wind farm. For the VD case, the cloud fraction drops by 10% while for the D case, it lowers by 6%. While these values may not seem to be significant, even this small decrease can have a big impact on the energy balance in the vicinity of the wind farm. Liquid water path (LWP) is a crucial quantity that defines the optical properties of the cloud and its interaction with radiation. The higher the LWP, more optically dense is the cloud. It is a measure of the liquid water content per unit area of a cloud. Its evolution with and without wind farms is shown in Fig. A2(b). Here the difference is considerably more dramatic with the VD case showing a difference of almost 60% at the end of 12 hours. Even the sparse wind farm causes close to a 15% drop in the LWP.

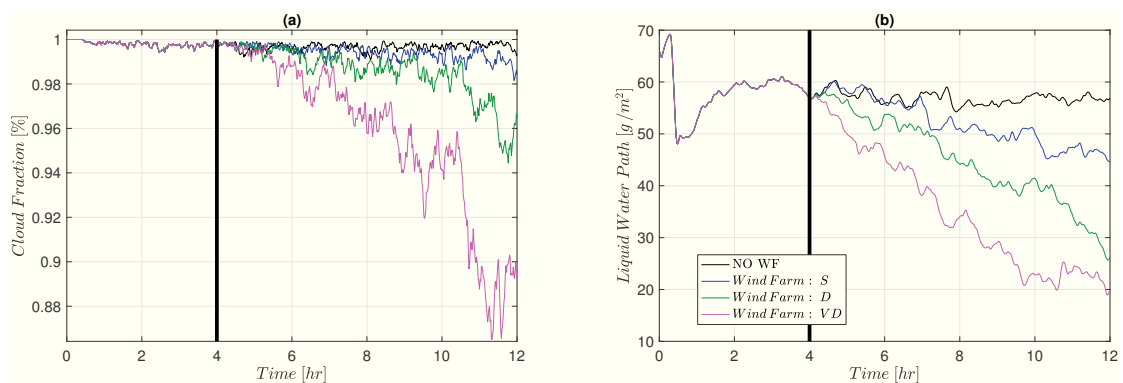


Figure A2 – Effect of Wind farms on a stratocumulus cloud: (a) Clouds Fraction and (b) Liquid Water Path

Figure A3 shows the differences in the location of the cloud-bottom and the cloud-top along with the cloud thickness for the four cases. In this and all subsequent figures, all data presented have been averaged over the last two hours of the simulation in combination with averaging along the horizontal directions. It can be seen that in the presence of wind farms, both the cloud-bottom as well as the cloud-top are shifted vertically upwards while the cloud thickness decreases with increasing loading.

In the final figure of this section, vertical profiles of the liquid water specific humidity are presented in Fig. A4. It can clearly be seen that the presence of the wind farm causes drying of the cloud, once again in proportion to the loading. The most dense case (VD) depletes the cloud liquid water by almost 60%, a result shown earlier in Fig. A2(b) for the LWP.

In summary, the presence of the wind farm causes the cloud layer to shift vertically upwards

Appendix A. Perturbation to a stratocumulus-topped boundary layer due to a very large wind farm

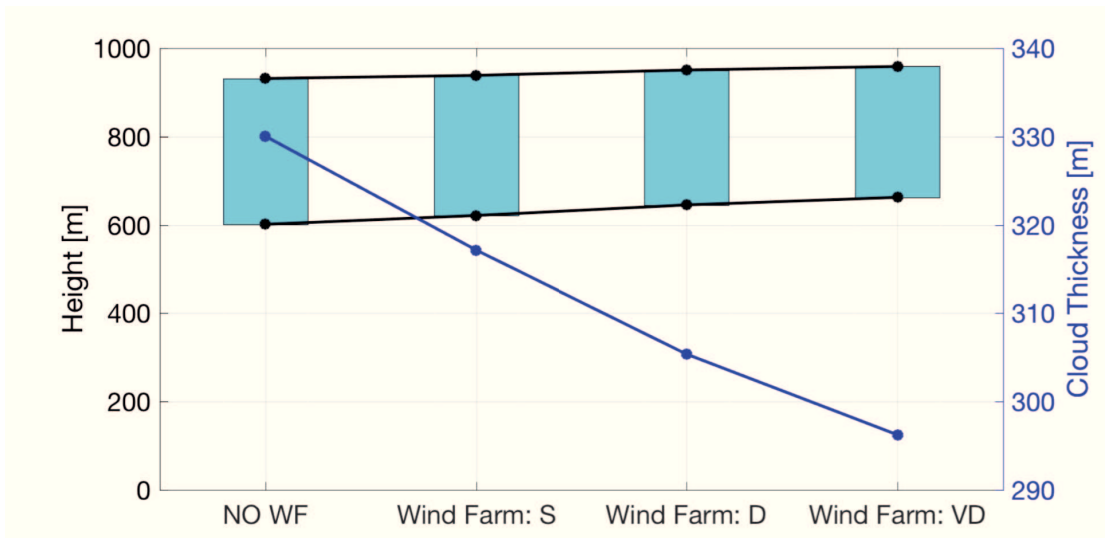


Figure A3 – Effect of Wind farms on a stratocumulus clouds: Cloud geometry. The blue region marks the cloud region as a function of height (left axis). The blue curve represents the cloud thickness.

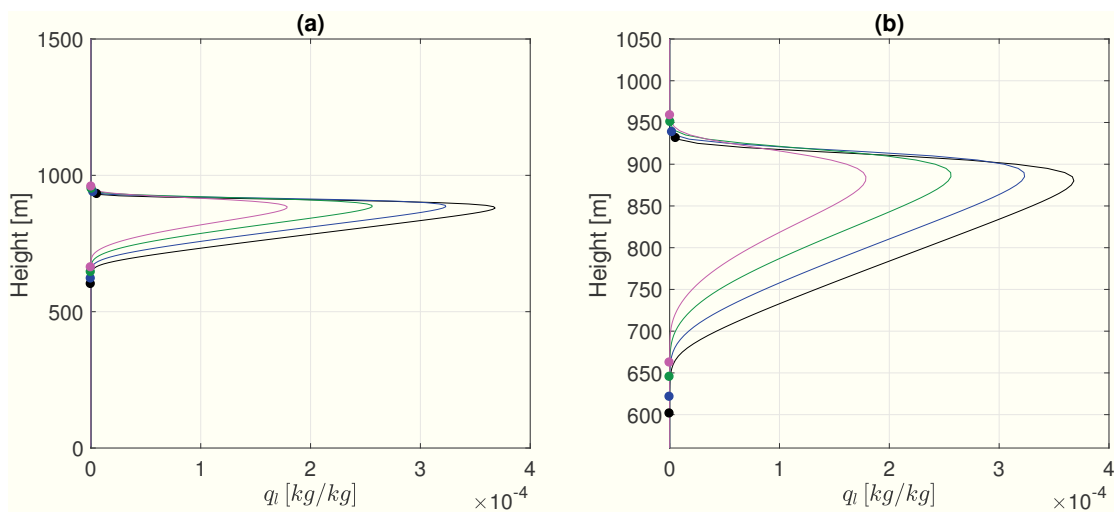


Figure A4 – Liquid Water Specific Humidity (q_l) of (a) the full domain and (b) a cloud region. The circular markers mark the extent of the cloud for each case. Legend is the same as in Fig. A2(b)

while making it thinner and drier. All these perturbations occur in direct proportion to the loading of the wind farm.

A.3.2 Some profiles of mean and turbulent statistics

In this section, vertical profiles of three quantities, namely, the liquid water potential temperature, the velocity magnitude and the vertical velocity variance are presented for the four simulated cases. Figure A5 shows the location of the capping inversion for the four cases. Notice that the inversion is extremely strong with a temperature jump of approximately 12 K over

a height of just 50 m! Despite the strong inversion, it can be seen, especially in Figure A5(b), that wind farms cause increasing entrainment across the capping inversion resulting in drying of the cloud as shown in the previous section as well as causing a slight warming in the sub-cloud region.

The velocity profiles in Fig. A6 provide an answer to how the wind farm causes increased entrainment and the destabilization of the cloud. Notice that while there is hardly any shear across the cloud as well as the capping inversion in the case without the wind farm, the wind farm causes a strong shear layer to be formed at the capping inversion. This shear layer is formed due to the fact that the presence of the wind farm causes a deceleration of the flow and since the wind farm is asymptotically infinite (due to the imposed periodic boundary conditions), the velocity deficit is mixed through the sub-cloud layer. The presence of the strong capping inversion prevents momentum recovery by the faster air aloft. This is a classic case of competition between the restoring force of buoyancy and the destabilizing effect of a shear layer. The instabilities in this type of a scenario are the Kelvin-Helmholtz type instability, only, in this case, instead of forming KH billow clouds, the instability causes the cloud layer to deplete!

A consequence of the shear driven instability can clearly be seen in the profiles of vertical velocity variance ($\overline{w''w''}$), shown in Fig. A7. All cases with wind farms show a peak at approximately 950 m, which is not to be found in the no wind farm case. Furthermore, this peak is found precisely at the location of the cloud-top. This is a clear signature of the enhanced entrainment of warm dry air aloft, into the STBL.

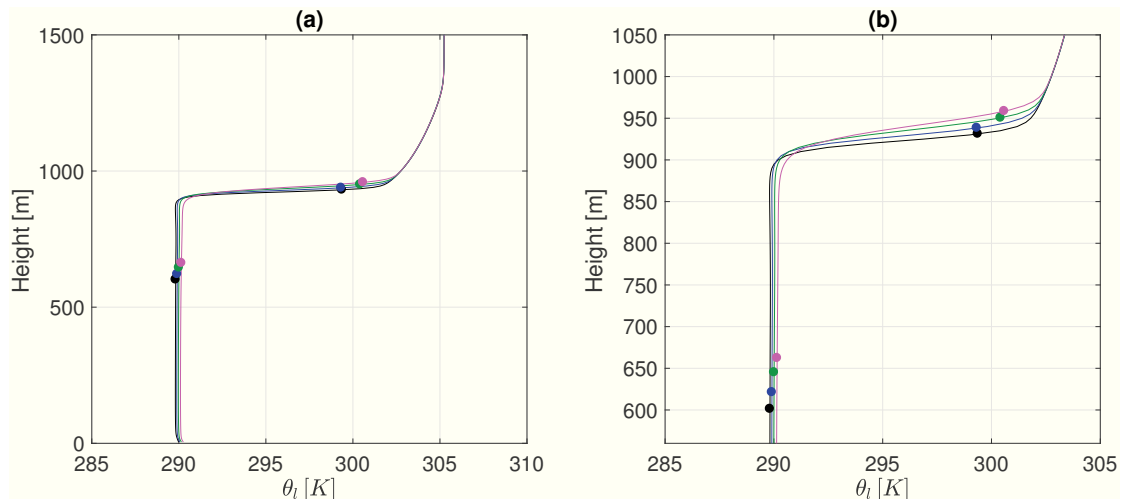


Figure A5 – Liquid Water Potential Temperature (θ_l) of (a) the full domain and (b) a cloud region. The circular markers mark the extent of the cloud for each case. Legend is the same as in Fig. A2(b)

Appendix A. Perturbation to a stratocumulus-topped boundary layer due to a very large wind farm

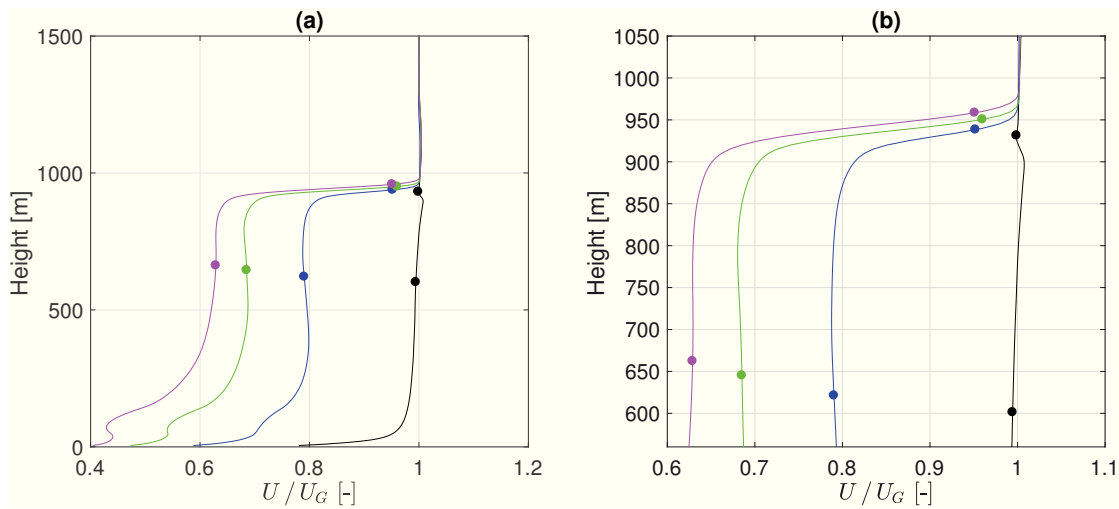


Figure A6 – Normalized wind speeds of (a) the full domain and (b) a cloud region. The circular markers mark the extent of the cloud for each case. Legend is the same as in Fig. A2(b)

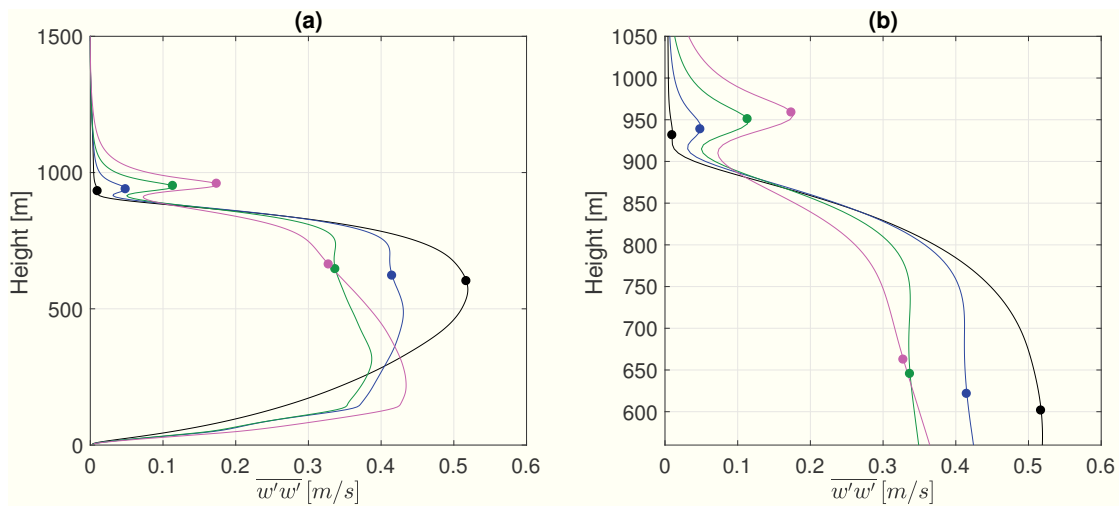


Figure A7 – Resolved vertical velocity variance of (a) the full domain and (b) a cloud region. The circular markers mark the extent of the cloud for each case. Legend is the same as in Fig. A2(b)

A.4 Conclusions

Results of a preliminary study to understand the effect of wind farms on stratocumulus clouds has been presented here. This work is directly inspired by the results in Chapter 2, where it was found that the large wind farms can significantly perturb the dynamics at the top of the atmospheric boundary layer. Results in this appendix show that the presence of a large wind farm causes a strong shear layer to develop at the capping inversion. This results in increases entrainment across the capping inversion resulting in shrinking and drying of the cloud layer and warming of the sub-cloud layer. This phenomenon deserves more attention and shall be explored in the future.

B Mean kinetic energy of finite sized wind farms

B.1 Introduction

In this appendix, we provide a mean kinetic energy budget based analysis of the evolution of the mean and turbulent flow quantities in a neutral atmospheric boundary layer (ABL) with a finite-sized wind farm. This appendix is an extension of Chapter 3.

B.2 Theoretical framework

Analysis of the LES data is based on performing time averaging followed by spanwise averaging of the flow quantities. Any variable $\phi(x, y, z, t)$ can be decomposed as $\langle \bar{\phi} \rangle_y(x, z) + \phi''(x, y, z) + \phi'(x, y, z, t)$, where the first term is the resultant time-averaged (denoted henceforth by the over-bar) and space-averaged (denoted henceforth by the angular brackets) value which is a function of only the streamwise distance and height, the following term being the spatial fluctuations in the time-averaged 3-D fields and the last term being the 4-D, time-fluctuating field at each point point of in the domain. Correlations between the time fluctuations of different velocity components at the same point in space result in the standard Reynolds flux terms which are further averaged in the spanwise direction, resulting in the form $\langle \overline{\phi'_1 \phi'_2} \rangle(x, z)$. The correlations between the spatial fluctuations in the time-averaged flow fields are known as the 'dispersive' stress terms of the form $\langle \overline{\phi_1'' \phi_2''} \rangle(x, z)$. The most important of these second-order statistics for this study are the vertical momentum fluxes. Correspondingly, the friction velocities $\{u_{*,hi}(x), u_{*,lo}(x)\}$ are given by $\sqrt{\langle \overline{u'w'} \rangle + \langle \overline{u''w''} \rangle + \langle \tau_{xz}^{sgs} \rangle}(x, z = z_h + D/2, z_h - D/2)$, where τ_{xz}^{sgs} is the vertical subgrid-scale flux. In these various different contexts such as flow over distributed forest canopies [Bailey and Stoll, 2013], flow over cubes [Belcher et al., 2003] and urban meteorology [Giometto et al., 2016], it is now recognised that modelling of this quantity is of principal importance for developing accurate parametrisations for mesoscale models. However, as we shall see further on, the highly organised, repeating arrangements in

Appendix B. Mean kinetic energy of finite sized wind farms

large (typically offshore) wind farms renders this quantity to be fairly negligible in the wind farm context.

The total momentum flux in the x and z directions (τ_x and τ_z , respectively) is computed as,

$$\langle \bar{\tau} \rangle_x = \langle \overline{u'u'} \rangle + \langle \overline{u''u''} \rangle + \langle \overline{\tau_{xx}^{sgs}} \rangle \quad (\text{B.1})$$

$$\langle \bar{\tau} \rangle_z = \langle \overline{u'w'} \rangle + \langle \overline{u''w''} \rangle + \langle \overline{\tau_{xz}^{sgs}} \rangle \quad (\text{B.2})$$

The principal tool for analysis in this study is the budget equation for the mean kinetic energy in the streamwise direction $\langle \bar{u} \rangle^2$ which can be written as,

$$0.5 \frac{\partial \langle \bar{u} \rangle^2}{\partial t} = \mathcal{H} + \mathcal{V} + \mathcal{P} + \mathcal{W}\mathcal{F}, \quad (\text{B.3})$$

where,

$$\mathcal{H} = -\frac{\partial [\langle \bar{\tau}_x \rangle \langle \bar{u} \rangle]}{\partial x} + \langle \bar{\tau}_x \rangle \frac{\partial \langle \bar{u} \rangle}{\partial x} - \langle \bar{u} \rangle^2 \frac{\partial \langle \bar{u} \rangle}{\partial x} - \langle \bar{u} \rangle \frac{\partial \langle \bar{p}^* \rangle}{\partial x}, \quad (\text{B.4})$$

$$\mathcal{V} = -\frac{\partial [\langle \bar{\tau}_z \rangle \langle \bar{u} \rangle]}{\partial z} + \langle \bar{\tau}_z \rangle \frac{\partial \langle \bar{u} \rangle}{\partial z} - \langle \bar{u} \rangle \langle \bar{w} \rangle \frac{\partial \langle \bar{u} \rangle}{\partial z}, \quad (\text{B.5})$$

$$\mathcal{P} = \langle \bar{u} \rangle \frac{\partial \bar{p}_\infty}{\partial x}, \quad (\text{B.6})$$

$$\mathcal{W}\mathcal{F} = \langle \bar{u} \rangle \langle \bar{F}_x \rangle \quad (\text{B.7})$$

Since the components of mean velocity in the spanwise direction ($\langle \bar{v} \rangle$) is 0 by definition and in the vertical direction ($\langle \bar{w} \rangle$) is negligible, the term $0.5 \langle \bar{u} \rangle^2$ is referred to as ‘MKE’ and Eq. (B.3) is referred to as ‘MKE budget’ in the remainder of the article. \mathcal{H} is the contribution to the MKE due to horizontal mean and turbulent motions. Terms from left to right in Eq. (B.4) are transport of MKE by horizontal turbulent momentum flux (\mathcal{H}_T), dissipation of MKE into TKE due to turbulence (\mathcal{H}_D), transport of MKE by mean motions or ‘advection’ (\mathcal{H}_A) and finally, MKE contribution due to streamwise gradients in the perturbed pressure field (\mathcal{H}_P). Except for the final term in Eq. (B.4), the remaining three terms have analogous counterparts in Eq. (B.5) denoted as \mathcal{V}_T , \mathcal{V}_D and \mathcal{V}_A respectively. \mathcal{P} represents the MKE contribution due to the mean pressure gradient, which in our case is imposed as the driving mechanism for the simulated flow (Eq. (B.6)). In turbulent channel flow, this term is negligible. Finally, in Eq. (B.7), $\mathcal{W}\mathcal{F}$ is the MKE lost due to drag induced by the wind turbines or correspondingly, the power lost by the ABL due to presence of the wind farm. All quantities are normalised by a velocity scale (U_∞) computed as the depth-averaged velocity far upstream of the windfarm. This ensures that all simulation results are for same mass inflow. The length scale used for the study is the height of the boundary layer.

Recalling Eqs. (B.1) and (B.2), the turbulent transport and dissipation terms can be further decomposed into contributions due to Reynolds, dispersive and subgrid-scale (SGS) fluxes.

These contributions are denoted by an additional subscript in symbols (r,c and s respectively). For example, $\mathcal{H}_T = \mathcal{H}_{T,r} + \mathcal{H}_{T,c} + \mathcal{H}_{T,s}$. Analogous expressions for \mathcal{H}_D , \mathcal{V}_T and \mathcal{V}_D exist.

This framework is valid for cases with no advection, which is valid far from the leading edge of the windfarm. In the fully-developed scenario, Eq. (B.3), the 1-D framework essentially reduces to a balance between \mathcal{V} and $\mathcal{W}\mathcal{F}$ (\mathcal{P} is negligible). In this study, we have extended the framework to include horizontal fluxes and thus, it is expected that the balance additionally includes \mathcal{H} .

Previous studies of flows over cubes or vegetated canopies have identified relevant regions of the flow based on a dominant term analysis of the above MKE budget equation. We have adapted the results of these studies to develop a theoretical framework for the wind farm scenario. This framework is schematically presented in Fig. B1.

Far upstream of the wind farm, the velocity profile $U(z)$ is that found in a standard neutrally stratified ABL, characterised by surface shear stress u_* and surface roughness z_0 . The first interesting region of the flow, immediately upstream of the wind farm is designated as the (i) ‘impact zone’. Here, the flow decelerates due to the adverse pressure gradients generated as a result of the upstream turbines in the leading row of the wind farm. This correspondingly results in the vertical mean velocity as a result of conservation of mass. Within the wind farm, downstream of the leading edge exists the (ii) ‘adjustment region’ - where the drag due to the obstacles in the flow is primarily balanced by advection and the mean flow decelerates rapidly. Above the wind farm, another region, known as (iii) ‘wind farm’ boundary layer is found. In this region of the flow, MKE is transported downwards towards the wind farm through vertical momentum fluxes. On the other hand, MKE is balanced through deceleration of the mean flow. If the wind farm is sufficiently long, the mean flow within the wind farm reaches a terminal velocity and instead of decelerating flow, the drag due to turbines is balanced by vertical flux of MKE. This region is the (iv) ‘fully-developed’ region. The region of flow within the wind farm between the adjustment region and the fully developed region is denoted as the ‘transition’ region where the mean flow decelerates much slower (in comparison to the adjustment region), while the vertical flux of MKE is increasing and is non-negligible in the MKE balance. An additional region of the flow within the internal boundary layer, known as the (v) ‘roughness sublayer’, is a region where the vertical turbulent motions are a source term in the MKE as opposed to being a sink term in the overlying IBL. The RSL extends deeper into the IBL with increasing distance from the leading edge of the windfarm. In wind energy literature, this region is also termed as the ‘wake’ layer. Lastly, the flow downstream of the trailing edge of the wind farm is called the (vi) ‘exit’ region, where the mean flow accelerates because the drag due to turbines is no longer present. Due to conservation of mass, a region of negative vertical velocity develops bringing MKE from aloft into the exit region. The exit region is complementary scenario of the impact zone with respect to the mean flow, but the exit region has significant turbulent transport of MKE as well that is not found in the impact zone.

Each of the flow regions defined above are characterised by relevant length scales. The impact, adjustment, transition, fully-developed and exit regions are characterised by L_I , L_A , L_T and

is region of downward flow at the top of the rotor disk. However this region does not extend to a larger distance downstream. This is in sharp contrast to the flow in the lower half of the rotor disk. Here is a large region of upward mean flow that occurs over the entire streamwise spacing. As we shall see in the following figure, these differences are directly related to the turbulent motions between turbines. It is important to keep in mind that the mean vertical velocity is an order of magnitude smaller than the mean horizontal velocity.

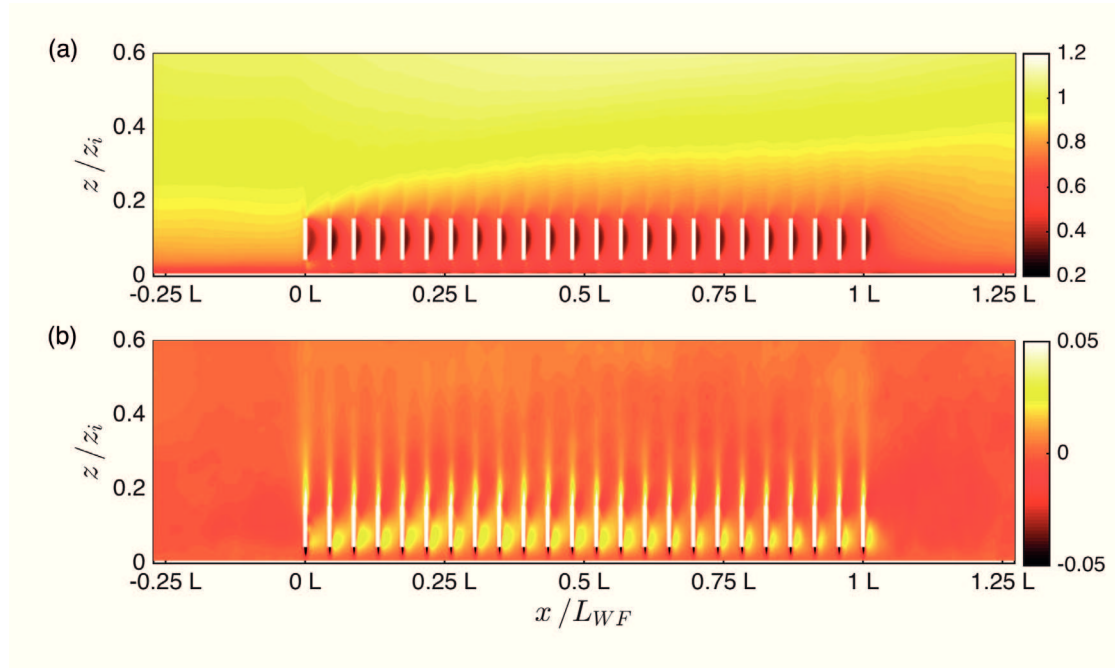


Figure B2 – Time-averaged velocity components in vertical plane through a column of wind turbines in AL-1 of (a) streamwise velocity component, (b) vertical velocity.

Figure B3 shows the evolution of spanwise-averaged turbulent quantities through the wind-farm. Figure B3a shows the turbulent kinetic energy ($TKE = 0.5\langle u'_i u'_i \rangle$) where it can be observed that the TKE seems to emanate from the top of the rotor disk and extends both downwards into the wind farm and upwards into the ABL. The high TKE region shows a distinctive triangular pattern. Vertical momentum flux ($\langle \overline{u' w'} \rangle$) is shown in Fig. B3b. A growing region of momentum flux can be observed, similar to the TKE. It has been shown in previous studies that vertical turbulent fluxes play a dominant role in the replenishment of momentum within the rotor-disk region in fully-developed conditions. Based on Fig. B3b, it is expected that with increasing distance within the wind farm, vertical turbulent motions become increasingly relevant. The lower half of the rotor disk shows a much lower momentum flux as compared to the upper-half of the rotor disk as well as the flux found in unperturbed ABL upstream of the wind-farm at the same height. In fact, the weak momentum flux in this region explains the dominance of mean vertical motions in this space shown in Fig. B2b. The final sub-figure in Fig. B3 shows the dispersive stress term $\langle \overline{u'' u''} \rangle$. We mentioned in passing in the previous section that dispersive stress terms have been shown to be important in previous studies of

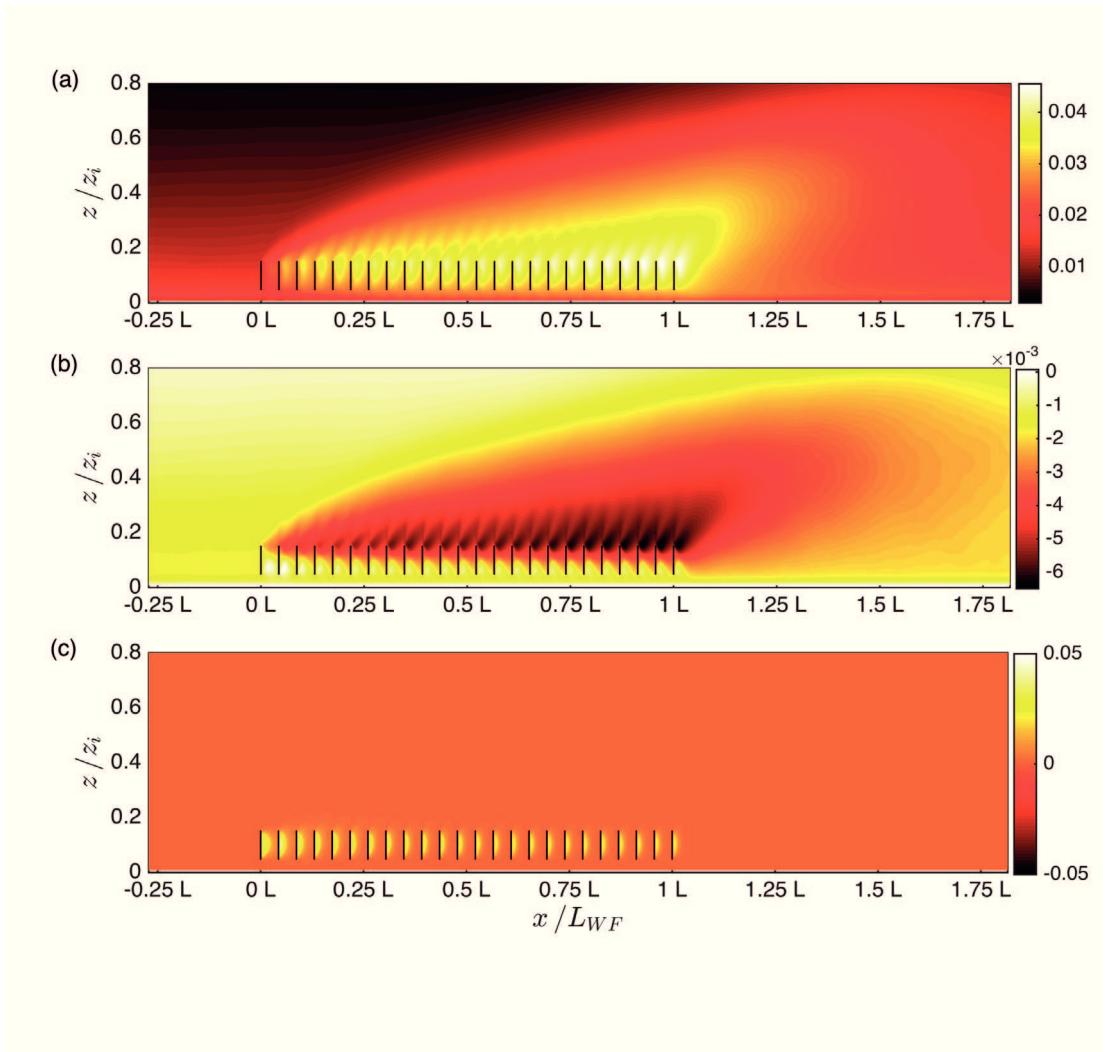


Figure B3 – Spanwise-averaged turbulent quantities for the AL-1 case, (a) TKE, (b) Vertical momentum flux, (c) Dispersive stress.

flows through sparse canopies. In Fig. B3c, it can be seen that dispersive stresses can be found only in localised regions of the flow, downstream of each wind turbine for a limited distance and is zero elsewhere. However, in these localised regions, the dispersive stress values are found to be comparable to the Reynolds flux terms shown in Fig. B3a,b.

B.3.2 Identification of relevant flow regions using MKE budgets

We now come to one of the main thrusts of this study, where different regions of the flow, as described in the theoretical framework in the previous section, are now identified. We begin by first studying the flow quantity \mathcal{H} which describes the MKE contribution due to horizontal mean and turbulent motions. Briefly revisiting the classical channel flow theory, $\mathcal{H} = 0$ in fully developed channel flow and \mathcal{P} is balanced by \mathcal{V} . An increase in surface roughness results in the formation of an internal boundary layer which begins at the point where the surface

transition occurs and the flow decelerates ($\mathcal{H} > 0$). In our simulations, \mathcal{H} is slightly negative (with magnitude comparable to standard ABL flow) far away from the wind-farm region due to the periodic boundary conditions and the fact that the flow accelerates downstream of the trailing edge of the wind farm. This fact however allows us to identify the IBL in LES-generated flow data by tracking the points where \mathcal{H} transitions from negative to positive, which is the upstream edge of the IBL and the transition from positive to negative, which is the downstream edge of the IBL. The flow quantity \mathcal{H} and the marked boundaries of the IBL are shown in Fig. B4, for all the five wind farm configurations. It can be qualitatively seen that spatial extent of the IBL is quite similar for all the five cases. There are three minor points of differences. Firstly, the initial growth of the IBL seems to show a signature of the wind farm configuration. This difference extends only for the first couple of rows of the wind farm. The second point of difference is found in the trailing edge of the IBL. Finally, within the spatial extent of the IBL, the magnitude of \mathcal{H} can be clearly seen to be directly proportional to the wind farm density - higher the density, more intense is the perturbation induced in values of \mathcal{H} . The first two points are quantified further in Fig. B5, where the boundaries of the IBL in each of the 5 cases are extracted and shown. A closer look reveals that the signature of the wind farm arrangement extends upto $0.2L_{WF}$ following which, the IBL of each of the five cases are very similar. Differences between the cases emerge once again when the IBLs reach a height of $0.7z_i$. While the difference is only minor, loading of the wind farm seems to result in faster growth of the IBL resulting in the fact that the ST-5 IBL is the first to reach the top of the channel, closely followed by its aligned counterpart. Next are IBLs by AL-2 and AL-3 followed by the least-dense wind farm AL-4 at the end. The top of the domain is reached for all the 5 cases between $0.75L_{WF}$ and $1L_{WF}$. The trailing edge of the wind farm shows much larger differences above $0.7z_i$ with the top of the IBL extending from $2.5L_{WF}$ for ST-5 to $3.5L_{WF}$ for the AL-2 case. Overall, \mathcal{H} values for the five cases show that growth of the IBL is only weakly dependent on actual wind farm density and indicates that the height of the ABL (z_i) may be the major modulating parameter.

Transition of \mathcal{H} upstream of the wind farm at hub-height can also be used to identify the ‘impact zone’ of the wind farm. It is found that all the five cases have an impact zone of $\sim 5D$, where D is the diameter of the rotor disk. This result is interesting because once again, the spatial arrangement of the wind turbines and the wind farm density does not seem to play a major role in modulating the spatial extent of the impact zone. Dynamical considerations of upstream pressure perturbation and the related velocity deceleration in the impact zone should not be different from the so-called ‘induction zone’ of wind turbines, which are incidentally reported to be of $\mathcal{O}(D)$ in literature. It can then be stated that the spatial extent of the impact zone scales with the diameter of the rotor disk alone.

Figure B6 shows the flow quantity \mathcal{V} for the five cases. \mathcal{V} is the contribution to MKE from vertical mean and turbulent motions. As mentioned earlier, in the standard turbulent channel flow, \mathcal{V} balances \mathcal{P} . Since \mathcal{P} is positive by definition, \mathcal{V} is negative throughout the depth of the channel flow. Within the internal boundary layer, as \mathcal{H} increases and become positive, \mathcal{V} must necessarily increase in magnitude to maintain the dynamic balance (while remaining < 0).

Appendix B. Mean kinetic energy of finite sized wind farms

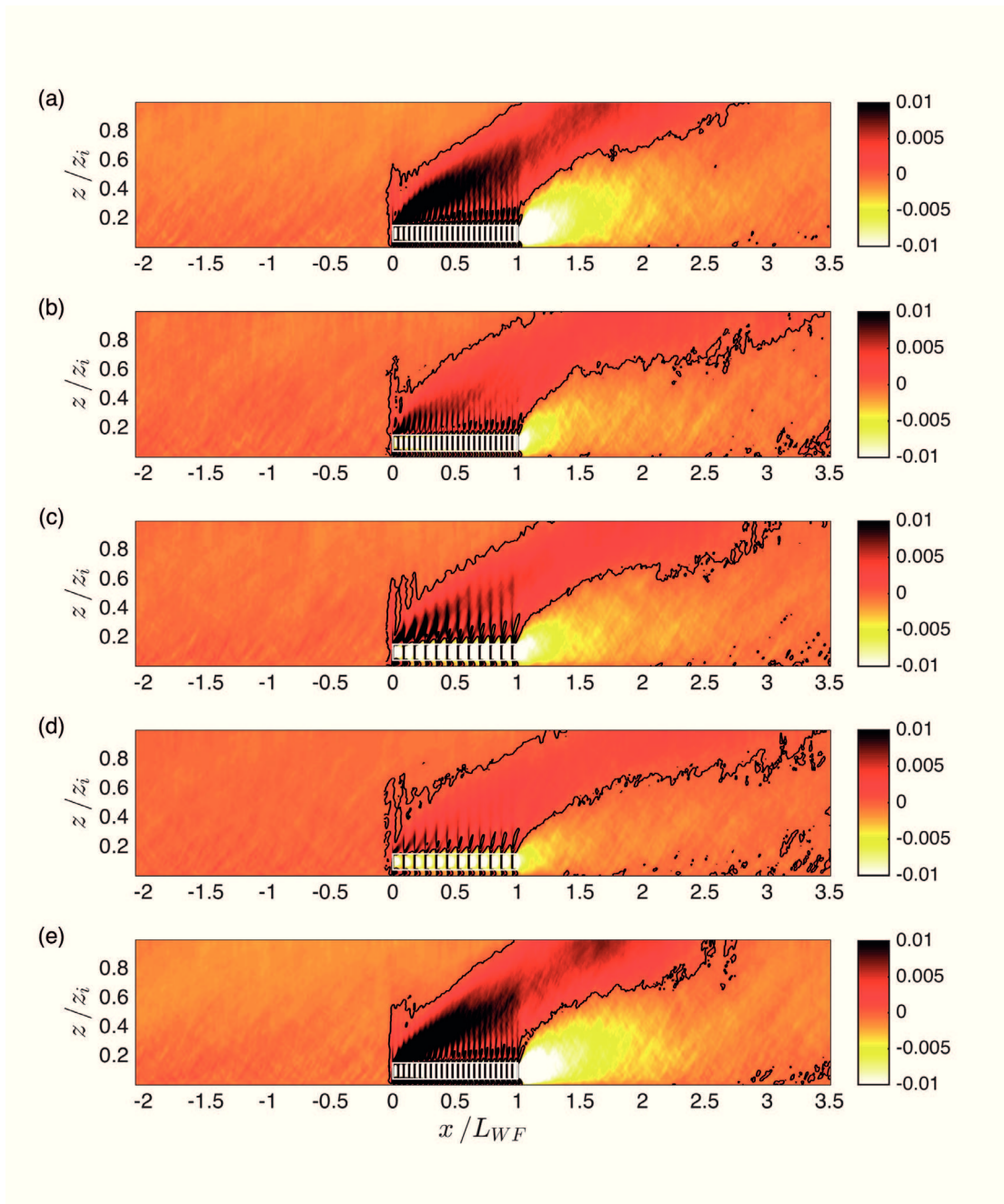


Figure B4 – Contribution to MKE due to horizontal motions \mathcal{H} for (a) AL-1, (b) AL-2, (c) AL-3, (d) AL-4, (e) ST.

This can be clearly seen in Fig. B6 by the fact that spatial extent of the IBL, marked by dotted lines neatly encompasses the intense blue region of the flow signifying high magnitude of \mathcal{V} . This, within the IBL, \mathcal{H} is positive highlighting the fact that deceleration of the flow results as a source of MKE while \mathcal{V} acts as a sink of MKE. The mean horizontal motions are converted in turbulent vertical motions. The sign of \mathcal{V} reverses within the wind farm, signifying that in this region of the flow, turbulent vertical motions act as net contributors to MKE, a fact already

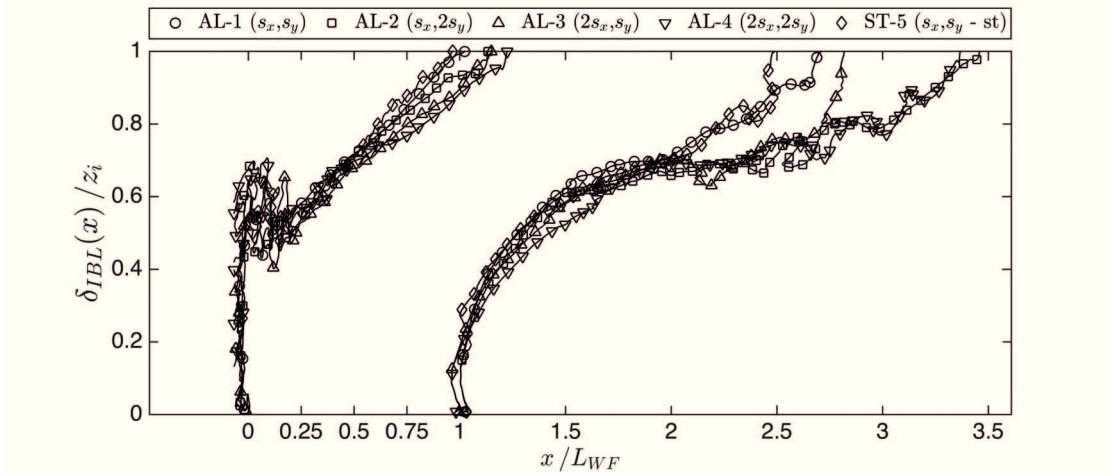


Figure B5 – Internal Boundary Layer for different wind farm configurations.

highlighted in this article and in previous studies. However, calculation of \mathcal{V} is further helpful in defining the boundaries of the ‘exit region’ of the flow. Downstream of the trailing edge of the windfarm, the flow suddenly accelerates due to removal of the wind-turbine drag force. Note that in this region, \mathcal{H} can be seen to be negative in Fig. B4 and correspondingly, the values of \mathcal{V} are positive. At the certain distance further downstream, values of \mathcal{V} transition to negative values and boundaries are marked in Fig. B6. We characterise the exit region in terms of the horizontal extent and height and the values extracted from the LES data are shown in Figs. B7 and B8 respectively. Both these quantities are found to be directly proportional to the wind farm density even though the differences are not quite large between the wind farms. Figure B7 shows that the horizontal extent of the exit zone ranges from $\approx 1 L_{WF}$ for the cases AL-1 and ST-5 to $0.5 L_{WF}$ for the case AL-4. There is a slight difference between the cases AL-2 and AL-3 of $0.1 L_{WF}$ even though these two cases have the same wind farm density. This shows a slight bias towards streamwise spacing as compared to the spanwise spacing. We shall see further evidence of this bias in the proceeding sections. The height of the exit zone is lowest for the least-dense wind farm (AL-4) and is equal to $0.3 z_i$. The exit zone for the AL-1 and ST-5 cases have the largest vertical extent of the exit zone at $0.48 z_i$. Interestingly, AL-2 and AL-3 cases show the same height of the exit zone at $0.4 z_i$.

A component of \mathcal{V} , $\mathcal{V}_{T,r}$ which is the contribution to MKE due to turbulent transport of MKE due to vertical momentum flux, is a useful flow quantity to track the ‘roughness’ sub-layer. $\mathcal{V}_{T,r}$ changes sign from negative within the overlying IBL to positive within the RSL. This implies that it changes from being a sink of MKE to a source within the RSL. In the wind-energy literature, this region is also denoted as the ‘wake-layer’. The values for $\mathcal{V}_{T,r}$ for the five cases are shown in Fig. B10. The oscillatory transition points for the sign of $\mathcal{V}_{T,r}$ are due to the individual wakes of the wind turbine. The RSL is tracked approximately by connecting the peaks of the oscillatory transition surface and shown in Fig. B10 by white lines. For better representation, the RSL is extracted and presented in Fig. B12. Similar to the IBLs described earlier, the RSLs for the different cases seem to be surprisingly similar.

To summarise the analysis thus far, the modus operandi to find the flow regions described

Appendix B. Mean kinetic energy of finite sized wind farms

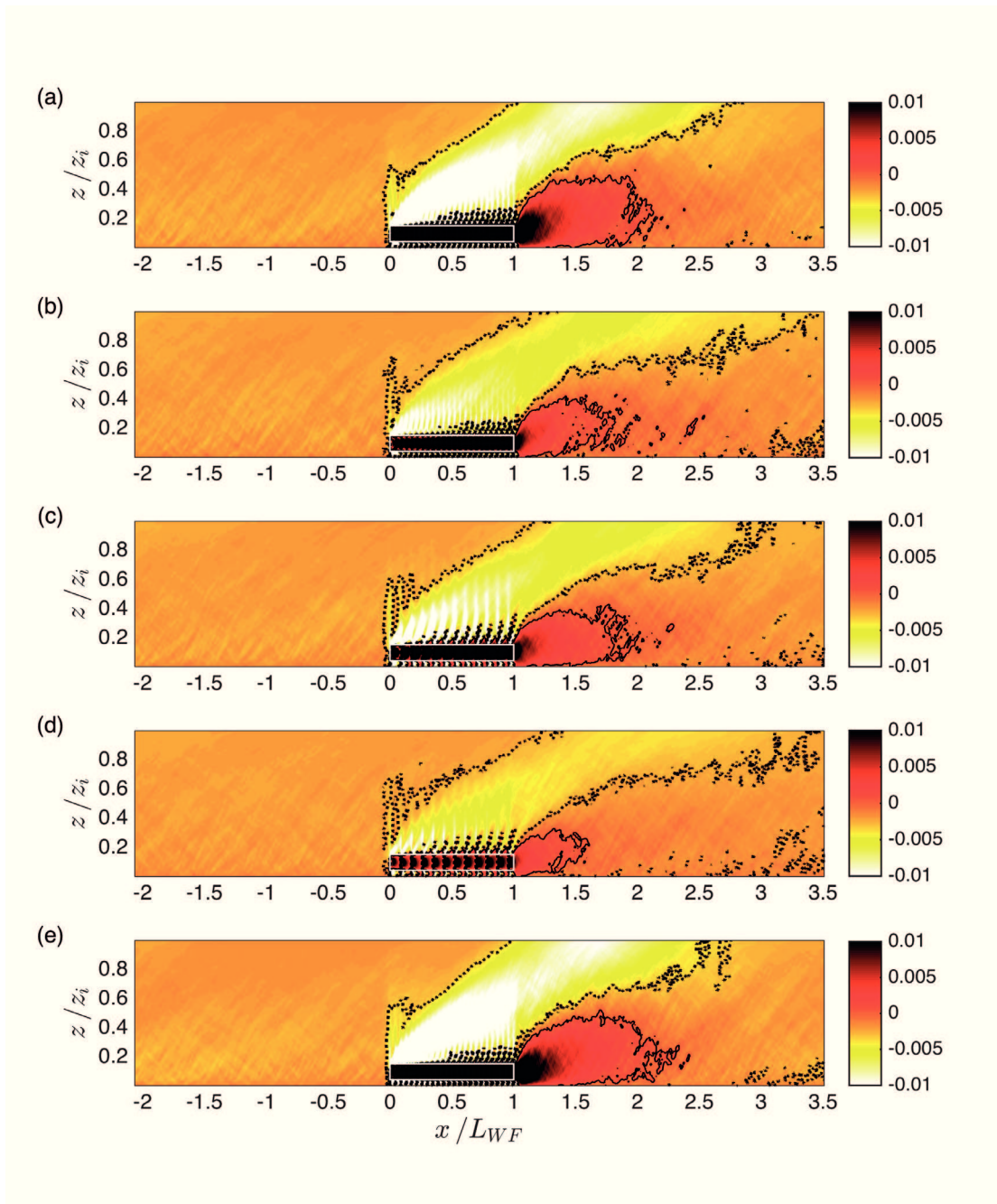


Figure B6 – Contribution to MKE due to vertical motions \mathcal{V} for (a) AL-1, (b) AL-2, (c) AL-3, (d) AL-4, (e) ST.

in the theoretical framework (see Sect. B.2) has been to track sign transitions of relevant flow quantities. Sign transitions indicate change of that particular flow mechanism from acting as source to becoming a sink of MKE or vice-versa. By tracking $\mathcal{H} = 0$, we have identified the spatial extent of the IBL and the ‘impact zone’ whereas $\mathcal{V} = 0$ and $\mathcal{V}_{T,r} = 0$ have been used to identify the exit zone and the RSL respectively.

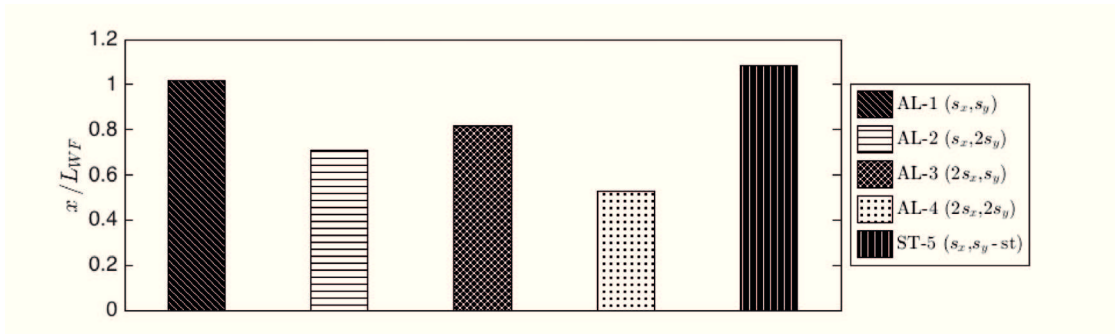


Figure B7 – Horizontal extent of exit region.

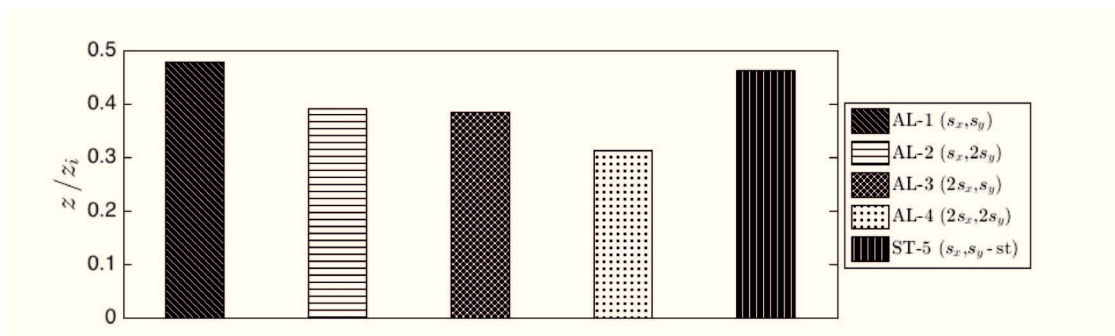


Figure B8 – Vertical extent of the exit region.

B.3.3 MKE budget within the windfarm

We now focus of the evolution of the terms of MKE budget within the wind farm. This helps us identify the remaining three relevant flow regions, i.e., the ‘adjustment’ and the ‘fully-developed’ region. MKE budget within the wind farm are relevant to many questions in the wind energy industry with regards to wind turbine spacing, arrangement and wind farm length.

Before the terms of the MKE budget are explored, some additional averaging is necessary to simplify the analysis. First, all terms are averaged vertically over the rotor-disk region. The terms are additionally averaged in the streamwise direction using a length of $l_x = 2s_x$. This allows results of cases AL-1, AL-2 and ST-5, with spacing of s_x to be compared with those from cases AL-3 and AL-4 which have double the spacing. The averaging scheme is summarised in the schematic shown in Fig. B11. The averaging box is shifted upstream by 1D from the turbine location so that the flow quantities within the induction zone of the turbine are included in the averaging. Finally, the averaging boxes are contiguous and thus cover the entire wind farm. We would like to point out that since the quantities we average are not symmetrical around the turbine, the width and the placement of the averaging is important. Different box sizes and whether the boxes are contiguous or not changes the averaged values and in this sense, the averaging scheme is certainly not objective. However, for the purpose of comparing the different cases, it is sufficient to adopt a uniform averaging scheme across the five cases. The averaged quantities must therefore be analysed keeping in mind the fact that an averaging block has different number of turbines for each case. For example, AL-1 and ST-5 have four

Appendix B. Mean kinetic energy of finite sized wind farms

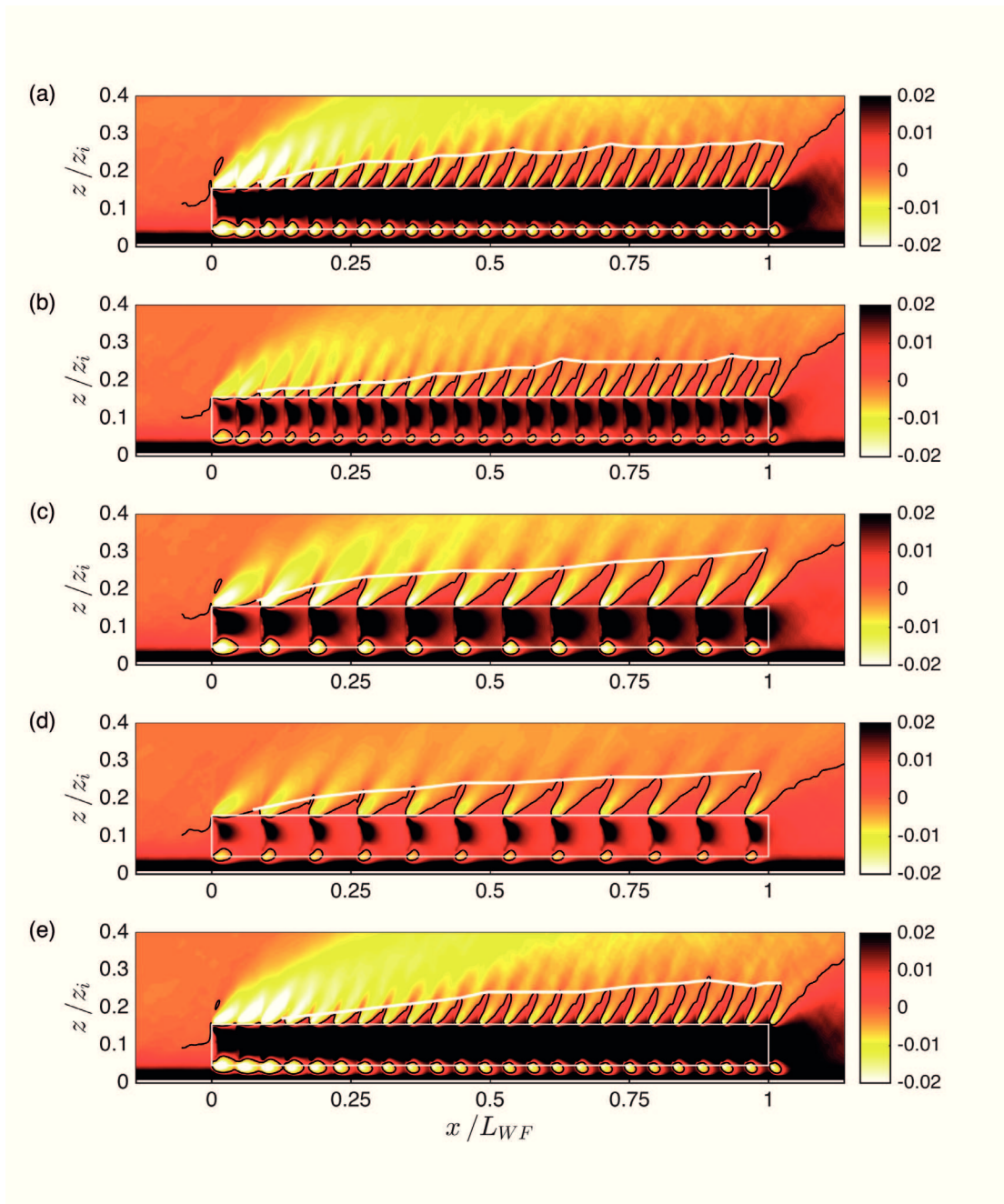


Figure B9 – Contribution to MKE due to vertical turbulent momentum flux $\mathcal{V}_{T,r}$ for (a) AL-1, (b) AL-2, (c) AL-3, (d) AL-4, (e) ST.

times as many turbines per averaging block as AL-4. Correspondingly, AL-2 and AL-3 have twice as many turbines.

Given the large number of terms in full MKE budget, complete results of only the representative case of AL-1 are shown. The purpose here is to identify the dominant terms in the MKE budget. Analysis of the other cases (not shown here) show exactly the same dominant terms and thus, comparing only the identified dominant terms from the different cases is sufficient for our

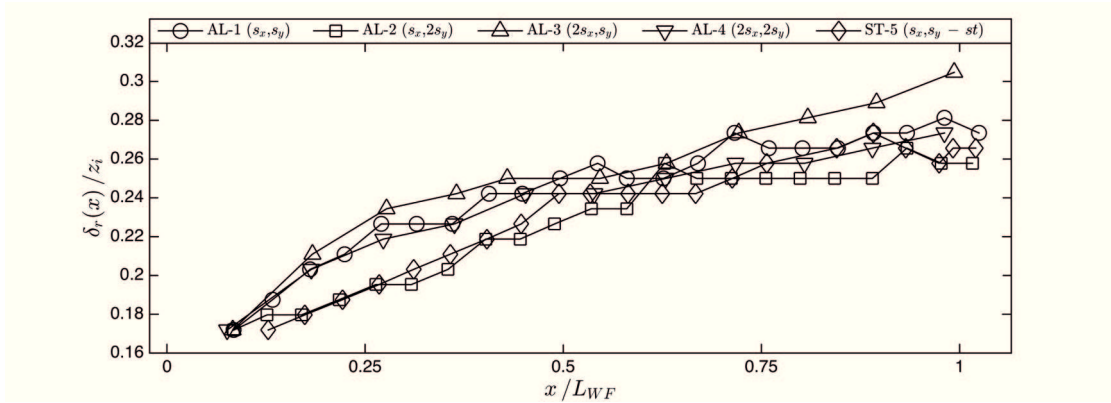


Figure B10 – Roughness sublayer (RSL) for different cases.

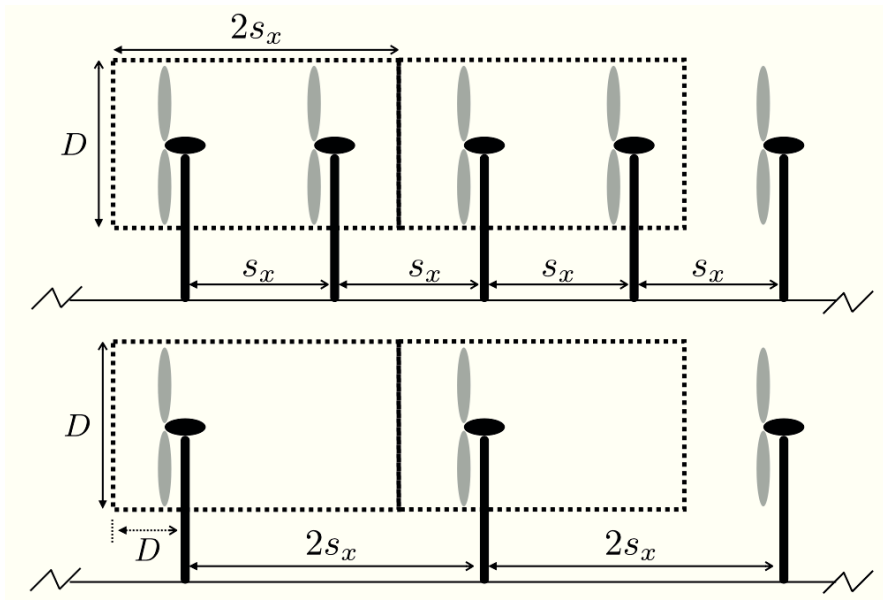


Figure B11 – Averaging Scheme for different wind farm cases.

purpose of highlighting the role played by turbine spacing and arrangement.

In Fig. B12a, terms of Eq. (B.3), namely, \mathcal{H} , \mathcal{V} , \mathcal{P} and \mathcal{WF} are shown along with the residual term. The residual term is zero for the length of the wind farm and is shown only to highlight that the budget is closed. Note that \mathcal{P} is found to be negligible as expected in turbulent channel flows. The most interesting result is the variation of \mathcal{H} vis-à-vis \mathcal{V} , where \mathcal{H} shows a monotonic decrease with a sharp gradient initially and the opposite trend of \mathcal{V} . These trends can be guessed intuitively by considering that the first row of the wind farm is directly impacted by the incoming, unperturbed flow and there is little or no vertical momentum flux. Deep into the windfarm, the flow can be expected to reach a terminal velocity and there is no flux of MKE through horizontal motions, mean or turbulent. \mathcal{H} thus reaches approximately zero by the end of the wind farm. However, it does not become exactly zero as expected. On the other hand, the contribution to MKE due to vertical motions, \mathcal{V} , reaches a steady state at

Appendix B. Mean kinetic energy of finite sized wind farms

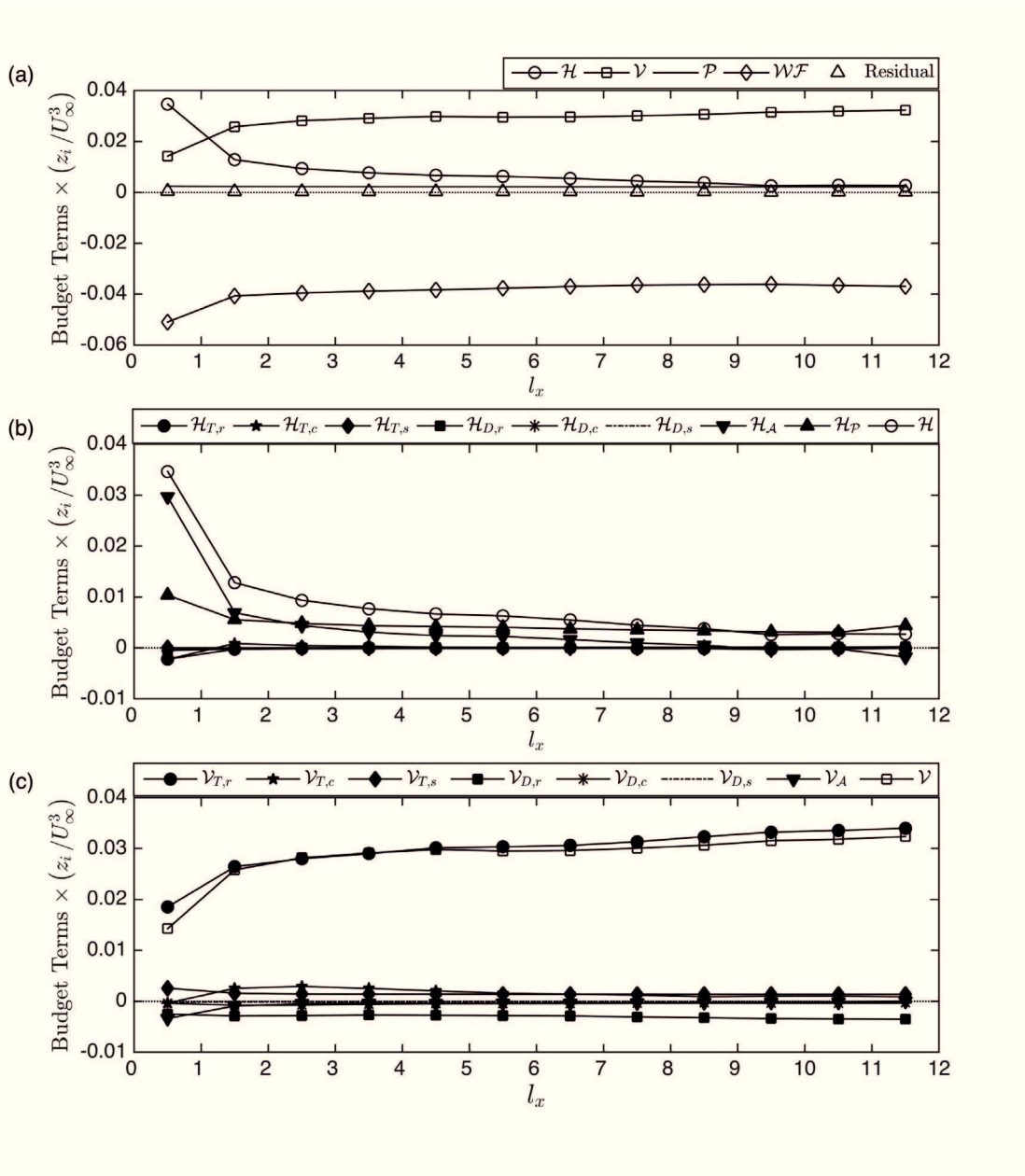


Figure B12 – Terms of the mean kinetic energy budget equation for the AL-1 case.

$6l_x$. Next, all components of \mathcal{H} are presented in Fig. B12b. It is clear that of the 8 components that add up to \mathcal{H} , only two components are dominant, namely, contribution to MKE through advection, \mathcal{H}_A and gradients in the pressure perturbation field, \mathcal{H}_P . Interestingly, \mathcal{H}_A is nearly zero beyond $9l_x$. This shows that the velocity gradients are zero and there is no advection. Instead, \mathcal{H}_P remains non-zero throughout the windfarm and remains nearly constant beyond $4l_x$. The dominant term analysis for \mathcal{V} , shown in Fig. B12c, reveals that there is only one dominant component, $\mathcal{V}_{T,r}$ out of the 7 components that add up to \mathcal{V} . $\mathcal{V}_{T,r}$ is the turbulent transport of MKE due vertical momentum flux. Thus, based on the dominant term

analysis, Eq. (B.3) can be restated as

$$0 \approx \mathcal{H}_A + \mathcal{H}_P + \mathcal{V}_{T,r} + \mathcal{W}\mathcal{F}, \quad (\text{B.8})$$

with two important points to keep in mind. Firstly, the above equation is valid only for within the windfarm. Secondly, the above flow quantities are averaged in the fashion described earlier in this sub-section, i.e, vertically averaged over the rotor-disk region and horizontally over a distance of $l_x = 2s_x$.

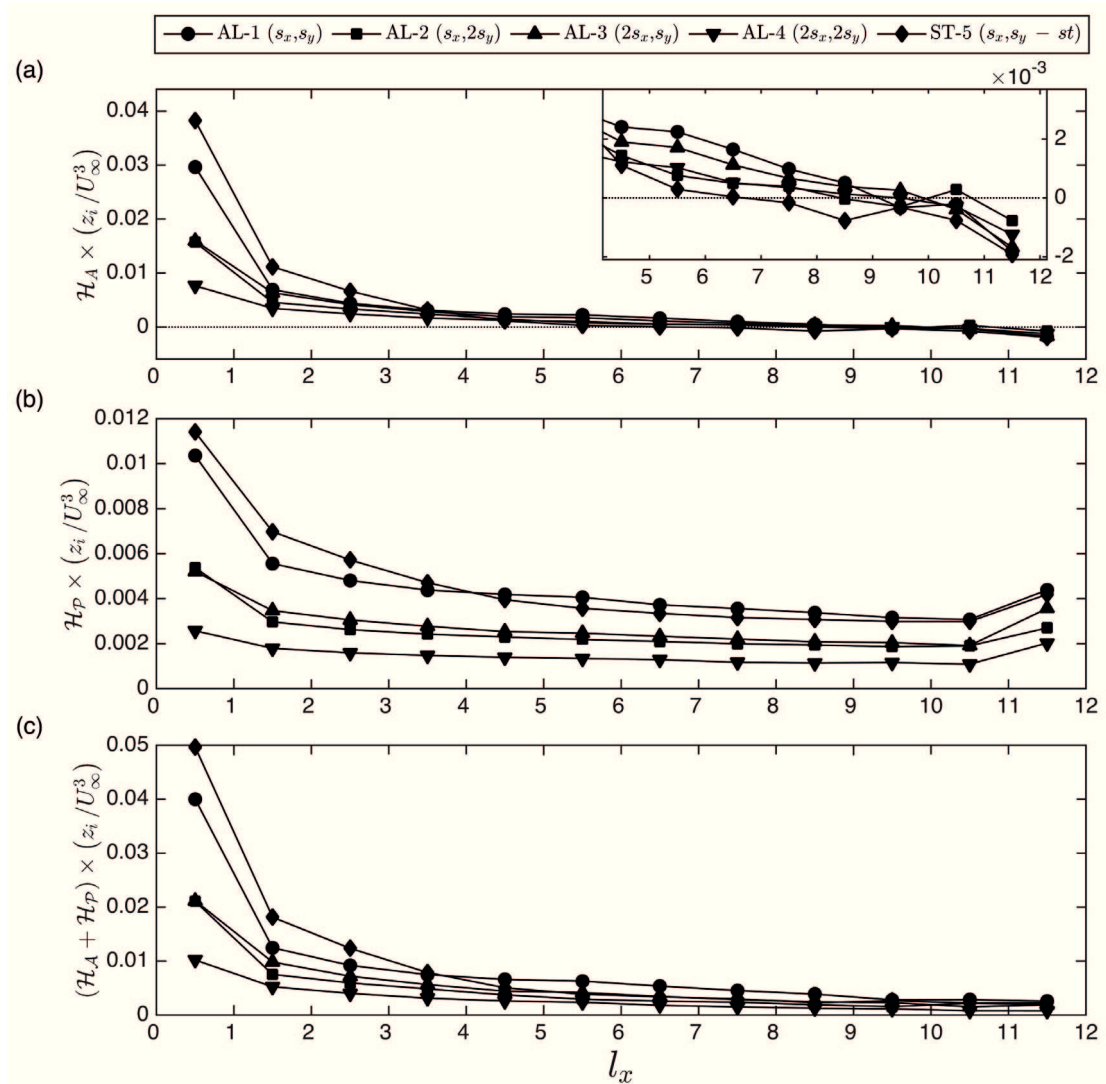


Figure B13 – Intercomparison of the terms of the mean kinetic energy budget equation for all the wind farm cases.

Having identified the dominant terms in the MKE budget, we can now focus our analysis on understanding how wind farm spacing and arrangement modulate the evolution of these flow quantities. Evolution of \mathcal{H}_A , \mathcal{H}_P and $\mathcal{H}_A + \mathcal{H}_P$ for the five cases is shown in Fig. B13a,b

Appendix B. Mean kinetic energy of finite sized wind farms

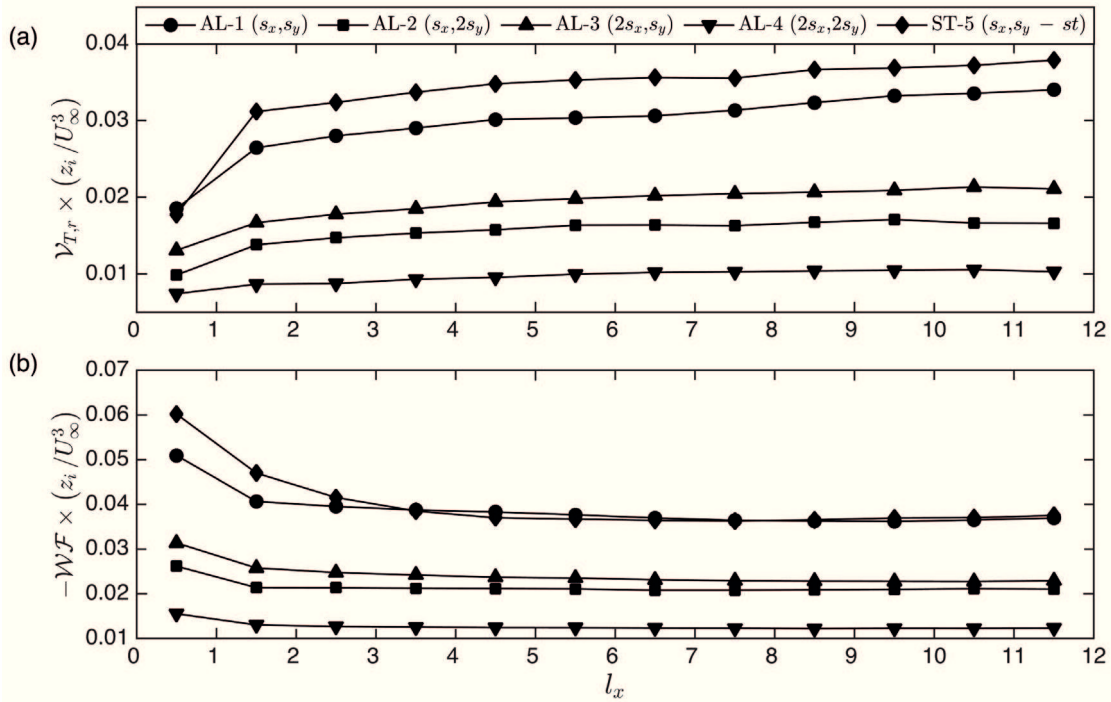


Figure B14 – Intercomparison of the terms of the mean kinetic energy budget equation for all the wind farm cases. (Continued from the previous figure)

and c respectively. There are a few surprising results to be noted. Firstly, evolution of \mathcal{H}_d shows no differences between the five cases beyond $\approx 4l_x$ and \mathcal{H}_A becomes negligible for all cases beyond $7l_x$. The initial values of \mathcal{H}_A show a clear signature of the wind farm setup and an increasing density results in higher values of \mathcal{H}_A as expected. Note that there is negligible difference between AL-2 and AL-3 showing that advection of MKE has no bias for streamwise or spanwise spacing. The staggered wind farm (ST-5) shows larger advection as compared to its aligned counterpart in this region. This is due to the fact that staggering results in higher effective blocking of the flow and thus the mean streamwise velocity gradients are larger than in the aligned scenario where there perturbation to the flow is limited to the wind turbine columns. In Fig. B13b, the evolution of \mathcal{H}_φ shows a clear influence of wind farm arrangement throughout the entire length of the wind farm. This term never goes to zero due to a continuous pressure drop across wind turbines. Thus it can be summarized that the effect of the wind farm setup on the evolution of \mathcal{H} is limited to the initial part of the wind farm upto $0.3L_{WF}$ and is negligible for the remaining wind farm.

The downstream evolution of $\mathcal{V}_{T,r}$ for the five cases is shown in Fig. B14a. Here, the influence of the wind farm setup is far more apparent in comparison to the dominant horizontal terms discussed in the previous paragraphs. In general, there is a direct correlation between the wind farm density and the values of $\mathcal{V}_{T,r}$ with two significant points. Firstly, we can see that the staggered wind farm induces stronger vertical turbulent motions and the resultant transport of MKE as compared to its aligned counterpart. Secondly, even though AL-2 and AL-3 have the same wind farm density, AL-3 shows larger values of $\mathcal{V}_{T,r}$ as compared to AL-2. The fact

that AL-3 has greater spacing in the streamwise direction whereas AL-2 has greater spacing in the spanwise direction seems to bias the evolution of $\mathcal{V}_{T,r}$ unlike the evolution of \mathcal{H}_A and \mathcal{H} for example.

The net effect of the different trends of \mathcal{H}_A , \mathcal{H}_D , $\mathcal{V}_{T,r}$ culminates in the trend of the power lost by the ABL due to wind-turbine drag, \mathcal{W}_F and is shown in Fig. B14b. ST-5 and AL-1 show negligible difference beyond $4l_x$ and the differences between AL-2 and AL-3 are small almost throughout the wind farm. Finally, AL-4 shows the minimum power as expected.

B.4 Conclusions

The analysis and results presented in this appendix are an extension of Chapter 3 with regards to the identification of the flow-adjustment and flow-equilibrium through a finite-sized wind farm. The analysis presented herein was motivated by the need to provide a more theoretical basis for identification of the relevant regions of the flow. The MKE budget analysis helped to identify the global-wake of the wind farm and its upstream as well as downstream impact. Finally, the roughness sublayer developed above the wind farm is identified. Intercomparison between terms of the MKE budget equation for wind farms with different spacings further confirmed the results in Chapter 3 that the streamwise spacing plays a dominant role in modulating the flow through a wind farm. The dominant terms identified in the MKE budget shall be useful in developing flexible low-order models for power outputs from wind farms in the near future.

Bibliography

- Brian N Bailey and Rob Stoll. Turbulence in sparse, organized vegetative canopies: a large-eddy simulation study. *Boundary-layer meteorology*, 147(3):369–400, 2013.
- SE Belcher, N Jerram, and JCR Hunt. Adjustment of a turbulent boundary layer to a canopy of roughness elements. *Journal of Fluid Mechanics*, 488:369–398, 2003.
- MG Giometto, A Christen, C Meneveau, J Fang, M Krafczyk, and MB Parlange. Spatial characteristics of roughness sublayer mean flow and turbulence over a realistic urban surface. *Boundary-Layer Meteorology*, 160(3):425–452, 2016.
- Dennis L Hartmann, Maureen E Ockert-Bell, and Marc L Michelsen. The effect of cloud type on earth’s energy balance: Global analysis. *Journal of Climate*, 5(11):1281–1304, 1992.
- MP Kirkpatrick, AS Ackerman, DE Stevens, and NN Mansour. On the application of the dynamic smagorinsky model to large-eddy simulations of the cloud-topped atmospheric boundary layer. *Journal of the atmospheric sciences*, 63(2):526–546, 2006.
- Chin-Hoh Moeng, Bjoern Stevens, and Peter P Sullivan. Where is the interface of the stratocumulus-topped pbl? *Journal of the atmospheric sciences*, 62(7):2626–2631, 2005.
- Olivier Pauluis. Thermodynamic consistency of the anelastic approximation for a moist atmosphere. *Journal of the Atmospheric Sciences*, 65(8):2719–2729, 2008.
- Kyle G Pressel, Colleen M Kaul, Tapio Schneider, Zhihong Tan, and Siddhartha Mishra. Large-eddy simulation in an anelastic framework with closed water and entropy balances. *Journal of Advances in Modeling Earth Systems*, 7(3):1425–1456, 2015.
- Kyle G Pressel, Siddhartha Mishra, Tapio Schneider, Colleen M Kaul, and Zhihong Tan. Numerics and subgrid-scale modeling in large eddy simulations of stratocumulus clouds. *Journal of Advances in Modeling Earth Systems*, 2017.
- Bjorn Stevens, Donald H Lenschow, Gabor Vali, Hermann Gerber, A Bandy, B Blomquist, JL Brenguier, CS Bretherton, F Burnet, Teresa Campos, et al. Dynamics and chemistry of

Bibliography

marine stratocumulus—dycoms-ii. *Bulletin of the American Meteorological Society*, 84(5): 579–593, 2003.

Bjorn Stevens, Chin-Hoh Moeng, Andrew S Ackerman, Christopher S Bretherton, Andreas Chlond, Stephan de Roode, James Edwards, Jean-Christophe Golaz, Hongli Jiang, Marat Khairoutdinov, et al. Evaluation of large-eddy simulations via observations of nocturnal marine stratocumulus. *Monthly weather review*, 133(6):1443–1462, 2005.

Robert Wood. Stratocumulus clouds. *Monthly Weather Review*, 140(8):2373–2423, 2012.

Takanobu Yamaguchi and David A Randall. Large-eddy simulation of evaporatively driven entrainment in cloud-topped mixed layers. *Journal of the Atmospheric Sciences*, 65(5): 1481–1504, 2008.

Varun Sharma

3, Rue de Crissier
1020 Renens, Switzerland
☎ +41 (77) 484 3011
☎ +41 (21) 693 6369
✉ varun.sharma@epfl.ch

Education

- 2013–present **Doctoral Studies in Environmental Fluid Mechanics**, *École Polytechnique Fédérale de Lausanne*, Lausanne.
Specialization in the Atmospheric Boundary Layer
- 2011–2013 **Masters in Mathematics**, *École Polytechnique Fédérale de Lausanne*, Lausanne.
Specialisation in Computational Sciences
- 2006–2010 **Bachelors in Civil Engineering**, *Indian Institute of Technology Bombay*, Mumbai.

Interests

- Atmospheric Boundary Layer, Turbulence, Buoyancy Effects, Large Eddy Simulation techniques

Doctoral Studies

- title *Numerical Experiments of Atmospheric Boundary Layer flows: Interplay between distributed drag elements and buoyancy effects*
- supervisors Prof. Michael Lehning (EPFL, SLF-Davos), Prof. Marc Parlange (Monash University, Australia, formerly at EPFL)
- description My thesis focuses on understanding a broad range of atmospheric flow scenarios ranging from idealised flat-terrain, on-shore wind-farms, alpine terrain and polar environments with particular emphasis on the role of buoyancy at small scales. Research published thus far has been limited to exploring the diurnally evolving atmospheric boundary layer for the flat-terrain and wind-farm scenarios. In collaboration with other colleagues, I have also worked on using numerical weather prediction (NWP) data for improved wind-resource assessment in complex alpine terrain. Current work is focussed on simulating aeolian transport of solid particulate matter using the Lagrangian stochastic modeling (LSM) framework coupled with the LES. The model is extended to account for heat and mass transfer between the suspended solid phase and the air and thus can simulate phenomena such as evaporating and sublimating hydrometeors. The aim at present is to simulate sublimation of drifting and blowing snow and its effect on the Atmospheric Boundary Layer (ABL) dynamics. By additionally simulating drifting and blowing snow around idealized hills, we would like to highlight zones of preferential erosion, deposition and sublimation of snow, a question of prime importance in understanding the water mass balance in alpine and polar environments.

Publications

- Journal Articles
- [Sharma, V., Cortina, G., Margairaz, F., Parlange, M.B. and Calaf M., \(2017\)](#) Evolution of flow characteristics through finite-sized wind farms and influence of turbine arrangement, *Renewable Energy*
 - [Cortina, G., Sharma, V. and Calaf, M., \(2017\)](#) Wind farm density and harvested power in very large wind farms: A low-order model, *Physical Review Fluids*
 - [Cortina, G., Sharma, V., and Calaf M., \(2017\)](#) Investigation of the incoming wind vector for improved wind turbine yaw-adjustment under different atmospheric and wind farm conditions, *Renewable Energy* 101, 376-386, doi: 10.1016/j.renene.2016.08.011
 - [Sharma, V., Parlange, M.B. and Calaf M., \(2016\)](#) Perturbations to the spatio-temporal characteristics of a diurnal ABL due to an idealised wind-farm, *Boundary Layer Meteorology*, doi:10.1007/s10546-016-0195-0
 - [Sharma, V., Calaf, M., Lehning, M., and Parlange, M. B. \(2015\)](#) Time-adaptive wind turbine model for an LES framework. *Wind Energy*, doi:10.1002/we.1877.
- Conferences
- [Sharma, V., Kruyt, B., Franziska, G., Lehning, M.,](#) Wind Energy Potential in Switzerland: Discovering Localized Thermo-topographic Flows and Associated Wind Resource, 22nd Symposium on Boundary Layers and Turbulence, Salt Lake City, Utah, USA, June 20-24, 2016
 - [Sharma, V., Ali, N., Cal, R.B., Parlange, M.B., Calaf, M.,](#) Role of coherent structures in mean kinetic energy entrainment by finite-sized wind farms and lessons from canopy flows, 22nd Symposium on Boundary Layers and Turbulence, Salt Lake City, Utah, USA, June 20-24, 2016
 - [Sharma V., Parlange M.B. and Calaf M.,](#) Adjustment of mean velocity and turbulence due to a finite-sized wind farm in a neutral ABL - a LES study, American Physical Society, Division of Fluid Dynamics 68th Annual Meeting 2015, Boston, United States
 - [Calaf M., Cortina G. and Sharma V.,](#) Wind Turbine Box - energy fluxes around a characteristic wind turbine, American Physical Society, Division of Fluid Dynamics 68th Annual Meeting 2015, Boston, United States
 - [Sharma V., Calaf M. and Parlange M.B.,](#) An LES study of a large wind farm during a realistic (CASES99) diurnal cycle, WINDFARMS 2015, Leuven, Belgium
 - [Cortina G., Sharma V. and Calaf M.,](#) Turbulence analysis upstream of a wind turbine: a LES approach to improve wind LIDAR technology, WINDFARMS 2015, Leuven, Belgium
 - [Calaf M., Cortina G., Dinkar Y. and Sharma V.,](#) Wind Turbine Box: the flow around a characteristic wind turbine, WINDFARMS 2015, Leuven, Belgium
 - [Sharma V., Calaf M. and Parlange M.B.,](#) Large Eddy Simulation of a large wind farm during a diurnal cycle: Analysis of Energy and Scalar Flux budgets, American Geophysical Union Fall Meeting 2014, San Francisco, United States

Teaching Assistantships

Fall 2014 Analysis III: Vector Calculus

- Spring 2015 Analysis IV: Complex analysis and Fourier Methods
- Fall 2015 Numerical Analysis: Computational methods for performing interpolation, derivation, integration, solving linear systems and ODEs / PDEs using MATLAB
- Spring 2016 Atmospheric Physics: Introductory course for undergraduates in Environmental Engineering
- Fall 2016 Numerical Analysis: Computational methods for performing interpolation, derivation, integration, solving linear systems and ODEs / PDEs using MATLAB
- Spring 2017 Atmospheric Physics: Introductory course for undergraduates in Environmental Engineering

Previous Research Experience

- 2013 **Research Assistant**, *Laboratory of Computational Neuroscience*, EPFL.
Bayesian Experimental Design for modelling risky decision making; role of noisy observations in inference of utility model parameters; concepts of coding theory to model human behaviour
- 2011–2013 **Research Assistant**, *Laboratory of Environmental Fluid Mechanics*, EPFL.
Development of multi-function heat pulse probes to accurately measure soil parameters; error analysis of sensor measurements with variable timescales
- July 2012–December 2012 **Research Intern**, *Waste Management Laboratory, Department of Nuclear Energy and Safety Research*, Paul Scherrer Institut.
Computing diffusion coefficients of clays using numerical methods; homogenisation of length scales; kinetic Monte-Carlo technique to simulate clay structures

Skills

- Mathematics Computational Fluid Dynamics, Linear Algebra, Finite Element Methods, Monte-carlo methods, Bayesian Statistics,
- Programming FORTRAN, C, C++, MATLAB, Python, BASH, \LaTeX
- Parallel Computing MPI, OpenMP, Intel MKL